

AD-A277 240



Approved for public release;
distribution unlimited.

(2)

FINAL TECHNICAL REPORT

November 1, 1990 - October 31, 1993

ON

Original contains color
plates: All DTIC reproduced
items will be in black and
white.

NEW MICRO- AND MACROSCOPIC MODELS
OF CONTACT AND FRICTION

W. W. Tworzydlo, J. T. Oden, W. Cecot, and C.H. Yew

Contract Number F49620-91-C-0011

DTIC
ELECTE
MAR 23 1994
S F D

TR-93-10
November 1993

94-09079

AIR FORCE OFFICE OF SCIENTIFIC RESEARCH

110 Duncan Avenue, Ste. B115, Building 410

Bolling Air Force Base, D.C. 20332-0001

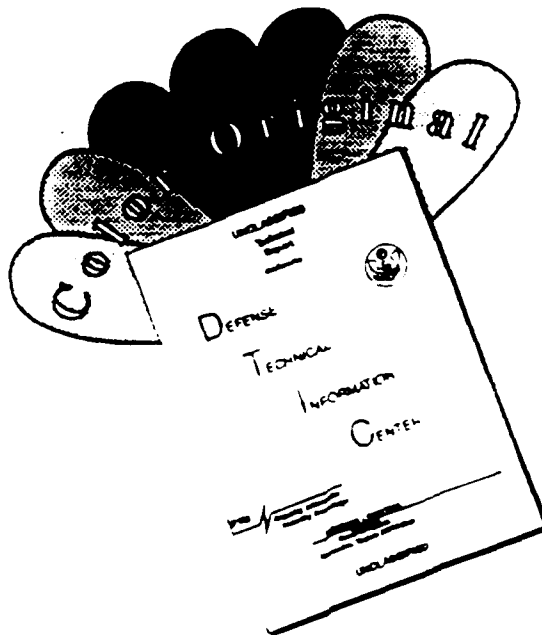
This document has been approved
for public release and sale; its
distribution is unlimited



Computational Mechanics Company, Inc.
7701 N. Lamar, Suite 200
Austin, TX 78752
(512) 467-0618

0500223394

DISCLAIMER NOTICE



THIS DOCUMENT IS BEST
QUALITY AVAILABLE. THE COPY
FURNISHED TO DTIC CONTAINED
A SIGNIFICANT NUMBER OF
COLOR PAGES WHICH DO NOT
REPRODUCE LEGIBLY ON BLACK
AND WHITE MICROFICHE.

REPORT DOCUMENTATION PAGE

Form Approved
OMB No. 0704-0188

Public reporting burden for this collection of information is estimated to average 1 hour per response, including the time for reviewing instructions, searching existing data sources, gathering and maintaining the data needed, and completing and reviewing the collection of information. Send comments regarding this burden estimate or any other aspect of this collection of information, including suggestions for reducing this burden to Washington Headquarters Services, Directorate for Information Operations and Reports, 1215 Jefferson Davis Highway, Suite 1204, Arlington, VA 22202-4302, and to the Office of Management and Budget, Paperwork Reduction Project (0704-0188), Washington, DC 20503.

1. AGENCY USE ONLY (Leave Blank)		2. REPORT DATE November 29, 1993	3. REPORT TYPE AND DATES COVERED Annual, Nov. 1, 1990-Oct. 31, 1993
4. TITLE AND SUBTITLE New Micro- and Macroscopic Models of Contact and Friction		5. FUNDING NUMBERS C-F49620-91-C-0011 PR-2304/A3-2302/C2 TA-0001AA	
6. AUTHORS W.W. Tworzydlo, W. Cecot, J.T. Oden, and C. H. Yew		7. PERFORMING ORGANIZATION NAME(S) AND ADDRESS(ES) The Computational Mechanics Co., Inc. 7701 North Lamar, Suite 200 Austin, TX 78752	
8. PERFORMING ORGANIZATION REPORT NUMBER AFOSR-TR-94-0045 TR-93-10		9. SPONSORING / MONITORING AGENCY NAME(S) AND ADDRESS(ES) The Air Force Office of Scientific Research 110 Duncan Avenue, Suite B115 Building 410 Bolling AFB, DC 20332-0001	
10. SPONSORING / MONITORING AGENCY REPORT NUMBER F49620-91-C 0011			
11. SUPPLEMENTARY NOTES			
12a. DISTRIBUTION / AVAILABILITY STATEMENT DOD Approved for public release; distribution unlimited.		12b. DISTRIBUTION CODE	
13. ABSTRACT (Maximum 200 words) This is the final report for the three year research project dedicated to the development of new asperity-based models of frictional interfaces. The main concept is to combine statistical homogenization methods with a realistic nonlinear finite element analysis of surface micro-asperities, and thus produce new asperity-based models of contact and friction.			
Research in the project started with the development of a complete theory and software for the statistical homogenization of random surface parameters. The next stage focused on the development of a finite element code for modeling surface asperities. This code is based on a proprietary h/p adaptive finite element kernel, which has been customized for the analysis of elastic and elasto-viscoplastic asperities with contact, molecular-range adhesion, and sliding resistance. To verify the new asperity-based interface models, special experiments were designed and performed for custom-shaped asperities and for rough engineering surfaces. The results of these experiments compare favorably with asperity-based theoretical and numerical predictions, and thus confirm the feasibility and practical value of the new models developed in this project.			
These models will be applicable in the analysis and control of a broad range of contact and friction phenomena, such as friction-induced squeaks and noises, tribology of bearings, electrical and thermal connectors, the mechanism of wear, and many others.			
14. SUBJECT TERMS micro-mechanics, contact, friction, asperity, adhesion, interface, finite elements, viscoplastic		15. NUMBER OF PAGES 179	
16. PRICE CODE N/A			
17. SECURITY CLASSIFICATION OF REPORT Unclassified	18. SECURITY CLASSIFICATION OF THIS PAGE Unclassified	19. SECURITY CLASSIFICATION OF ABSTRACT Unclassified	20. LIMITATION OF ABSTRACT UL

FINAL TECHNICAL REPORT

November 1, 1990 - October 31, 1993

on

**NEW MICRO- AND MACROSCOPIC MODELS
OF CONTACT AND FRICTION**

W. W. Tworzydlo, J. T. Oden, W. Cecot, and C.H. Yew

Contract Number F49620-91-C-0011

TR-93-10
November 1993

Accession For	
NTIS	CRA&I
DTIC	TAB
Unannounced	
Justification	
By _____	
Distribution / _____	
Availability Codes	
Dist	Avail and/or Special
A-1	

AIR FORCE OFFICE OF SCIENTIFIC RESEARCH
110 Duncan Avenue, Ste. B115, Building 410
Bolling Air Force Base, D.C. 20332-0001



Computational Mechanics Company, Inc.
7701 N. Lamar, Suite 200
Austin, TX 78752
(512) 467-0618

Contents

1	Introduction	1
1.1	Objectives of the Project	2
1.2	Research Summary	2
1.3	Personnel	4
1.4	Presentations, Publications, and Technology Transition	5
1.4.1	Presentations	5
1.4.2	Publications	5
1.4.3	Technology Transition	6
1.5	Outline of the Report	7
2	Asperity-Based Models of Contact and Friction	8
2.1	Microstructure of the Frictional Interface	13
2.2	Statistics of a Random Surface	16
2.3	Calculation of Surface Statistics From Profile Data	19
2.3.1	Profiles on Gaussian Isotropic Surfaces	19
2.3.2	Profiles on Gaussian Anisotropic Surfaces	22
2.4	Calculation of Asperity Statistics From Surface Statistics	23
2.4.1	Asperity Statistics for Gaussian Isotropic Surfaces	23
2.4.2	Asperity Statistics for Gaussian Anisotropic Surfaces	24
2.4.3	Asperity Statistics for Deterministic Surfaces	24
2.5	Calculation of Macrocontact Expectations of Interface Parameters	29
2.5.1	Expectation Calculation for Gaussian Isotropic Surfaces	29
2.5.2	Expectation Calculation for Random Anisotropic Surfaces	32
2.5.3	Expectation Calculation for Deterministic Surfaces	33
2.6	Numerical Verification of Statistical Postprocessing	33
2.6.1	Verification of Profile Postprocessing	33
2.6.2	Verification of Expectation Calculation	34
3	Deformation Mechanics of a Single Asperity	39
3.1	Momentum and Geometric Equations	40

3.2	Constitutive Equations	40
3.2.1	Linearly Elastic Constitutive Models	41
3.2.2	Elasto-Viscoplastic Constitutive Model With Damage	41
3.3	Boundary Conditions	45
3.3.1	Support Conditions	45
3.3.2	Contact Condition	46
3.3.3	Adhesion	48
3.3.4	Shear Resistance	51
3.3.5	Initial Conditions	52
3.4	Variational Formulation	53
3.4.1	Boundary Integrals	54
3.5	Solution Method for Elastic Contact Problems	60
3.6	Solution Method for Viscoplastic Contact Problems	62
4	Finite Element Analysis of Contact Problems with Friction	66
4.1	General Information About the 3D Finite Element Code	66
4.2	Formulation of a Structural Deformation Problem in the 3D Code	72
5	Basic Verification of Numerical Models	74
7	Verification of Numerical Models of Asperity	80
7.1	Elastic Sphere in Contact with a Rigid Flat	80
7.2	Experimental Studies of Models of Asperity	85
7.2.1	The Test Apparatus	88
7.2.2	Tests Results From the Above Apparatus	88
7.2.3	Deformation of Asperities Under a Larger Normal Load	89
7.3	Numerical Simulation of Experimental Measurements	95
7.3.1	Viscoplastic Uniaxial Stress State	95
7.3.2	Viscoplastic Cylindrical Asperity	97
7.3.3	Viscoplastic Custom Surface Model	97
8	Studies of Asperity-Based Models of Contact and Friction	106

8.1	Simulation of a Greenwood-Williamson Asperity-Based Contact Model	106
8.2	Effects of Asperity Shape	107
8.3	A very smooth engineering surface	109
8.4	Studies of a rough surface	120
9	Experimental Verification of Asperity-Based Contact Models	125
9.1	Experimental Samples, Apparatus, and Measurements	125
9.1.1	Specimen Preparation and Experimental Arrangement:	125
9.1.2	Measurement of Surface Roughness	126
9.1.3	Experimental Measurements of Contact Compliance	127
9.1.4	Specimen Preparation and Experimental Arrangement for Determining the Coefficient of Friction	138
9.2	Numerical Prediction of Interface Contact	140
9.2.1	Data for Numerical Calculations	140
9.2.2	Modeling of Surface Loading	142
9.3	Studies of Unloading	155
10	Studies of Friction	161
10.1	Static Coefficient of Friction	161
10.2	Studies of Frictional Sliding	162
11	Towards Application of Asperity-Based Models in Modeling of Dynamic Friction	170
12	Conclusions	174
13	References	175

1 Introduction

Friction and rubbing of materials are among the most common phenomena in mechanics, occurring whenever two solid bodies come into contact. These phenomena are responsible for a variety of occurrences in everyday life. Some of them, such as tire traction, are very useful; others, like violin music, are asthetic and pleasing, and many others, such as noises, vibrations, and wear, are extremely unpleasant and deleterious to mechanical systems. This common occurrence of friction and the diversity of its effects underscore the extreme importance of a deep understanding, and the need for modeling, and control of friction phenomena. It is well known, however, that the phenomena of contact and friction of solid bodies are among the most complex and difficult to model of all mechanical events, primarily due to the complex structure of engineering surfaces, the severe elasto-plastic deformation, damage, heat generation, atomic-range interactions that take place on typical contact surfaces, the presence of contaminants, lubrication, and even chemical reactions on these contact surfaces.

Efforts toward an understanding of friction phenomena and of modeling friction began with the historical works of Amontons [2] and Coulomb [32] over two centuries ago. Since then, an extensive body of experimental and theoretical work has accumulated on general tribology, and a good empirical understanding of the subject exists today. However, the progress in formulating a theoretical background and designing models of frictional interfaces have been much slower to evolve than experimental investigations. Although considerable progress in this direction has been made in recent years, there are still several issues that need to be resolved in order to model friction and predict friction phenomena with practical reliability. One of the most difficult problems encountered is the estimation of material constants occurring in new constitutive models of frictional interfaces. These difficulties reflect an urgent need for constructing new constitutive models of contact and friction and for estimating the necessary material coefficients.

Presently, there are two basic approaches for the development of mechanical constitutive models of friction and two resulting types of frictional interface models. These are:

1. phenomenological models based primarily on experimental observations, and
2. asperity-based models, formulated via a theoretical analysis and statistical homogenization of the microscale deformation of surface asperities in contact with an opposing surface.

Unfortunately, to date, none of these approaches has produced completely satisfactory results. It is well known that experimental results depend strongly on the characteristics of the test apparatus, so the results of different tests on the same sample can be considerably

scattered. Moreover, these macroscopic experimental measurements do not provide sufficient insight into the nature of the phenomena occurring on the contacting surfaces, the severity of the deformation, propagation of damage, etc. Such an insight can be provided by asperity-based models, which are based on the microscale analysis of deformation and the relative sliding of surface asperities. However, predictions made using classical or existing asperity-based models were not generally applicable to the environments normally met in engineering applications. The main reason is that these classical models were based on analytical, closed-form solutions of the deformation of a surface asperity, which required gross simplifications of the geometry of the asperity and of the constitutive models of the contacting materials (elastic, plastic, or at most elasto-plastic).

1.1 Objectives of the Project

In this project, a new approach for constructing constitutive models of friction has been developed that provides a realistic link between microscale phenomena occurring on contacting surfaces and macroscale phenomenological models of the interface. This approach involves the use of special finite element methods in the modeling of complex deformations of asperities of arbitrary shape, with realistic nonlinear constitutive models of the contacting materials. The technical approach for the evaluation of the microasperity-based models of contact and friction consists of two stages:

1. Apply the finite element technique to analyze the nonlinear mechanical responses of surface asperities of different heights, shapes, and with general viscoelastoplastic material properties.
2. Apply statistical homogenization techniques to evaluate macroscopic, phenomenological constitutive models of the interface.

The approach developed here provides a means for generating a variety of new and useful models of frictional interfaces. Depending on the selected level of complexity of the model of the asperity, a viscoelastoplastic, hyperelastic, or brittle material can be considered, the evolution of the damage to the surface can be modeled, and the effects of lubrication and surface contamination can be taken into account.

1.2 Research Summary

This final report presents the results of research work performed during the three-year project. The major tasks and results of each year are briefly summarized in this section.

The first year of the project was dedicated to building a solid foundation for the statistical homogenization procedures, as well as initial work on the finite element modeling capability. In particular, the following tasks were accomplished in the first year:

1. A detailed study of the mechanics and statistics of asperity-based models of contact, friction, and adhesion.
2. Formulation of a complete theoretical background, and development of computer codes for the calculation of macro-scale interface parameters from profilometric data of the surface and from finite element analysis of a family of representative asperities.
3. Initial work on the research-type finite element code for the nonlinear analysis of surface asperities in contact with the opposing surfaces.

In the second year of the project, the work focused on the complete development of the finite element asperity-modeling code, and on initial tests and experimental verification. This included the following tasks:

4. Development of the three-dimensional adaptive finite element code for the analysis of surface asperities in contact with opposing surfaces. The starting point for this effort was an existing in-house finite element kernel, which was extended and customized to satisfy the objectives of this project. The development effort focused on the implementation of elastic and viscoplastic three-dimensional solid models, on the development of contact and sliding resistance algorithms, as well as on extensions of the graphics, user interface, and adaptive algorithms needed for this project.
5. Design, development, and performance of Phase I of the verification experiments, which were oriented on the testing of numerical models of nonelastic surface asperities in contact with a rigid flat. Special custom-shaped “asperities” were used at this stage.
6. Verification of finite element asperity models by comparison with the analytical and experimental results. The numerical predictions were compared with existing analytical solutions for selected simplified cases (Hertz problem) and with the experimental results obtained for fully nonlinear, elastoplastic contact problems.
7. Introductory tests of the complete homogenization procedure, to study the macroscopic behavior of homogenized interfaces.

The third and final year of the project was dedicated to the actual development of new, asperity-based constitutive models for a variety of interfaces, and to their comparisons with analytical and experimental results. The particular tasks completed in the third year include:

8. Evaluation of the results of experimental verifications performed in the second year of the project.
9. Design and performance of the Phase II verification experiment, dedicated to detailed studies of the behavior of real engineering surfaces under normal and tangential loads.
10. Development of asperity-based constitutive models for the surfaces studied in the experiment, and comparison of numerical and experimental results.
11. Additional studies of the influence of surface roughness on the elasto-plastic response of the interface, as well as introductory modeling of asperity behavior under frictional loads.
12. Formulation of a theoretical background for the application of asperity-based models of interfaces in the modeling of dynamic friction phenomena. This included, in particular, development of analytical formulas (models) representing the behavior of asperity-based models.

Additionally, an extensive study of error estimation techniques and hp-adaptive mesh refinement strategies was performed for various classes of problems involving contact and friction.

The final result of this project is a proven and workable approach to the development of asperity-based constitutive models of frictional interfaces, together with relevant research-type homogenization software. These results are directly applicable in the analysis of a variety of friction phenomena, such as the kinetic coefficient of friction, friction-induced noises and vibrations, surface compliance for bearing applications, real contact area for electric and heat interfaces, and introductory studies of models of surface damage and wear.

1.3 Personnel

The research effort during the course of this project was performed by a highly specialized team of COMCO researchers. The principal investigator on the project was Dr. J. Tinsley Oden, President and Senior Scientist at COMCO. Assisting extensively on the project were Dr. W. Woytek Tworzydlo, Director of Continuum Mechanics group, and Dr. Witold Cecot, Senior Research Engineer. Additional help was provided by Dr. Jon Bass, Vice-President for Research and Technology and Mr. Olivier Hardy, Graduate Research Engineer.

A starting point for the finite element modeling capability was a proprietary adaptive finite element kernel, developed by COMCO software group.

The specialized experimental work was performed by Professor C. H. Yew of the University of Texas at Austin. The error estimation study and hp-adaptive strategy development

for problems with contact and friction was performed by C.Y. Lee, Graduate Student at the Texas Institute for Computational Mechanics (TICOM), University of Texas at Austin.

1.4 Presentations, Publications, and Technology Transition

1.4.1 Presentations

The research related to new models of contact and friction was presented at the following professional meetings:

1. 113th ASME Winter Annual Meeting,
Anaheim, California, November 8-13, 1992.
2. AFOSR Grantees and Contractors Meeting,
"Research in Computational Mechanics",
Washington University, St. Louis, May 20-21, 1993.
3. 114th ASME Winter Annual Meeting,
New Orleans, Louisiana, November 28-December 3, 1993.

1.4.2 Publications

The following friction-related papers were published or submitted for publication during the course of the project:

Ibrahim, R. A. and Soom, A., Editors, Friction-Induced Vibration, Chatter, Squeal, and Chaos, ASME, De-Vol. 49, New York, 1992, Tworzydlo, W. W., Becker, E. B., and Oden, J. T., "Numerical Modeling of Friction-Induced Vibrations and Dynamic Instabilities", pp. 13-32.

Wriggers, P. and Wagner, W., Editors, Nonlinear Computational Mechanics - State of the Art, Springer-Verlag, Berlin, 1992, Lee, C. Y., Oden, J. T. , and Ainsworth, M., "Local A Posteriori Error Estimates and Numerical Results for Contact Problems and Problems of Flow Through Porous Media", pp. 671-689.

Tworzydlo, W. W. and Oden, J. T., "Towards an automated environment in computational mechanics", Computer Methods in Applied Mechanics and Engineering, Vol. 104, pp. 87-143, 1993.

Lee, C. Y. and Oden, J. T., "A Priori Error Estimation of hp-Finite Element Approximations of Frictional Contact Problems with Normal Compliance", International Journal of Engineering Science, Vol. 31, pp. 927-952, 1993.

Ainsworth, M., Oden, J. T., and Lee, C. Y., "Local A Posteriori Error Estimators for Variational Inequalities", International Journal for Numerical Methods in Partial Differential Equations, Vol. 9, pp. 23-33, 1993.

Lee, C. Y. and Oden, J. T., "Theory and Approximation of Quasistatic Frictional Contact Problems", Computer Methods in Applied Mechanics and Engineering, Vol. 106, pp. 407-429, 1993.

Tworzydlo, W. W., Oden, J. T., Cecot, W., and Yew, C. H., "New Asperity-Based Models of Contact and Friction", ASME Publications, to appear in December, 1993.

Tworzydlo, W. W., Becker, E. B., and Oden, J. T., "Numerical Modeling of Friction-Induced Vibrations and Dynamic Instabilities", Applied Mechanics Reviews, to appear.

Two additional papers dedicated to asperity-based models of contact and friction are currently in preparation.

1.4.3 Technology Transition

The results of this contract and previous AFOSR-sponsored contracts dedicated to friction modeling are finding their way into practical applications in engineering. This includes, for example:

Tire modeling

The Oden-Martins friction model, was implemented in the TIRE3D tire modeling code, developed by COMCO under the National Tire Modeling Program (NTMP). The code is presently being used by NASA and Goodyear for analysis and design of rolling tires.

Modeling and Prediction of Friction-Induced Noises

The results of AFOSR-sponsored friction projects are being applied in practical attempts to understand, model, and eliminate friction-induced noises in industrial applications. In particular, Ford Motor Company and ORTECH International Research Institute are using the approach developed in our projects to eliminate noises in automotive components, such as the squeaking window seal in the Ford Taurus. Presently, the Computational Mechanics Company is being involved in this team to provide expertise in friction modeling.

Modeling of Earthquakes

Recently the Computational Mechanics Company was awarded a research grant from the U.S. Geological Survey, for a project dedicated to *Modeling and Prediction of Earthquakes as Unstable Phenomena of Dynamic Friction*. The research work in this project is directly based on the methodology and experience developed in previous and present contracts sponsored by the AFOSR.

Modeling of Bearings

Currently several potential R & D projects are being discussed with major bearing manufacturers. The projects under consideration will apply the results of AFOSR-sponsored research to precise modeling of contact problems inherent in bearing design, such as:

- compliance of the interface,
- real contact area,
- surface wear mechanisms, etc.

1.5 Outline of the Report

This report presents the results of the second year of effort on this project, as well as a brief compilation of the most important results of year I. In particular, Section 2 presents a study of statistical methods of homogenization of interface parameters. Of particular interest are such issues as extraction of surface statistics from profilometric data, calculation of an asperity distribution for random surfaces, and the practical calculation of expected macroscopic parameters from a microasperity analysis. In Section 3, a detailed formulation of the boundary value problem representing the deformation of a surface asperity is developed. This formulation includes elastic and viscoelastoplastic material properties, damage modeling, a nonpenetration condition on the contact plane, and boundary conditions resulting from adhesion forces and sliding resistance of the interface. Section 4 presents the background of the adaptive finite element technology developed for the analysis of the deformation of a microasperity. A general idea of the *hp*-adaptive finite element methodology is discussed in this section, together with a detailed presentation of the numerical algorithms used for the solution of elastic and viscoplastic contact problems.

The above theoretical part of the report is followed by examples and tests of the microasperity analysis. In particular, Section 5 presents some basic tests of numerical models of viscoplastic material behavior. Then, in Section 6, finite element models of asperity response are verified by comparison with the Hertz solution and with experimental measurements performed for custom-shaped asperities. This section is followed by studies of asperity-based interface models for various types of engineering surfaces (Section 7). Then, in Section 8, detailed comparisons of asperity-based models with results of specially designed experiments are presented. Following Section 9 is dedicated to studies of the static coefficient of friction for the interfaces. Section 10 presents studies directed towards application of asperity-based interface models in modeling of dynamic friction phenomena. Finally, in Section 11, conclusions of this work are summarized together with remaining research challenges.

2 Asperity-Based Models of Contact and Friction

One of the major missions in tribology is the development of constitutive models of frictional interfaces. Throughout the decades a variety of approaches and types of models have been developed. They can be classified into several groups, including:

- models based on experimental observations,
- microasperity-based models,
- phenomenological models developed from basic principles of mechanics, and
- models of the type related to plasticity theory.

It should be noted here that this distinction is only of a general nature and most of the models presented in the literature combine, in some sense, features of more than one of these groups.

In this project we focus on the development of new asperity-based models of contact and friction. These models are aimed at the development of constitutive equations of frictional interfaces via the statistical homogenization of the deformation of surface asperities subject to contact with an opposing surface. The advantage of the asperity-based models is that they provide good quantitative insight into the phenomena occurring at the interface and predict additional information hardly available from the experiment-based laws, such as the surface plasticity indices, microfracture indices, etc.

The first contact model that was constructed to predict the true contact area can be found in a paper by Abbott and Firestone [1], in which the contact surface was simulated in a network of spheres that are truncated upon indentation into a hard flat. By knowing the hardness of the softer of the two materials in contact, an estimate of the true contact area could be made, assuming perfectly plastic deformations.

An important advance in development of asperity-based models of contact is represented by the pioneering paper of Greenwood and Williamson [44], in which the rough surfaces were viewed as a randomly distributed population of elastic asperities with randomly distributed asperity heights. Each asperity was assumed to be spherical and elastic and its deformation properties governed by the Hertz solution for elastic contact. Experimental evidence was provided to support the assertion, now widely held by tribologists, that for normally isotropic engineering surfaces, a Gaussian distribution of asperities heights generally exists. In such models, there are no microfrictional effects on the asperities, such effects leading to second-order changes in contact pressure, a result established nearly two decades earlier by Mindlin [62]. In a related paper, Greenwood and Tripp [43] showed that contact of two rough surfaces

with Gaussian distributions of asperity heights on which asperity contacts were misaligned was equivalent to a single elastic surface with a Gaussian distribution of asperity heights impinging on a rigid flat. The use of such statistical representations of surface topography has since become a popular approach in modeling both elastic and inelastic contact.

The Greenwood-Williamson model was based on the assumption that only the asperity height was a random variable, and that the radius R of each peak was constant. Several generalizations of such random topography models appeared in the literature of the 1970s. The paper of Whitehouse and Archard [95] extends the random-asperity models to include random heights and curvatures, and Nayak [68] provided a general approach to random surface modeling using notions of joint probability distribution functions. In this same vein, we mention the work of Bush, Gibson, and Thomas [23], who derived a joint probability distribution density function for random asperity heights and curvatures of a random population of elliptic paraboloids in elastic contact with a smooth rigid flat.

Such random-microtopography models that employ a deterministic function for asperity peak shapes are called *asperity models*. One source of possible inconsistency in such models has to do with the fact that a Gaussian distribution of asperity heights and curvatures for a given asperity shape may lead to a non-Gaussian cumulative probability distribution of the surface height, an unrealistic result for most “engineering surfaces.” This problem was addressed by Hisakado [49] and Hisakado and Tsukizoe [50], by assuming a Gaussian PDF (Probability Density Function) for surface heights, with a given deterministic asperity shape, and then deriving the PDF for peak heights. Hisakado [49] assumed a paraboloidal asperity shape and Hisakado and Tsukizoe [50] a conical shape. Francis [41] points out that the Hisakado models may lead to unrealistic PDFs for asperity heights, since they may be strongly dependent on the asperity shape and may become negative for paraboloidal and conical shapes.

Extensions of asperity-based models to microcontact deformation laws involving elasto-plastic deformations were first contributed by Hisakado [49]. Halling and Nuri [47] account for plastic deformation of the interface by assuming that a rough surface deforms elastically while contacting a nonlinearly elastic flat, representing strain-hardening, with each micro-contact defined by a fully-plastic spherical indentation. Significant generalizations of these types of asperity models can be found in the detailed studies of Francis [41], who introduces the notion of the *sum surface*, discussed later in the present work. This enables one to model Gaussian engineering surfaces with asperity shapes that are paraboloidal only at their vertices, but which have random heights and curvatures, using the joint PDF of Nayak [68]. Moreover, Francis [41] also takes into account elastic and fully plastic deformations, with strain-hardening, using functions determined empirically from spherical indentations of various metals. We also mention that an extension of the Greenwood-Williamson model of spherical asperities with Hertzian elastic contact, constant radii, and random heights to

cases in which a transition to perfectly plastic deformations occur was recently proposed by Chang, Etsion, and Bogy [26-28].

We note that most of the references cited above dealt with attempts to model either contact without sliding motion, or purely static or quasi-static friction effects.

The asperity-based models of frictional interfaces are constructed in five basic steps:

1. Perform a statistical analysis for the surface profile (profiles),
2. calculate the surface statistics (distribution of surface height, gradient, and curvature) from one or more set of profile data,
3. calculate, from surface statistics, the probability distribution and density of surface asperities of different heights and (possibly) peak shapes,
4. calculate, by analytical or numerical methods, responses of representatives of a family of surface asperities of different shapes to prescribed load programs,
5. calculate, from asperity data and the probabilistic distribution of asperities, the expected values of the interface response (normal and tangential forces, damage, etc.) to prescribed load programs. This response characterizes constitutive properties of the interface.

Several variations of this basic scheme may be derived for random and deterministic surfaces, isotropic or anisotropic finish, etc. In this case a general classification of surfaces presented (after Nayak [68]) in Fig. 2.1 is helpful.

For practical purposes, it is reasonable to consider the following three classes:

- (i) Gaussian isotropic surfaces,
- (ii) Gaussian anisotropic surfaces, and
- (iii) other surfaces, in particular deterministic surfaces obtained by special finishing techniques.

The flowchart illustrating the homogenization procedure for these three groups is presented in Fig. 2.2.

The details of these procedures will be discussed later. Here it is important to observe that for Gaussian isotropic surfaces it suffices to gather profilometric data along only one profile on the surface and to consider asperities of axisymmetric peak shapes. For Gaussian *anisotropic* surfaces, however, one needs at least three nonparallel profiles and asperities of

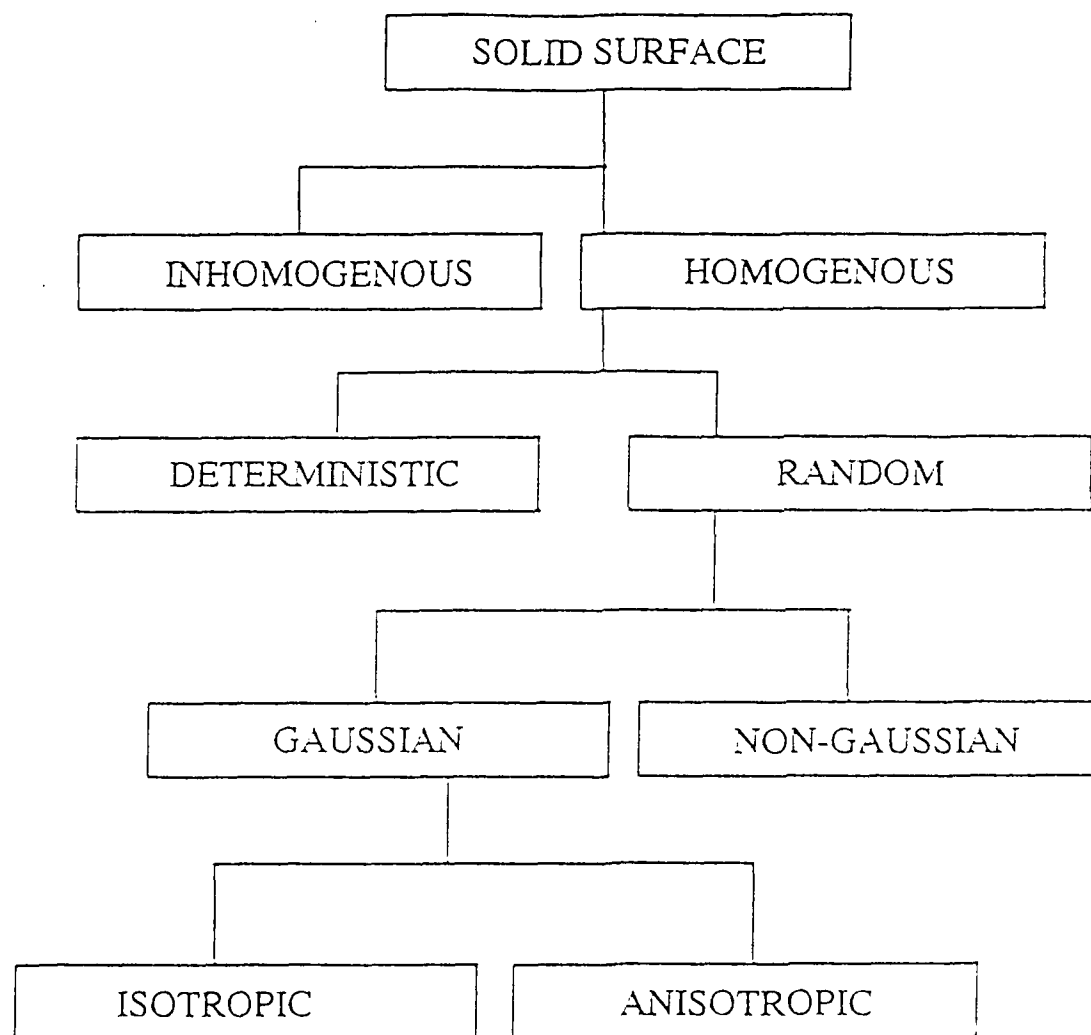


Figure 2.1: A general classification of surfaces.

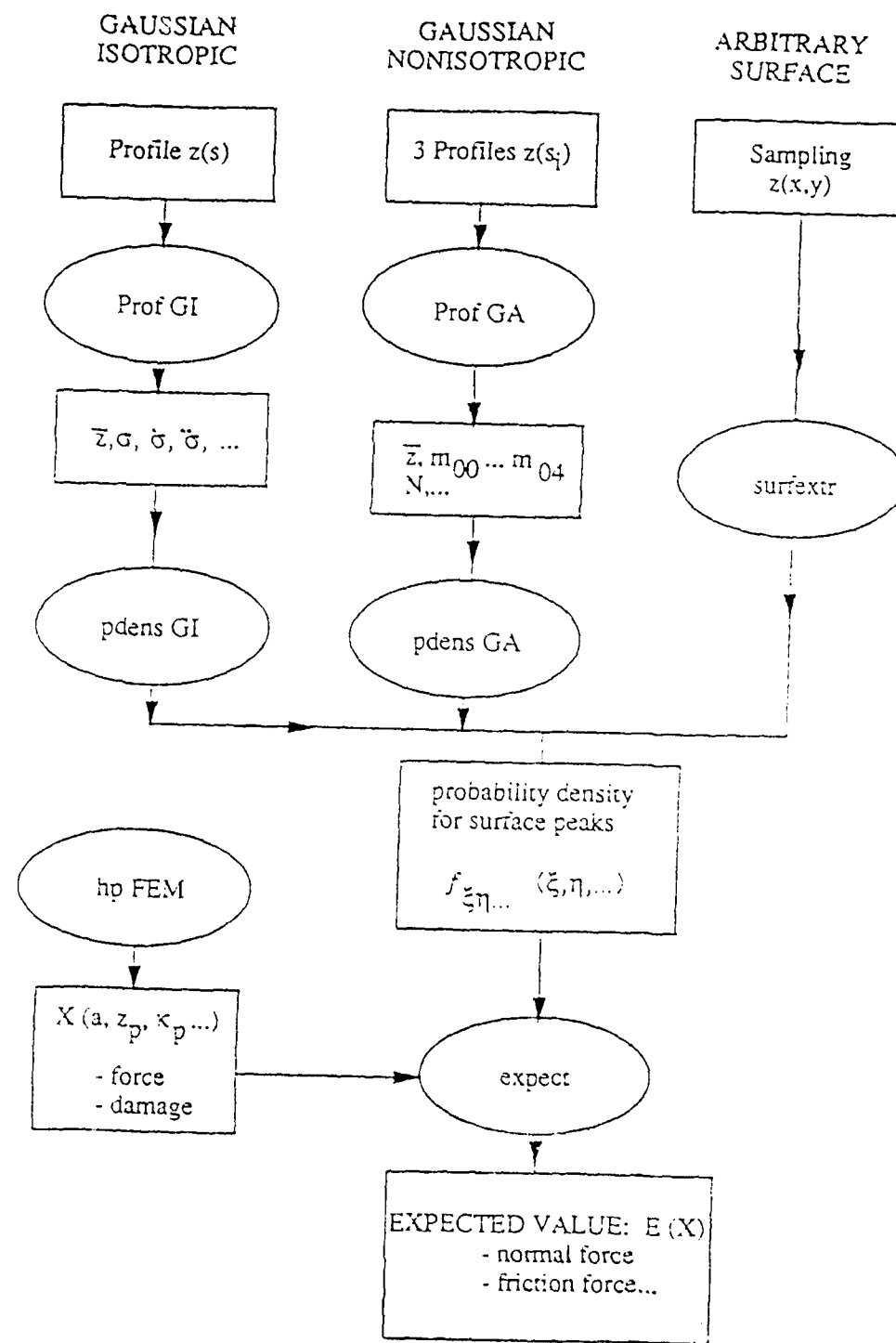


Figure 2.2: Flowchart for statistical homogenization of interfaces.

different principal curvatures and orientations. Finally, for non-random surfaces, a full two-dimensional map $z = z(x, y)$ of the surface may be needed, and asperities may have various deterministic shapes, depending on the surface finish.

2.1 Microstructure of the Frictional Interface

We begin by considering the contact of two deformable bodies, I and II , over a nominal contact area A_0 , as illustrated in Fig. 2.3. An element of unit nominal contact area is isolated for study, as indicated in the figure. The average stress vector Σ over the unit contact area has components of force P and Q normal and tangential to the unit area, respectively. The situation is equivalent to that of two typical coupons of surface material, one taken from the material near the contact surface of each body, pressed together with a force P normal to the tangent plane at the center of the coupon interface and simultaneously subjected to a shear force Q tangent to the plane. The bulk deformations of bodies I and II are ignored, our aim being only to characterize the mechanical properties of the contact interface. The nominal unit surfaces in contact are, for the present, assumed to be initially flat and parallel to one another.

It is standard practice to depict the approximate profile of rough engineering surfaces with a profilometer or stylus, drawn across the surface, which generally yields a jagged profile with an exaggerated vertical scale of the type shown in Fig. 2.4(a). We consider two such opposing surfaces 1 and 2 which are to ultimately come in contact. Reference planes defining the mean asperity height of each surface profile are established, and we characterize the shape of each profile by introducing functions z_1 and z_2 , given the height of asperities above the respective reference planes, i.e., the functions $z_i = z_i(x, y)$, $i = 1, 2$, with (x, y) a point in the parallel mean-height reference planes, define the profiles of the rough material surfaces 1 and 2, respectively. The distance h between planes is the separation of the surfaces, and the distance between actual opposing material points is denoted s . Thus, at a point (x, y) on the reference plane, we have

$$s = h - z \quad (2.1)$$

where z is the *sum surface* (see Francis [41]),

$$z = z_1 + z_2$$

Francis has pointed out that, from the fact that the sum z of the surface heights appears in the geometric relation (2.1), the situation is equivalent to that of a single deformable surface of height $z = z_1 + z_2$ approaching a rigid flat, as suggested in Fig. 2.4(b).

Clearly, the undeformed surfaces overlap whenever

$$s(x, y) < 0$$

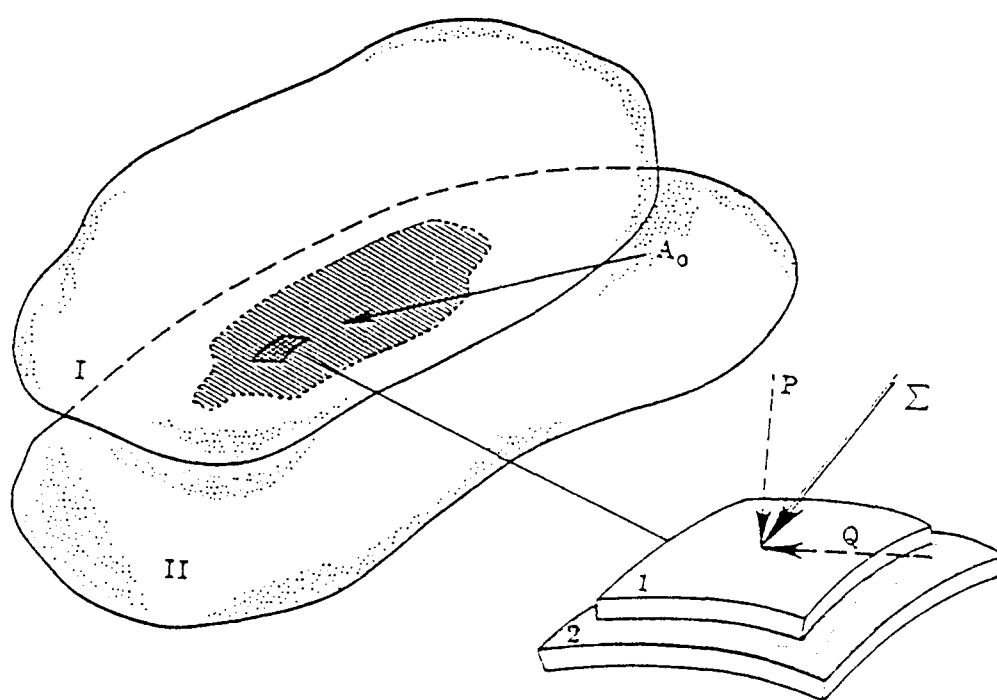


Figure 2.3: Contacting bodies and coupons near the contact interface subjected to an average stress vector of magnitude Σ .

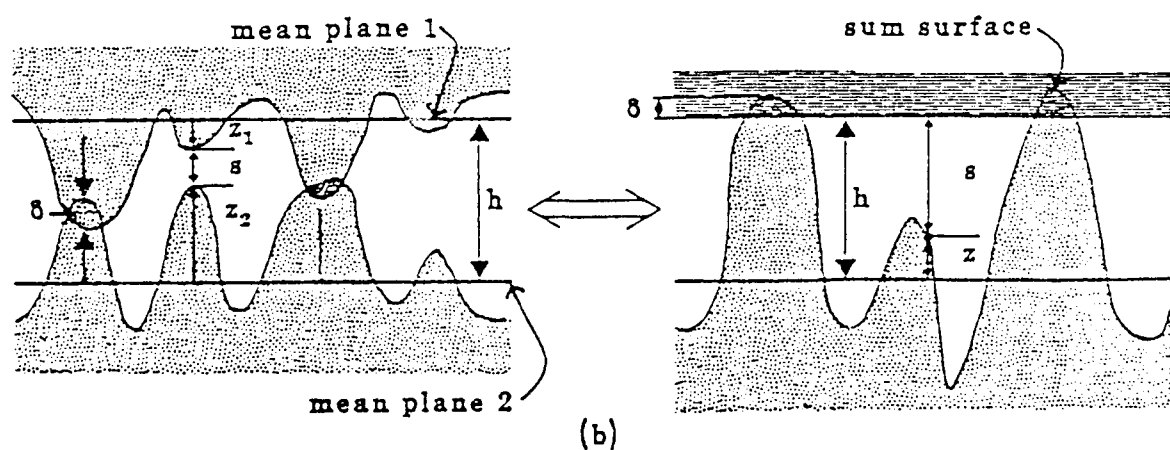
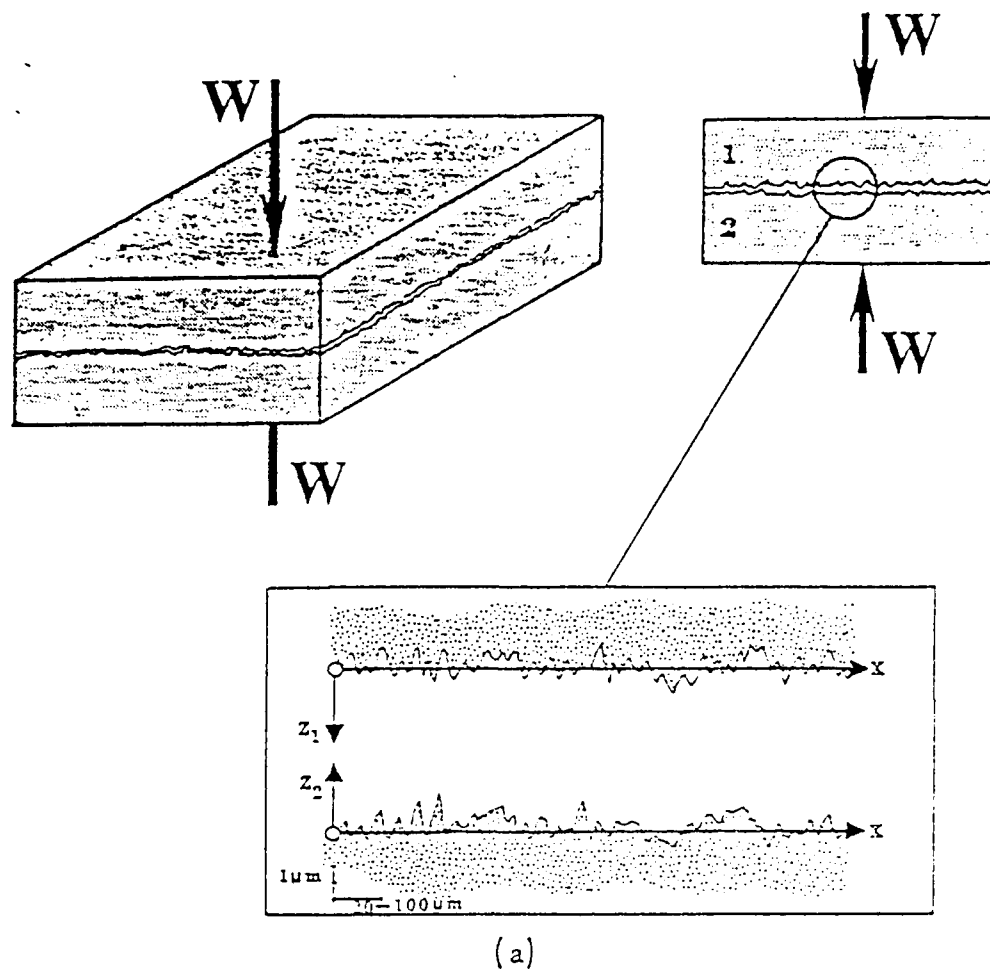


Figure 2.4: (a) Profiles of opposing rough surfaces, and (b) microtopography of surfaces and the equivalent sum surface z .

As the normal load pressing the surfaces together increases, the separation h decreases and at each minimum of the function s a microcontact nucleates and expands due to local deformation of the surfaces.

It is of importance to note that arguments presented by Francis [41] are of a purely geometric nature. From a mechanical point of view, two major objections can be raised here:

1. The sum of two asperities (say, spherical) in contact with a rigid flat is not mechanically equivalent to two spheres in contact—see Fig. 2.5.

In particular, the distance-force curves $P = P(a)$ for the two models are different. Moreover, the “asperity” peak on the sum surface corresponding to two spheres is not spherical. It can be shown, however, using the Hertz solution, that these differences vanish when the ratio of asperity radius R to the contact radius r goes to infinity (relatively smooth surfaces at moderate loads).

2. In the case of contact with friction, the sum surface approach will not model the friction component due to the interlocking of asperities. Similarly as above, the importance of this effect diminishes with increasing surface smoothness.

In view of these remarks, the sum surface approach seems to be correct and justified for typical engineering surface finishes at moderate loads. Note that this condition is also required for the satisfaction of the assumption that separate microcontacts do not interact mechanically and that contacts do not merge.

It is well known in tribology that techniques used to produce engineering surfaces usually produce a Gaussian distribution of the surface heights z_i . Moreover, the sum z of two Gaussian surfaces is also Gaussian; indeed, Tallian [85] points out that if z_1 and z_2 are not exactly Gaussian, their sum surface will be closer to Gaussian than either surface. If the shape of an asperity is assumed to be paraboloidal, as have been done by several authors, then the peak heights and curvatures are correlated random variables, with the result that a Gaussian distribution of heights and curvatures may lead to a cumulative probability distribution of surface heights which is non-Gaussian. This issue has been studied by Hisakado [49], Hisakado and Tsukizoe [50], and by Francis [41], who assert that if the peak shape is paraboloidal only at its vertex, then the ensemble of peaks can be made to conform to the Gaussian distribution.

2.2 Statistics of a Random Surface

There are several methods of homogenization that can be found in the literature. Few have been effectively used for describing nonlinear frictional phenomena. As one possible

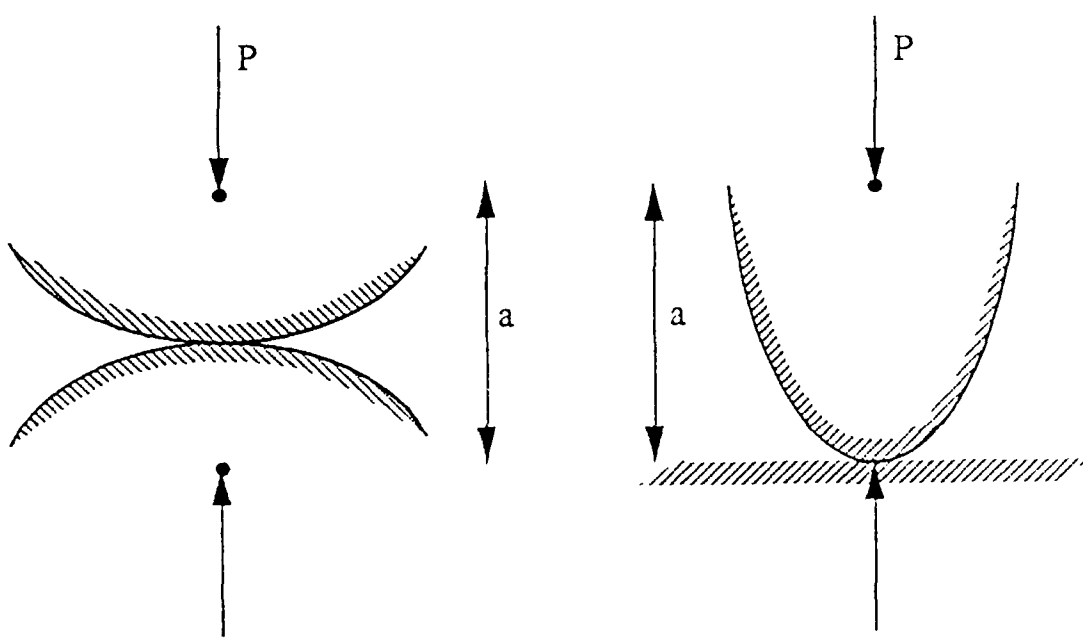


Figure 2.5: Mechanical difference between asperity behavior and sum surface model.

technique we describe a general approach inspired by the works of Lonquet-Higgins [57-59], Nayak [68], and Francis [41]; see also Chang, Etsion, and Bogy [26-28]. To fix some of these ideas, we note that for a given asperity profile, one defines the autocorrelation function $C(X, Y)$ for the random variable $z = z(x, y)$ (the surface height),

$$C(X, Y) = \lim_{\substack{a \rightarrow \infty \\ b \rightarrow \infty}} \frac{1}{ab} \int_0^a \int_0^b z(x, y)z(x + X, y + Y) dx dy$$

and the power spectral density $P(k_x, k_y)$ as its Fourier transform,

$$P(k_x, k_y) = \frac{1}{4\pi^2} \int_{-\infty}^{\infty} \int_{-\infty}^{\infty} C(X, Y) \exp[-i(Xk_x + Yk_y)] dX dY$$

The power spectral moments are

$$m_{ij} = \int_{-\infty}^{\infty} \int_{-\infty}^{\infty} P(k_x, k_y) k_x^i k_y^j dk_x dk_y \quad (2.2)$$

and the r.m.s. roughness σ is the variance,

$$\sigma^2 = m_{00} = C(0, 0) = \int_{-\infty}^{\infty} \int_{-\infty}^{\infty} P(k_x, k_y) dk_x dk_y$$

A convenient representation of a continuous random surface is of the form [58,68]:

$$z(x, y) = \sum_{n=1}^{\infty} C_n \cos(xk_{xn} + yk_{yn} + \varepsilon_n) \quad (2.3)$$

where amplitudes C_n , wave numbers k_{xn} and k_{yn} , and phase ε_n are random variables. It is assumed that there are an infinite number of wave vectors in any area $dk_x dk_y$ and that ε has a uniform probability density in the range $(0, 2\pi)$. The power spectral density is related to representation (2.3) by

$$P(k_x, k_y) dk_x dk_y = \frac{1}{2} \sum_{\Delta k} C_n^2$$

the summation being over all terms with (k_{nx}, k_{ny}) lying in the area $dk_x dk_y$ around (k_x, k_y) . The power spectral moments m_{pq} can then be expressed as

$$m_{pq} = \frac{1}{2} \sum_n k_{xn}^p k_{yn}^q C_n^2 \quad (2.4)$$

Similar definitions and representations as above can be introduced for arbitrary surface profile $z(s)$, s being a parameter on the surface. Of particular interest are spectral moments of a profile m_0 , m_2 , and m_4 .

2.3 Calculation of Surface Statistics From Profile Data

Information about the statistics of a two-dimensional surface can be effectively obtained from profilometric data for one or more profiles on the surface. This greatly simplifies the homogenization procedure because both experimental measurements and statistical post-processing are much easier for one-dimensional profiles. In this section we discuss details of these computations for both isotropic and anisotropic surfaces.

2.3.1 Profiles on Gaussian Isotropic Surfaces

It was shown by Lonquet-Higgins [57-59] and Nayak [68] that for random isotropic surfaces the mean surface height and non-zero spectral moments are expressed in terms of mean profile height and profile spectral moments:

$$\begin{aligned}\bar{z}_{\text{surface}} &= \bar{z}_{\text{profile}} \\ m_{00} &= m_0 \\ m_{20} = m_{02} &= m_2 \\ 3m_{22} = m_{04} = m_{40} &= m_4\end{aligned}$$

Therefore, in order to calculate surface statistics it suffices to perform measurements for one profile on the surface. The spectral moments of the profile can be calculated in several ways:

- from the definition as moments of power spectral density
- from statistical postprocessing (sampling) of profile data
- from counting zeros and extrema of the profile

Calculation from definition:

$$m_i = \int_{-\infty}^{\infty} \Phi(k) k^i dk$$

where k is a wave number and $\Phi(k)$ is a power spectral density. This particular method is rather expensive because it requires evaluation of the autocorrelation function and the power spectral density as its Fourier transform.

It is much easier to calculate profile spectral moments if one reinterprets them as standard deviations $\sigma, \dot{\sigma}, \ddot{\sigma}$ of profile heights z , slopes \dot{z} , and curvatures \ddot{z} , respectively:

$$m_0 = \sigma^2$$

$$m_2 = \dot{\sigma}^2$$

$$m_4 = \ddot{\sigma}^2$$

Assuming that the profile data was sampled at n points separated by the interval Δs (see Fig. 2.6), the profile statistics can be calculated from the following sampling formulas [16]:

(a) mean height, slope and curvature:

$$\bar{z} = \frac{1}{n} \sum_{i=1}^n z_i$$

$$\bar{\dot{z}} = \frac{1}{n} \sum_{i=1}^n \dot{z}_i$$

$$\bar{\ddot{z}} = \frac{1}{n} \sum_{i=1}^n \ddot{z}_i$$

(b) variations of height, slope and curvature:

$$\sigma^2 = \frac{1}{n-1} \sum_{i=1}^n (z_i - \bar{z})^2$$

$$\dot{\sigma}^2 = \frac{1}{n-1} \sum_{i=1}^n (\dot{z}_i - \bar{\dot{z}})^2$$

$$\ddot{\sigma}^2 = \frac{1}{n-1} \sum_{i=1}^n (\ddot{z}_i - \bar{\ddot{z}})^2$$

The values of first and second derivatives can be calculated from a second order approximation of the profile shape, discussed in Appendix A.1. Note that the mean slope and mean curvature of a perfect Gaussian profile should be zero. For real profiles they may slightly differ from zero. Also note that for the above procedure, shorter wavelengths can be automatically filtered out by appropriate selection of the sampling interval Δs .

An ingenuous alternative way of calculating m_2 and m_4 was proposed by Lonquet-Higgins [58], see also Nayak [68]. The densities of zeros and of extrema of the profile are expressed through spectral moments as:

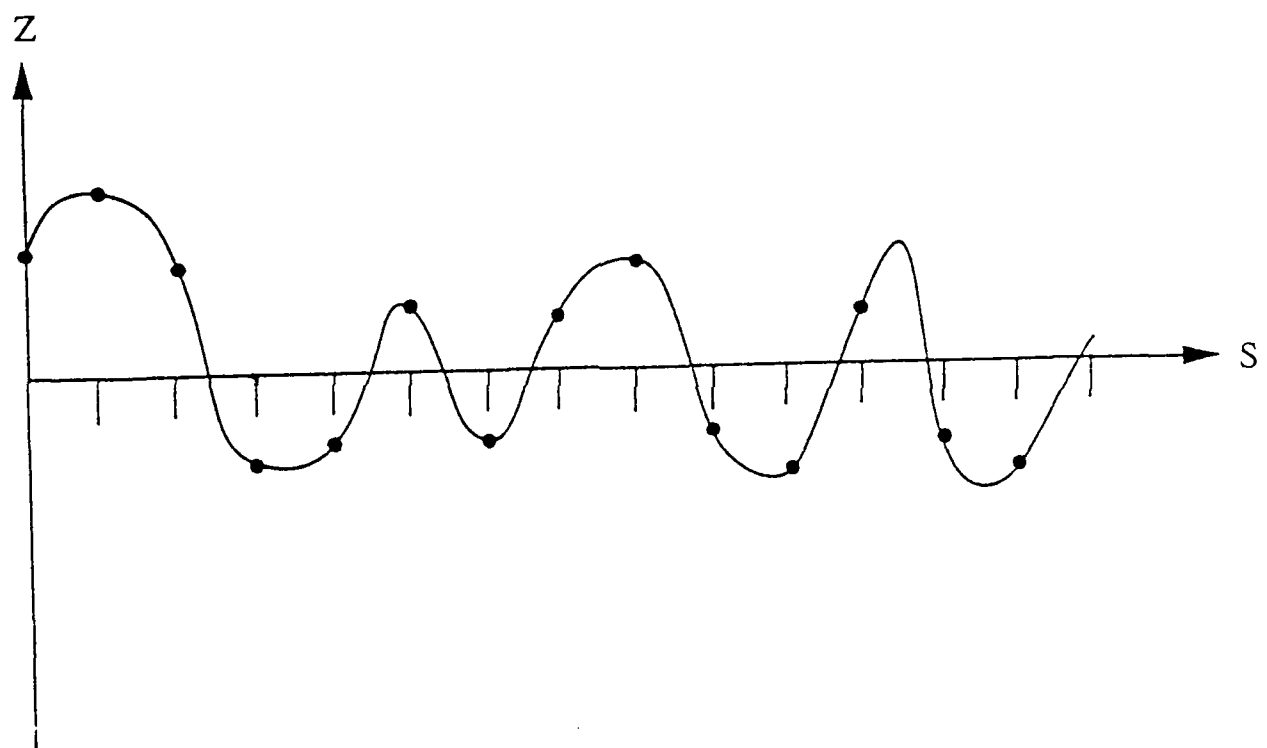


Figure 2.6: Sampling of profilometric data.

$$D_{\text{zero}} = \frac{1}{\pi} \left(\frac{m_2}{m_0} \right)^{\frac{1}{2}} = \frac{1}{\pi} \frac{\dot{\sigma}}{\sigma}$$

$$D_{\text{extr}} = \frac{1}{\pi} \left(\frac{m_4}{m_2} \right)^{\frac{1}{2}} = \frac{1}{\pi} \frac{\ddot{\sigma}}{\dot{\sigma}}$$

By zero point we mean here the point where $z(s) = \bar{z}$. The counting of zeros and extrema can be performed simultaneously with the sampling procedure described above. Then, after calculation of the variation σ , variations of slopes and curvatures can be obtained as:

$$\begin{aligned}\dot{\sigma} &= \pi\sigma D_{\text{zero}} \\ \ddot{\sigma} &= \pi\dot{\sigma} D_{\text{extr}}\end{aligned}$$

In practice, both sampling and counting methods can be easily implemented in the same sampling program. Practical comparisons of these procedures are presented further in this report.

Another parameter necessary for the homogenization procedure is a density of peaks on the surface, defined for homogenous surfaces as:

$$D_p = \lim_{\substack{dx \rightarrow \infty \\ dy \rightarrow \infty}} \frac{N_p}{dA}$$

where $dA = dx dy$ is the surface area and N_p is the number of asperity peaks within this area. The density of surface peaks can be calculated from profile parameters [68] as:

$$D_p = \frac{1}{6\pi\sqrt{3}} \frac{m_4}{m_2}$$

2.3.2 Profiles on Gaussian Anisotropic Surfaces

Basic statistical information for anisotropic random surfaces consists of nine moments of the power spectral density: m_{00}, \dots, m_{40} . However, since the properties of the surface do not depend on the orientation of the x, y axes, only certain invariant combinations appear in the probability distribution of the surface statistics [59,68]. These invariants are:

1. m_{00}
2. $m_{02} + m_{20}$

3. $m_{20}m_{02} - m_{11}^2$
4. $m_{40} + 2m_{22} + m_{04}$
5. $m_{40}m_{04} - 4m_{13}m_{31} + 3m_{22}^2$
6. $(m_{40} + m_{22})(m_{22} + m_{04}) - (m_{31} + m_{13})^2$
7. $\{m_{40}(m_{22}m_{04} - m_{13}^2) - m_{31}(m_{31}m_{04} - m_{13}m_{22}) + m_{22}(m_{31}m_{13} - m_{22}^2)\}$

From three profiles in three nonparallel directions $\theta_i, i = 1, 2, 3$ nine parameters can be defined: $m_{0(i)}, m_{2(i)}, m_{4(i)}, i = 1, 2, 3$. However, since $m_{0(1)} = m_{0(2)} = m_{0(3)}$, then these three profiles define seven constants— invariants described above. This means that three nonparallel profiles suffice to define surface statistics for Gaussian anisotropic surfaces. (Detailed equations will not be derived here.)

2.4 Calculation of Asperity Statistics From Surface Statistics

The primary idea of asperity-based interface models is to calculate interface parameters (normal force, friction force, etc.) for a family of asperities of certain deterministic shapes and to obtain expected values of these parameters for the interface from a statistical distribution of asperities. This requires the calculation of probability density of surface asperities. For random surfaces, this probability density can be expressed in terms of surface statistics. This problem will be addressed in this section.

2.4.1 Asperity Statistics for Gaussian Isotropic Surfaces

For Gaussian isotropic surfaces two random variables are assumed to govern the distribution of asperities: asperity peak height z_p and mean curvature κ . The joint probability density function of these parameters was derived by Nayak [68] and recast in a different form by Francis [41]. Here we present the formula due to Francis:

$$f_{\xi\eta}(\xi, \eta) = \frac{\sqrt{3}}{\pi\sqrt{1-\beta^2}} \left\{ \eta^2 - 1 + e^{-\eta^2} \right\} e^{\frac{-1}{2(1-\beta^2)}(\xi^2 - 2\beta\xi^2\eta + \eta^2)}$$

where

$$\xi = \frac{z_p}{\sigma} \quad \text{nondimensional peak height}$$

$$\eta = \sqrt{1.5} \frac{\kappa}{\bar{\sigma}} \quad \text{nondimensional peak curvature}$$

$$\beta = \sqrt{1.5} \frac{\dot{\sigma}^2}{\sigma\ddot{\sigma}} \quad \text{wavelength spectrum parameter}$$

The wavelength spectrum parameter varies for random surfaces between 0 and 1: zero corresponds to the widest wavelength spectrum (asperity heights and wave numbers are not correlated), and one corresponds to the narrow spectrum (longer asperities have bigger heights). Note that deterministic surfaces may have $\beta > 1$, see Section 2.6.1.

2.4.2 Asperity Statistics for Gaussian Anisotropic Surfaces

For Gaussian anisotropic surfaces the representative asperities are no longer of axisymmetric shape. Instead, one should consider asperities with elliptic horizontal cross sections, shown in Fig. 2.7b.

The peaks of these asperities can be characterized by four parameters:

1. z_p — peak height
2. κ_1, κ_2 — principal curvatures
3. α — orientation of the main axis of curvature

Equivalently, peak height z_p and three Cartesian curvatures (second derivatives of z) $\kappa_{xx}, \kappa_{xy}, \kappa_{yy}$ can be used. The joint probability density function based on all these parameters should be defined as $f_{\xi\eta_1\eta_2\alpha}(\xi, \eta_1, \eta_2, \alpha)$. In principle, this function can be defined from surface statistics, in particular spectral moments m_{00}, \dots, m_{40} [59,68]. To the author's knowledge, no such formula is presently available in a closed form.

2.4.3 Asperity Statistics for Deterministic Surfaces

Some special types of finish may produce surfaces of non-Gaussian random distribution or deterministic distribution. For such arbitrary surfaces the distribution of asperity peaks cannot be obtained from profile data and need to be calculated directly from a surface map. In this section we present a simple sampling procedure to calculate asperity statistics from surface data.

We assume that:

- The surface is homogenous.
- The function $z(x, y)$ (surface height) for the surface is given. This can be obtained from two-dimensional sampling, holography or other methods.
- Asperity peaks are characterized by the peak height z_p and mean curvature κ .

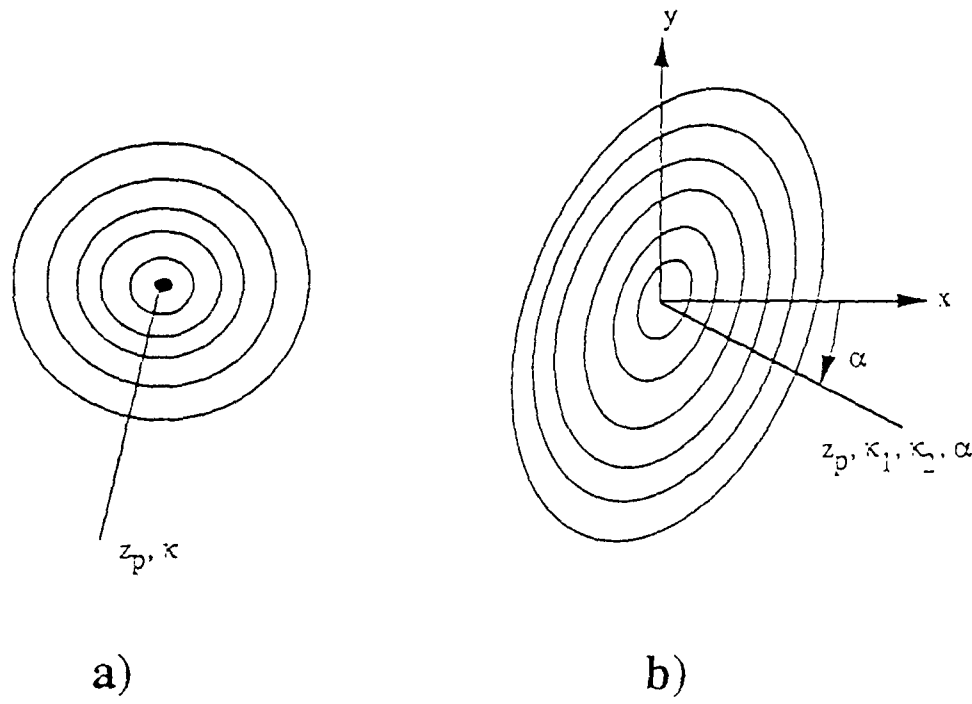


Figure 2.7: Typical asperity: (a) isotropic random surface, (b) anisotropic random surface.

The probability density of asperity height and curvature $f_{z_p \kappa}(z_p, \kappa)$ can be obtained from the following sampling procedure: Cover the domain Ω with a regular mesh of points (x_i, y_i) , $i = 1, n$ presented in Fig. 2.8. The mesh spacing h can be defined so as to filter out high-frequency noise. The sampling is performed by looping through the points (x_i, y_i) , $i = 1, n$ and for each point:

1. Check if the point is a peak or near a peak within resolution h . The peak is identified as a peak if its height $z(x_p, y_p)$ is greater than all its nearest neighbors (eight for interior points). Alternatively, more elaborate criteria may be used.
2. If the point is a peak, then calculate the second derivatives z_{xx} , z_{yy} and z_{xy} . Here simple finite difference formulas may be used or a generalized minimization procedure as presented in Appendix A.

The mean surface height and standard deviation of the surface height are calculated as:

$$\bar{z} = \frac{1}{n} \sum_{i=1}^n z_i$$

$$\sigma^2 = \frac{1}{n-1} \sum_{i=1}^n (z_i - \bar{z})^2$$

The joint probability density of asperity peak heights and curvatures can be calculated after locating all the peaks by dividing the range of peak heights and curvatures $[z_{p\min}, z_{p\max}] \times [\kappa_{\min}, \kappa_{\max}]$ into area elements $\Delta z_p \Delta \kappa$ (see Fig. 2.9). Then for each area element with a center point (z_{pi}, κ_j) define

$$f_{z\kappa}(z_{pi}, \kappa_j) = \frac{1}{N_p} n_p(i, j)$$

Here N_p is the total number of peaks and $n_p(i, j)$ is the number of peaks within the area element $\Delta z_p \Delta \kappa$, identified by:

$$z_{p\min} + (i-1)\Delta z \leq z_p < z_{p\min} + i\Delta z$$

$$\kappa_{\min} + (j-1)\Delta \kappa \leq \kappa_p < \kappa_{\min} + j\Delta \kappa$$

The values above define the discrete values of the joint probability density function of asperity peak heights and curvatures. This function may then be regularized by an application of appropriate approximation techniques. A similar procedure can be used if one chooses to characterize asperity peaks with more than two parameters, such as z_p, κ_1, κ_2 and α for anisotropic surfaces.

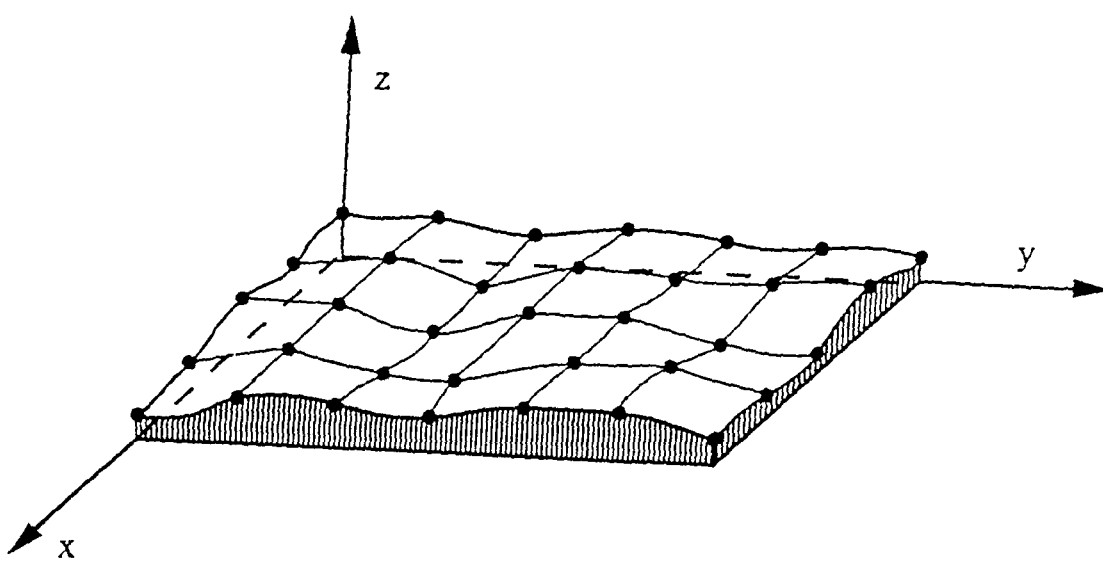


Figure 2.8: Sampling of arbitrary surface.

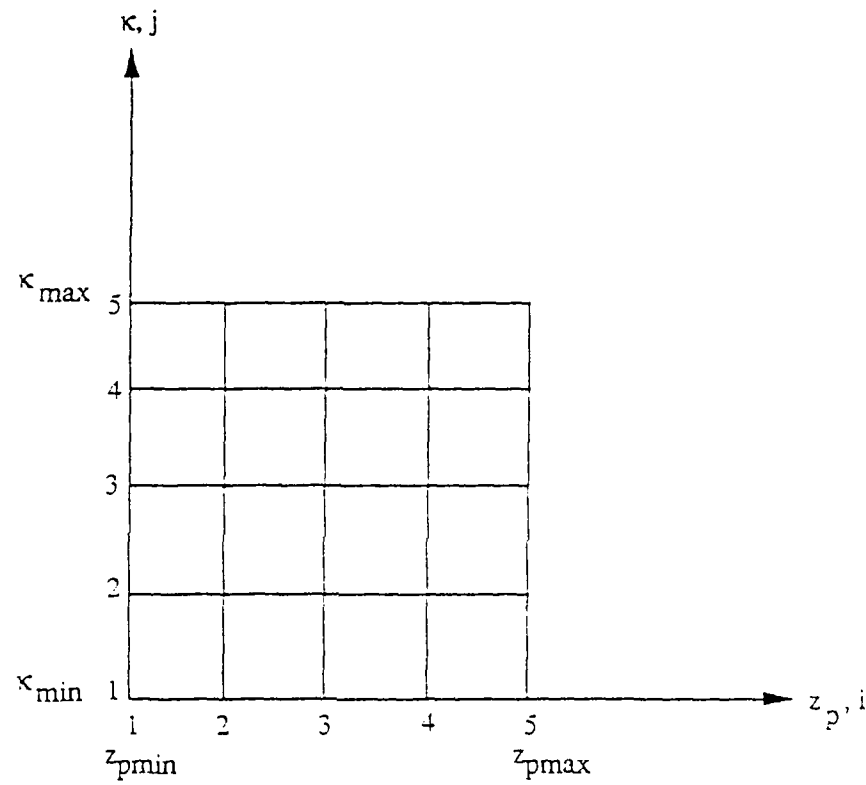


Figure 2.9: Accumulation of joint probability density $f_{z\kappa}(z_p, \kappa)$ for arbitrary surfaces.

2.5 Calculation of Macrocontact Expectations of Interface Parameters

Once we know the probability distribution of asperity heights and shapes as well as the values of any parameter X for single asperity, it is possible to calculate the expected value of X for the interface. This procedure varies somewhat depending on the classification of surface type. In this section we present a detailed procedure of the expectation calculation for Gaussian isotropic surfaces and outline its extensions to other surface types.

2.5.1 Expectation Calculation for Gaussian Isotropic Surfaces

For Gaussian isotropic surfaces, the following parameters are needed to calculate the expected value of the macroscopic interface parameter X :

- i) N_p The number of peaks within the contact area A_0 .
- ii) $f_{\xi\eta}(\xi, \eta)$ Probability density of asperity peaks of (nondimensional) height ξ and mean curvature η . By a simple change of variables one can define $f_{\xi\eta}(z_p, \kappa)$.
- iii) $X(z_p, \kappa, a, d)$ The value of parameter X for different peak heights z_p and curvatures κ , subjected to a normal approach a and sliding distance d .
- iv) $\sigma, \dot{\sigma}, \ddot{\sigma}$ Deviations of profile heights, slopes, and curvatures used to nondimensionalize peak heights and curvatures.

The expected value of X per asperity is calculated as

$$E(X(a, d)) = \int_{-\infty}^{\infty} \int_0^{\infty} X(z_p, \kappa, a, d) f_{\xi\eta}(z_p, \kappa) d\kappa dz_p \quad (2.5)$$

and the macrocontact expectation of X is

$$\widehat{X}(a, d) = N_p E(X(a, d))$$

Note that even for Gaussian isotropic surfaces there exist asperities of non-axisymmetric cross sections. However, due to isotropy, it suffices to consider only axisymmetric representatives of certain mean peak curvature κ . In this project we choose the asperity to be a cosine hill defined in a local coordinate system as:

$$z(x, y) = C \cos kx \cos ky$$

For this asperity the peak height and mean curvature are defined as

$$\begin{aligned} z_p &= C \\ \kappa &= Ck^2 \end{aligned}$$

The above shape is consistent with a generic representation of a Gaussian surface presented in formula (2.3). This is different than approaches presented to date in the literature, in which asperity peaks were usually assumed to be spherical or paraboloidal. This was because these works were based on analytical solutions for asperity deformation, such as Hertz' solution. In this work we are modeling the asperity by the finite element method, so it is possible to use the model which does not suffer from inconsistencies of spherical or paraboloidal asperity peaks.

Although for Gaussian isotropic surfaces the probability density of asperity heights and curvatures is analytic, the values of $X(z_p, \kappa, \dots)$ that we obtain from finite element computations are not. Therefore the expected value of X must be calculated using numerical quadrature. This quadrature was implemented under the following assumptions:

- (a) The domain of integration is truncated to the subregion $[z_{\min}, z_{\max}] \times [\kappa_{\min}, \kappa_{\max}]$, where the probability density $f_{\xi\eta}$ is large enough to effectively contribute to the final integral $E(X)$. This region is defined adaptively (see Section 2.6.2).
- (b) The parameter values $X(z_p, \kappa, \dots)$ are given (calculated by FEM) for certain selected values of peak heights and curvatures in the domain of integration. These points are not necessarily regularly distributed within the domain of integration.

The numerical procedure for the calculation of the integral consists of the following steps:

1. Divide area $[z_{\min}, z_{\max}] \times [\kappa_{\min}, \kappa_{\max}]$ into area elements $\Delta z \times \Delta \kappa$ (see Fig. 2.10).
2. Calculate the integral by looping over cells and applying numerical quadrature (trapezoidal, Simpson, Gauss, or any other) according to the formula

$$E(X) = \sum_{i=1}^N \left[\sum_{\alpha=1}^m \left\{ X(z_{p(\alpha)}, \kappa_{(\alpha)}, \dots) f_{\xi\eta}(z_{p(\alpha)}, \kappa_{(\alpha)}) w_{\alpha} \Delta z \Delta \kappa \right\} \right] \quad (2.6)$$

where i is the number of integration cells, α is the number of quadrature points within a cell, and w_{α} is the corresponding weight factor.

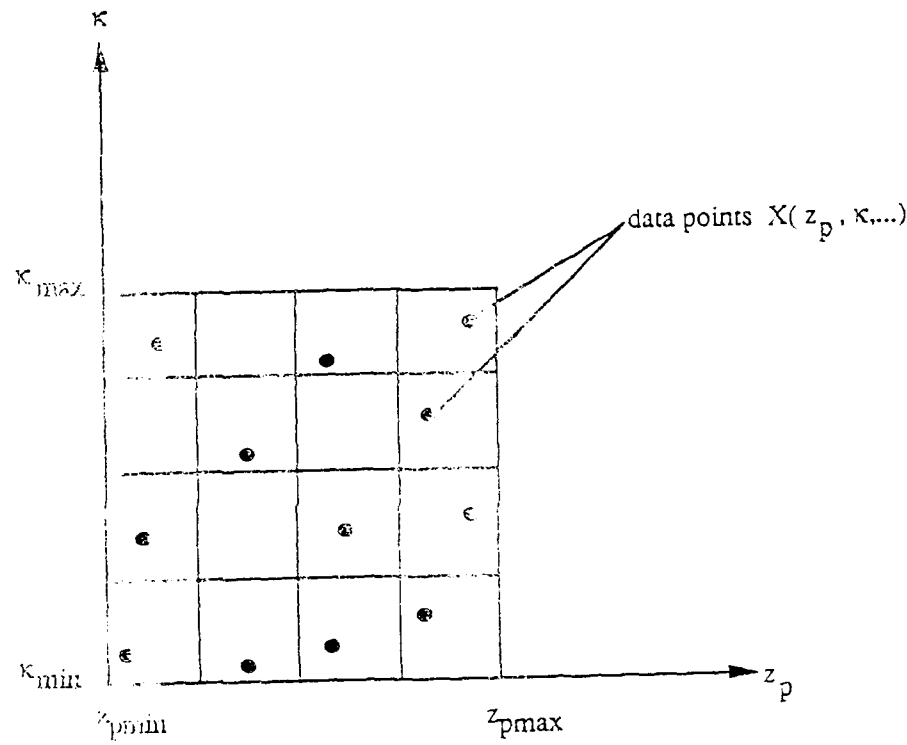


Figure 2.10: Numerical integration of expectation value $E(X)$.

Note that this integration requires the value of X at integration points $(z_{p(\alpha)}, \kappa_{(\alpha)})$ within each cell. Since it may be difficult to perform finite element analysis for values of z_p and κ corresponding exactly to all the integration points, these values are calculated from the original data points using the error minimization procedure presented in Appendix A. The quadrature rule currently implemented for integration are the trapezoidal and four-point Gauss rule.

Note that the above procedure introduces error due to truncation of the integration domain and due to numerical integration. This leads to a rather unwelcome result that even for constant X , the calculated expected value $E(X)$ would be different than X . In order to compensate for this error, we additionally calculate the integral of the probability density (which should be one):

$$I = \sum_{i=1}^N \left[\sum_{\alpha=1}^m f_{\xi\eta} (z_{(\alpha)}, \kappa_{p(\alpha)}) w_{\alpha} \Delta z \Delta \kappa \right]$$

Then the corrected value of expectation of X is calculated as:

$$\hat{E}(X) = E(X)/I \quad (2.7)$$

This procedure assures that for constant X the expected value $\hat{E}(X)$ is equal to X .

2.5.2 Expectation Calculation for Random Anisotropic Surfaces

As mentioned previously, for anisotropic Gaussian surfaces one has to consider asperities of random peak heights z_p , principal curvatures κ_1 and κ_2 , and orientations of the principal axis α . The calculation of expected values of the interface parameters is similar to equation (2.5):

$$E(X(z_p, \kappa_1, \kappa_2, \alpha, \dots)) = \int_{-\infty}^{\infty} \int_0^{\infty} \int_0^{\infty} \int_0^{2\pi} X(z_p, \kappa_1, \kappa_2, \alpha, \dots) f_{\xi\eta_1\eta_2\alpha}(z_p, \kappa_1, \kappa_2, \alpha) d\alpha d\kappa_1 d\kappa_2 dz_p \quad (2.8)$$

Note that presently there exist no closed form solution for the probability density $f_{\xi\eta_1\eta_2\alpha}$ of asperity peaks of random heights, principal curvatures and orientations. Also note that in order to span the integration space, one would need to obtain finite element solutions for a large family of asperities, corresponding to various combinations of z_p , κ_1 , κ_2 , and α . This would be a very expensive task computationally, and will not be considered in this project.

2.5.3 Expectation Calculation for Deterministic Surfaces

The calculation of expectation values $E(X)$ for non-random surfaces follows essentially the same numerical procedure as for Gaussian isotropic or anisotropic surfaces. Depending on the surface type, the peak height z_p , curvature κ and other parameters may be selected to represent typical asperities. The joint probability density $f_{\xi\eta\ldots}(z_p, \kappa, \ldots)$ can be obtained from surface sampling as discussed in Section 2.4.3.

2.6 Numerical Verification of Statistical Postprocessing

The homogenization procedures discussed in the previous section for Gaussian isotropic surfaces were used as the basis for the implementation of specialized software for this purpose. In this section, certain basic tests of this software will be presented.

2.6.1 Verification of Profile Postprocessing

The program for profile postprocessing was designed to read in the data $z(s)$ for one or more profiles on the surface, and use them to calculate mean profile height, slope and curvature as well as spectral moments and peak density for the surface. Both statistical sampling and counting methods were implemented (see Section 2.3.1).

Example 1

In the first example a deterministic cosine profile was generated:

$$z(s) = C \cos ks$$

with $C = 1$ and $k = 2$. For such a profile, the mean profile height, slope and curvature are zero. The standard deviations of height, slope and surface curvature can be calculated exactly to be:

$$\sigma = \frac{C}{\sqrt{2}} = 0.7071$$

$$\dot{\sigma} = k \frac{C}{\sqrt{2}} = 1.4142$$

$$\ddot{\sigma} = k^2 \frac{C}{\sqrt{2}} = 2.8284$$

The corresponding wavelength spectrum parameter is $\beta = 1.2247$.

The above profile was sampled with the interval 0.2 which corresponds to about 100 points per one wavelength. The results of this sampling are presented in Fig. 2.11.

The calculation of mean surface heights, slopes and curvatures (which should all be zero) is very accurate. So is the calculation of the standard deviation of surface height. Deviations of surface slopes and curvatures are less accurate (up to 7 percent error), which is caused by an approximate calculation of slopes and curvatures. For this particular case, the counting method gives better results than the statistical sampling method.

Example 2

In the second example we have generated a quasi-random profile by using a one-dimensional version of the formula (2.3). A series with 40 components of a quasi-random distribution of C_i , k_i and ε_i were specified. The resulting profile is presented graphically in Fig. 2.12a.

For a fully infinite series and random C_i , k_i and ε_i the power spectral moments are expressed by a one-dimensional equivalent of formula (2.4). For truncated series this is not true, but a reasonable approximation can be expected for the values of spectral moments. These values, calculated for the above profile, are shown in Fig. 2.12b. The profile was then sampled using the procedure described in Section 2.3.1. The results are shown in Fig. 2.12c.

It is somewhat more difficult to verify the results in this case, since neither of the methods produce exact results. It can be noted, though, that the results for surface height (mean height and deviation) are the most accurate, while for curvatures the differences reach up to about 20 percent. Other tests, not discussed here, show that with a decreasing sampling interval, these differences become smaller (but they do not vanish).

2.6.2 Verification of Expectation Calculation

To perform a basic test for the calculation of joint probability density of surface asperities and for expectation values of X , we considered the following set of test data:

1. The profile and surface statistics were taken from Example 2 in the previous section, in particular:

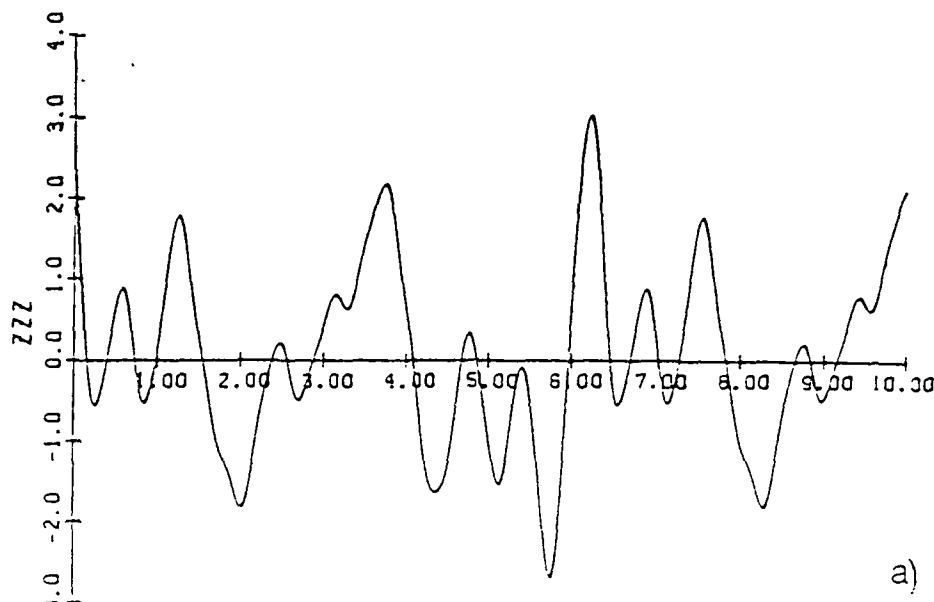
sampling results for single wave, C=1, k=2.
+++++

Sampling interval: .2

R E S U L T S

	Method 1 (sampling)	Method 2 (counting)
Mean height:	-2.8846e-05	
Mean slope:	-3.3431e-05	
Mean curvature:	-4.3874e-04	
St.D. of height:	7.0715e-01	
St.D. of slope:	1.3628e+00	1.4143e+00
St.D. of curvature:	2.6272e+00	2.7222e+00
Surface peak density:	1.1384e-01	1.2222e-01
Wavelength spectrum:	1.2243e+00	1.2727e+00

Figure 2.11: Sampling result for a simple cosinusoidal profile.



SSS X !0***!

a)

Sampling interval: .005

SURFACE STATISTICS FROM SERIES

St.D. of height:	1.1620e-00
St.D. of slope:	5.9221e-01
St.D. of curvature:	4.9315e-01
Wavelength spectrum:	7.4954e-01

b)

R E S U L T S

	Method 1 (sampling)	Method 2 (counting)
Mean height:	.6.7472e-02	
Mean slope:	-2.4911e-03	
Mean curvature:	-1.3438e-02	
St.D. of height:	1.1259e+00	
St.D. of slope:	6.5342e-01	7.0748e-01
St.D. of curvature:	5.9455e-01	5.1324e-01
Surface peak density:	2.5359e-02	1.8898e-02
Wavelength spectrum:	7.8117e-01	1.0609e+00

c)

Figure 2.12: Profile sampling test: (a) quasi-random surface profile, (b) surface statistics from series expansion, and (c) surface statistics from sampling.

$$\begin{aligned}
\sigma &= 1.1620 \\
\dot{\sigma} &= 0.59221 \\
\ddot{\sigma} &= 0.49315 \\
N_p &= 0.025359 \\
A_0 &= 1
\end{aligned}$$

2. The area of integration of expectation values $E(X)$ was defined by:

$$\begin{aligned}
z_{p\min} &= -5, \quad z_{p\max} = 10 \\
\kappa_{\min} &= 0, \quad \kappa_{\max} = 5
\end{aligned}$$

This domain was subdivided into 20×20 integration cells, with trapezoidal integration within each cell.

3. The variable X was assumed to be identically equal to one (so that the expectation value should be one). This was implemented by specifying eight data points with a value 1.0, randomly distributed within the integration domain.

The results of the numerical calculation of expectation values are presented in Fig. 2.13.

Note that the program estimates the effective support of the probability density function $f_{\xi\eta}(z_p, \kappa)$, which is identified as the loci of points where $f_{\xi\eta}(z_p, \kappa)$ is greater than 10^{-4} . This is done to avoid integration over too large a domain. The above estimate is still very safe—for example, for the profile considered here the estimated effective support of $f_{\xi\eta}(z_p, \kappa)$ corresponds to peak heights between:

$$z_{p\min} = -3.5 \quad z_{p\max} = 7.0$$

while the real profile had a maximum peak height of only 2.5 and a minimum peak height of about -0.8 .

The value of expectation $E(X)$ calculated by integration (formula (2.6)) is 1.0043. This is an effect of truncation of the integration domain and of numerical integration. After correction according to formula (2.7), the value of expectation $E(X)$ is exactly one.

This simple example confirms the correctness of the theoretical formulation and the software used for calculation of joint probability density $f_{\xi\eta}(\xi, \eta)$ and for the expectation value of X for Gaussian isotropic surfaces.

I N P U T E C H O

```
zpmmin=-5.0000e+00  zpmmax= 1.0000e+01  kapmin= 0.0000e+00  kapmax= 1.0000e+01
nksi=20  neta=20  irule=1

sigma= 1.1620e+00  sigdot= 5.9221e-01  sigdble= 4.9315e-01
npeak= 2.5359e-02  area= 1.0000e+00
```

R E S U L T S

```
Effective support of probability density:
zsmin=-3.5000e+00  zsmax= 7.0000e+00  kasmin= 0.0000e+00  kasmax= 3.0000e+00

Integrated value of X= 1.0043e+00
Expectation value of X= 1.0000e+00
Macroscopic value of X= 2.5359e-02
Value X per unit area = 2.5359e-02
```

Figure 2.13: The calculation of expection values of X .

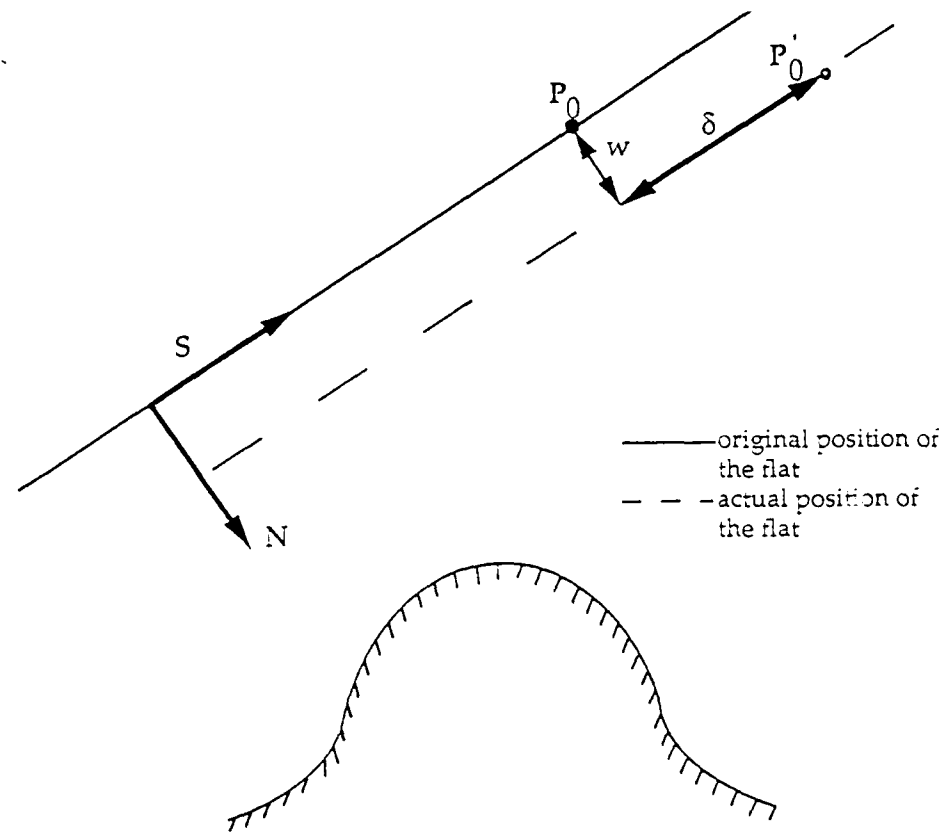


Figure 3.1: Surface asperity in contact with a rigid flat (a section).

3 Deformation Mechanics of a Single Asperity

We now focus on the analysis of a typical asperity in contact with a rigid flat. The asperity is a body of revolution, symmetric about its $z = x_3$ -axis, and subjected to adhesion pressures q on its exterior surfaces that are not in contact with the rigid flat, and to contact pressures due to its indentation into the rigid flat (see Fig. 3.1). The equations governing the deformation of the asperity are discussed below.

3.1 Momentum and Geometric Equations

The momentum equations for the asperity are:

$$\sigma_{ij,j} = 0 \quad (3.9)$$

where σ_{ij} is the Cauchy stress tensor at a point $\mathbf{x} = (x_1, x_2, x_3) \in \Omega$, Ω being the open material domain of the asperity and $\sigma_{ij,j}$ is the divergence of the stress σ_{ij} .

In rate-dependent viscoplastic applications a rate form of the equilibrium equations is used:

$$\dot{\sigma}_{ij,j} = 0 \quad (3.10)$$

where the dot denotes the time derivative.

Geometric equations express strains in terms of displacements:

$$\varepsilon_{ij} = \frac{1}{2} (u_{i,j} + u_{j,i})$$

Strains can be decomposed into elastic and nonelastic strains:

$$\varepsilon_{ij} = \varepsilon_{ij}^{(e)} + \varepsilon_{ij}^{(n)}$$

Similarly as for the momentum equations, the rate form of geometric equations will also be used:

$$\dot{\varepsilon}_{ij} = \frac{1}{2} (\dot{u}_{i,j} + \dot{u}_{j,i})$$

3.2 Constitutive Equations

Surface asperities for typical engineering surfaces consist of the same material as the bulk body with possible contaminations and structure change from oxidation and surface finish processes. Therefore, for general surfaces a variety of material classes should be considered, such as elastic, hypoelastic, elastoplastic, etc. In this project two major material classes are considered, namely:

- linearly elastic (isotropic or anisotropic) for some metal surfaces, ceramics, composites, and hard rubbers, and

- viscoelastoplastic models for metallic surfaces and modern ductile ceramics.

3.2.1 Linearly Elastic Constitutive Models

The general linearly elastic constitutive relations are given as:

$$\sigma_{ij} = E_{ijkl}\epsilon_{kl}$$

where E_{ijkl} are the components of the fourth order elasticity tensor. It has up to 36 independent coefficients for general anisotropic materials. However, for most material classes, the number of material coefficients is much smaller and, for isotropic materials, there are only two coefficients, E and ν . The specific forms of tensor E for various materials are well known and will not be presented here.

3.2.2 Elasto-Viscoplastic Constitutive Model With Damage

We now describe the Bodner-Partom constitutive equations [10,11] used in the modeling of viscoelastoplastic asperities. The elastic-viscoplastic analysis is based on decomposition of strain rates

$$\dot{\epsilon}_{ij} = \dot{\epsilon}_{ij}^{(e)} + \dot{\epsilon}_{ij}^{(n)} \quad (3.11)$$

where superscripts (e) and (n) denote elastic and nonelastic strain components, respectively. The constitutive relations are

$$\dot{\sigma}_{ij} = E_{ijkl}(\dot{\epsilon}_{kl} - \dot{\epsilon}_{kl}^{(n)}) \quad (3.12)$$

A nonelastic deformation is governed by the flow rule:

$$\dot{\epsilon}_{ij}^{(n)} = f_{ij}(\sigma_{ij}, z_k, \omega_k)$$

$$\dot{z}_i = g_i(\sigma_{ij}, z_k)$$

$$\dot{\omega}_i = h_i(\sigma_{ij}, \omega_i)$$

where f_{ij} , g_i and h_i are constitutive functions, z_i are internal state variables, and ω_i are damage variables. These functions and state variables characterize the viscoplastic response of the material with continuum damage effects.

In the particular version of the Bodner-Partom theory applied in this work, the nonelastic flow rule is of the form:

$$\dot{\varepsilon}_{ij}^{(n)} = \lambda s_{ij}$$

where s_{ij} are the deviatoric components of a stress tensor

$$s_{ij} = \sigma_{ij} - \frac{1}{3}\sigma_{kk}\delta_{ij}$$

The current value of parameter λ is given by

$$\lambda^2 = \frac{1}{J_2} D_0^2 \exp \left[- \left(\frac{z^2(1 - \omega^2)}{3J_2} \right)^n \right] , \lambda > 0$$

where J_2 is the second invariant of a deviatoric stress tensor

$$J_2 = \frac{1}{2} s_{ij} s_{ij}$$

D_0 is a limiting strain rate in shear, n is a material constant and z and ω are state variables which evolve during deformation. In particular, z is the hardness variable, which represents viscoplastic hardening (or softening) of a material. The variable ω is the damage variable. This variable represents weakening of the material due to nucleation and propagation of microscopic voids and cracks in the material. The micro-cracks considered here are in the range of 0.01 mm in length. The rupture criterion is $\omega = 1$, which corresponds to the saturation of the material with voids. Alternatively, a single crack may grow to a size on the order of 1 mm. In the latter case, crack is too big to be treated in a continuum sense, and its propagation should be followed using the methods of fracture mechanics.

In the framework of materials science the value of ω is usually interpreted as ratio of the area of voids to the total area of a certain cross section of a sample:

$$\omega = \frac{A_{\text{void}}}{A}$$

The state variables z and ω evolve according to the specific equations of the viscoplastic theory:

1. Evolution equations of hardness variable

The internal state variable z consists of isotropic and directional components,

$$z = z^I + z^D$$

The evolution equation proposed for the isotropic hardening component [10,11,24,25] is

$$\dot{z}^I(t) = m_1[z_1 - z^I(t)]\dot{W}_p(t) - A_1 z_1 \left[\frac{z^I(t) - z_2}{z_1} \right]^{r_1} \quad (3.13)$$

with the initial condition, $z^I(0) = z_0$. In the first term, z_1 is the limiting (saturation) value of z^I , m_1 is the hardening rate, and the plastic work rate is

$$\dot{W}_p = \sigma_{ij}\dot{\varepsilon}_{ij}^{(n)}$$

which is taken as the measure of hardening. z_2 is the minimum value of z^I at a given temperature, and A_1 and r_1 are temperature dependent material constants. The evolution form of the directional hardening component (Refs. [10,11,24,25]) is defined as

$$z^D(t) = \beta_{ij}(t)u_{ij}(t)$$

where u_{ij} are the direction cosines of the current stress state,

$$u_{ij}(t) = \sigma_{ij}(t)/[\sigma_{kl}\sigma_{kl}]^{\frac{1}{2}} \quad (3.14)$$

The evolution equation for $\beta_{ij}(t)$ has the same general form as that for isotropic hardening but has tensorial character,

$$\begin{aligned} \dot{\beta}_{ij} &= m_2[z_3 u_{ij}(t) - \beta_{ij}(t)]\dot{W}_p(t) \\ &- A_2 z_1 \left\{ \frac{[\beta_{kl}(t)\beta_{kl}(t)]^{\frac{1}{2}}}{Z_1} \right\}^{r_2} v_{ij}(t) \end{aligned}$$

where

$$v_{ij}(t) = \beta_{ij}(t)/[\beta_{kl}(t)\beta_{kl}(t)]^{\frac{1}{2}}$$

and

$$\beta_{ij}(0) = 0$$

As in Eq. (3.13), m_2 is the hardening rate. A_2 and r_2 are temperature dependent material constants.

2. Evolution of damage

The damage parameter consists, in general, of isotropic and directional components,

$$\omega = \omega^I + \omega^D$$

The evolution of isotropic damage proposed in reference [11] is of the form

$$\dot{\omega}^I = \frac{P}{H} \left\{ \left[\ln \left(\frac{1}{\omega^I} \right) \right]^{\frac{p+1}{p}} \right\} \omega^I Q \quad (3.15)$$

In the above P and H are material constants, Q is the stress intensity function, given by

$$Q = \left[A\sigma_{\max}^+ + B\sqrt{3J_2} + CI_1^+ \right]^\nu$$

where σ_{\max}^+ is the maximum principal tensile stress, I_1^+ is the first stress invariant (nonnegative) and J_2 is the previously introduced second invariant of deviatoric stress.

A, B, C , and ν are material constants. A, B, C must satisfy the condition

$$A + B + C = 1$$

Clearly, the actual proportion of these constants selects the factor for stress state which is most important in the development of internal damage.

The initial condition for isotropic damage is $\omega^I(0) = 0$. In practical analyses the coefficient ν is of the order 10 (compare ref. [11]). Thus, when *SI* (metric) units are used in the analysis, the factor Q as well as the constant H reach extremely high values, beyond the limit of real number capacity on some computers. Thus, for numerical analysis, equation (3.15) was recast in the equivalent, but more convenient form:

$$\dot{\omega}^I = \hat{p} \left\{ \left[\ln \left(\frac{1}{\omega^I} \right) \right]^{\frac{p+1}{p}} \right\} \left(\frac{\hat{Q}}{\hat{H}} \right)^\nu$$

where:

$$\hat{Q} = Q^{\frac{1}{\nu}} = A\sigma_{\max}^+ + B\sqrt{3J_2} + CI_1^+$$

$$\hat{H} = (H \frac{1}{\sec})^{\frac{1}{\nu}}$$

$$\hat{p} = p \cdot \frac{1}{\sec}$$

The additional advantage of this formulation is that both \hat{Q} and \hat{H} are in the stress units (MPa) instead of the somewhat cumbersome (MPa)^v. The directional damage is defined in a manner very similar to directional hardening, namely

$$\omega^D = \omega_{ij}^D u_{ij}$$

where u_{IJ} are directional cosines defined in equation (3.14) and the components of a tensor ω^D evolve according to equation

$$\omega_{ij}^D = \frac{q}{M} \left\{ \left[\ln \left(\frac{1}{\omega^D} \right) \right]^{\frac{q+1}{q}} \right\} \omega^D Q u_{ij}$$

where q and M are material constants. The initial condition is

$$\omega_{ij}^D(0) = 0$$

Note that there are several problems with practical application of directional damage, reliability of the above model and conducting experiments relevant for the evolution of necessary parameters. Even the extensive experiments presented in references [11,24,25] did not provide all the necessary data and, hence, the damage model is usually limited to the isotropic damage.

3.3 Boundary Conditions

The asperity can be viewed as a protuberance of a deformable half space (see Fig. 3.1). It is subject to boundary conditions resulting from its support, contact with the opposing surface, adhesion and sliding resistance.

3.3.1 Support Conditions

If the asperity is viewed as the protuberance on a deformable half space, the support conditions are defined as zero displacements at infinity:

$$\lim_{\substack{\|\mathbf{x}\| \rightarrow \infty \\ x_3 \leq 0}} \mathbf{u} = 0$$

In practical computations we will usually consider only a certain section of the bulk material surrounding the asperity. Then the support condition will be:

$$\mathbf{u} = 0 \text{ on } \Gamma_u$$

on the cut-off boundary Γ_u .

3.3.2 Contact Condition

Let the position of the rigid flat (see figure 3.2) be defined by:

- a point $\mathbf{p}_o(x_o, y_o, z_o)$ which belongs to the flat, where x_o, y_o, z_o are its coordinates in the initial configuration,
- unit vector \mathbf{N} , normal to the flat,
- displacement w of the flat in direction \mathbf{N} .

Separation of material point in the deformable body from the flat is then given by the following formula

$$s = (\mathbf{x} + \mathbf{u} - \mathbf{p}_o) \cdot \mathbf{N} - w - d$$

where:

- \mathbf{x} - initial position of a material point,
- \mathbf{u} - displacement of this point,
- d - intermolecular distance which is important when adhesion is taken into account, otherwise $d = 0$.

The condition that the asperity cannot penetrate the rigid flat is:

$$s \geq 0 \quad \text{on } \Gamma$$

The actual contact region is $\Gamma_c = \{\mathbf{x} \in \Gamma, s(\mathbf{x}) = 0\}$. The difficulty associated with the contact condition in the above form is that it results in a weak formulation of the problem in the form of variational inequality, rather than the equation. In order to avoid difficulties involved in solving variational inequalities, the contact condition is usually regularized [54,71]. In this work we will use the penalty-type regularization of the form:

$$t_N^c = t_N^c(a) \text{ on } \Gamma_c$$

where $a = -s$ is the approach (penetration) and t_N^c is the value of traction normal to the flat which defines resistance of the surface to penetration. Because we will be using rate formulation in viscoelastoplastic analysis, it is beneficial to introduce a continuously differentiable penalty function, for example in the form presented graphically in Fig. 3.2:

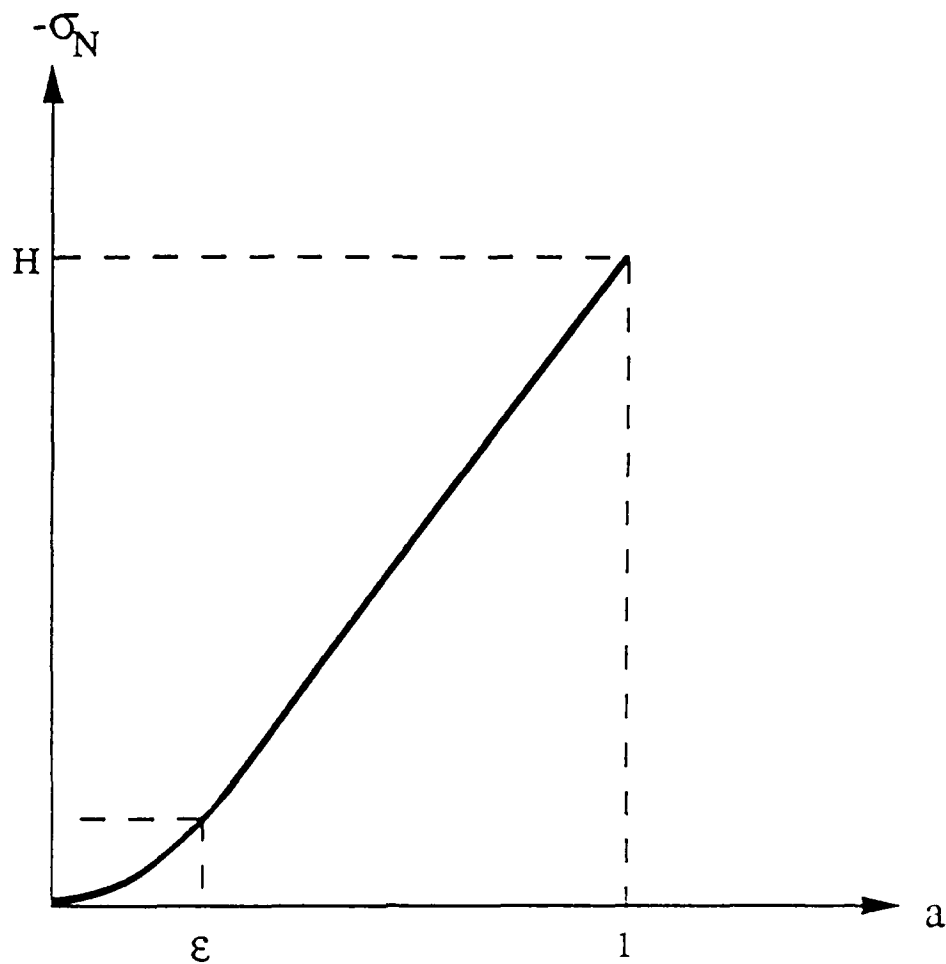


Figure 3.2: Penalty function for contact condition.

$$t_N^c = \begin{cases} 0 & \text{if } a < 0 \\ \frac{H}{2\varepsilon} a^2 & \text{if } 0 \leq a < \varepsilon \\ H \left(a - \frac{\varepsilon}{2} \right) & \text{if } a \geq \varepsilon \end{cases}$$

Here H is a large number (normal stress) and ε is a small number (penetration). The above penalty function guarantees continuous derivative of the normal traction with respect to a , which greatly improves practical performance of the numerical computations.

3.3.3 Adhesion

An important contributing factor to friction on contact surfaces is adhesion: the intermolecular attractive forces that depend on atomic spacing and the corresponding surface energies of materials. For highly polished uncontaminated surfaces, adhesion forces can be very large, leading to the virtual welding of one surface to another, while for rough contaminated surfaces, adhesion effects are often negligible. For engineering surfaces under common working conditions, adhesion effects can be significant, so that a rational model of contact and friction should take them into account.

The DMT adhesion model, proposed by Derjaguin, Muller, and Toporov [36] and later refined by Muller, Derjaguin, and Toporov [66], attempts to characterize the attractive forces on a spherical elastic asperity in contact with a rigid flat, assuming that the shape of the deformed asperity is given by the Hertz theory and that no attractive forces exist in the contact region. The JKR model, due to Johnson, Kendall, and Roberts [52] also analyzes the elastic spherical asperity-flat problem with Hertz theory, but assumes that attractive forces are confined to the contact area and that the attractive forces produce an elastic deformation of the asperity. The JKR model has been found to be more suitable for soft materials, such as rubbers, while the DMT model is claimed to be more suitable for harder materials with high surface energies (see Chang, Etsion, and Bogy [26–28] and Pashley [73]). Survey papers on developments in adhesion models have been contributed by Pashley, Pethica, and Tabor [75] and by Pashley and Pethica [74]. See also MacFarlane and Tabor [58].

We shall include adhesion effects in our contact and friction theory by using an approach similar to, but more general than that of the DMT model. We continue to assume that the surfaces are isotropic, rough, and have a Gaussian distribution of peak heights, that there is no interaction between asperities, and that it suffices to consider a single asperity impending on a rigid flat. Following Muller, et al. [67], we characterize the *attractive adhesion pressure* $q(s)$ as that attractive force per unit surface area, acting normal to the mean asperity height plane, resulting from the Lennard-Jones interaction (interatomic) potential Φ of surface physical chemistry. Then,

$$q(s) = \frac{8\Delta\gamma}{3d} \left[\left(\frac{d}{s}\right)^3 - \left(\frac{d}{s}\right)^9 \right] \quad (3.16)$$

where

s = the separation of the two surfaces *outside* the contact area

d = the intermolecular distance (generally $d = 0.3 - 0.5\text{nm}$)

In (3.6), $\Delta\gamma$ is the surface energy of adhesion and is defined as follows: if γ_1 and γ_2 are the surface energies of surfaces 1 and 2, respectively, before contact, and γ_{12} is the joint surface energy of the interface after contact, then

$$\Delta\gamma = \gamma_1 + \gamma_2 - \gamma_{12} \quad (3.17)$$

For values of surface energies of adhesion for various metals, see Rabinowicz [78] or Ferrante, Smith, and Rose [39]. Traction resulting from adhesion can be expressed by the following formula

$$t^a = -q(s)N = q(a)N$$

where s is calculated according to the formula defined in the previous subsection.

The principal mathematical difficulty inherent in characterizing the adhesion pressure is that it is developed only on surface material outside the contact area, which, *a priori*, is unknown. Several concluding remarks on adhesion, however, are in order at this point.

Remarks

1. Fuller and Tabor [42], using the JKR model of adhesion and the rough surface asperity-based model of Greenwood and Williamson [44], presented an *adhesion parameter* θ of the form

$$\theta = \frac{E\sigma}{\Delta\gamma} \sqrt{\frac{\sigma}{R}} \quad (3.18)$$

where E is the effective modulus of elasticity of the contact surfaces

$$E^{-1} = (1 - v_1^2) E_1^{-1} + (1 - v_2^2) E_2^{-1}$$

E_i , v_i being Young's modulus and Poisson's ratio of surface i , σ is the standard deviation of surface heights, and R the mean radius of spherical elastic asperities. The larger the value of θ , the less significant the effects of adhesion, and for rubber spheres, experiments showed that adhesion become negligible for $\theta > 10$.

2. Chang, Etsion, and Bogy [26–28] presented a study of adhesion effects using the DMT model and an elasto-plastic asperity model of the contact surface. They investigated the importance of adhesion with varying values of surface energy and plasticity, as measured by the *plasticity index* of Greenwood and Williamson [44],

$$\Psi = \frac{2E}{\pi K H} \sqrt{\frac{\sigma}{R}} \quad (3.19)$$

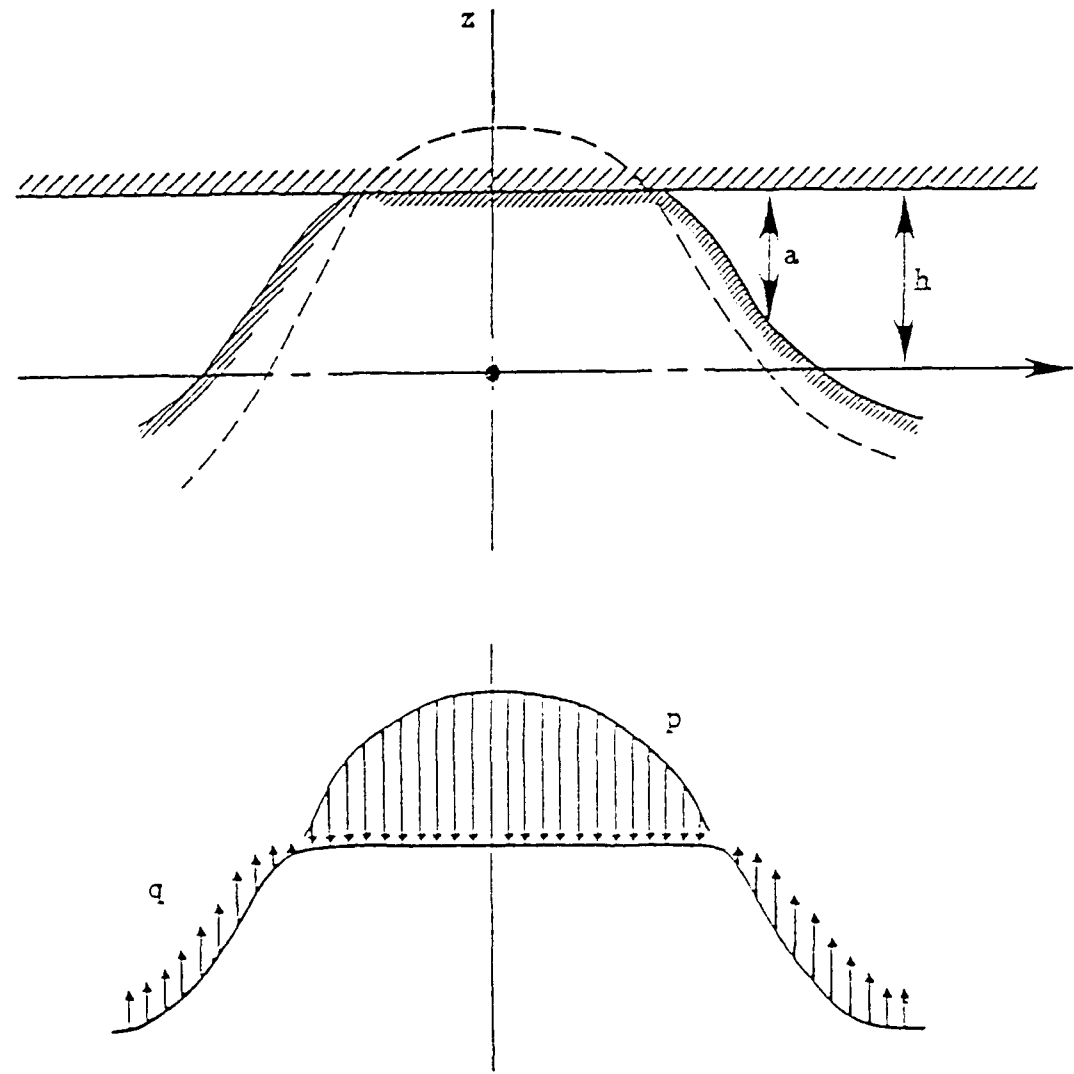


Figure 3.3: Pressure on a deformed asperity; the adhesion pressures q due to molecular attraction and the pressure p on the contact surface.

where H is the Brinell hardness (of the softer of the two materials) and $K = 0.454 + 0.41\nu_1$, ν_1 being the Poisson ratio of this material. These authors concluded that the "pull-off force" due to adhesion (i.e., the integrated suction force due to adhesion) becomes negligible for hard steel when the adhesion index θ is greater than 100, as compared to $\theta > 10$ for rubber; the adhesion force is negligible compared to the contact load when the plasticity index $\Psi \geq 2.5$ or when the surface energy $\Delta\gamma \leq 0.5 \text{ J/m}^2$ for a sufficiently small external force. They concluded that "for smooth clean surfaces the adhesion can be well over 20 percent of the contact load and, thus, cannot be neglected."

3. Adhesion forces are time dependent and generally increase with time of contact, eventually acquiring a constant value for static contact. Thus, the static adhesion models generally attempt to predict the maximum value of adhesion forces and can overestimate adhesion effects for dynamic contact.

3.3.4 Shear Resistance

To construct new constitutive models of friction it is necessary to characterize the resistance of the rough interface to sliding (i.e., to tangential motions of the reference planes relative to one another). While this aspect of the modeling approach still requires much study, there appears to be at least three methods available for this purpose. First, Bowden and Tabor [13, 14] estimated the resistance to impending motion (more precisely, the static coefficient of friction) by calculating the shear strength of metallic oxide junctions developed on the contact surface. Similarly, Chang, Etsion, and Bogy [26-28] calculated the tangential load required to reach the fracture strength of metallic junctions as an indication of the tangential force required to produce sliding. Villaggio [97], on the other hand, studied the problem of contact of periodically spaced elastic asperities and defined the load at which sliding initiates as that which reduces the curvature of the resisting elastic asperities to zero. Francis [41] modeled the micro sliding resistance using empirical relations based on existing experimental data.

Extensive sequences of experiments on sliding resistance of thin films, involving 27 different materials and a wide range of normal loads, are described in the papers of Boyd and Robertson [15], Briscoe, Scruton, and Willis [17], Towle [92], and Briscoe and Tabor [18]. In all of these studies, it was discovered that (on a microcontact interface) the interfacial shear stress τ , during sliding was a function of the normal stress $\sigma_n = \sigma_{ij}n_jn_i$, and, according to

Francis [41], their empirical findings suggest that

$$\tau_s = \begin{cases} c_1 + c_2 \sigma_n & \text{for light loads} \\ c_3 \sigma_n^m \ (0.6 < m < 1.4) & \text{for intermediate loads} \\ \log^{-1} [c_5 + c(\sigma_n) \log \sigma_n] & \text{for heavy loads} \\ \text{where } 0.0 \leq c(\sigma_n) < 1.9 ; \frac{d(\log \tau_s)}{d(\log \sigma_n)} \geq 0 \end{cases} \quad (3.20)$$

wherein loads were varied over a factor of 10 or more and starting from 15 MPa (light), 40 MPa (intermediate) and 200 MPa (heavy). Francis [41] points out that a good approximation to all of these cases is the simple quadratic function,

$$\tau_s = c_0 + c_1 \sigma_n + c_2 \sigma_n^2 \quad (3.21)$$

where c_0, c_1, c_2 are material constants.

Once a micro-shear resistance is characterized, the macro sliding resistance can be computed using the statistical summation procedures described earlier.

3.3.5 Initial Conditions

Smooth functions $\mathbf{u}^0(\mathbf{x})$ and $\mathbf{z}^0(\mathbf{x})$ are prescribed such that for $\mathbf{x} \in \Omega$,

$$\begin{aligned} u_i(\mathbf{x}, 0) &= u_i^0(\mathbf{x}) \\ z_i(\mathbf{x}, 0) &= z_i^0(\mathbf{x}) \\ \omega_i(\mathbf{x}, 0) &= 0 \end{aligned}$$

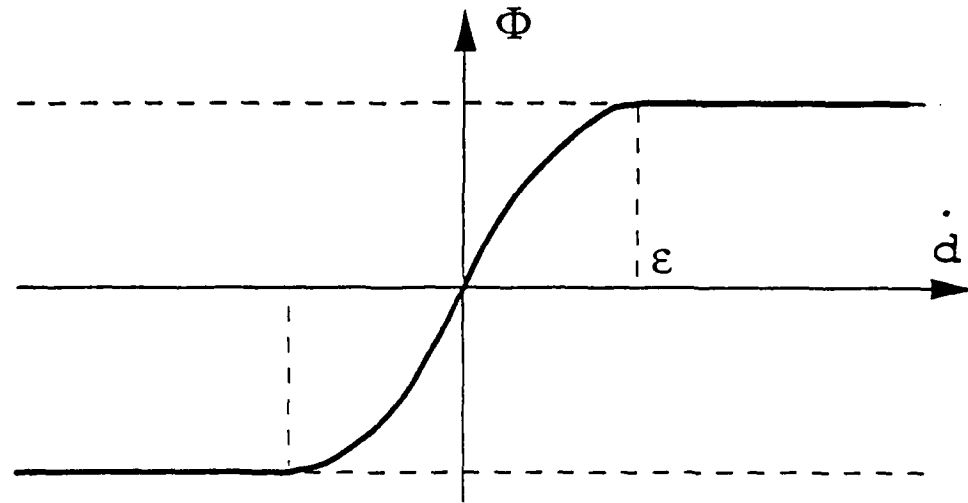


Figure 3.4: A regularization function ϕ

3.4 Variational Formulation

In order to obtain a weak formulation of a boundary-value problem we introduce the space of functions

$$V = \left\{ \mathbf{v} \in [W^{m,q}(\Omega)]^N, \mathbf{v}(\mathbf{x}) \rightarrow 0 \text{ as } \|\mathbf{x}\| \rightarrow \infty \right\}$$

where Ω is a computational domain, N is the dimension of the physical space (2 or 3), and $W^{m,p}(\Omega)$ is the Sobolev space, where specific values of m, p and q depend on the particular form of constitutive equations.

Multiplying the equilibrium equation (3.10) by a test function and integrating over Ω we obtain the weak form of the rate equilibrium equations:

$$\int_{\Omega} v_i \dot{\sigma}_{ij,j} d\Omega = 0 \quad \forall \mathbf{v} \in V$$

After the substitution of the constitutive equations, application of the divergence theorem and a grouping of terms the following variational problem is obtained:

Find a displacement rate field $t \rightarrow \dot{\mathbf{u}}(\mathbf{x}, t) \in V$ such that

$$\int_{\Omega} v_{i,j} E_{ijkl} \dot{u}_{k,l} d\Omega = \int_{\Omega} v_{i,j} E_{ijkl} \dot{\varepsilon}_{kl}^{(n)} d\Omega + \int_{\partial\Omega} v_i t_i ds \quad \forall \mathbf{v} \in V \quad (3.22)$$

The rates of nonelastic strains $\dot{\varepsilon}_{kl}^{(n)}$ can be obtained from the relevant constitutive theory (see Section 3.2.2). For elastic materials they are identically equal to zero. Therefore for these materials it is also possible and computationally more efficient to use a total formulation of the problem which is as follows.

Find a displacement field $\mathbf{u}(\mathbf{x}) \in V$, such that

$$\int_{\Omega} v_{i,j} E_{ijkl} u_{k,l} d\Omega = \int_{\partial\Omega} v_i t_i ds \quad \forall \mathbf{v} \in V \quad (3.23)$$

Note that the values or the rates of tractions on $\partial\Omega$ need to be expressed in terms of displacements using formulas presented in previous sections (contact condition, adhesion, and sliding resistance).

3.4.1 Boundary Integrals

The boundary $\partial\Omega$ can be decomposed in the following way

$$\partial\Omega = \Gamma_u \cup \Gamma_t \cup \Gamma_a \cup \Gamma_c$$

where

- Γ_u – support zone (kinematic boundary conditions),
- Γ_t – static zone (static boundary conditions),
- Γ_a – adhesion zone (adhesion traction is not negligible),
- Γ_c – contact zone ($a \geq 0$).

The integrals over $\partial\Omega$ in formulas (3.22) and (3.23) can be calculated as sums of integrals over these four parts of the boundary.

- Support zone

According to the formula (3.3.1)

$$u_i = 0 \text{ on } \Gamma_u$$

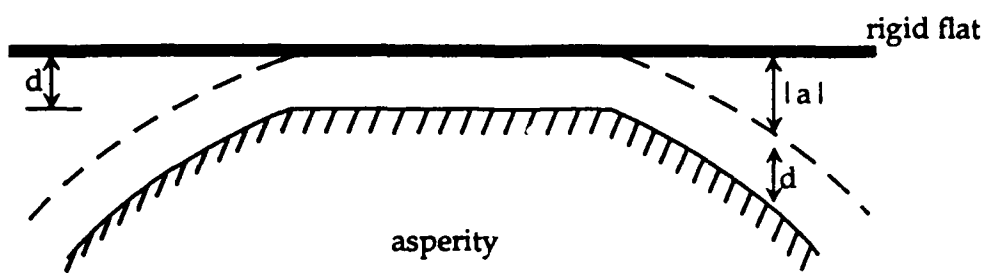


Figure 3.5: Separation and contact when intermolecular forces are taken into account.

so there is no need to compute integrals over Γ_u

- Static zone

Traction on this part of the boundary is known, so it can be integrated. In the case of asperities this traction is usually equal to zero.

- Adhesion zone

The integrals over Γ_a have the following forms:

(a) total formulation

$$\int_{\Gamma_a} v_i t_i ds = \int_{\Gamma_a} v_i q(a) N_i ds$$

(b) rate formulation

X Graph

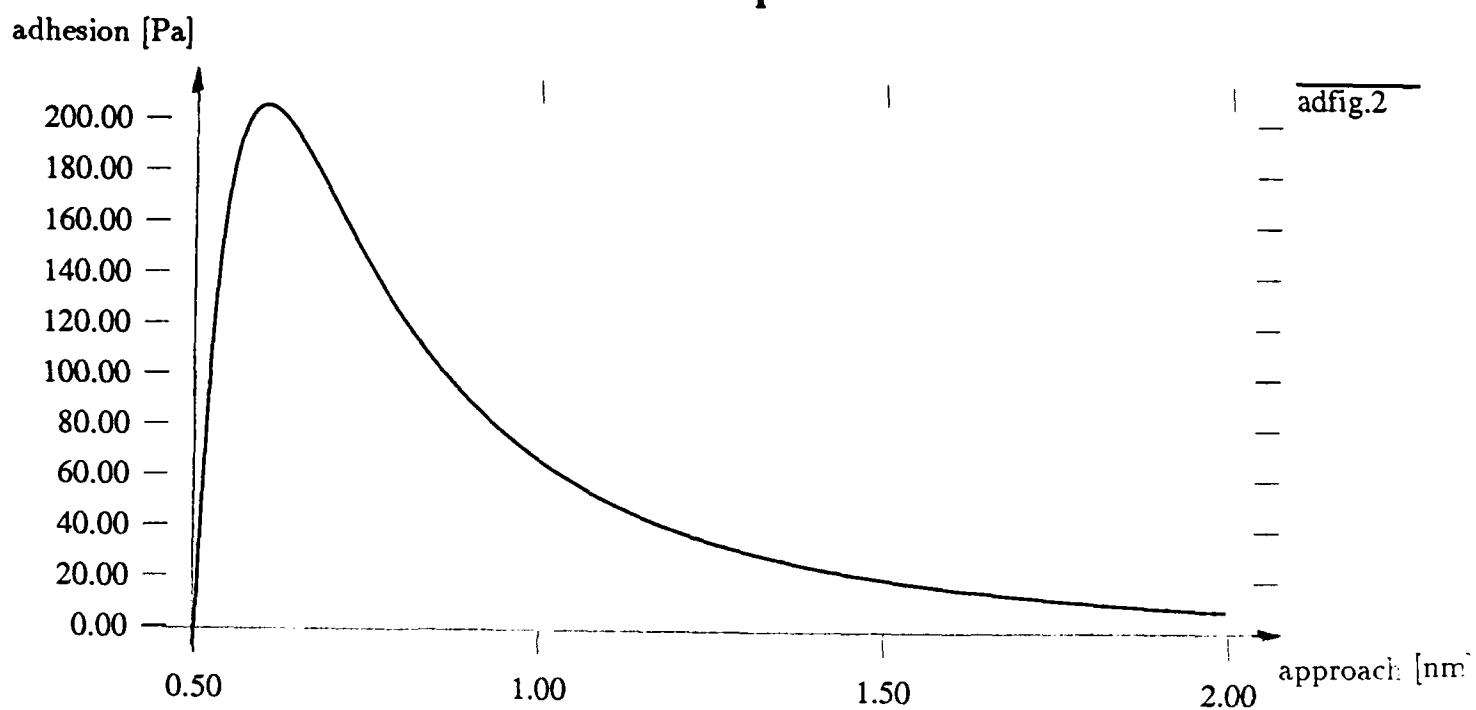


Figure 3.6: Graph of adhesion traction in terms of separation.

$$\int_{\Gamma_a} v_i \dot{t}_i ds = - \int_{\Gamma_a} v_i \alpha N_i N_k \dot{u}_k ds + \int_{\Gamma_a} v_i \alpha \dot{w} N_i ds$$

where

$$\alpha = \frac{dt^a}{da} = 8 \frac{\Delta\gamma}{ad} \left[3 \left(\frac{d}{a} \right)^9 - \left(\frac{d}{a} \right)^3 \right]$$

When adhesion forces are taken into account then the intermolecular distance d plays an important role. A graph of traction resulting from adhesion for $d = 0.5$ nm and $\Delta\gamma = 0.1$ J / m² in terms of the separation is shown in figure 3.6. Clearly, the adhesion traction is strongly nonlinear, and practically vanishes at separations greater than $4d$.

Integration of adhesion derivative with respect to separation is required in formulas 3.4.1. Figure 3.7 shows this function. Because the function changes very rapidly, it has to be integrated with higher accuracy than e.g. shape functions. Some numerical experiments were carried out to check how many integration points are necessary to compute accurately these integrals. They showed that 10 integration points in one direction are enough to integrate influence of adhesion forces over an element face which has dimensions less than 10^*d , providing that the slope i.e. angle between the face and the flat is small (less than 10°). We have such a situation in the case of asperities. Moreover, integration need only be performed on part of Γ_a on which separation is less than $4 * d$. At this and higher distance, adhesion traction and its derivatives are practically equal to zero.

- Traction on the contact zone Γ_c

Penalty method which we use here to solve variational inequality problem is equivalent to allowing for penetration of the rigid flat by the asperity ($a > 0$). But this penetration results in a big normal traction in the form

$$t_N = \frac{1}{\epsilon} a N$$

where ϵ is a small number.

In addition to normal traction there exists also a tangential traction (sliding resistance) on the contact zone. There exist several theories which give formulas for sliding resistance in terms of normal pressure [41] see section 4.3.4 for discussion. Generally all of them can be expressed in the following form

$$t = \begin{cases} 0 & \text{when } \mathbf{b} = 0 \\ h(t_N) \frac{\mathbf{b}}{\|\mathbf{b}\|} & \text{when } \mathbf{b} \neq 0 \end{cases} \quad (3.24)$$

X Graph

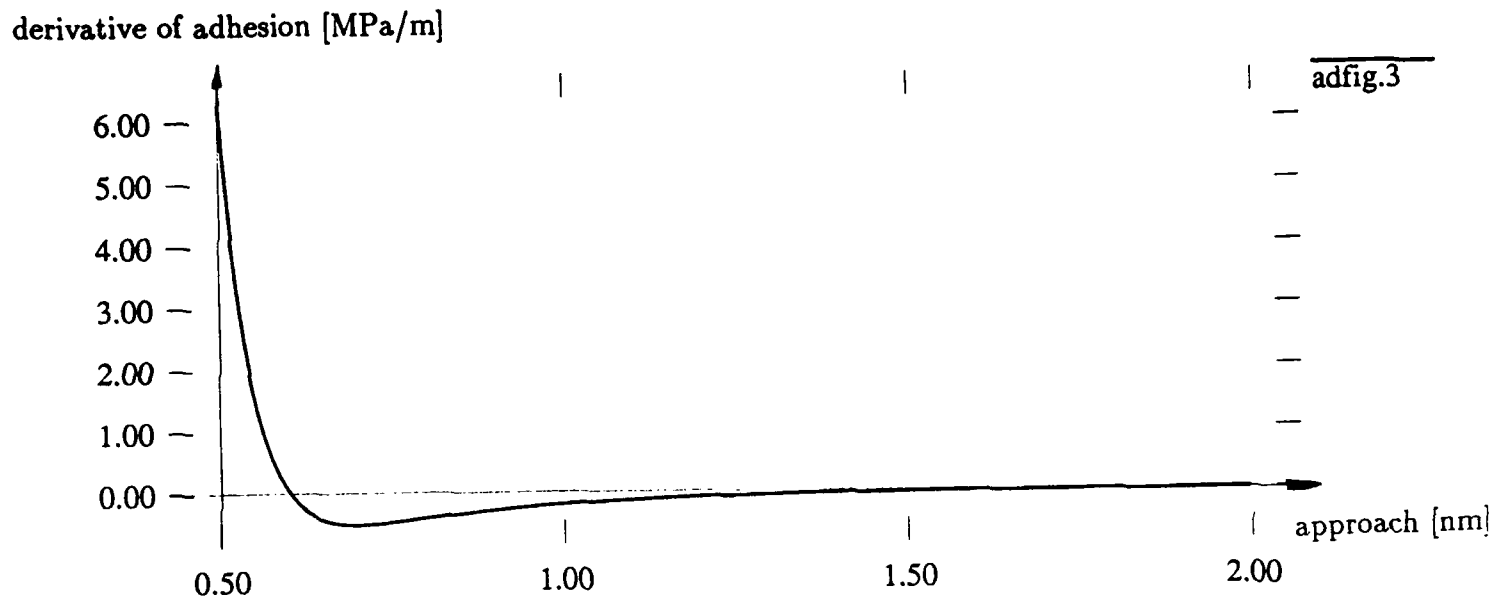


Figure 3.7: Graph of derivative of adhesion traction in terms of separation.

where

- t — sliding resistance,
- h — function which defines the relation between sliding and normal tractions, its form depends on adopted model of sliding resistance,
- b — vector of relative displacement between the asperity and the flat.

Components of t are not continuous with respect to b when $b = 0$. To facilitate numerical solution of the contact problem a regularization of the function t is introduced. The regularization will be done for components of sliding resistance. This vector has at most two non zero components. Let the first component t_S have direction of an arbitrary vector S parallel to the flat. Let the second component t_T have direction of vector product $\mathbf{N} \times \mathbf{S} = \mathbf{T}$, where \mathbf{N} is normal to the flat and pointing towards the asperity. If b_S and b_T are coordinates of b then the components of t after regularization can be expressed by the following formulas

$$t_S = h(t_N)\phi(b)\Psi_S(b_S, b_T)$$

$$t_T = h(t_N)\phi(b)\Psi_T(b_S, b_T)$$

where ϕ is a function which provides smooth approximation (of class C^1) for function h , and has the following form

$$\phi(x) = \begin{cases} -1 & \text{for } x \leq -\epsilon_b \\ 2\frac{x}{\epsilon_b} + \left(\frac{x}{\epsilon_b}\right)^2 & \text{for } -\epsilon_b \leq x \leq 0 \\ 2\frac{x}{\epsilon_b} - \left(\frac{x}{\epsilon_b}\right)^2 & \text{for } 0 \leq x \leq \epsilon_b \\ 1 & \text{for } \epsilon_b \leq x \end{cases} \quad (3.25)$$

where ϵ_b is a small number.

Ψ_S and Ψ_T are functions which guarantee a proper decomposition of vector t , i.e. they provide that $\|t\| = t_S^2 + t_T^2$. Functions Ψ_S, Ψ_T have the following forms

$$\Psi_S = \frac{b_S}{\sqrt{b_S^2 + b_T^2}}$$

$$\Psi_T = \frac{b_T}{\sqrt{b_S^2 + b_T^2}}$$

Combination of the above formulas leads to the following contributions to the weak statement of the problems:

for the total formulation

$$\int_{\Gamma_c} v_i t_i ds = \int_{\Gamma_c} v_i \left(\frac{a}{\epsilon} N_i + t_S S_i + t_T T_i \right) ds$$

for the incremental formulation

$$\begin{aligned} \int_{\Gamma_c} v_i t_i ds &= \int v_i \alpha_{ij} \dot{u}_j ds + \\ &+ \int_{\Gamma_c} v_i \left[\frac{1}{\epsilon} \dot{w} N_i + \left(\frac{\partial t_S}{\partial a} \dot{w} + \frac{\partial t_S}{\partial b_S} \dot{\delta} \right) S_i + \left(\frac{\partial t_T}{\partial a} \dot{w} + \frac{\partial t_T}{\partial b_T} \dot{\delta} \right) T_i \right] ds \end{aligned}$$

where

$$\alpha_{ij} = \frac{1}{\epsilon} N_i N_j + \frac{\partial t_S}{\partial a} S_i N_j \frac{\partial t_S}{\partial b_S} S_i S_j + \frac{\partial t_S}{\partial b_T} S_i T_j + \quad (3.26)$$

$$+ \frac{\partial t_T}{\partial a} T_i N_j + \frac{\partial t_T}{\partial b_S} T_i S_j + \frac{\partial t_T}{\partial b_T} T_i T_j \quad (3.27)$$

w – displacement of the flat in N direction,
 δ – displacement of the flat in S direction.

3.5 Solution Method for Elastic Contact Problems

Formulation of the contact problem is nonlinear even in the case of contact with an elastic body because the area of contact depends on displacements ($\Gamma_c = \Gamma_c(\mathbf{u})$). Generally, requiring that variational equation (3.23) be satisfied for every test function leads to the following nonlinear system of equations:

$$\mathbf{L}(\mathbf{u}) - \mathbf{R} = 0, \quad (3.28)$$

where \mathbf{L} stands for the left-hand side and \mathbf{R} for the right-hand side.

To solve the problem effectively, Newton-Raphson iteration technique was used. The idea of the method is to substitute a nonlinear functional by its linear part. Linearization is made at a series of points. Each point is the solution of the problem linearized at the previous point. If the series is convergent, it is convergent to a solution of the nonlinear problem. For a simple case of a simple nonlinear equation with one unknown, two steps of Newton-Raphson method are shown in Fig. 3.8.

Basic formulas of the Newton-Raphson method are presented below. Let us assume that we know a field \mathbf{u}^n which is an approximate solution of the equation (3.28). $\mathbf{u}_0 \equiv \mathbf{0}$ can be assumed. First two components of the Taylor series evolution of left hand side of equation (3.28) give

$$\mathbf{L}(\mathbf{u}^n) - \mathbf{R} - \text{grad}_{\mathbf{u}}[\mathbf{L}(\mathbf{u}^n) - \mathbf{R}] \delta \mathbf{u} \approx 0$$

Assuming that $\delta \mathbf{u} = \mathbf{u}^{n+1} - \mathbf{u}^n$ we obtain

$$\mathbf{L}(\mathbf{u}^n) - \mathbf{R} + \text{grad}_{\mathbf{u}} \mathbf{L}(\mathbf{u}^n) (\mathbf{u}^{n+1} - \mathbf{u}^n) = 0$$

Equation (3.28) is a linear equation for \mathbf{u}^{n+1} . We use this equation to compute a sequence of approximate solutions $\mathbf{u}^1, \dots, \mathbf{u}^M$. The process is stopped when $\|\mathbf{u}^M - \mathbf{u}^{M-1}\|$ and $\|\mathbf{L}(\mathbf{u}^M) - \mathbf{R}\|$ are small enough.

For contact with elastic bodies, equation (3.28) has the following form

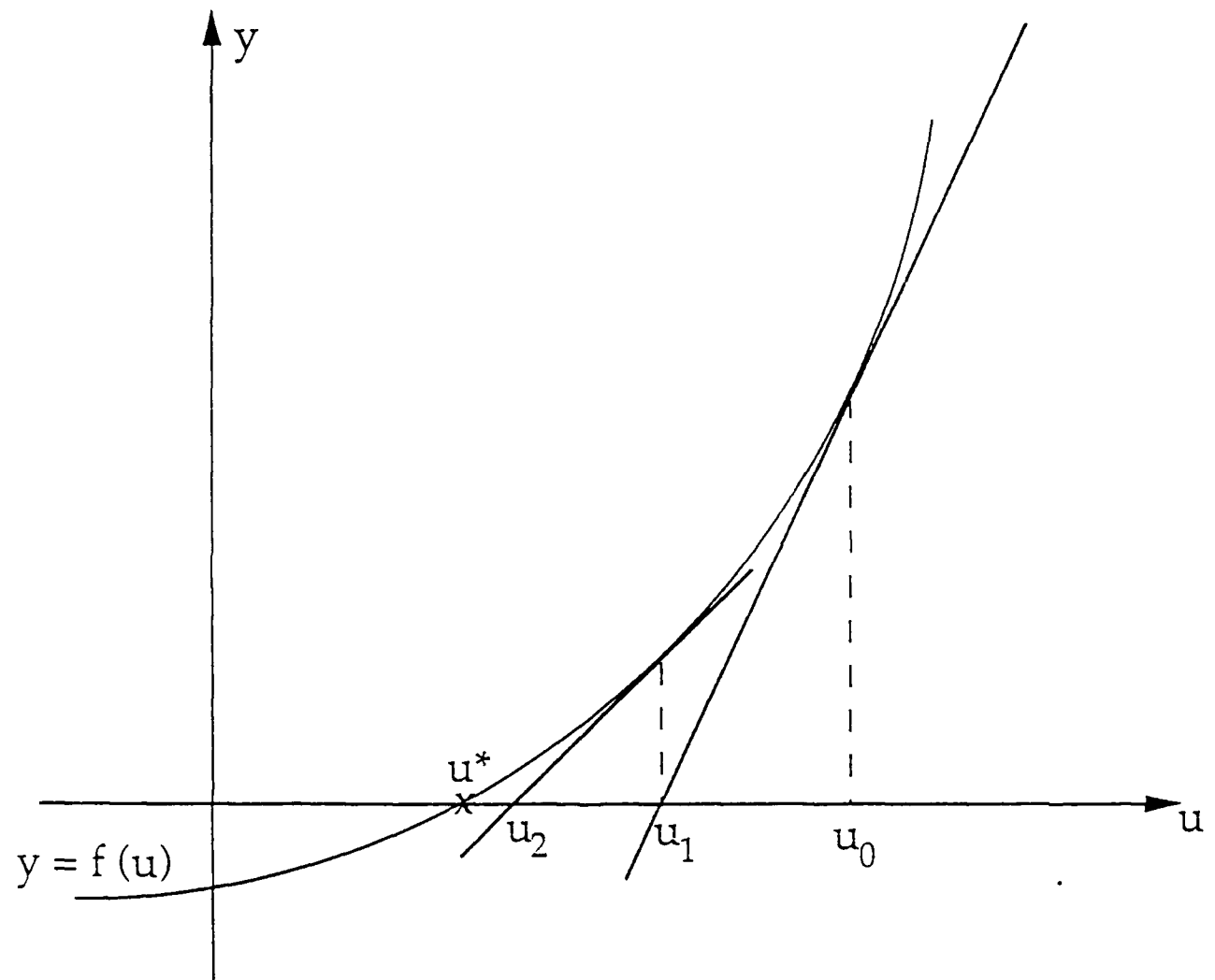


Figure 3.8: Graphical presentation of construction of a series u_0, u_1, u_2, \dots convergent to a solution u^* of equation $f(u) = 0$.

$$\int_{\Omega} v_{i,j} E_{ijkl} u_{k,l}^{n+1} d\Omega + \int_{\Gamma_c} v_i \alpha_{ij} u_j^{n+1} ds + \int_{\Gamma_a} v_i \beta_{ij} u_j^{n+1} ds = \int_{\Gamma_c} v_i [\alpha_{ij} u_j^{(n)} + p_i] ds + \int_{\Gamma_a} v_i [\beta_{ij} u_j^{(n)} + q_i] ds$$

where

$$\alpha_{ij} \quad \text{is the same as in the incremental formulation} \quad (3.29)$$

$$\beta_{ij} = 8 \frac{\Delta\gamma}{da} \left[3 \left(\frac{d}{a} \right)^9 - \left(\frac{d}{a} \right)^3 \right] N_i N_j \quad (3.30)$$

$$p_i = \frac{1}{\epsilon} (w + d - \mathbf{P} \mathbf{N} + \mathbf{P}_o \mathbf{N}) N_i \quad (3.31)$$

$$q_i = \frac{8 \Delta\gamma}{3 d} \left[\left(\frac{d}{a} \right)^3 - \left(\frac{d}{a} \right)^9 \right] N_i \quad (3.32)$$

Variations were evaluated neglecting dependence $\Gamma_c = \Gamma_c(\mathbf{u})$. The above linearized problem is solved by the standard FEM.

In order to provide automatic control of the performance of nonlinear procedures, an expert system-like approach has been applied. This application is based on our previous research on automation of computational procedures [96], and employs several heuristic rules to monitor and control the performance of nonlinear iterations. While in the original implementation discussed in reference [96] the specialized knowledge engineering software was used to develop the expert system, in this project the essential features of the expert system were coded in FORTRAN and included in the code. The expert system is activated at each time step after completing a prescribed number of iterations (sufficient to estimate trends in error histories). The decisions of the expert system are used to control the solution process and obtain a converged solution at minimum cost.

3.6 Solution Method for Viscoplastic Contact Problems

Formulation of the problem in this case is time-dependent.

The strategy employed in the solution of this problem is as follows: with the initial distribution of stress, temperature and internal variables specified use the rate form of the equilibrium condition (Eq. (2.23)) to obtain the nodal displacement rates. Then integrate the constitutive equations forward in time at the element Gauss integration points. With updated value of the stress, temperature and internal variables at the new time, the equilibrium equation is solved again. This sequence of determining the nodal displacement rates,

then advancing the constitutive equations in time is continued until the desired history of the initial boundary-value problem has been obtained.

Thus, the algorithm proceeds through the following steps:

1. At time t , initialize σ_{ij}, Z_i for each element;
2. Calculate $\dot{\epsilon}_{ij}^n = f_{ij}(\sigma_{ij}, Z_k)$ for each element;
3. Assemble and solve $[K]\dot{U} = \dot{F}$;
4. Calculate $\dot{\epsilon}_{ij}$ for each element, $\dot{\epsilon} = [B]\dot{U}$;
5. Calculate $\dot{\sigma}_{ij}$ for each element, $\dot{\sigma} = [E](\dot{\epsilon} - \dot{\epsilon}^n)$;
6. Calculate \dot{Z}_i for each element, $\dot{Z}_i = g_i(\sigma_{ij}, Z_k)$;
7. Integrate $\dot{\sigma}_{ij}, \dot{Z}$ forward for each element to get σ_{ij} and Z_i at $t + \Delta t$;
8. If $t + \Delta t_s < t_{\text{final}}$ go to 2, otherwise stop.

The computational method above has been presented for a constant time step Δt_s . Computational experience by several investigators (see refs. [7,8,55]) indicates that a very small time step can be required because of the "stiff" nature of the ordinary differential equations describing the internal state variables. To gain improved efficiency and reliability a variable time step algorithm has been implemented. The basic idea of this variable time step algorithm is presented below for a scalar evolution equation.

The solution is advanced using a predictor-corrector scheme. The predictor phase consists of an Euler step:

$$\dot{y} = f(y, t) \quad (3.33)$$

The solution is advanced using a predictor-corrector scheme. The predictor phase consists of an Euler step:

$$y_{t+\Delta t}^P = y_t + \Delta t \dot{y}_t \quad (3.34)$$

$$\dot{y}_{t+\Delta t}^P = f(y_{t+\Delta t}^P, t + \Delta t) \quad (3.35)$$

An error indicator E [15,24] is then computed from

$$E = \frac{|\Delta t (\dot{y}_{t+\Delta t}^P - \dot{y}_t)|}{2 |\dot{y}_{t+\Delta t}^P|} \quad (3.36)$$

The error indicator is next compared with a preset error criterion and if the criterion is met, the time step is small enough to proceed to the corrector stage. Otherwise, the predictor phase for Eqs. (3.34)–(3.35) is repeated with a smaller time step. For the viscoplastic evolution equations with damage modeling, the control variables used to calculate the error indicator were the components of a stress tensor σ_{ij} , internal state variables Z_i , and the damage variables ω_i , with the maximum of these selected as the controlling error.

The corrector phase is the modified Newton scheme,

$$\dot{y}_{avg} = (\dot{y}_t + \dot{y}_{t+\Delta t}^P) / 2$$

$$\dot{y}_{t+\Delta t}^C = y_t + \Delta t \dot{y}_{avg}$$

A flowchart depicting the adaptive scheme is shown in Fig. 3.9.

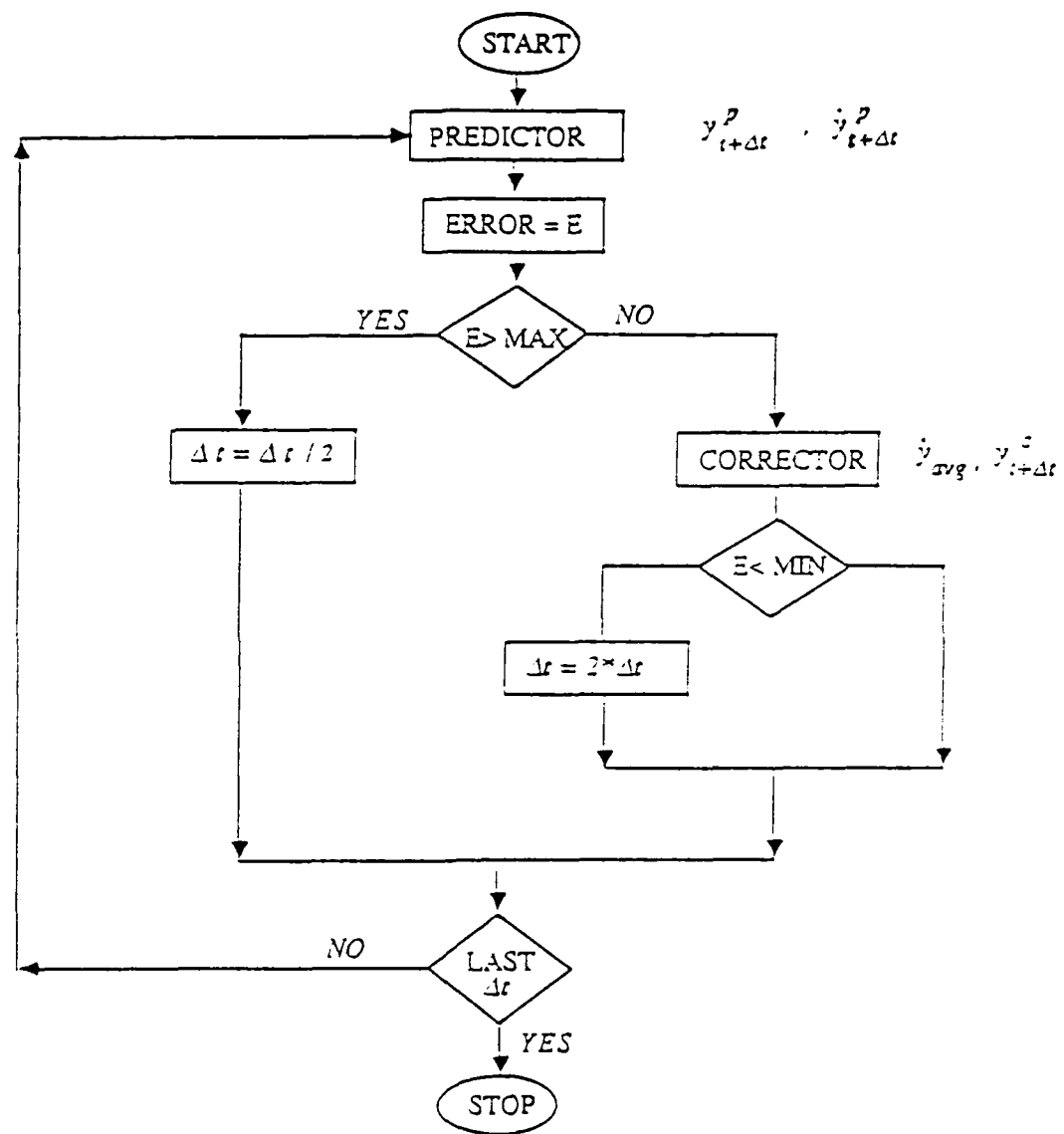


Figure 3.9: Flowchart for the solution of viscoelastoplastic evolution problem with adaptive timestepping

4 Finite Element Analysis of Contact Problems with Friction

4.1 General Information About the 3D Finite Element Code

The development of asperity modeling capabilities was based on existing, state-of-the-art three-dimensional adaptive finite element kernel code, which consists of several separate modules organized around the common data structure and execution supervisor. Figure 4.1 shows a general structure of the code directories. The most important modules are:

- an object-based data structure designed specifically for the $h-p$ adaptive finite element method,
- an execution supervisor controlling the overall execution of the computations,
- pre- and postprocessors,
- an adaptive package,
- linear equation solvers, and
- a solver for a specific boundary value problem (in this case, asperity modeling).

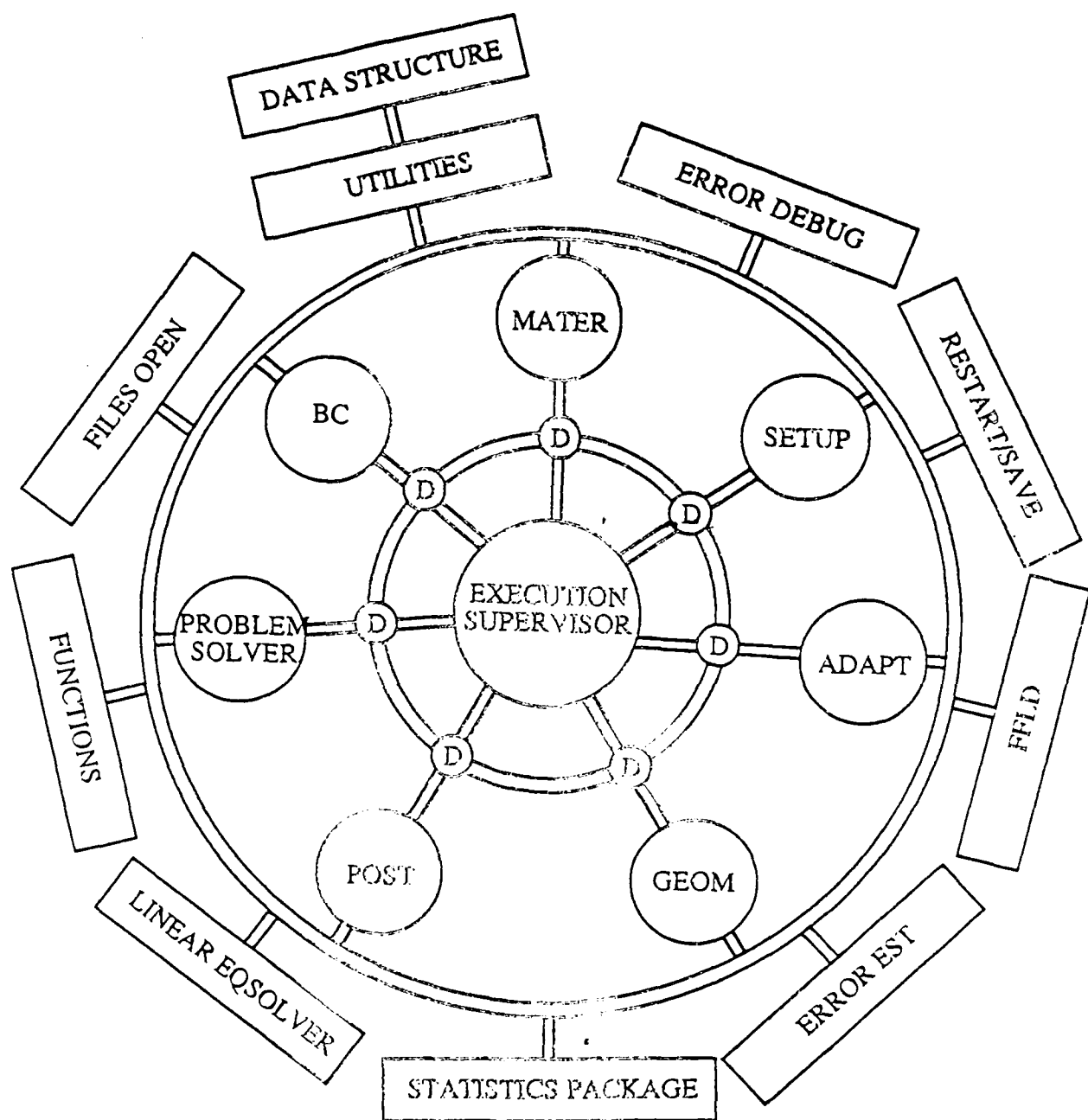
Importantly, the elements of the finite element data structure, adaptive package, graphical interfaces and linear equations solvers were designed to be applicable to a general class of problems, and relatively easy customizable to specific problems in solid mechanics or fluid mechanics. Below, selected modules of the above kernel are discussed in more detail.

Object-based Data Structure

A new state-of-the-art data structure was designed and implemented in the kernel to avoid typical limitations of traditional finite element codes, such as:

- fixed size common blocks and arrays,
- predefined limits on problem size,
- element information spread throughout memory in variety of arrays.

The object-based data structure was coded in C computer language, which allows for dynamic memory allocation and more flexible handling of objects and structures. Typical examples of objects handled by this data structure are:



D driver access routines

Figure 4.1: A general finite element code structure

- elements,
- nodes,
- boundary condition data,
- set of degrees of freedom, etc.

The major advantages of object-based handling of these structures are listed below:

- the objects are created only when needed,
- all related information is contained in one structure, and closely packed in memory,
- all the objects are automatically saved/restarted,
- the memory is reused when object is deleted, say during mesh refinement.

It is of importance to note here, that the elements in the above data structure are grouped and colored in order to facilitate vector and parallel processing. The basic idea of this vectorization and parallelization is presented in figure 4.2. Importantly, all the elements in a batch are of the same type, so that the generation of element stiffness matrices and right-hand sides can be effectively vectorized by putting loop over elements as the innermost loop. On the other hand, since the elements in different colors have no common nodes or sides, the generation of element of element matrices and assembly for different colors can be performed in parallel.

Adaptive three-dimensional finite element meshes

The finite element kernel is designed to handle h-p adaptive finite element meshed for three- and two- dimensional problems. By h-p adaption we understand a finite element technique, wherein the elements can be automatically subdivided into smaller elements (h-refinement /unrefinement) and the polynomial order of approximation can be locally increased or reduced. A major advantage of properly designed h-p mesh is that it can achieve a higher order of accuracy with much less degrees of freedom than traditional finite element methods. Moreover, the optimal mesh is designed automatically by adaptive procedure driven by appropriate error estimators.

For three-dimensional problems, anisotropic h -refinement can offer a wide improvement in computational effort over more conventional isotropic refinement schemes. This is primarily true because anisotropic refinement allows for selected refinement in the directions of interest

```

loop over colors
loop over groups
loop over batches
loop over integration points
possible parallel execution
vector code
  { compute element data
    get problem coefficients
    (MCOEFF, BCOEFF)
    assemble l.h.s. and r.h.s.
  } for batch
endloop
endloop
endloop
endloop

```

color — not connected elements
group — "topologically" identical elements
batch — optimal vector length

Figure 4.2: Vectorization and parallelizaton for groups and colors

only (i.e., directions of high error). Thus, anisotropic refinement may greatly reduce the total number of unknowns in many problems, in turn reducing the required computational effort.

Isotropic refinement implies that an element is identically refined in each local direction. For a hexahedral element, an isotropic refinement is a division into two along each of the three local directions, which results in eight sub-elements. In contrast, an anisotropic refinement of a hexahedral element is a division into two along a single local direction, resulting, of course, in only two sub-elements. Thus, if solution phenomena is oriented with respect to a particular local direction, then anisotropic refinement allows for degrees of freedom to be introduced only in the direction which actually reduces the total error. Isotropic refinement, on the other hand, would have introduced degrees of freedom in all directions, many of them providing little improvement to the overall solution. Anisotropic refinement can, therefore, provide a higher level of accuracy than isotropic refinement using the same number of degrees of freedom.

Several examples of h-adapted meshes in three dimensions will be shown in Section 6. Note that the mesh refinement introduces several theoretical and numerical complications into the algorithm, such as:

- constrained or "hanging" nodes between elements of different refinement level,
- propagation of constraints and possible "deadlocks" in the case of directional refinements for complex geometries,
- complications of unrefinement due to one-to-two approximation rule.

Detailed discussion of these issues is beyond the scope of this report. It is sufficient to note, that before application of the above kernel to asperity modeling all these difficulties have been successfully resolved and the existing kernel offers operational unique automated directional refinement capability for three-dimensional hexagonal meshes.

Interactive user's interface and graphical postprocessing

have been implemented in the adaptive kernel to enable user-friendly operation of the code and viewing of three-dimensional result. The interactive graphic interface is based on a window environment, with a menu-driven selection of options. A sample view of the screen with several windows open is presented in figure 4.3.

The graphic interface can be customized for specific applications, such as contact and friction modeling, so that the solution process and essential data can be controlled interactively by the user.

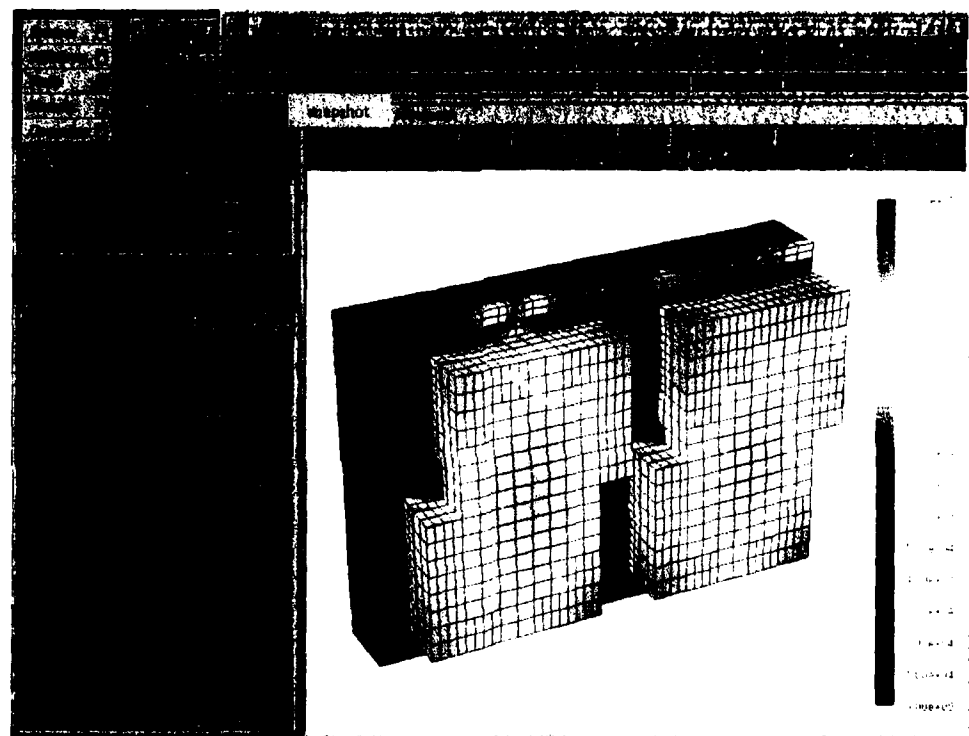


Figure 4.3: Sample screen with interactive window environment

The most important feature of the graphical user interface is a three-dimensional interactive postprocessing capability. For two-dimensional models, such visualization is rather trivial as all of the computational domain is always visible and it is a simple matter to zoom and/or pan through the mesh to closely review the results. The real challenge comes from the need to visualize phenomena in three-dimensional domains where most of the numerical data is actually hidden from the observer and one needs to enter the domain to view the local structure of the solution.

The postprocessing capability implemented in the kernel is capable of displaying solution obtained on structured and unstructured meshes, with both h-refinement and p-enrichment present in the mesh. The package is fully interactive and operates efficiently on high-end workstations. The basic graphic features displayed include:

- mesh plots,
- isosurfaces of selected quantities,
- slicing planes with overlaying isolines,
- deformed configurations,
- three-dimensional cursor for picking pointwise values of the solution,

All the above displays are available with interactive translation, rotation and zoom options, hidden line removal, panning, etc.

Importantly, the graphics package is designed to take advantage of specialized graphic hardware and software available on many platforms. The primary platform for the package is the SGI Iris family, which is also a primary platform in this project. Alternatively, X-windows graphics is supported, which is operational on most Unix workstations.

4.2 Formulation of a Structural Deformation Problem in the 3D Code

In the project, the 3D kernel was customized to solve contact problems. It was supplemented with over 8,000 instructions. They enable to run specialized drivers when a contact problem is to be solved. The drivers solve the contact problem using either total formulation or incremental formulations (see section 3.4). The first one uses Newton-Raphson iterative method and calls the FEM linear solver at each iteration step. The second driver uses Euler predictor corrector integration method with automatic time step control and calls the FEM linear solver twice at each time step.

To solve solid mechanics problems with contact, additional customization of the kernel FEM code had to be implemented. They define, in a special format, coefficients of the volume and boundary integrals introduced in previous section. As regards the contact condition, it was assumed that contact can take place at any point of the boundary on which static boundary conditions are applied. Therefore, while the integrals over this part of boundary are evaluated, the program examines whether an integral point is in contact with the flat. If penetration is greater than zero, then integrals corresponding to contact and friction are added to the coefficients of the stiffness matrix and the right-hand side. Additionally, adhesion integrals are being evaluated right outside the contact zone. In order to properly capture the strongly nonlinear separation-dependent adhesion forces, very fine integration schemes are being used.

To enable automatic generation of meshes for asperity analysis, five additional programs were prepared. They generate customized grid files for:

- 3D axisymmetric asperity (cosine hill),
- 3D axisymmetric asperity (spherical),
- 2D asperity (cosine hill),
- 2D asperity (cylindrical),
- 2D trapezoidal asperity.

The first two programs make use of an in-house GAMMA3D mesh generator . All of them provide generation of meshes with first and second order of geometry approximation.

5 Basic Verification of Numerical Models

To confirm reliability of the code and material models several numerical tests were performed. Selected tests are described in this section.

Several basic tests were carried out to verify the linear elasticity formulation. They were performed for both 3D and 2D problems with second and first order geometry approximation. The results of tests were compared with analytical solutions. Satisfactory results were obtained for all the polynomial orders (1 through 8).

The objective of the next group of tests was to verify incremental formulation of the viscoplastic problem. They were carried out for alloy B1900+Hf at temperature 871°C. Material constants as well as experimental results for this material are given in reference [10]. For Bodner-Partom model the material constants are as follows:

D_o =	10^4 s^{-1}	m_1 =	0.270 MPa^{-1}
n =	1.03	m_2 =	1.52 MPa^{-1}
z_o =	2400 MPa	r_1 =	$r_2 = 2$
z_2 =	2400 MPa	A_1 =	$A_2 = 0.0055 \text{ s}^{-1}$
z_1 =	3000 MPa	E =	142 GPa
z_3 =	1150 MPa	ν =	0.0805

Some of these tests are listed below:

- (a) Solution of the uniaxial tension for a purely elastic body using the incremental formulation. The results were the same as obtained with the total formulation.
- (b) Solution of the uniaxial creep test for an elasto-visco-plastic body. The results were compared with an experiment presented in reference [56]. Certain discrepancy of results was observed. This discrepancy was caused by an erroneous value of the Young modulus given in reference [56]. After a correction of Young modulus ($E = 132 \text{ GPa}$) the numerical and experimental results agreed satisfactorily (see Fig. 5.1). The test verified mathematical and numerical models for this simple loading (uniaxial tension).
- (c) Next three tests were carried out in order to examine the performance of the computer program for more complicated loading histories. The tests included:
 - Uniaxial cyclic tension and compression shown in Fig. 5.2.
 - Uniaxial loading for 5,000 s and relaxation for next 5,000 s. See Fig. 5.3.
 - Loading for 1,000 s and creep for next 1,000 s. See Fig. 5.4.

The above basic tests verified the formulation of the viscoplastic problem as well as its implementation in the code.

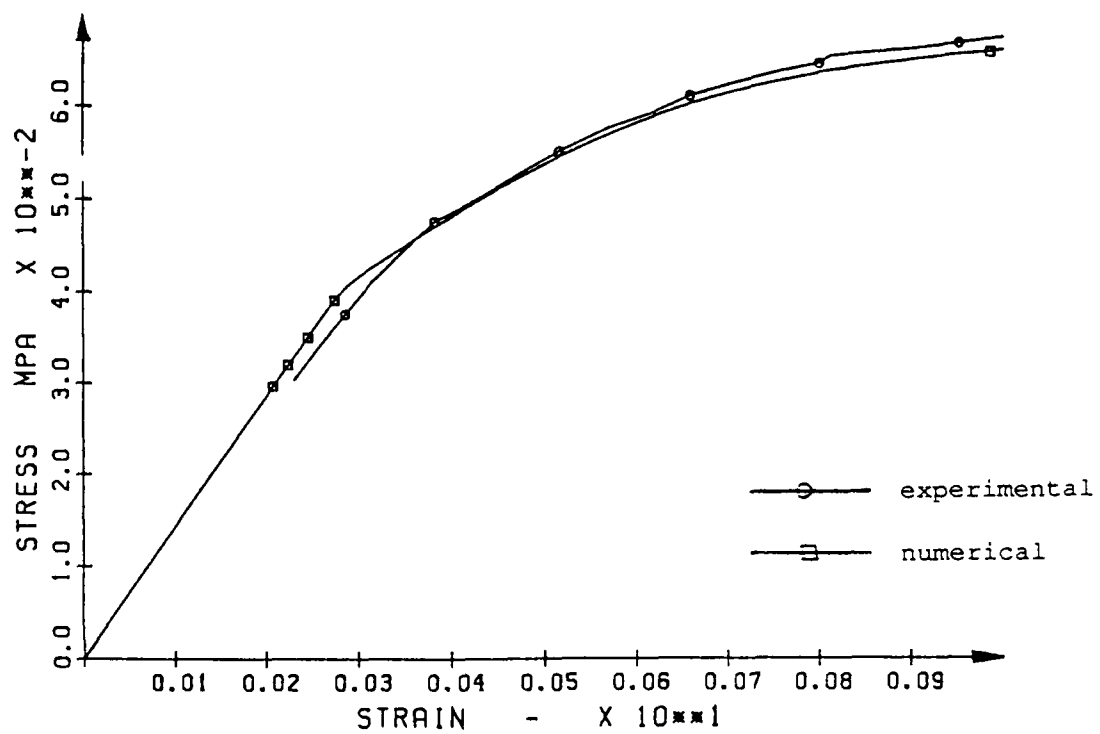


Figure 5.1: Experimental and numerical results of uniaxial tension of a specimen with corrected Young modulus

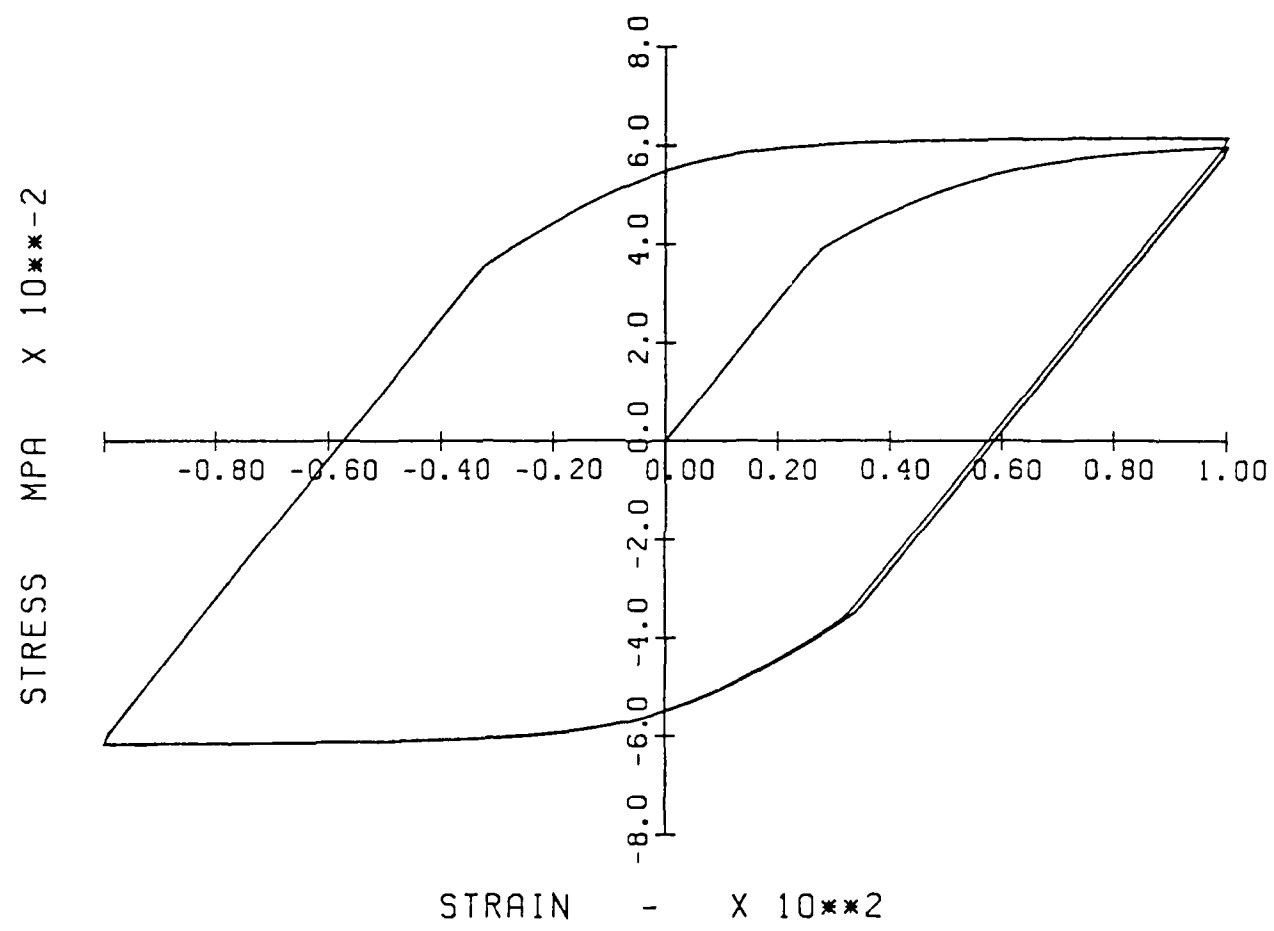


Figure 5.2: Cyclic loading test of the viscoplastic model - 10 cycles.

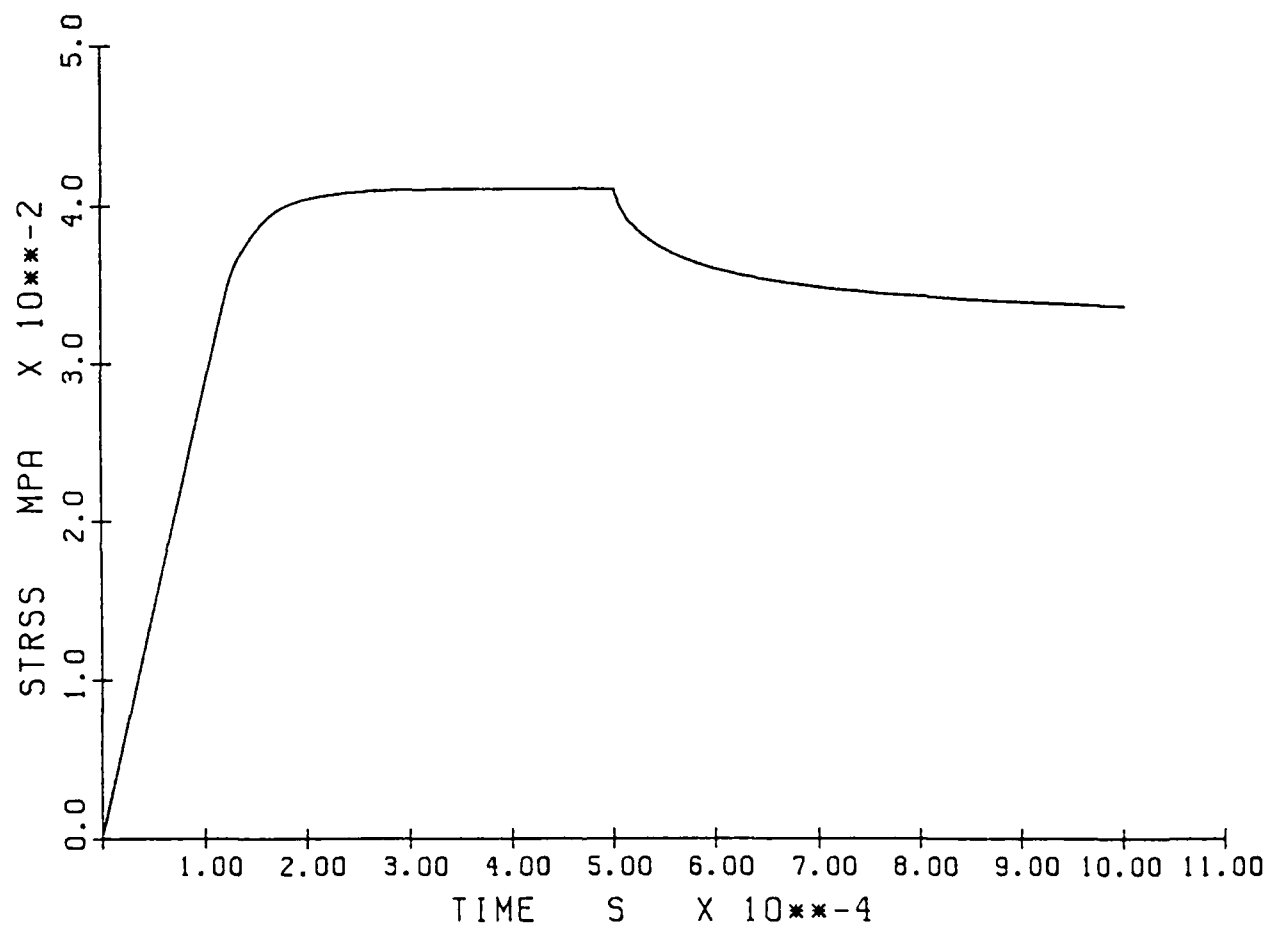


Figure 5.3: Relaxation test of the viscoplastic model

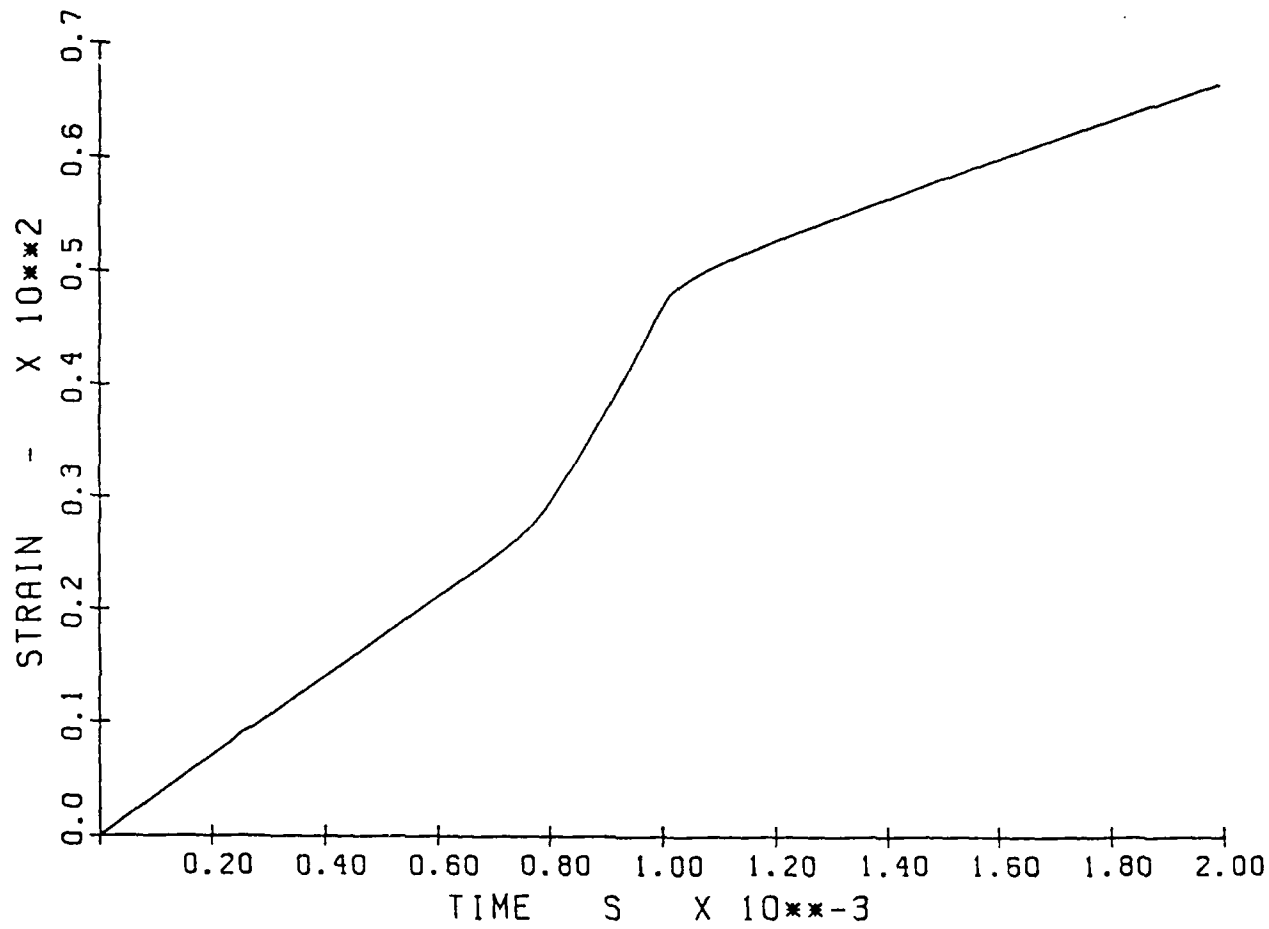


Figure 5.4: Creep test of the viscoplastic model

6 Verification of Numerical Models of Asperity

Numerical modeling of response of surface asperities to contact and friction loads is one of basic components of the new asperity-based interface models developed in this project. In order to verify correctness of finite element asperity simulations, we performed several tests and comparisons, in particular:

- modeling of elastic sphere in contact with a rigid flat, (Hertz problem). Analytical solution is available for this problem [48,91],
- numerical modeling and experimental measurements for custom-made asperities with strongly pronounced nonelastic properties.

Details of these tests are presented further in this section.

6.1 Elastic Sphere in Contact with a Rigid Flat

In order to verify the contact algorithm and the nonlinear solution procedure, a finite element solution was obtained for the contact of elastic sphere with a rigid flat. The finite element solution of this problem was compared with theoretical solution due to Hertz [48,91]. For a given sphere of radius R and prescribed normal displacements of the flat equal w , the theoretical predictions of the contact radius r , contact area A and total load P are given by:

$$\begin{aligned} r &= \sqrt{Rw} \\ A &= \pi R w \\ P &= \frac{4}{3} \frac{E}{(1-\nu^2)} R^{\frac{1}{2}} w^{\frac{3}{2}} \end{aligned}$$

The above problem was solved numerically using the following dimensionless data:

$$\begin{aligned} R &= 1.0 \\ E &= 1000. \\ \nu &= 0.3 \\ w &= .001, .002, .005, .01, .02 \end{aligned}$$

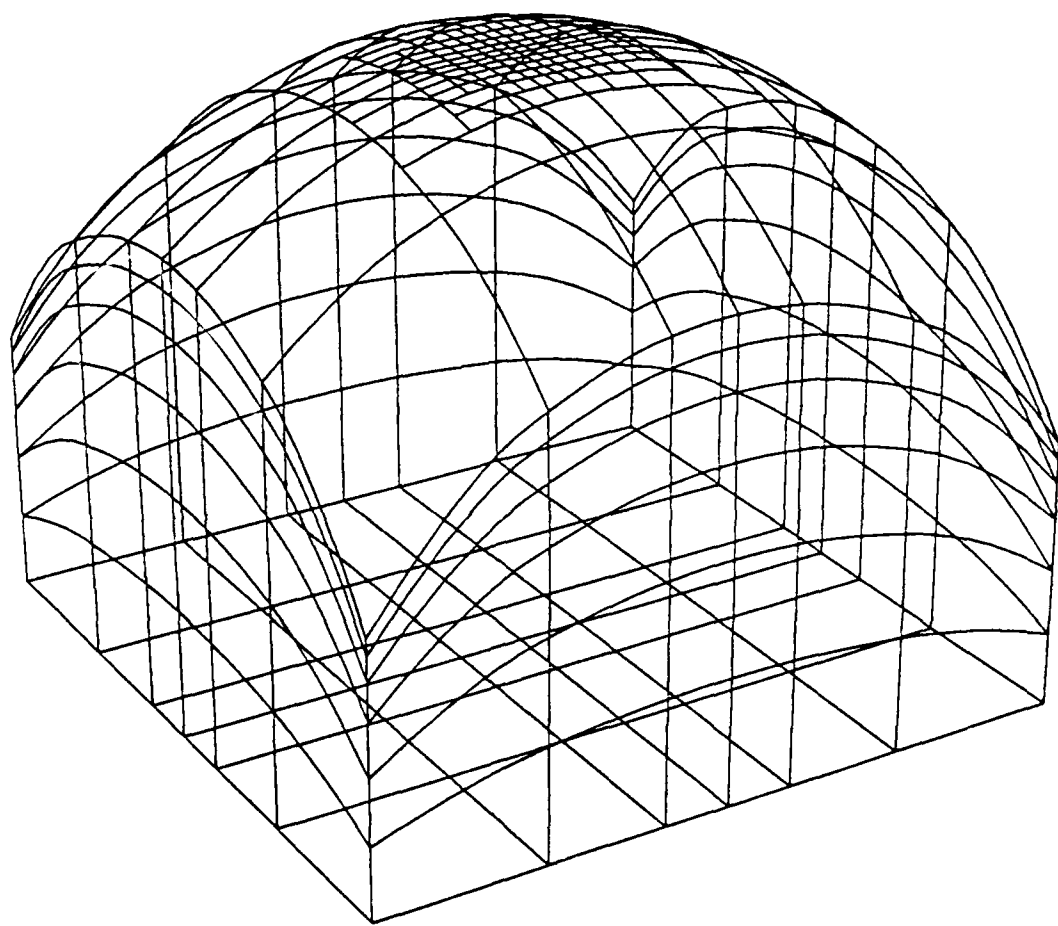


Figure 6.1: h-p refined mesh for the Hertz problem, $w = .02$, deformed configuration. Only boundary elements shown. P-order up to three.

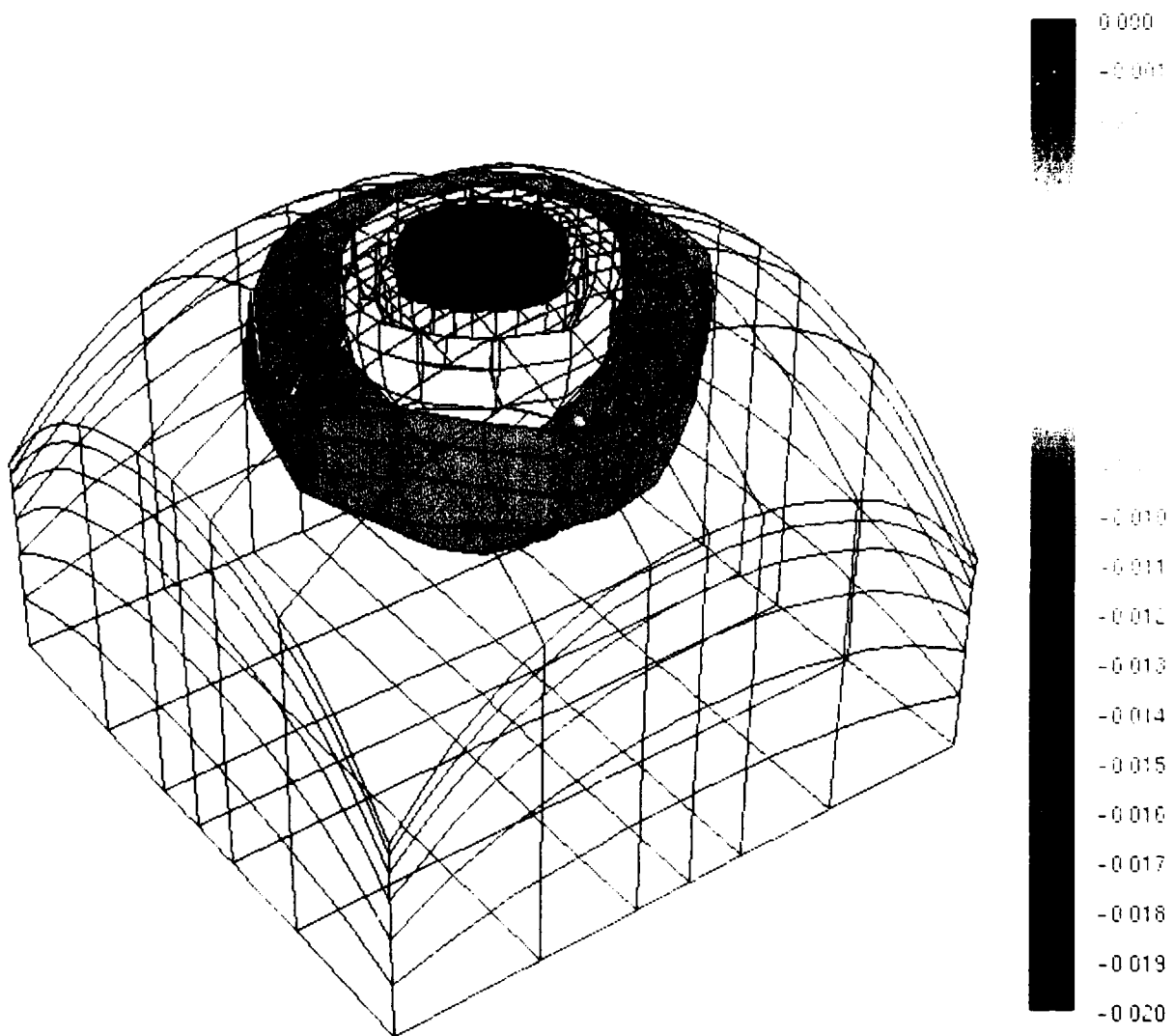


Figure 6.2: Isosurfaces of the vertical displacement for the Hertz problem, $w=.02$

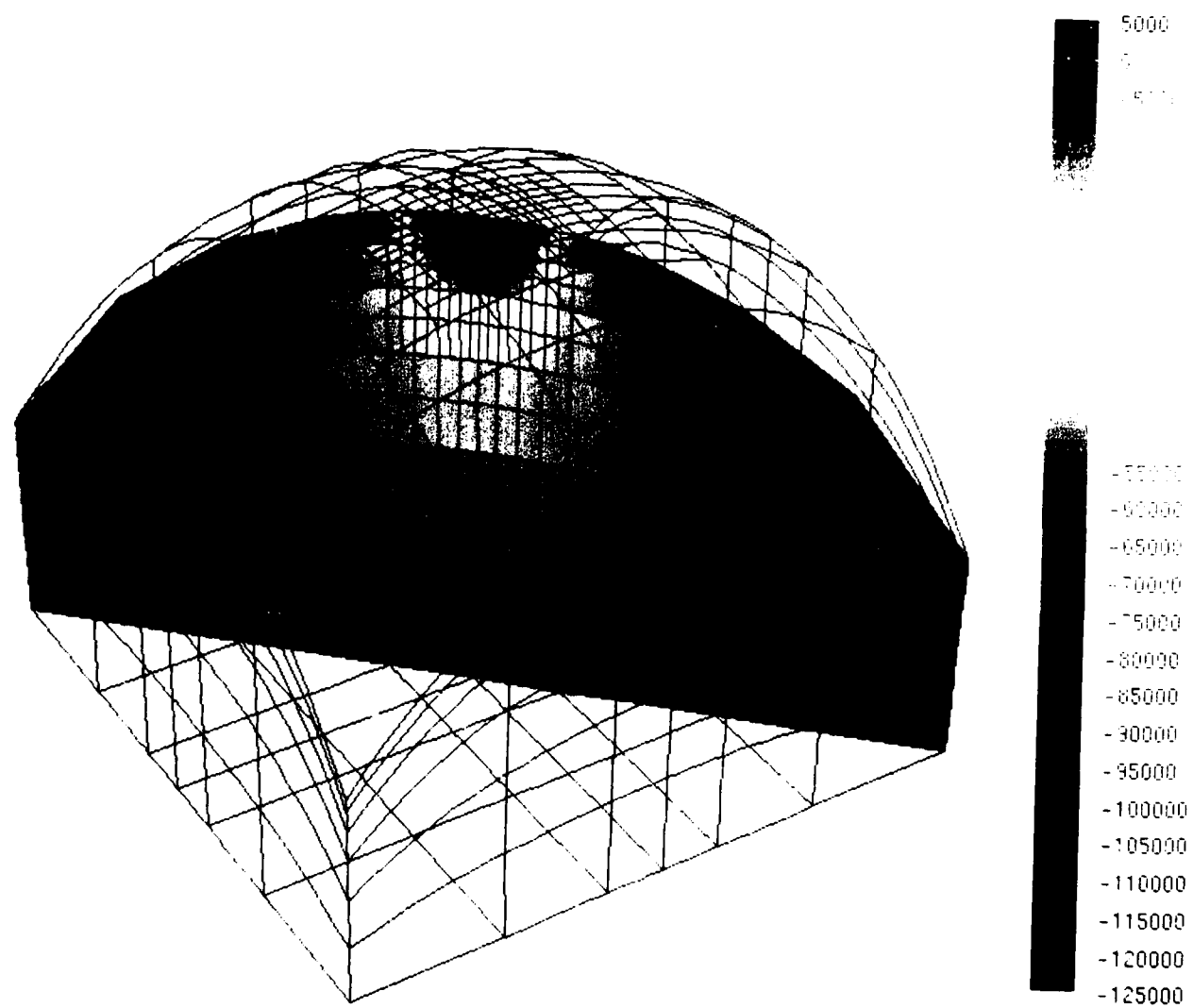


Figure 6.3: Isosurfaces of the σ_{yy} for the Hertz problem, $w=.02$

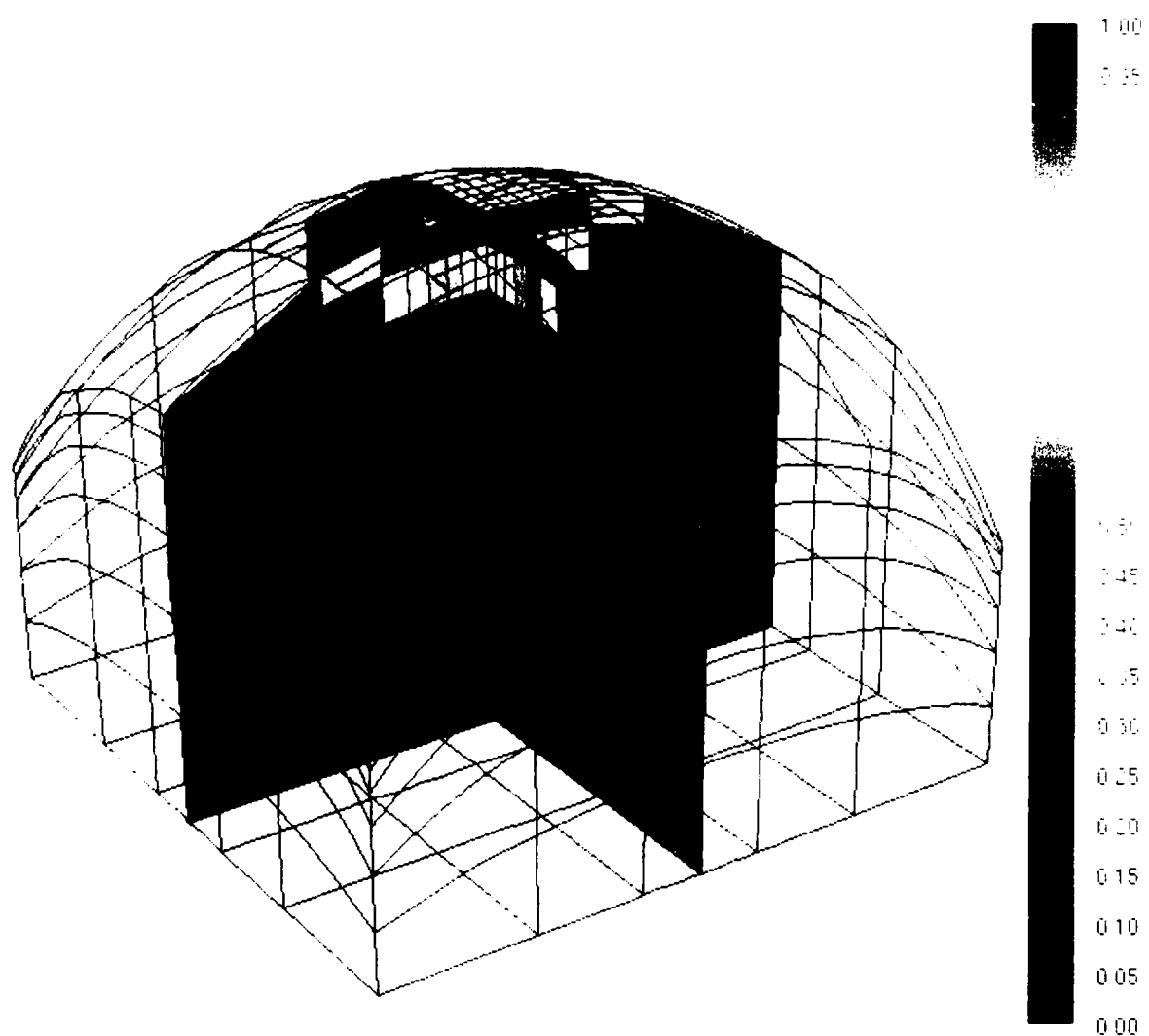


Figure 6.4: Distribution of error indicator for the Hertz problem, $w = .02$

Due to a localized nature of the contact, the finite element mesh was defined only for a section of the sphere around the contact zone. The problem was solved using the Newton procedure combined with adaptive mesh refinement. An example of the final refined mesh obtained for $w=.02$ is shown in figure 6.1 (deformed configuration is displayed and only boundary elements are shown for clarity). The same mesh with isosurfaces of vertical displacement is presented in figure 6.2, the slicing plane, with stress σ_{yy} , is shown in figure 6.3, and the error indicators projected on two slicing planes are displayed in figure 6.4.

The results obtained numerically compare favorably with numerical predictions. A detailed comparison of theoretical and numerical results are shown in table 6.5, and the graphical comparisons of predicted contact area and total load are shown in figure 6.6.

6.2 Experimental Studies of Models of Asperity

In order to verify numerical simulation of nonelastic behavior of asperities, several experimental measurements were performed and then compared with numerical predictions.

These tests included simple tension and compression problems designed to verify nonelastic material constants for aluminum, as well as contact tests for two types of custom-made asperities. In this phase of experiments, which we refer to as Phase I, custom asperities were chosen in order to eliminate random surface factor from the comparisons. In Phase II, which will be performed in the next year of the project, real random surfaces will be considered.

The objective of this Phase I experimental study is to study the deformation of contact surface asperities and to verify the analytical prediction by experimentation. In design of the experimental study, it is initially conceived that the test is to be carried out under a small normal load (500 Lbf) condition. A controlled surface asperities are machined onto both surfaces of an aluminum block. In the test arrangement, the aluminum block is sandwiched between two hardened steel blocks with smooth surfaces, and the steel-aluminum-steel block assembly is compressibly loaded to approximately 500 Lbf. The deformation of asperities on the aluminum block is monitored during loading. After completing the normal loading, a horizontal load is slowly applied to the aluminum block until the block begins to slip. An estimation of the coefficient of friction can thus be made by using the measured normal and horizontal loads, and be compared with that from the analytical prediction. A test apparatus is built for this purpose, and tests are carried out with this apparatus. After reviewing the test results, it is decided that the deformation of surface asperities on the aluminum specimen is too large for the purpose of model verification. The shape of asperity is changed, and the tests are carried out under a normal load of approximately 2,000 Lbf. The results from both arrangements are reported in this section.

ELASTIC SPHERE IN CONTACT WITH A RIGID FLAT

E = 1.0000E+03 nu= 0.3000 R= 1.0000

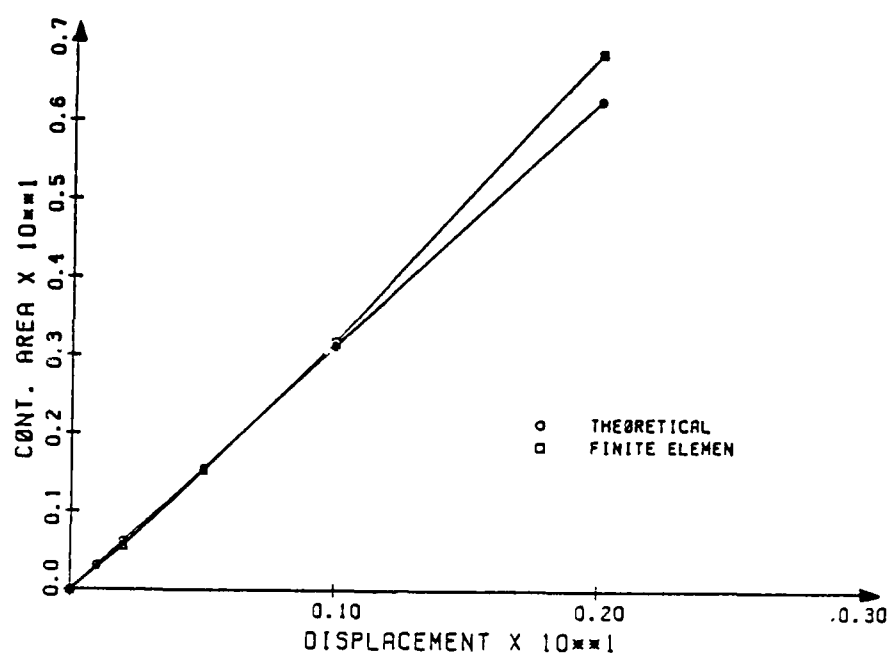
THEORY

Displ	Cont. rad.	Area	Load	Max. pres.
0.00200	0.04472	0.006283	1.3105E-01	3.1286E+01
0.00500	0.07071	0.015708	5.1803E-01	4.9468E+01
0.01000	0.10000	0.031416	1.4652E+00	6.9958E+01
0.02000	0.14142	0.062832	4.1442E+00	9.8936E+01

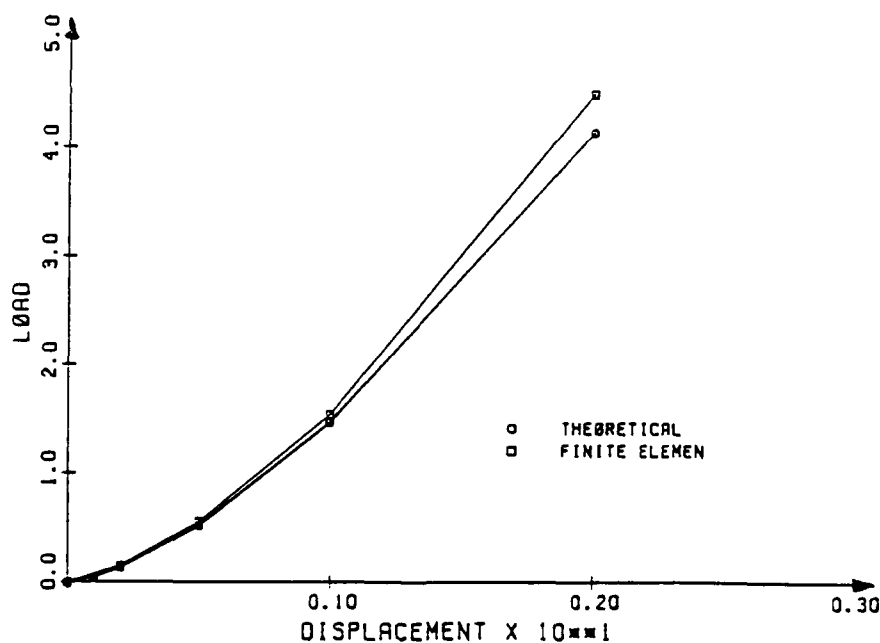
NUMERICAL

Displ	Cont. rad.	Area	Load	Max. pres.
0.00200	0.04237	0.00564	1.5400E-01	4.3600E+01
0.00500	0.07001	0.0154	5.5400E-01	5.4000E+01
0.01000	0.10092	0.0320	1.5400E+00	7.9200E+01
0.02000	0.14809	0.0689	4.5000E+00	1.0840E+02

Figure 6.5: Comparison of theoretical and numerical results for the Hertz problem



a)



b)

Figure 6.6: Comparison of theoretical and numerical results for the Hertz problem; (a) displacement versus contact area, and (b) displacement versus contact load

6.2.1 The Test Apparatus

A sketch of the apparatus is shown in Fig. 6.7. An aluminum (6061, T4) block of 1' x 1' x 0.25" is sandwiched between two steel blocks of the same dimension as shown in the figure. The V-shaped grooves of angle 45 deg, pitch spacing of 0.1 inch, and depth of 0.125 inch are machined with a specially designed cutter on both surfaces of the aluminum block to simulate the surface asperities. A sketch of the grooves is shown in Fig. 6.8. The surfaces of the steel blocks are machined smooth and (water) quench hardened to RC-30. It should be mentioned that, due to the angle of the cutting tool and the pitch spacing, the tips of the grooves are not in a plane, the heights of tips vary alternatively as shown in the photograph (Fig. 6.8) to be discussed in a later section.

A normal load is applied to the specimen assembly through a mechanical screw jack from the bottom of the apparatus. The normal load is monitored with a small "load transducer" of capacity 500 Lbf. The normal deformation of the simulated asperities on aluminum block is measured with a "proximate sensor" with an operation range from 0 to 0.1 inch. The sandwiched specimen assembly is first installed in position, and an initial load of approximately 50 Lbfs is applied to the specimen prior to "zero adjustment" of the recording instrument (an X-Y plotter). A total normal load of 500 Lbs is then applied to the specimen at a rate of approximately 10 Lbf per minute. After the normal load has reached 500 Lbf, a horizontal load (by lead blocks and beads) is slowly applied to the aluminum block until the block starts to slide. The horizontal load is monitored with a ring-shaped load transducer (laboratory built) as shown in Fig. 6.7.

Note that even with very precise calibration of the test apparatus, certain compliance or "setting in" occurs during loading and pollutes the measurements. This is especially true in case of high loads and very small displacements considered in this experiment. It is a standard practice in experimental tests to discard the initial part of the load curve and appropriately translate the remaining part. In this section, we present results in the "raw" form, but numerical comparisons refer to corrected graphs.

6.2.2 Tests Results From the Above Apparatus

Two tests are carried out. A representative force-deformation plot is shown in Fig. 6.9. It is seen that there is an appreciable amount of plastic deformation of the surface asperities on the aluminum block (neglect the bulk deformation of both aluminum and steel blocks) when the block assembly is loaded to 500 Lbf. A horizontal force is then slowly applied to the aluminum block. It is visually observed that the aluminum block starts to slip when the horizontal load reaches 108 Lbf. Since there are two contact surfaces between the aluminum block (with asperities on both surfaces as shown in Fig. 6.8) and steel blocks (with smooth

surfaces) in the test arrangements, the nominal coefficient of friction is $(108 / 2) / 500 = 0.108$.

6.2.3 Deformation of Asperities Under a Larger Normal Load

The asperities shown in Fig. 6.8 have pointed tips, the deformation of tip is difficult to calculate. It is then decided to change the geometry of asperity as those shown in Figs. 6.8(b) and 6.8 (c). In Fig. 6.8 (b), the asperity is modeled as a 45-deg grooved with a truncated tip. In Fig. 6.8 (c), the asperity is modeled by spaced circular rods. The force-deformation relationship for the specimen with asperities as shown in Fig. 6.8 (b) and 6.8 (c) are measured. The test arrangements are the same as that described in the previous section. Since the maximum load in these test are much higher than 500 Lbf, the tests are carried out and the representative force-deformation curves are shown in Figs. 6.10 and 6.11, respectively. A photograph of the cross-section of the deformed grooves is shown if Fig. 6.12. It is seen that only the alternate grooves were deformed. There are seven grooves on each surface of the aluminum block, therefore only eight (four on each surface) of them are deformed. Since the maximum horizontal load required to move the aluminum block in this exceeds the capacity of the ring load cell used in previous section, the horizontal pulling test has yet to be carried out (we need to build a new load cell and loading frame).

Finally, a test for the tensile property of the aluminum used in this study is carried out. The stress-strain curve from an aluminum (6061, T4) specimen is shown in Fig. 6.13. Again, the test is carried out at a slow loading rate (approximately 20 Lbf per minute).

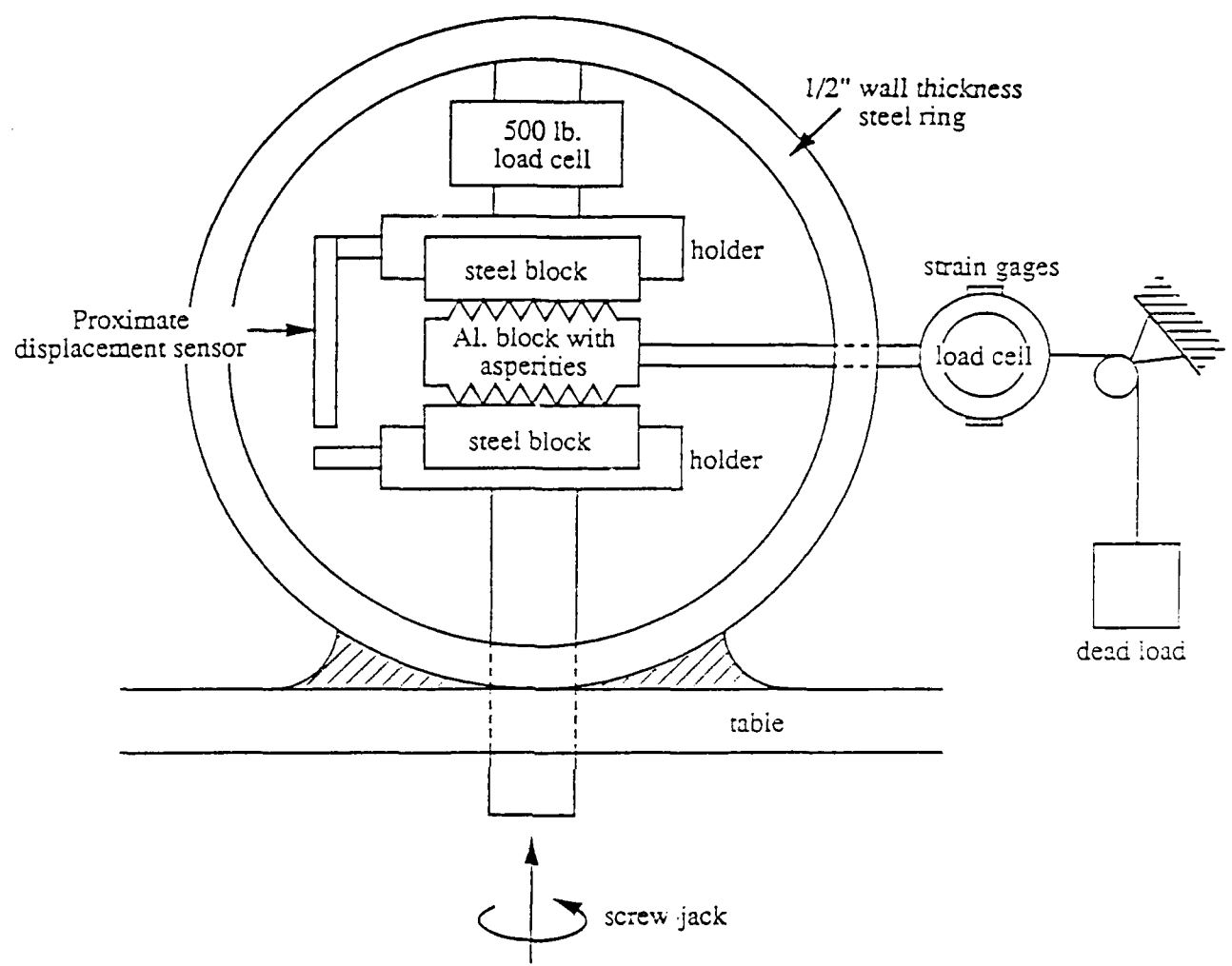


Figure 6.7: A sketch of test apparatus (not to scale).

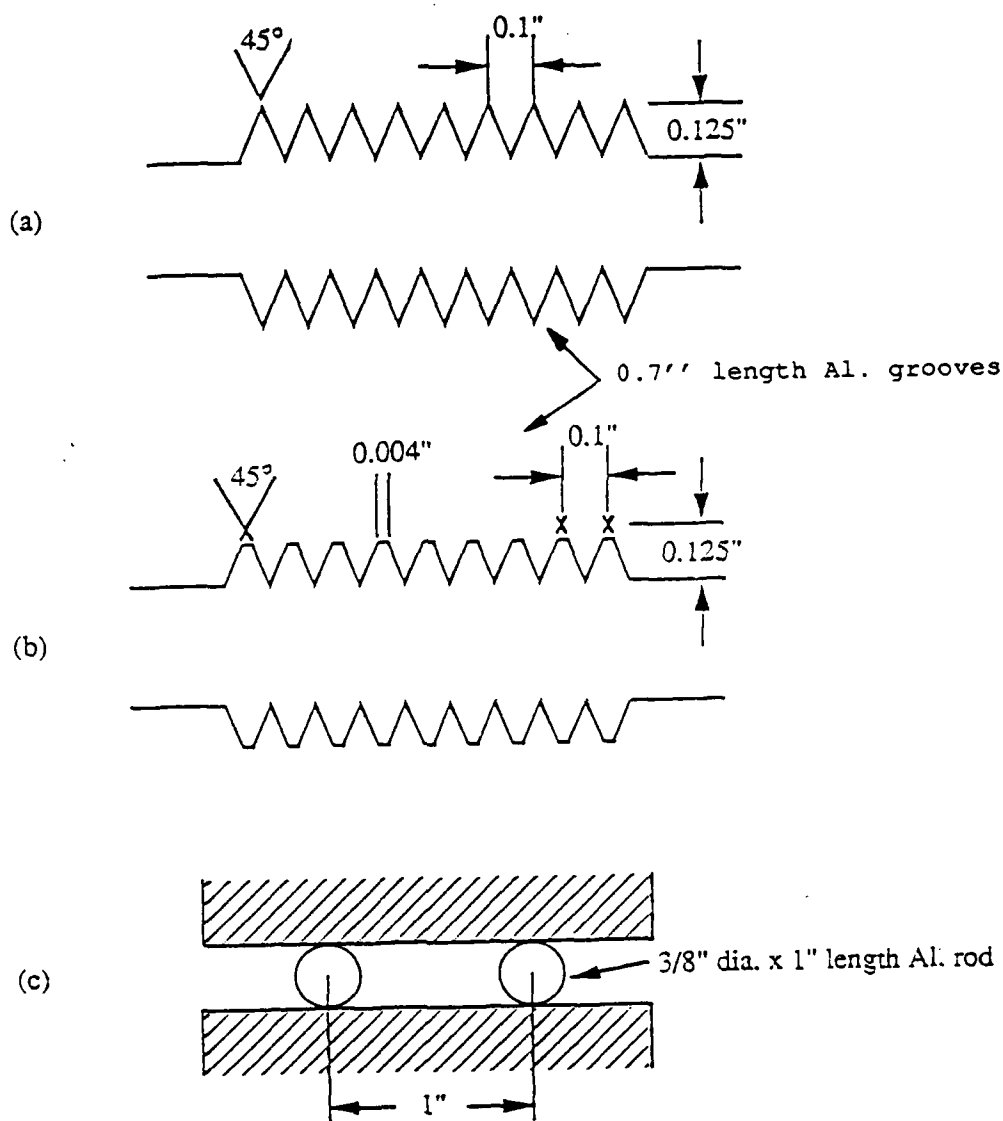


Figure 6.8: Different models of asperities studied experimentally.

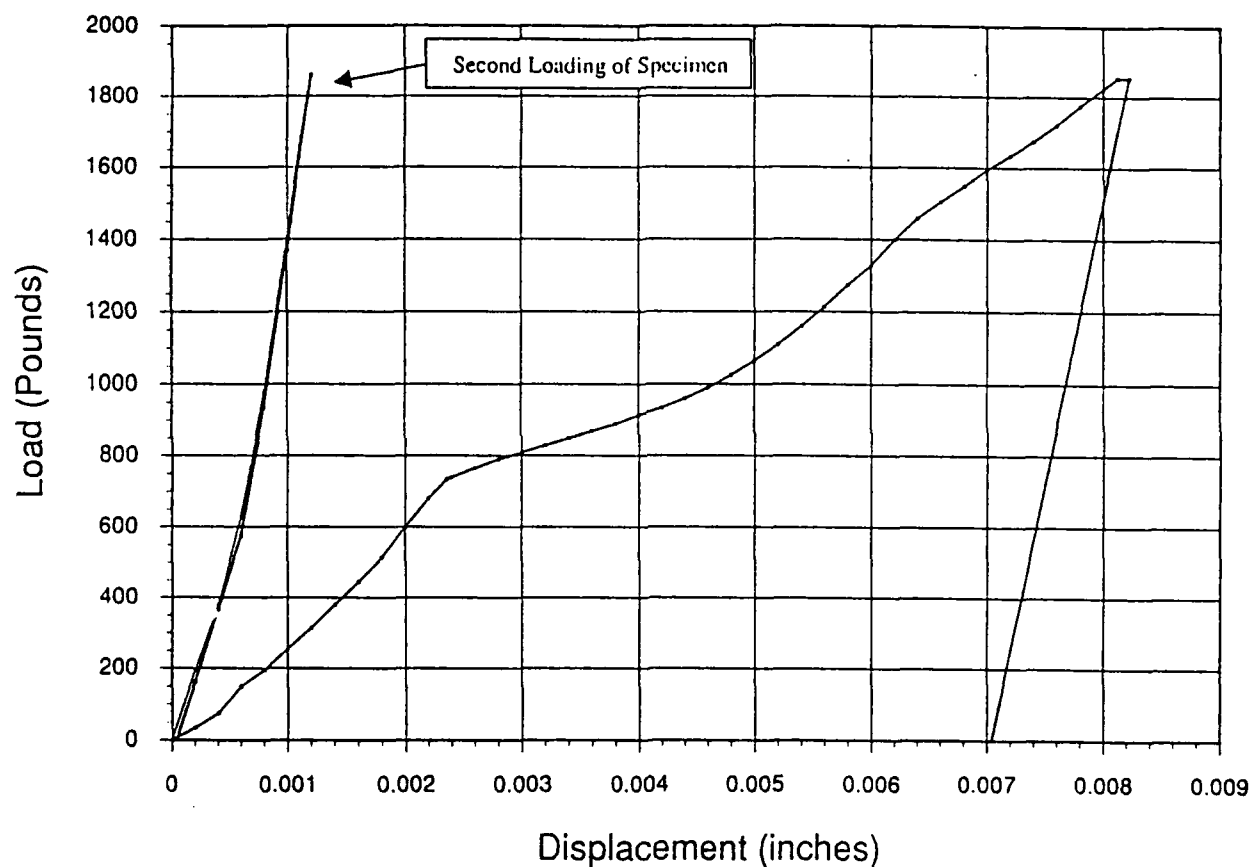


Figure 6.9: Load-displacement curve for V-shaped asperity

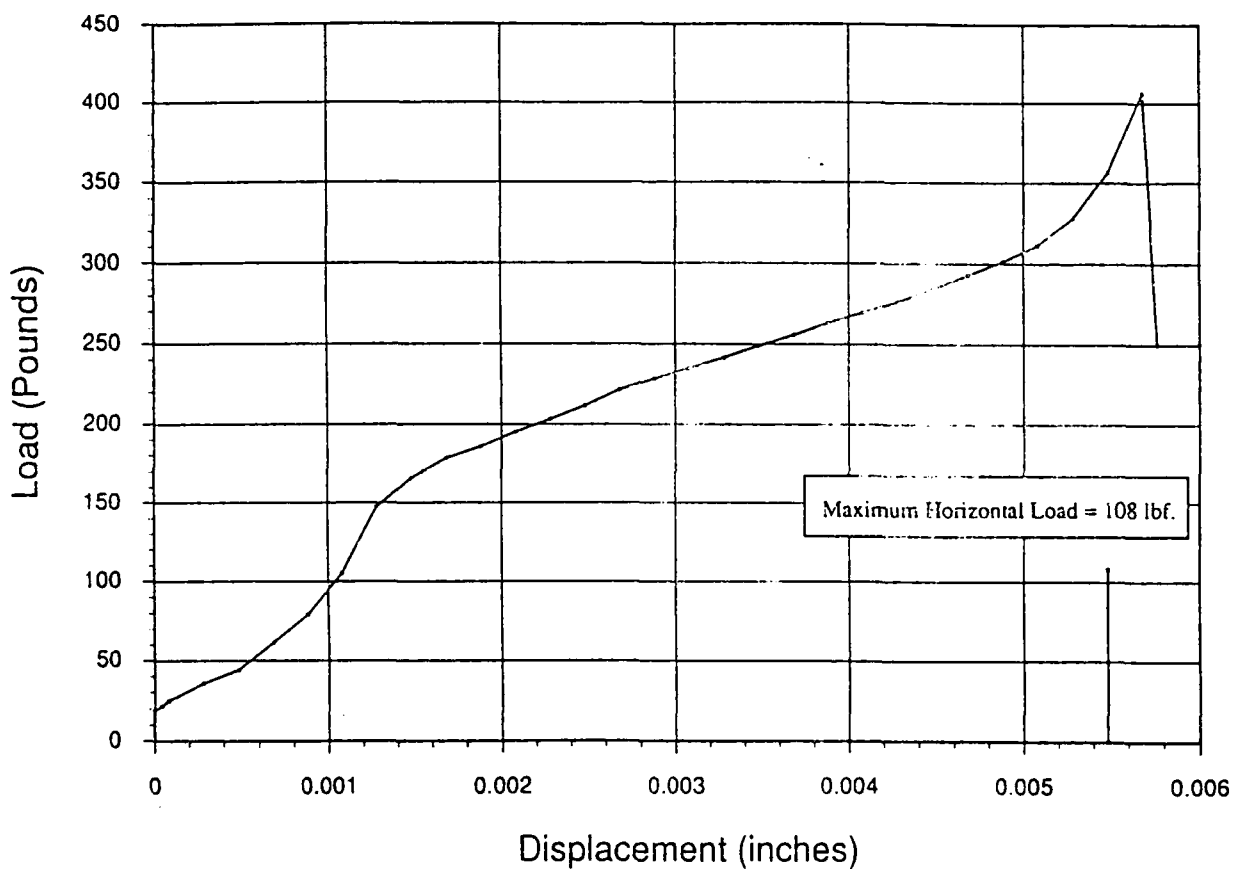


Figure 6.10: Load-displacement curve for truncated asperity

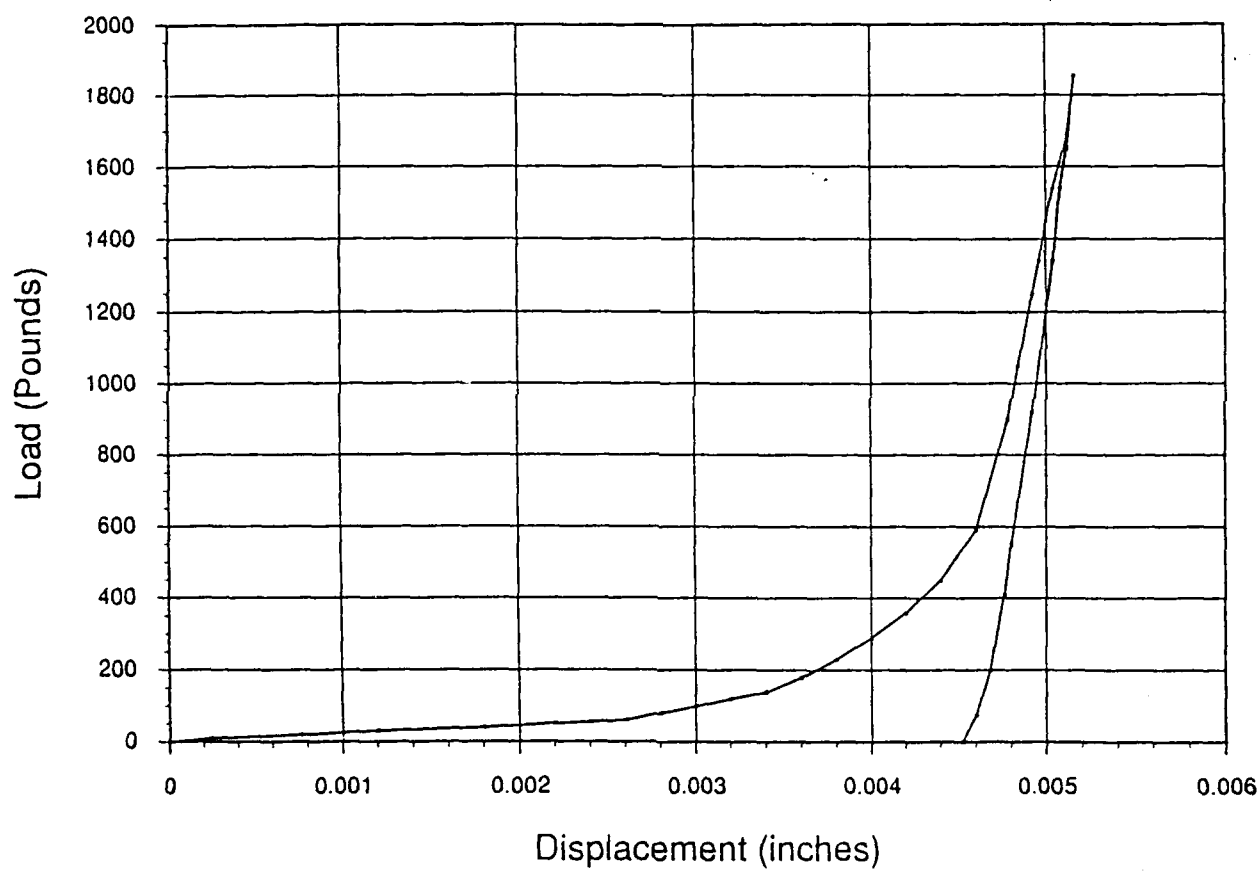


Figure 6.11: Load-displacement curve for cylindrical asperity

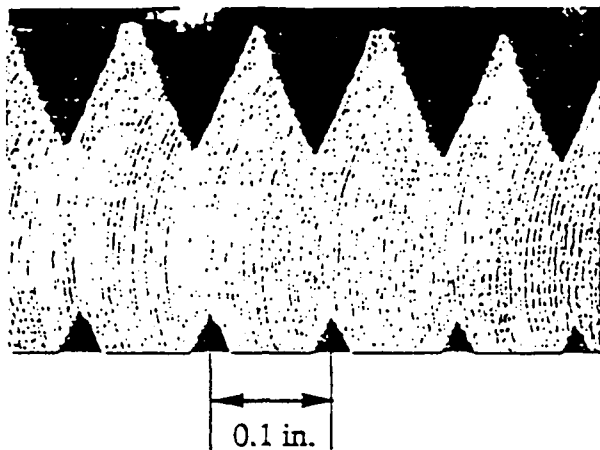


Figure 6.12: A photograph of deformed asperity

6.3 Numerical Simulation of Experimental Measurements

6.3.1 Viscoplastic Uniaxial Stress State

The aim of this final test was to determine viscoplastic material constants for aluminum 6061 T4. Bodner-Partom model of viscoplastic materials uses a total of 14 material constants. However, for aluminum alloys at room temperature only 7 material constants are of primary importance. Their values obtained from reference [10] for a different heat treatment (T6) are listed below:

$$\begin{aligned}
 E &= 73.9 \text{ GPa} \\
 \nu &= 0.33 \\
 z_0 &= 450 \text{ MPa} \\
 z_1 &= 550 \text{ MPa} \\
 m_1 &= 0.12 \text{ MPa}^{-1} \\
 D &= 10^8 \text{ s}^{-1} \\
 n &= 5.0
 \end{aligned}$$

In order to verify these values, a tension test was performed and compared with numerical results. The test indicated that the 6061 T4 sample has slightly different values of Young modulus and the kinematic hardening parameter. These values are:

$$\begin{aligned}
 E &= 65.0 \text{ GPa} \\
 n &= 5.8
 \end{aligned}$$

These material constants were used in further computations. Fig. 6.14 shows the plot of stress-strain relation for initial and modified material constants in comparison with the experimental results.

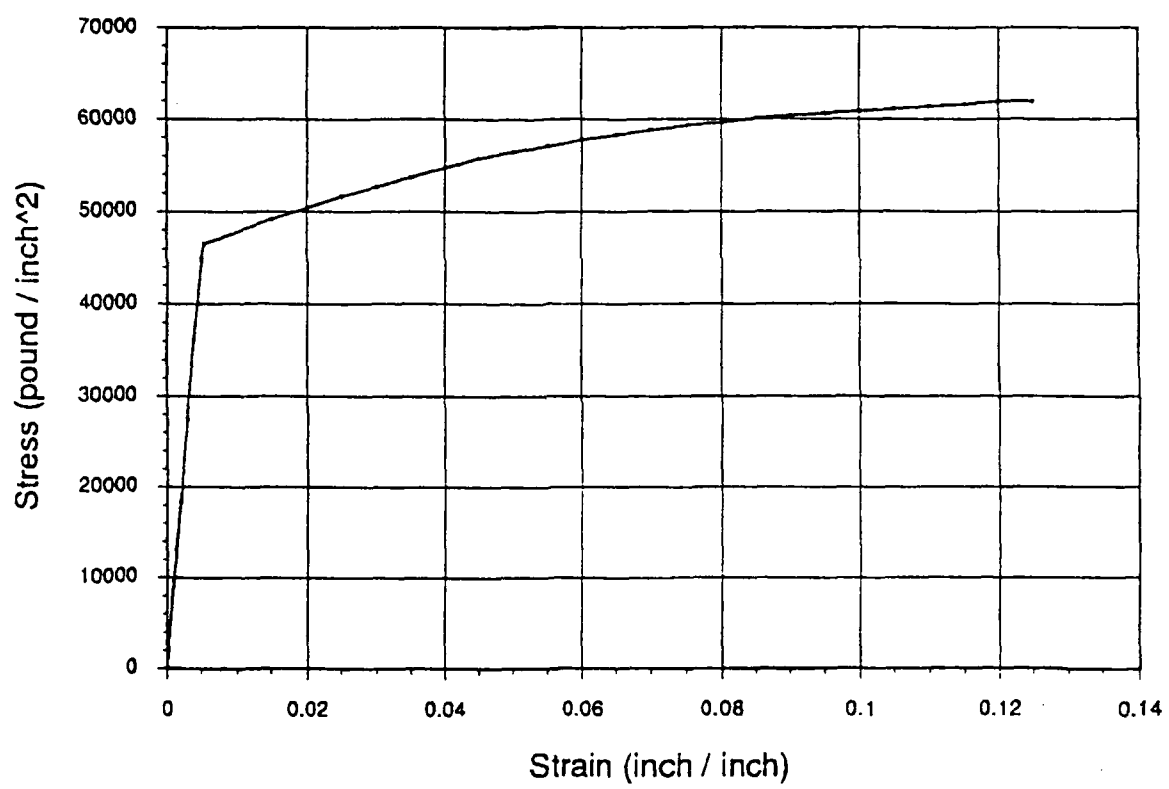


Figure 6.13: A tensile stress-strain curve for aluminum

6.3.2 Viscoplastic Cylindrical Asperity

Aluminum cylinder was used as a model of a "macro asperity". Numerical and experimental tests were carried out. It was assumed that the cylinder can be analyzed as a 2D case. The original mesh used for discretization of a section of a circle is shown in Fig. 6.15. After the first solution pass the mesh was automatically refined. It is shown in Fig. 6.16. The viscoplastic results obtained at both meshes as well as a purely elastic solution for the first mesh are compared in Fig. 6.17. The conclusions are that:

- behavior of the specimen under applied loading is almost elastic,
- viscoplastic solution is reasonable – it gives smaller values of the contact force,
- the refined mesh gives results which can be treated as a final numerical solution (the difference between solutions obtained at coarse and fine meshes is small.)

The numerical and experimental solutions are compared in Fig. 6.18. Note that the experimental results have been rescaled. Instead of the total force - total displacement relation measured in the experiment, Fig. 6.18 shows force per unit length of upper half-cylinder. Moreover, metric units were used.

It can be observed that the numerical results compare favorably with experimental measurements. Recall, however, that the experimental data were translated, to correct for settling in the apparatus (see Section 6.1).

6.3.3 Viscoplastic Custom Surface Model

Comparisons of results for a model truncated V-shaped of asperity are described in this section. Two meshes which were used for discretization of this specimen are shown in Fig. 6.19 and 6.20. Numerical results for both meshes are shown in Fig. 6.22 and 6.21. While for the cylindrical model the behavior of the material was almost elastic, in this case the influence of yielding was significant. Maximum nonlinear strain was about 80%. It means that at least locally solution is beyond the theory of small strains which we use. The comparison of numerical results and experimental ones is shown in Fig. 6.23. A good agreement of results can be observed for both models of asperity.

Some of inevitable sources of discrepancy are the following:

- error of experimented measurements,
- modeling of inelastic behavior of the material beyond the small deformation range,

- unknown deformation history of the specimens, prior to the experiment,
- errors of time-integration and other numerical errors.

Comparison of numerical and experimental results as well as the basic numerical tests lead to a conclusion that the adaptive finite elements represents nonelastic deformation of asperities with sufficient accuracy.

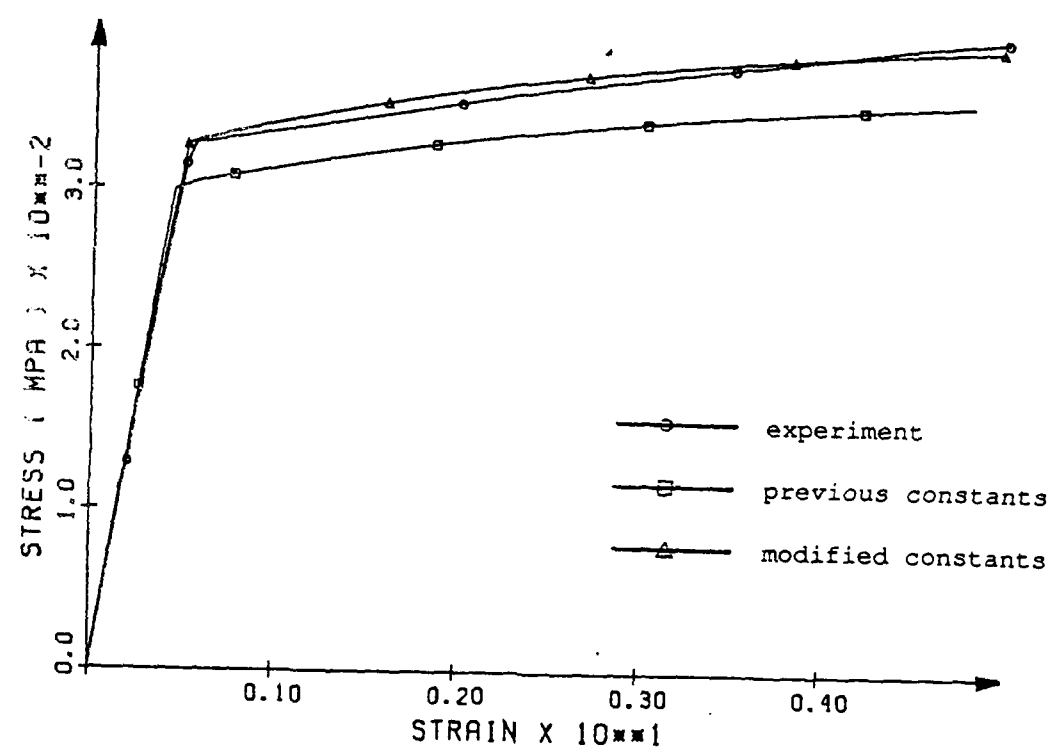


Figure 6.14: Comparison of stress-strain relation behavior for uniaxial tension test.

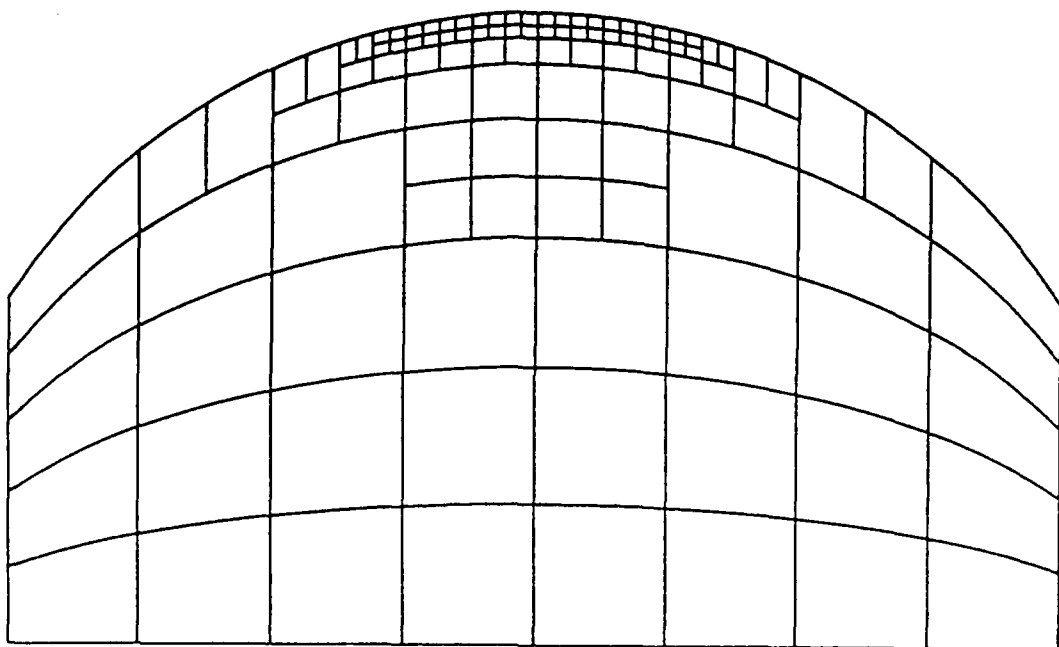


Figure 6.15: Original discretization of the cylindrical sample

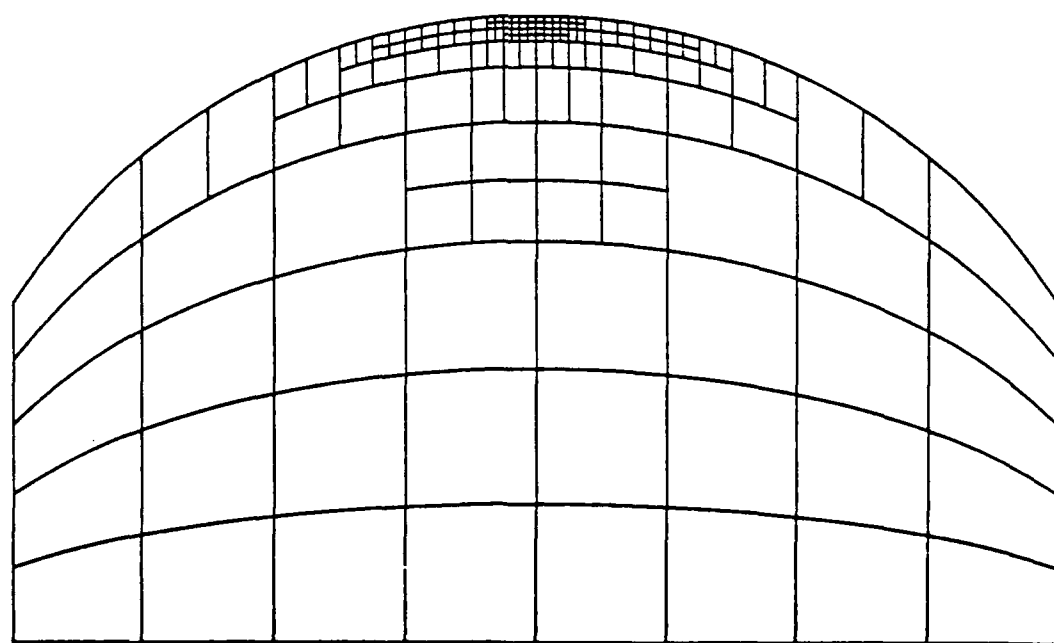


Figure 6.16: Refined discretization of the cylindrical sample

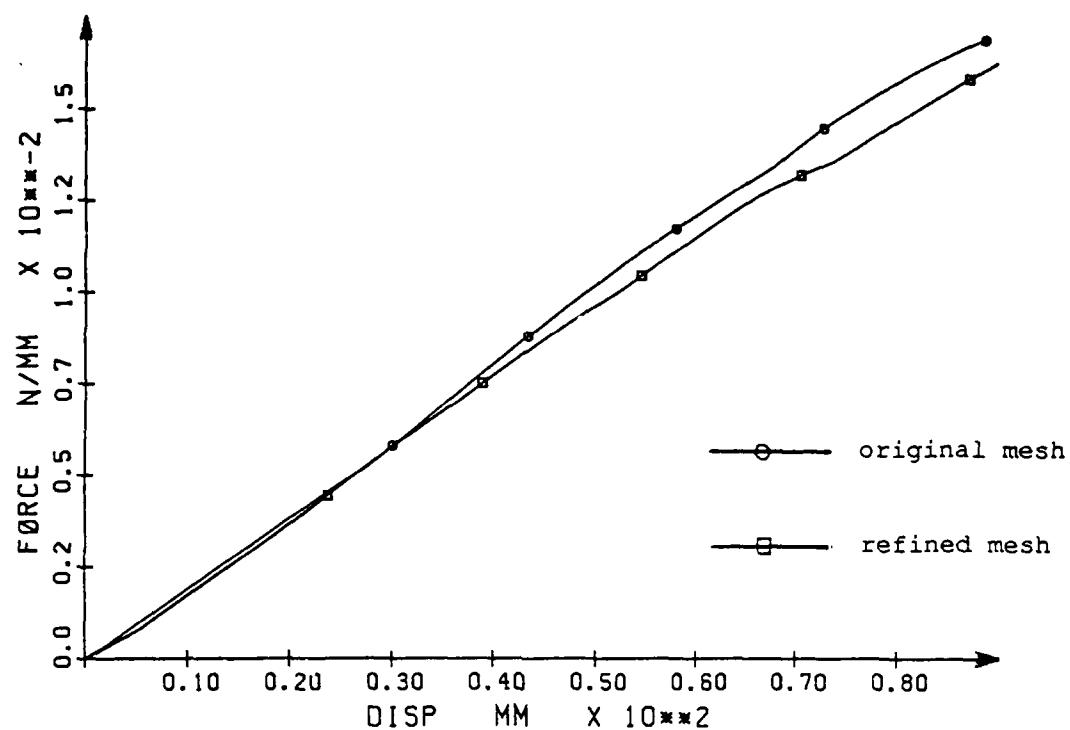


Figure 6.17: Numerical results for the cylinder

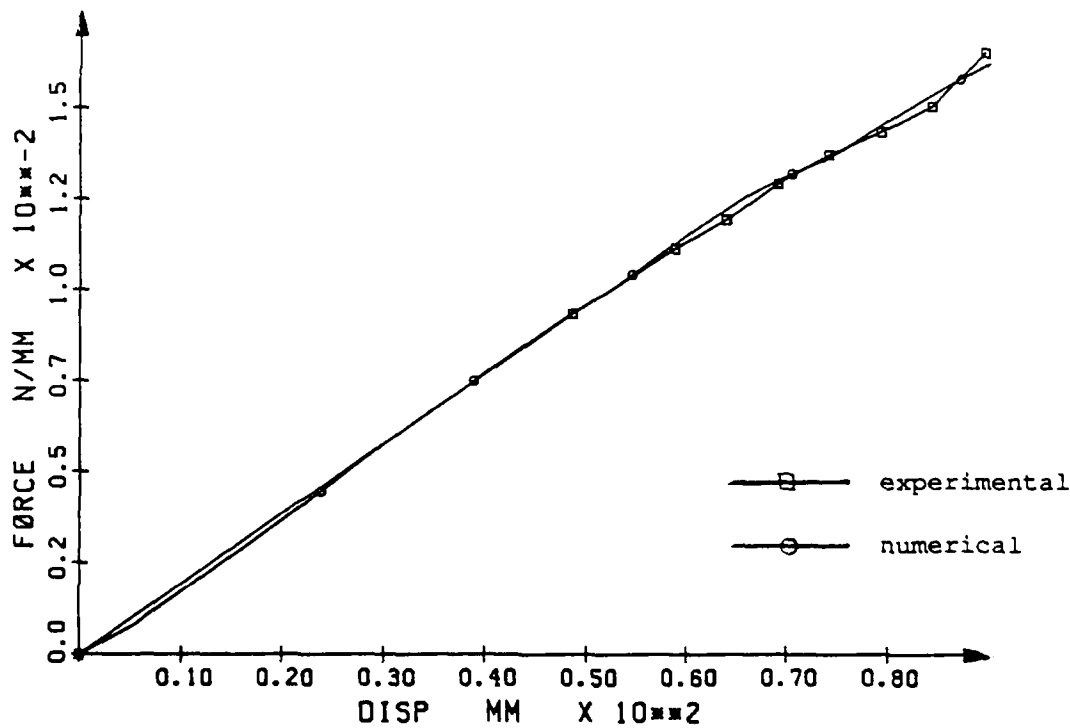


Figure 6.18: Comparison of numerical and experimental results for the cylindrical sample

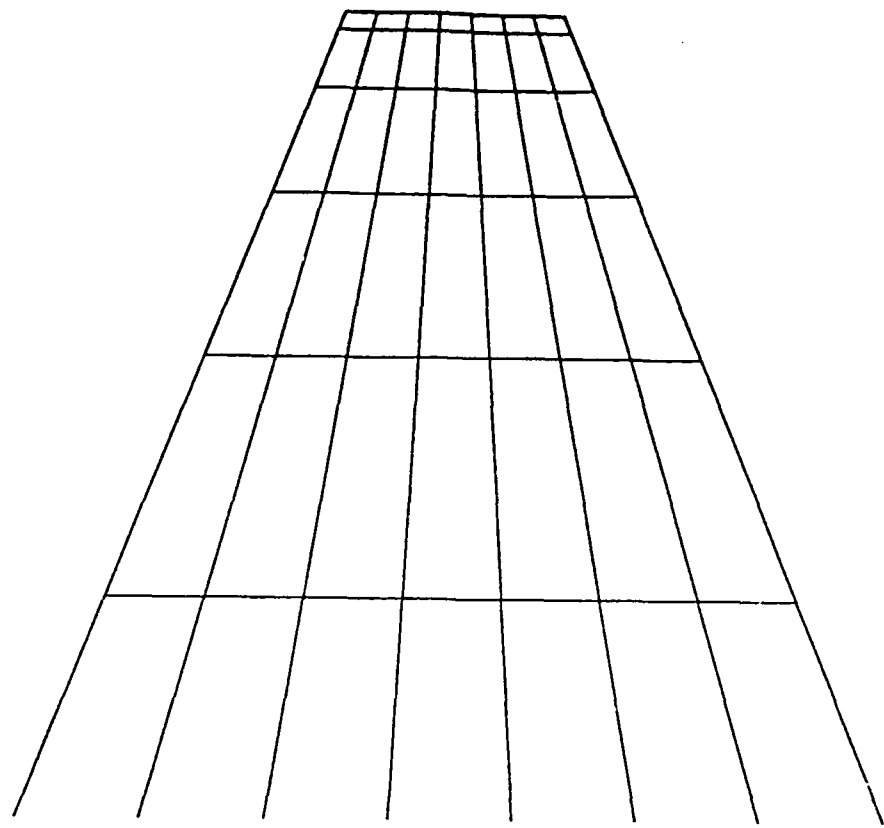


Figure 6.19: Original discretization of the second specimen (truncated V-shaped asperity)

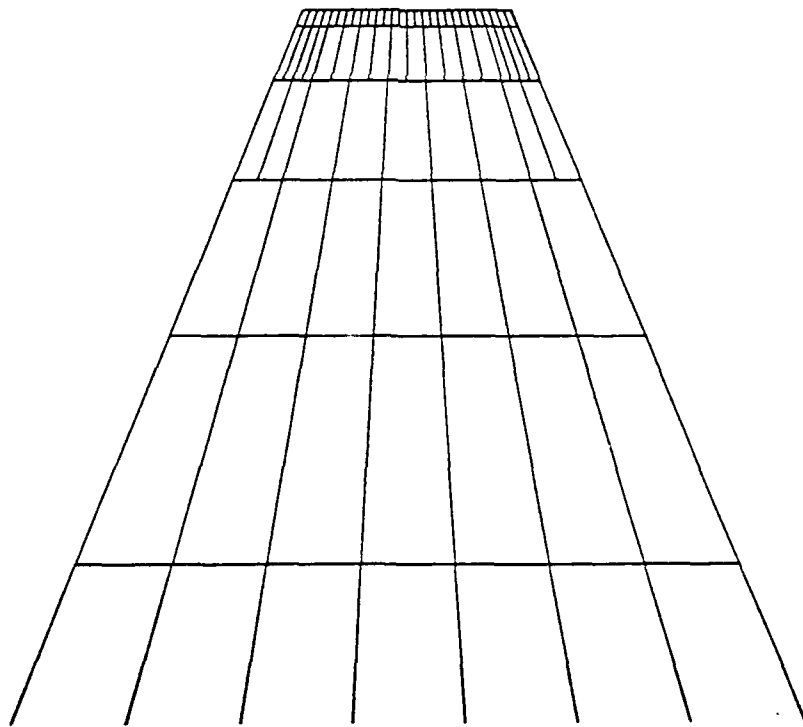


Figure 6.20: Refined discretization of the second specimen

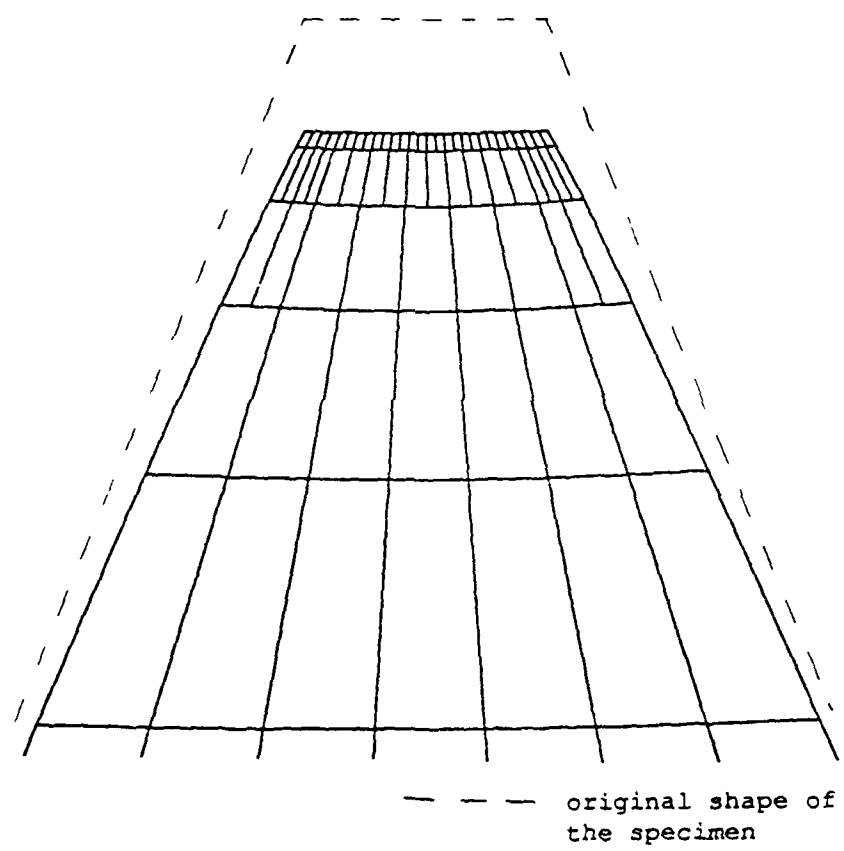


Figure 6.21: Deformation of the V-shaped asperity

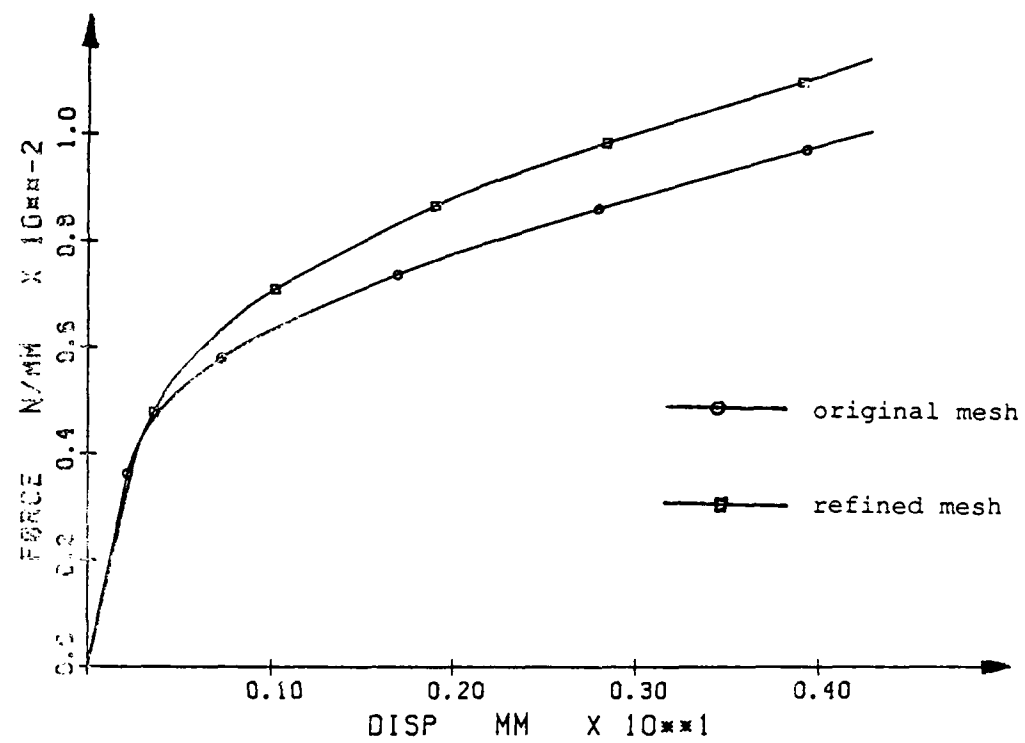


Figure 6.22: Numerical results for the second specimen obtained on two different meshes

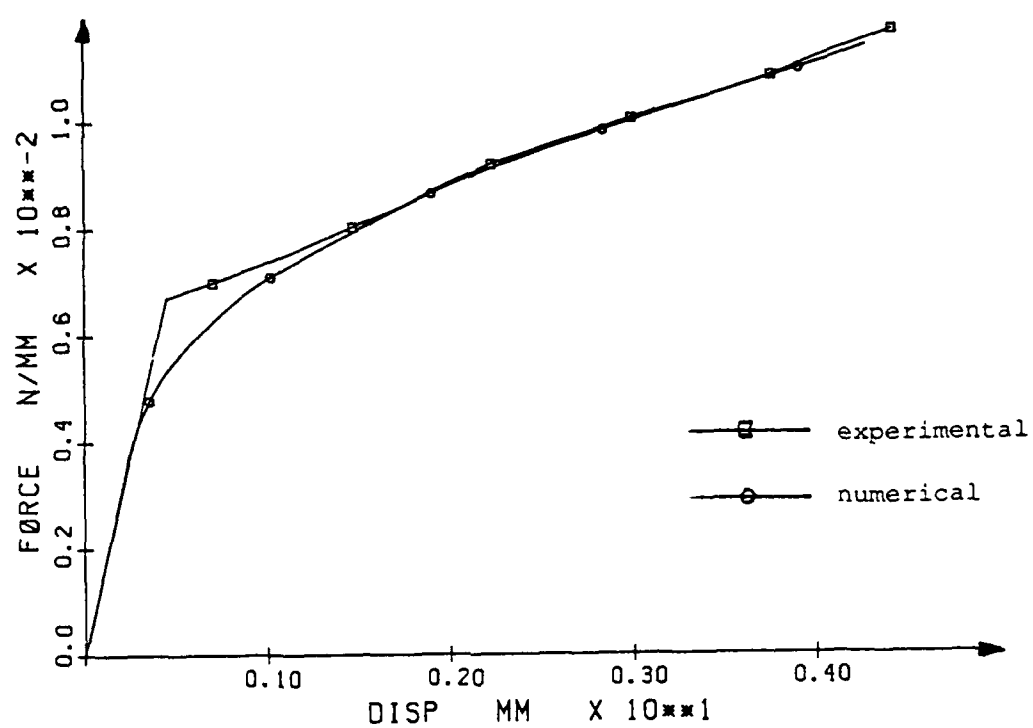


Figure 6.23: Numerical and experimental results for the second specimen

7 Studies of Asperity-Based Models of Contact and Friction

In this section we present examples of constitutive interface models, developed through a complete statistical homogenization procedure. The basic questions addressed here, besides the quality of these models, are as follows:

- what is the dominant type of asperity deformation (elastic or nonelastic),
- what is the effect of adhesion at the asperity level and after homogenization,
- what is the effect of surface roughness,
- how do theoretical predictions compare with experimental measurements.

To answer these questions four different types of surfaces were analyzed. The first three were made of aluminum. Their profiles were taken from literature [44]. The fourth type of surface was made of steel. The pressure-approach relationship was measured experimentally and compared with its numerical prediction. The profile was scanned with an electronic microscope. Having the profile of a surface as a discrete function it was possible to compute its statistical characteristics such as medium height, standard deviations of height, slope and curvature. Those statistical characteristics were used to compute expected values of real area and force of contact as functions of approach. Deterministic solutions to a contact of two asperities were computed by the hp adaptive code using different assumptions about shape of asperities, its material model and with or without taking into account the adhesion forces. The results include also estimation of friction coefficient.

7.1 Simulation of a Greenwood-Williamson Asperity-Based Contact Model

The results of elastic solution of spherical contact problem were used for initial tests of a complete statistical homogenization procedure. In particular, we compared our finite element based predictions with a classical asperity-based contact model due to Greenwood and Williamson [44]. This is one of historically first asperity-based models, derived under the following simplifying assumptions:

- the tips of asperities are spherical,
- all asperities have the same radius of curvature R ,

- asperity height is a random variable with Gaussian distribution,
- contact is elastic and described by the theoretical solution of the Hertz problem.

Although this model is much simpler than the ultimate objective of this project (random asperity height and curvature, nonelastic deformation, etc.), it provides a very good initial test for the homogenization procedure. Importantly, our modeling of this problem differs from Greenwood's approach in that:

- solution of elastic contact problem has been obtained from finite element modeling, rather than from Hertz theory,
- expected values of contact load and area have been calculated using general numerical quadrature, instead of analytical integration.

The simulation of the Greenwood-Williamson model was performed for the following set of parameters:

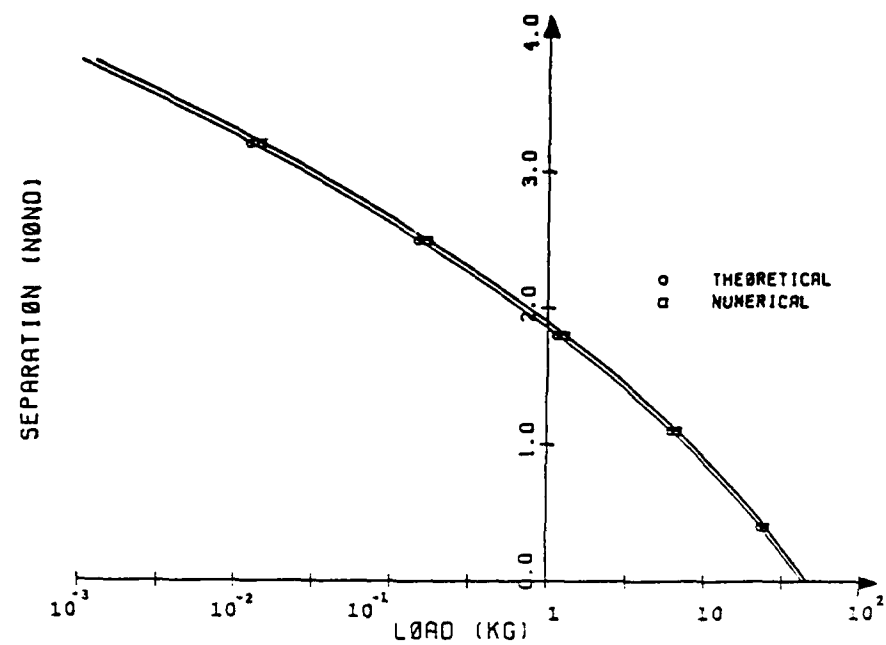
$$\begin{aligned}
 R &= 0.1414 \text{ mm} \\
 \sigma_p &= 7.07106 \times 10^{-4} \text{ mm} \\
 \nu &= 0.3 \\
 E &= 321.7335 \text{ kG/mm}^2 \\
 n &= 300 \text{ peaks/mm}^2
 \end{aligned}$$

where R is the radius of asperity tips, σ_p is the standard deviation of asperity height and n is the surface density of asperity peaks. The results are presented in figure 7.1, which shows respective comparisons of load-separation and load vs. contact area curves. It can be seen that the difference introduced by numerical modeling of asperity and numerical integration of expectation values is within acceptable bounds (note that these differences could be further reduced by application of finer meshes for the asperity contact problem.)

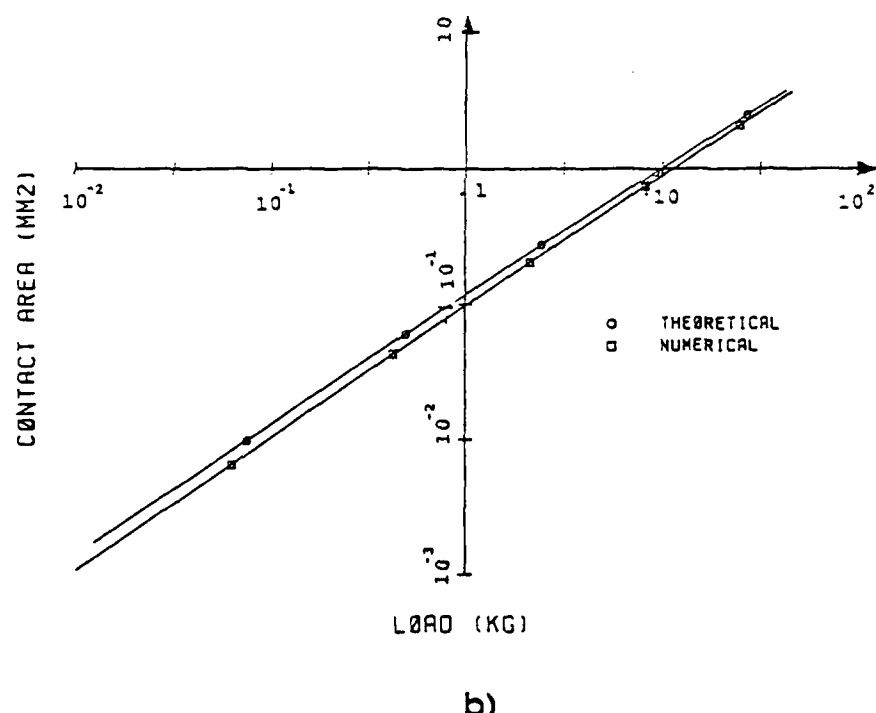
7.2 Effects of Asperity Shape

Next test of the homogenization procedure was performed for an aluminum interface with surface characterized by the following parameters: $\sigma = 1.3 \mu\text{m}$, $\dot{\sigma} = 0.13$, $\ddot{\sigma} = 0.018 \mu\text{m}^{-1}$, $D_p = 0.00044 \text{ peaks}/\mu\text{m}^2$. During this test the force and area of contact for a single asperity were computed in two ways, using

- homogenization procedure based on elastic solution for spherical asperities, with random distribution not only of heights but also of curvatures, (Hertz solution was used).



a)



b)

Figure 7.1: Comparison of Greenwood-Williamson theory with numerical predictions; (a) load-separation curve and (b) load-area curve.

- Homogenization procedure based on numerical solutions for elastic, sinusoidal asperities. These asperities better simulate the actual shape of a rough surface.

Numerical solution for sinusoidal asperities was computed with taking advantage of the fact that the problem is axisymmetric. Comparison of the computed contact force and area versus penetration is shown in figures 7.2 and 7.3. Results for contact of two surfaces obtained by those two models are compared in figure 7.4.

The results of this test show that influence of asperity geometry (sinusoidal rather of spherical) is important, especially for higher loadings. However, after homogenization, these differences are less pronounced. This is because major contribution to expected values of contact pressure and area come from asperities deformed at their tips only.

7.3 A very smooth engineering surface

The next case analyzed is normal contact of two very smooth aluminum surfaces, with profiles corresponding to that shown by Greenwood and Williamson in Reference [18], Figure 5. The material is aluminum alloy (6061, T4), with constitutive parameters defined in Section 6. The surface roughness corresponds approximately to a very well polished bearing surface, and is defined by the following parameters:

$$\begin{aligned}\sigma &= 0.013 \mu m \\ \dot{\sigma} &= 0.013 \\ \ddot{\sigma} &= 0.018 \mu m^{-1} \\ D_p &= 0.058 \mu m^{-2}\end{aligned}$$

To represent relative surface roughness, it is convenient to use a so-called plasticity index, defined by Greenwood and Williamson [44] as:

$$\Psi = \frac{E'}{H} \sqrt{\sigma} R$$

where $E' = E(1 - \nu^2)$, H is the material hardness, and R is the asperity radius. According to arguments presented by Greenwood and Williamson, for the values of Ψ smaller than 1 the surface deformation is essentially elastic at a wide range of normal loads, while for $\Psi > 1$ plastic deformation can be expected. Since in the present approach the asperity peak curvature is a random variable, we obtain a range of plasticity indices corresponding to various asperities under consideration. For the surface considered here, the value of plasticity index varies between $\Psi = 0.8$ and $\Psi = 3.5$.

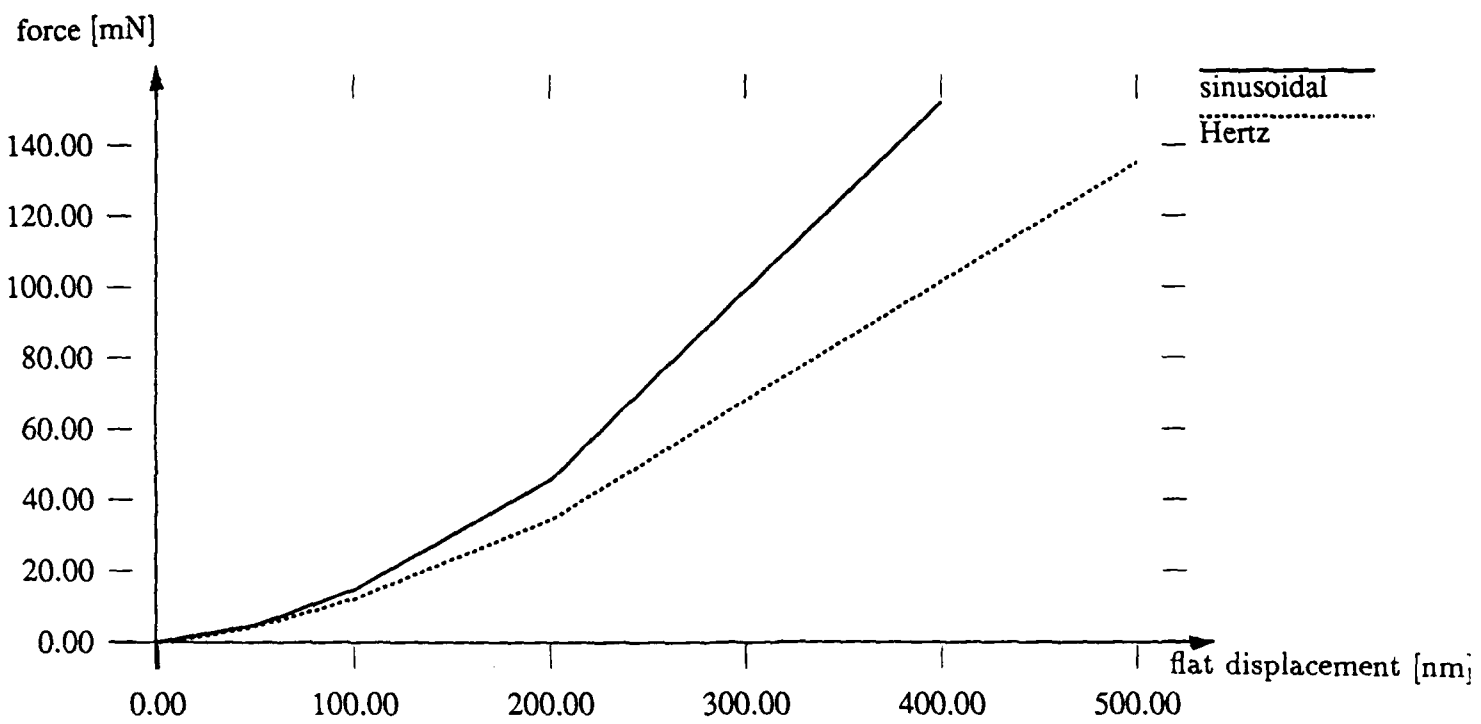


Figure 7.2: Contact force for a sinusoidal asperity

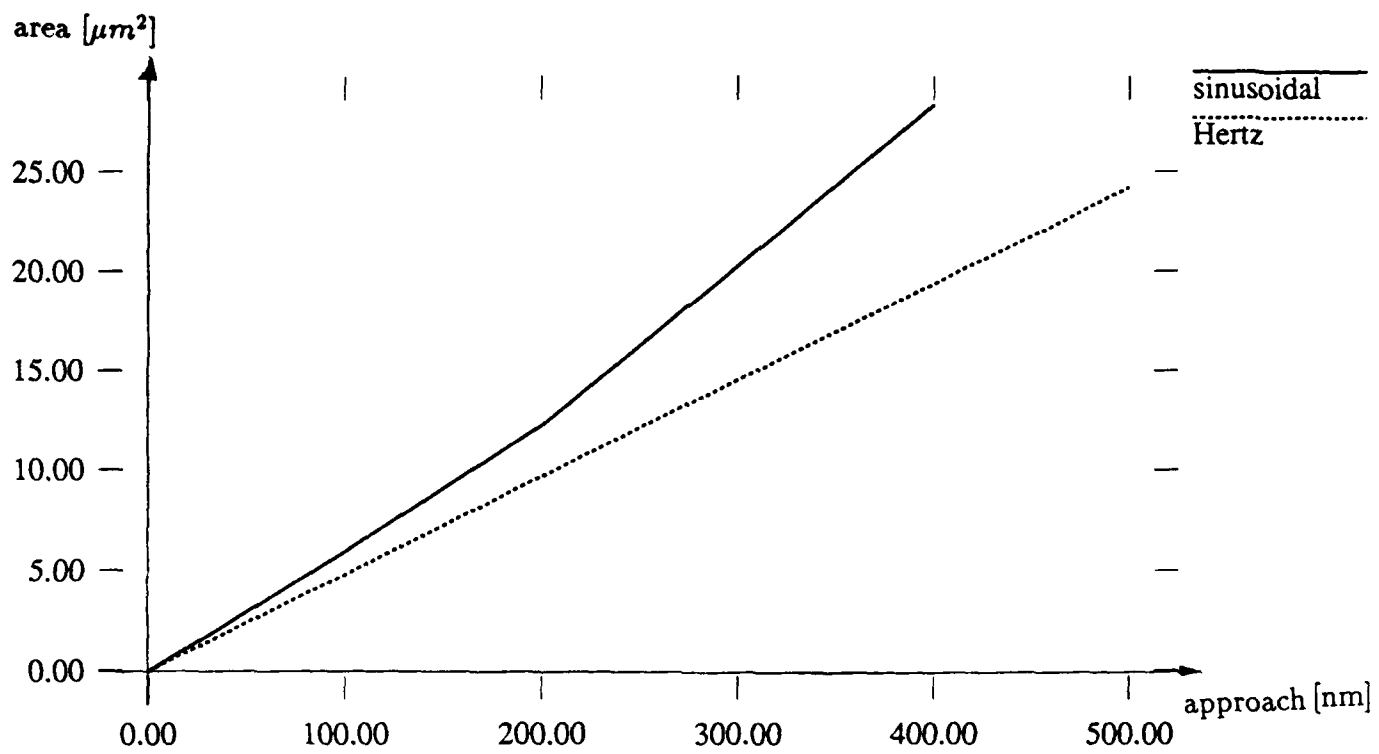


Figure 7.3: Area of contact for a sinusoidal asperity

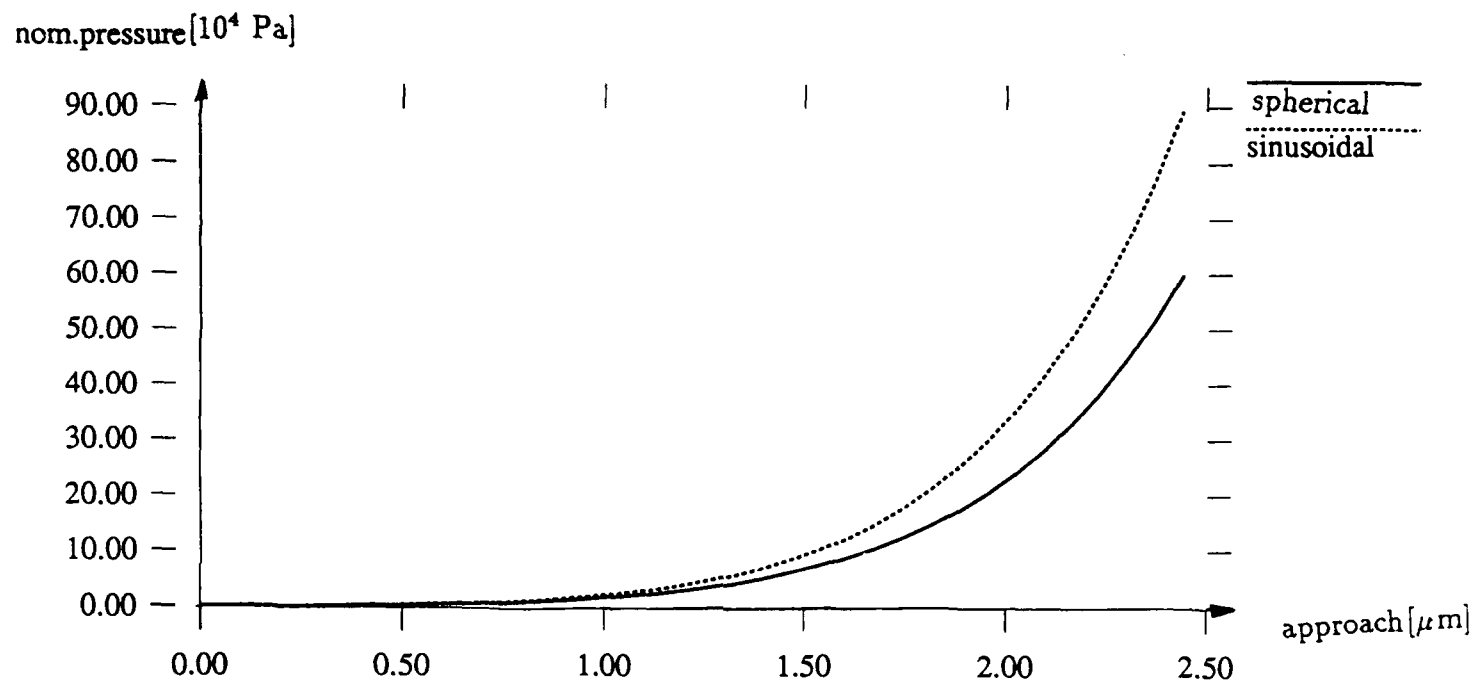


Figure 7.4: Nominal pressure vs. approach for an interface; spherical (a) and sinusoidal (b) asperities

In order to study the effect of adhesion for smooth surfaces, considered cases with and without adhesion forces (clean and contaminated surfaces, respectively). The model of adhesion corresponds to the one discussed in this work, with the surface energy of adhesion $\Delta\gamma = |J/m^2|$ [52].

The first step of the analysis was to use finite element method to model loading of several individual asperities, with radii spanning the effective support of the probability density function, namely from $R=15$ microns to $R=300$ microns. A typical mesh for such an analysis is shown in Figure 7.5. A very fine refinement around the perimeter of the contact zone was needed to correctly resolve the strongly nonlinear adhesion forces. A sample solution for a selected asperity of radius $R=15.4$ microns is shown in the form of load-deflection curves in figure 7.6. It is of interest to notice, that in presence of adhesion (clean surfaces in vacuum), certain attractive force develops *before* the asperities come into contact. In these computations, elastic asperity behavior was assumed.

After sending the finite element results through the statistical homogenization package, one obtains pressure-approach and contact area approach curves as shown in Figures 7.7 and 7.8. Interestingly, due to a specific statistical distribution of asperity heights, the effect of adhesion is more pronounced on the surface level than for a single asperity and, for clean smooth surfaces in vacuum, a considerable attractive force can be expected.

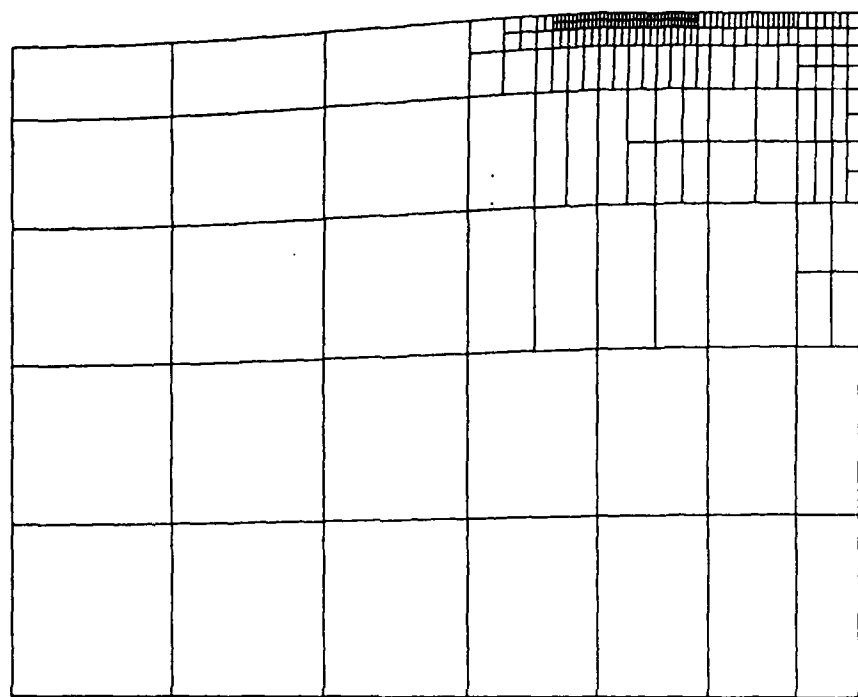


Figure 7.5: An adapted finite element mesh for surface asperity analysis

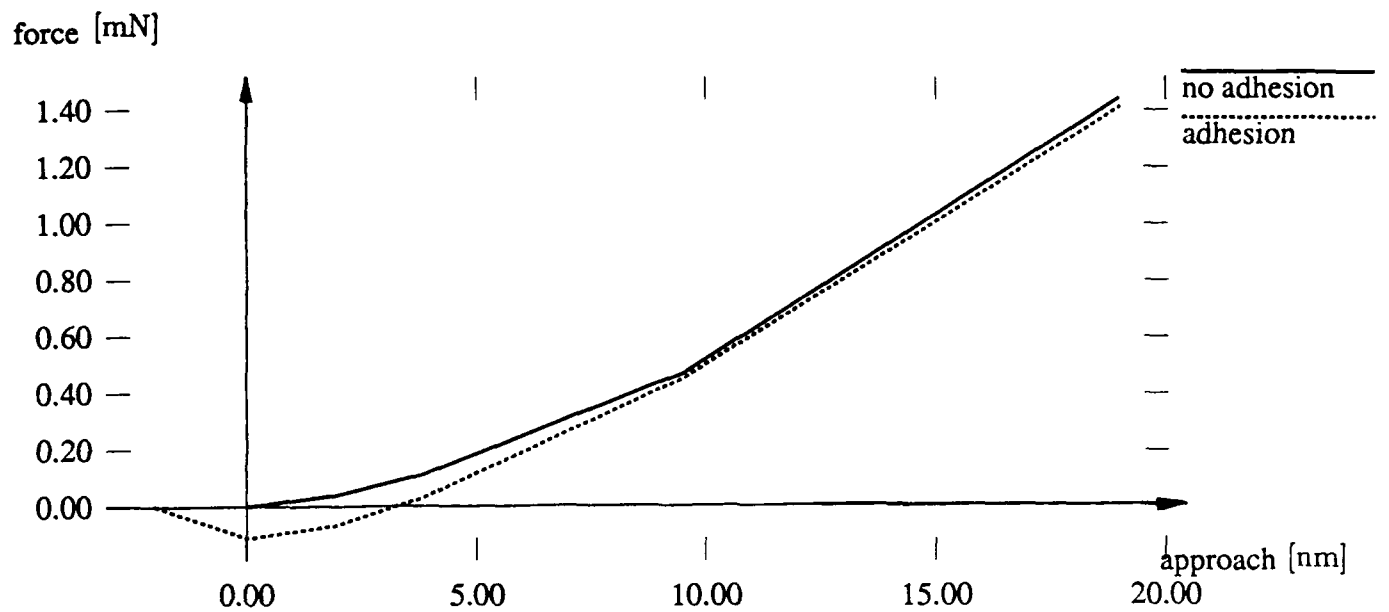


Figure 7.6: Smooth aluminum surface: load deflection curves for a single asperity

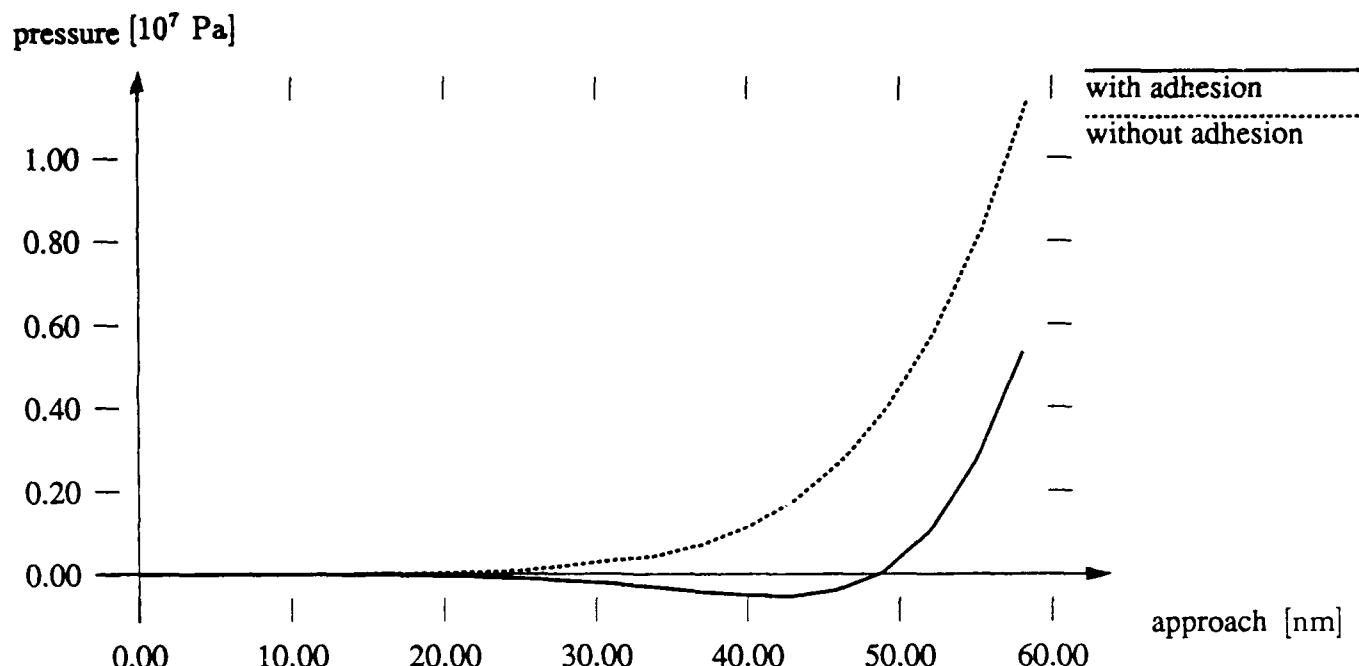


Figure 7.7: Smooth aluminum surface: normal stress versus approach curve

One comment is in place regarding the “approach” axis in Figure 7.6. By definition, the approach between two surfaces is measured from the moment when the surfaces (the highest asperity tips) come into contact. For real surfaces this initial contact is relatively easy to capture. However, in theoretical analysis, with Gaussian distribution of surface height, it is not the case – the maximum asperity height is not clearly defined (in fact it grows to infinity, with probability density vanishing to zero). As a consequence, the selection of the zero point on the “approach” axis is somewhat arbitrary – for practical purposes it may be chosen as a point where some noticeable normal load develops on the interface. In Figure 7.7, for illustration purposes, the approach was measured from a rather large separation between the surfaces. Importantly, this approach measurement does not affect the relationship between the real contact area, normal load and normal stiffness, which is of greater practical importance. For the surface under consideration the real contact area calculated for increasing load is shown in Figure 7.9.

As mentioned, the above asperity analysis was performed using small deformation theory, with additional assumption of elastic asperity deformation. Therefore a question arises: *Of all the asperities in contact, how many satisfy the above assumptions?* An answer to this question is shown in Figure 7.10, which presents, for increasing approach, the percentage of

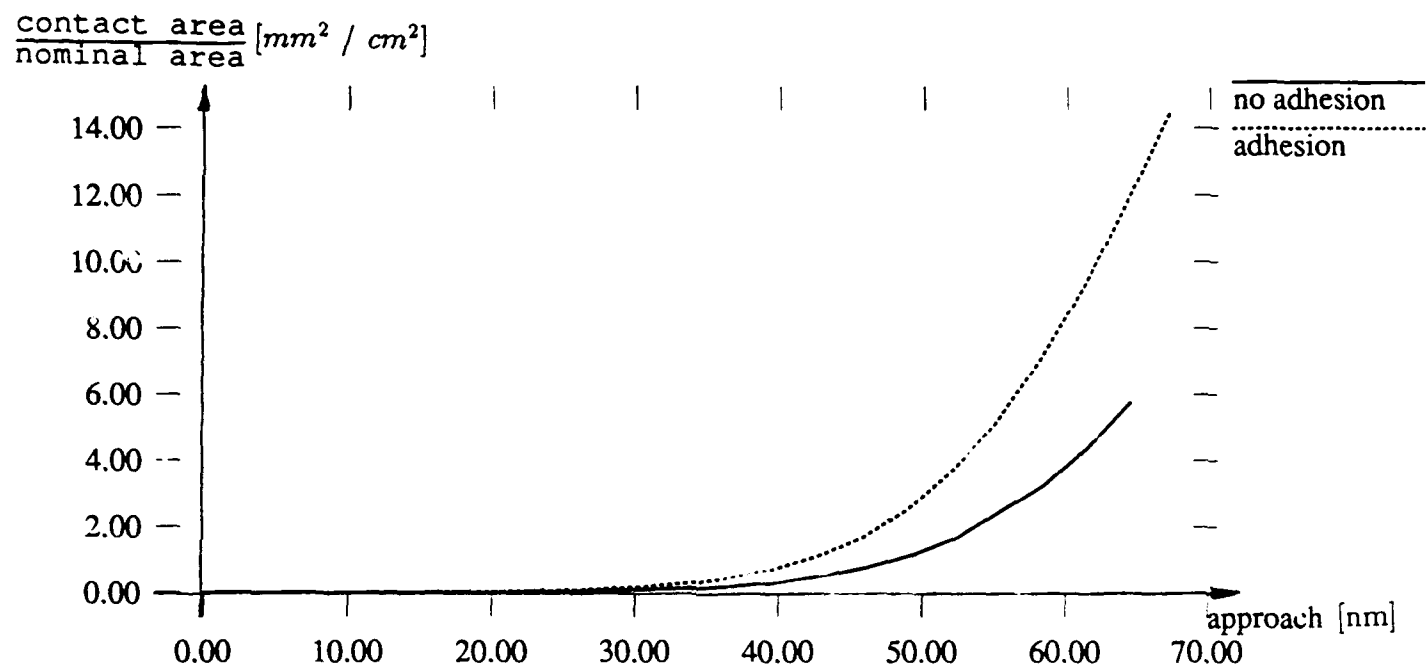


Figure 7.8: Smooth aluminum surface: contact area versus approach curve

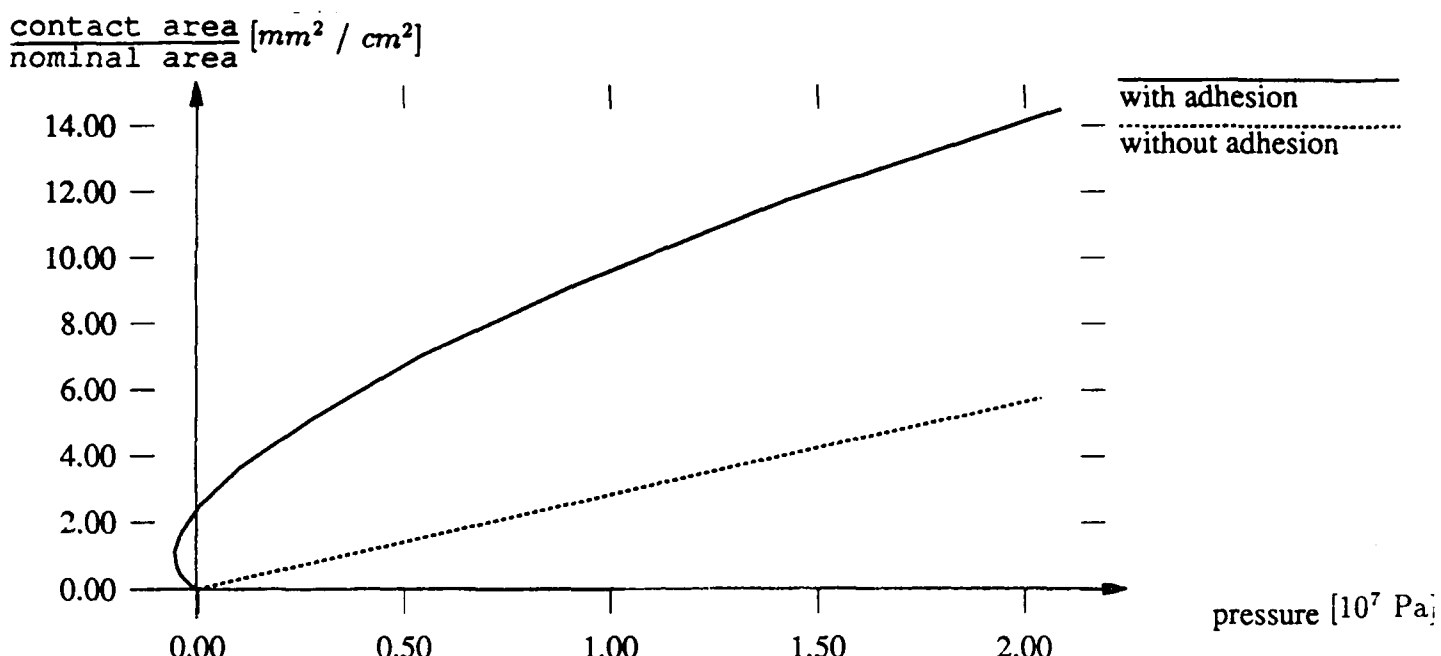


Figure 7.9: Smooth aluminum surface: contact area for increasing normal pressure

asperities that are in purely elastic contact, as well as the percentage of asperities within the range of small deformation theory ($|\epsilon|_{max} < 8\%$). Clearly, the surface deformation remains well within the range of small deformation theory. However, the number of nonelastic asperities increases with increasing approach (load). This corresponds quite well to the behavior suggested by the range of plasticity index for the surface under consideration. In order to assess the importance of nonelastic effects, an additional, fully nonlinear derivation was performed, for the case without adhesion. A comparison of approach-pressure curves obtained with purely elastic and elasto-plastic approaches is shown in figure 7.10. The maximum difference between elastic and elasto-plastic results was less than 5%.

It can be noted, that a very localized occurrence of plastic deformation in an asperity does not strongly affect the values of load and contact area, and that the load-deflection and load-area curves obtained with the elastic theory are quite reliable, even with 50 percent of asperities outside the purely elastic range. This is because only for about 7% of asperities the elasto-plastic solution was significantly different than the purely elastic one.

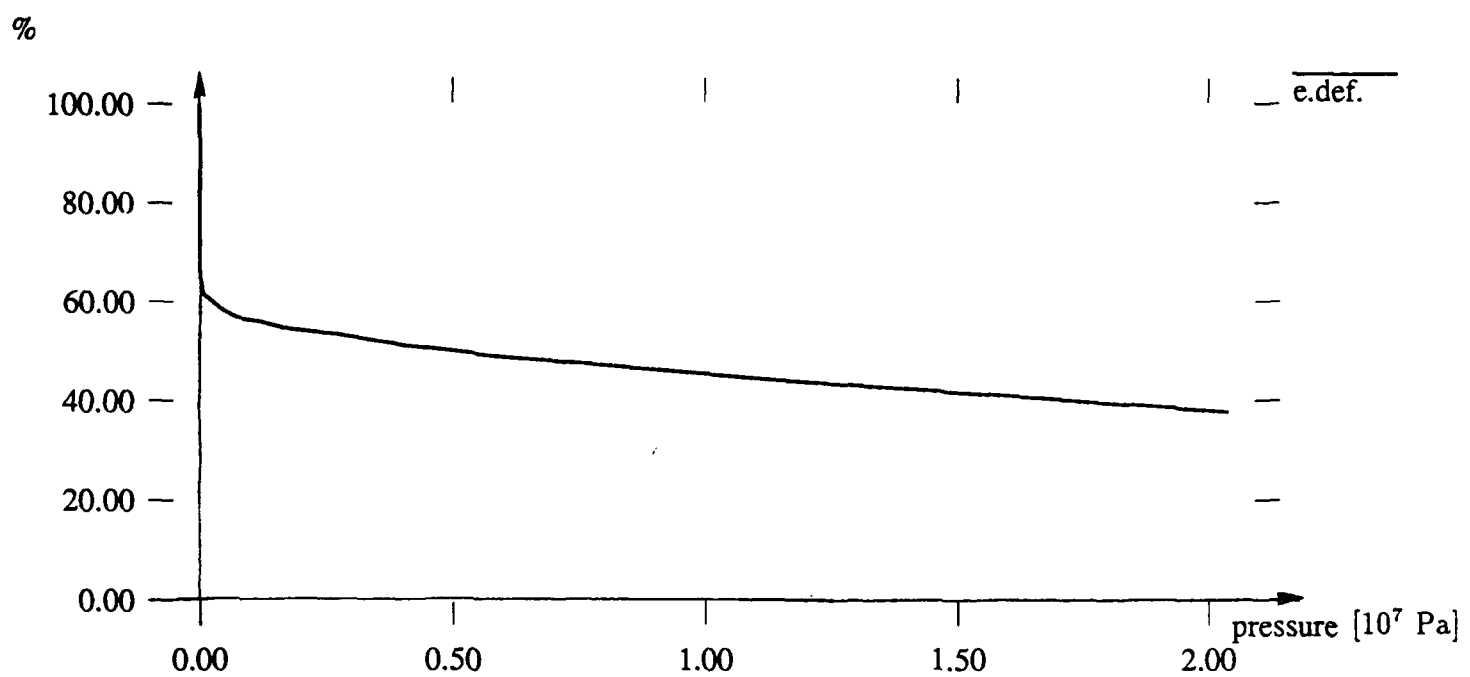


Figure 7.10: Smooth aluminum surface: percentage of asperities satisfying assumptions of purely elastic deformation

7.4 Studies of a rough surface

A second example considered here is that of a hypothetical rough engineering surface. Similarly as in the previous case, the material is aluminum alloy, and the surface statistics is defined by:

$$\begin{aligned}\sigma &= 1.3 \mu m \\ \dot{\sigma} &= 0.13 \\ \ddot{\sigma} &= 0.018 \mu m^{-1} \\ D_p &= 0.00044 \mu m^{-2}\end{aligned}$$

For this surface, the plasticity index is well over the value of 30.0, so that extensive plastic deformation can be expected. In order to derive asperity-based model of the interface, several asperities with various peak curvatures were analyzed by the finite element method. The deformation was fully elasto-viscoplastic, and the asperities were subjected to normal load executed by a rigid flat surface. Importantly, for the rough surface the results were not strongly affected by adhesion. This effect corresponds well to the observations of Chang, et. al. [26-28], that the effect of adhesion, even for clean surfaces, diminishes with increasing surface roughness. On the other hand, for rough surfaces the effect of nonelastic deformation is very significant – this can be seen from the comparison of elastic and elasto-plastic pressure-approach curves shown in Figure 7.11. Clearly, the difference between elastic and elasto-plastic solution is very pronounced. A similar effect can be observed on the plot showing the dependence of real contact area on the normal pressure - Figure 7.13. Importantly, this difference will have a very strong effect on the values of the coefficient of friction.

It is of interest to look again at the percentage of asperities within elastic range and within small deformation range. These numbers are shown in figure 7.14. It can be observed, that *for rough surfaces even a very small load causes significant plastic deformation* - the percentage of elastic asperities is essentially zero. Moreover, at higher loads, some asperities experience strain levels exceeding the range of small strain theory – an important observation, especially for more flexible polymer surfaces.

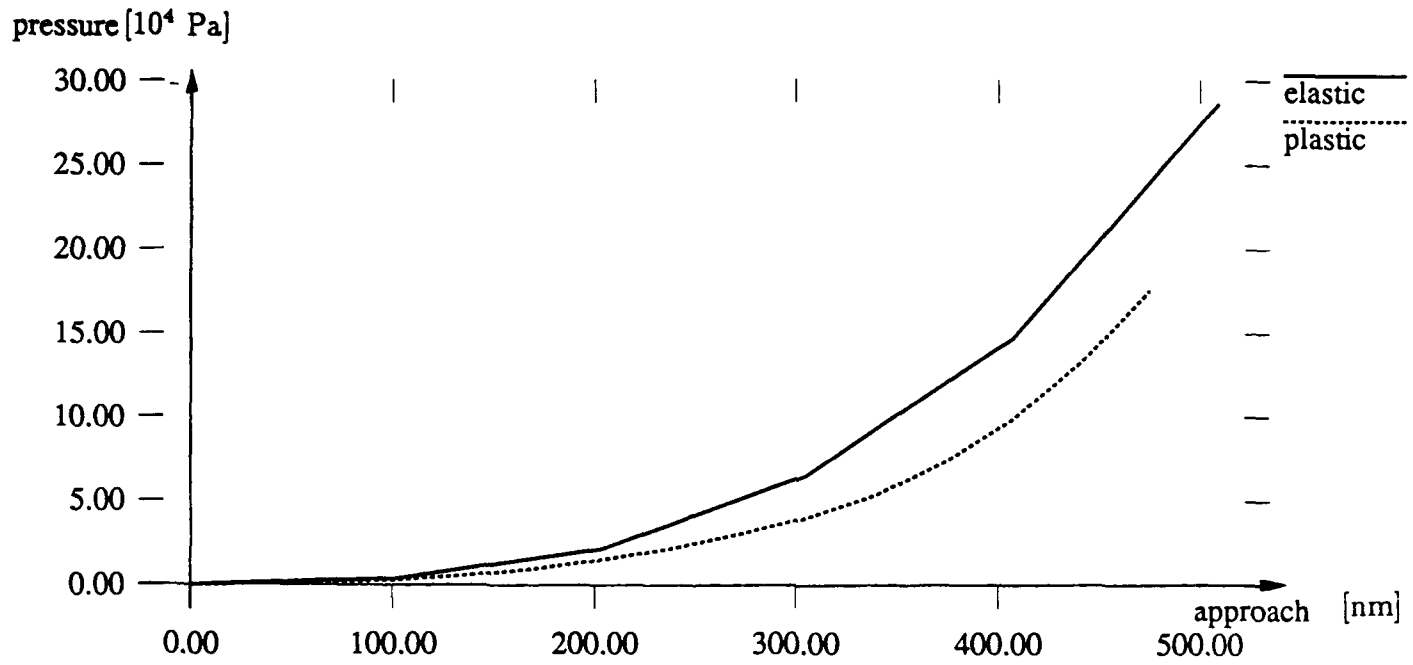


Figure 7.11: Rough aluminum surface: normal stress versus approach curve

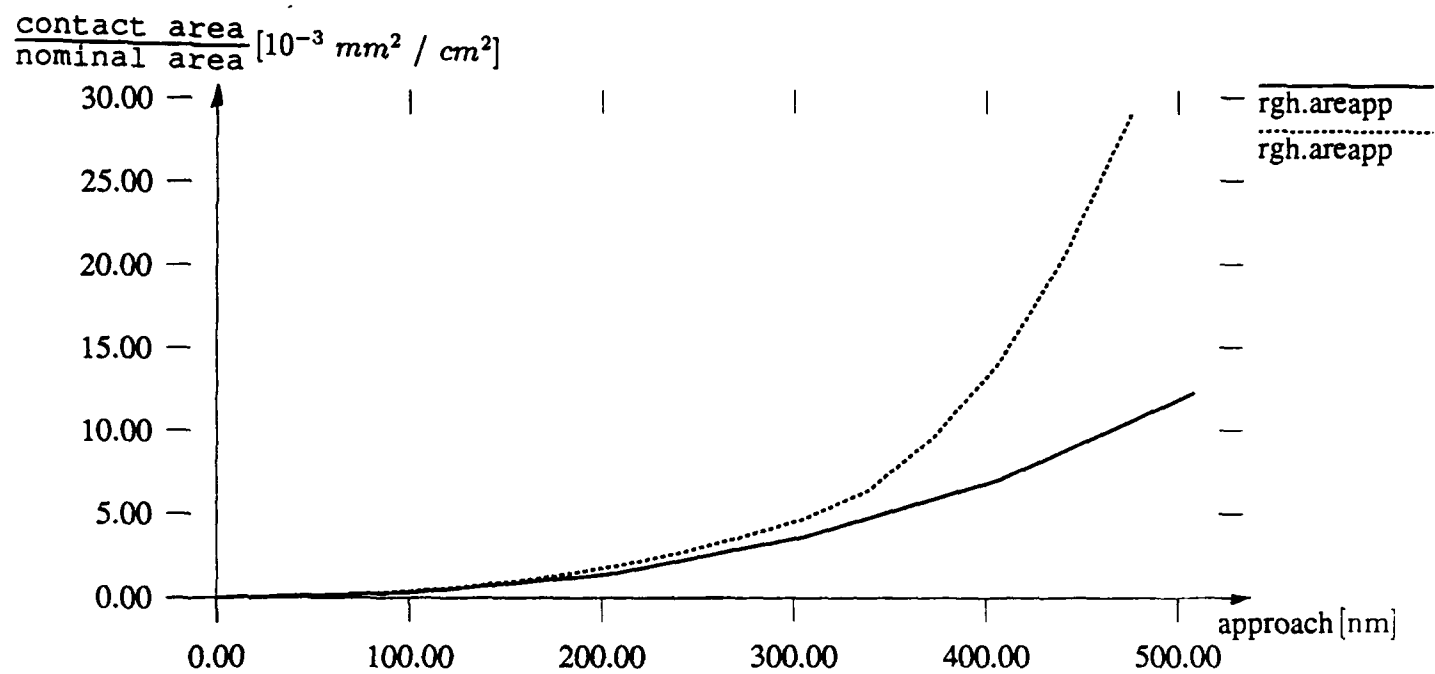


Figure 7.12: Rough aluminum surface: contact area versus approach curve

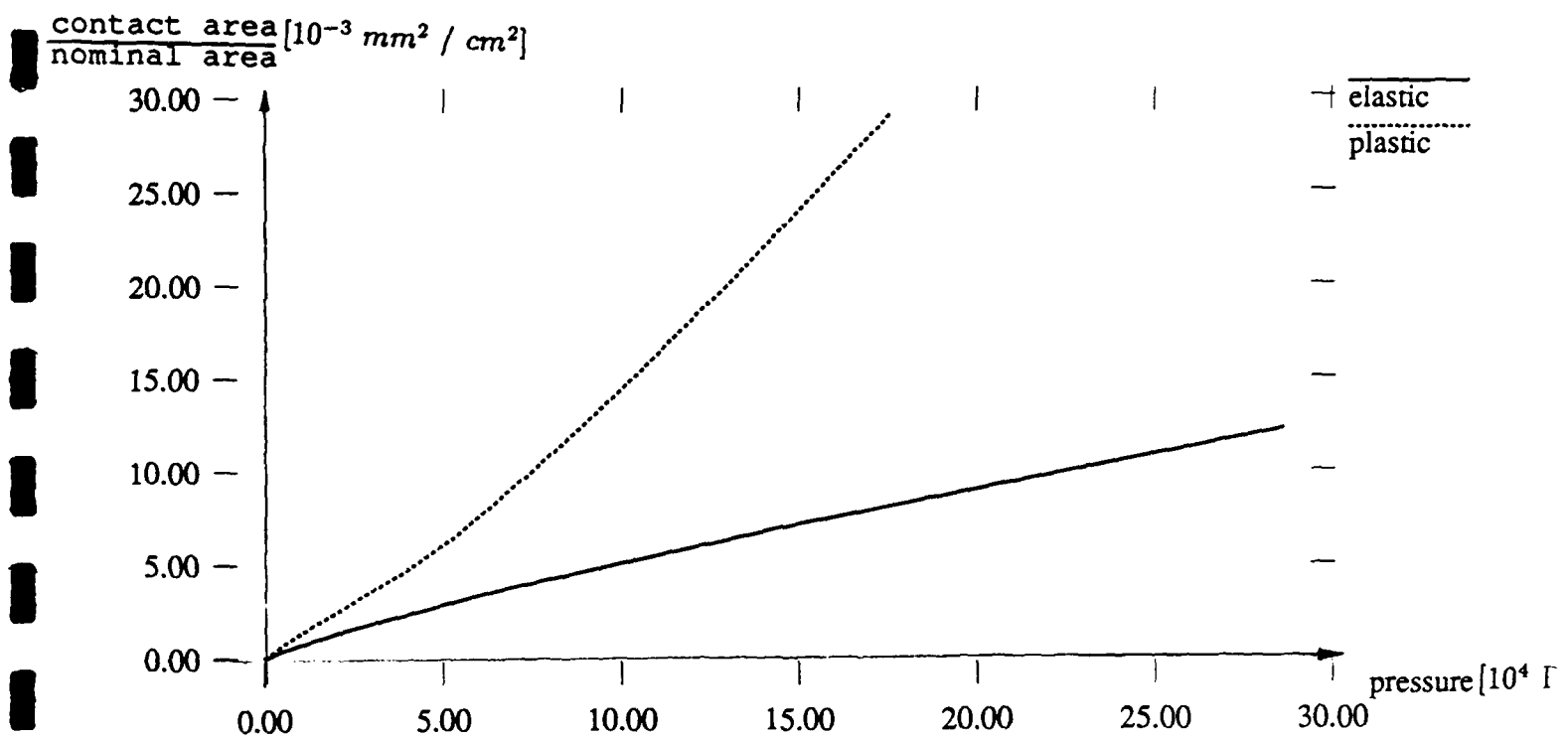


Figure 7.13: Rough aluminum surface: real contact area for increasing normal pressure

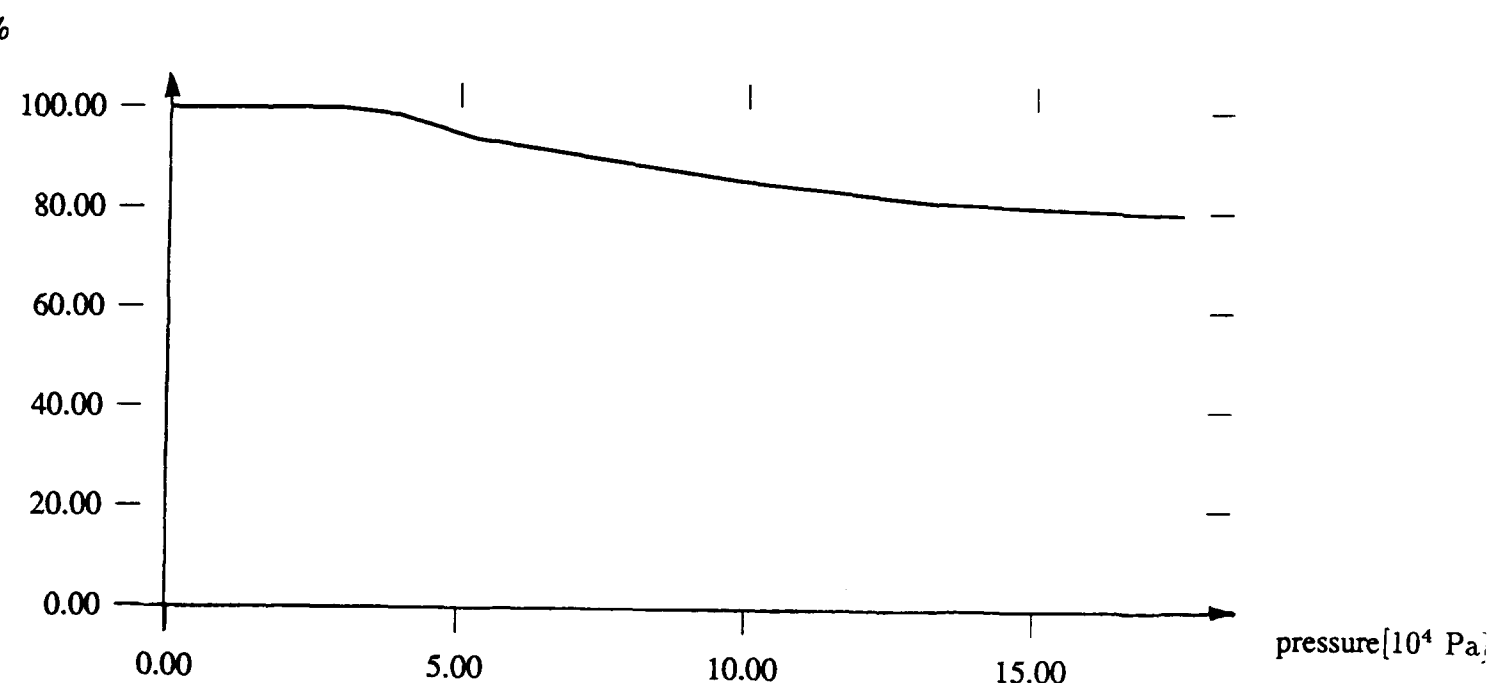


Figure 7.14: Rough aluminum surface: percentage of asperities satisfying assumptions of small deformation

8 Experimental Verification of Asperity-Based Contact Models

The ultimate test of new asperity-based models of contact interfaces comes in applications to predicting phenomenological behavior of real engineering surfaces.

To verify these new models, a special experiment was designed and performed. The main objective was to compare experimental force-deflection relationship with the asperity-based theoretical prediction. Additionally, measured and computed coefficients of friction were also compared. The following subsections describe the experiment and numerical computations.

8.1 Experimental Samples, Apparatus, and Measurements

A major difficulty in experimental verifications of models of frictional interfaces is caused by relatively small height of surface asperities and resulting small compliance of the interface. Under these conditions, it is rather difficult to avoid pollution of the results by such effects as:

- deformation of a bulk material,
- departure of experimental contacting surfaces from ideally flat, which spoils homogeneous distribution of contacting asperities and creates additional, plate-bending type compliance,
- compliance of the loading apparatus,
- departure of loads from purely axial, etc.

In order to minimize these negative effects, special specimens and apparatus were used, as described below.

8.1.1 Specimen Preparation and Experimental Arrangement:

The disk specimens of 1/8 in. thickness and 1 in. diameter were cut from a cold rolled 1020 steel rod. The rod has a hardness of $89 R_b$, and the tensile stress-strain relationship of the rod material is shown in figure 8.1. The material has an elastic modulus $E = 30 \times 10^6$ psi, and a yield stress approximately 42×10^3 psi.

Ten disks were used in each test. The disks were first lapped with a milling machine to ensure the same surface flatness among them. Both surfaces of the disks were then sandblasted with steel and glass beads to produce an artificial surface roughness. In the test

arrangement, ten disks were stacked to form a column of nine (9) contact surfaces as shown in figure 8.2. Note that, for the first disk (no. 1) and the last disks (no. 10), only the contact surfaces with the adjacent disks were sand-blasted, the contact surfaces of these disks (no. 1 and 10) with anvils of the testing machine were kept smooth as lapped. The purpose of using the stacked column was to increase the deformation of contact surfaces nine times so that the average value of deformation of the contact surface asperities could be measured with a reasonable accuracy. As portrayed in the figure, the applied load was measured with a load cell, and the displacement was measured with a LVDT which has a resolution of 0.001 inch.

8.1.2 Measurement of Surface Roughness

The average depth of surface asperities produced by sand-blasting was first estimated with a comparator which is a device commonly used by the sand-blasting industries. It was estimated that the surface which was sandblasted by the glass beads has an average asperity depth of 20μ , and the surface which was sandblasted by the steel beads has an average asperity depth of 40μ . These asperities are too small to be monitored by a standard stylus profilometer. That is why the surface roughness of the specimen were determined with a scanning electronic microscope (courtesy of NASA-JSC). The surface of the disk specimen was first scanned to determine the distribution of asperities (i.e., a top view). The disk specimen was then sectioned, lapped, polished, and scanned from the side to determine the depth variation of surface asperities (i.e. a side view profile). The results are presented in the following paragraphs:

1. The top and side view pictures of surface asperities produced by sand-blasting the surface with glass beads are shown in Figs. 8.3 and 8.4, respectively. The variation of asperity depth, traced from Fig. 8.4, is shown in Fig. 8.5. In view of Fig. 8.3, it is seen that the sand-blasting had indeed produced a reasonably homogeneous distribution of surface asperities. From Figs. 8.4 and 8.5, it is seen that the surface damage produced by glass beads blasting is not severe; the depth variation of asperities is gentle and their distribution appears to be random. Based on Fig. 8.5, the average depth of asperities is estimated to be approximately 15μ which is slightly smaller than that estimated by using the comparator.
2. The corresponding information on surface asperities produced by sand-blasting the surface with steel beads are shown in Fig. 8.6, 8.7, and 8.8 respectively. It is seen that, although the distribution of asperities appears to be uniform, blasting the surface with steel beads has produced severe micro-scale damage on the surface. The surface asperities are more rough and abrupt than that produced by sandblasting the surface

with glass beads. Based on Fig. 8.8, the average depth of asperities is estimated to be 40μ – the same as that from the comparator. Figure 8.9 shows a steel bead wedged between asperities.

8.1.3 Experimental Measurements of Contact Compliance

The sand-blasted disks were stacked together to form a cylinder, and the cylindrical specimen was then installed to a MTS testing machine. A compressive force was applied to the stacked cylinder at an approximate rate of 100 Lbf/min. The overall deformation (between the smooth surfaces of no. 1 and no. 10 disks) was measured with a LVDT displacement sensor (with a resolution of 0.001 in) as shown in Fig. 8.2. Two tests for each stacked cylinders, which were made of disks with a glass-bead blasted surface and with a steel-bead blasted surface, were carried out to ensure the repeatability of the testing. The corresponding results are presented in Figs. 8.10 and 8.11, respectively. The following observation is made:

1. Figure 8.10 shows the compressive force-displacement curve of a cylinder made by stacking ten disks (SAE 1020) whose surfaces were sandblasted with glass beads. The cylinder was compressively loaded to 1,000 Lbf, unloaded, and then reloaded to 3,000 Lbf. Note that the diameter of the cylinder is 1 inch, the nominal compressive stress in the cylinder under a load of 3,000 Lbf is approximately 3820 psi – well within the elastic limit of the cylinder material. Furthermore, each disk has a thickness of 0.125 in. the elastic deformation of the equivalent solid cylinder is expected to be

$$\delta = \frac{PL}{AE} = \frac{3000 \times (10 \times 0.125)}{\pi \times (0.5)^2 \times 30 \times 10^6} = 0.000159 \text{ in.}$$

Referring to the force deformation curve shown in Fig. 8.10, it is interesting to note that the initial portion of the curve is nonlinear, and there is a permanent deformation of approximately 0.0007 inch after unloading, and the reloading curve joins the initial loading curve as shown in the figure. At a load of 3,000 Lbf, the measured deformation of the stacked cylinder is approximately 0.004 inch which is substantially larger than the above calculated elastic deformation. This phenomenon implies that the deformation of asperities between the contact surfaces (there are nine contact surfaces in the stacked cylinder) in the stacked cylinder are plastic, and the contact surface compliance is nonlinear.

2. The corresponding force-displacement curve for a cylinder made by stacking ten disks which surfaces are sandblasted with steel beads is shown in Fig. 8.11. It is seen that the characteristics of the force-deformation relation is similar to that displayed in Fig.

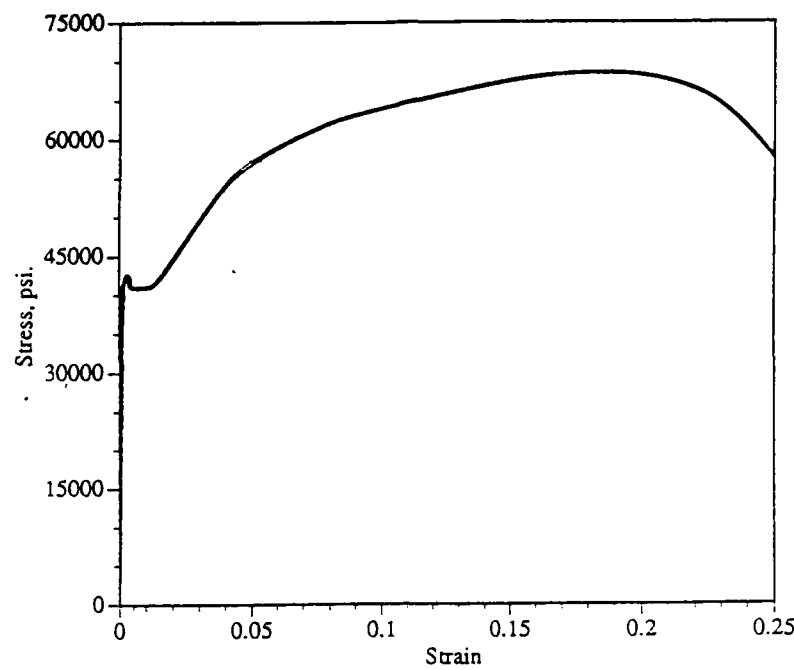


Figure 8.1: Tensile stress-strain relationship of a SAE 1020 steel

8.10. The permanent deformation of the cylinder when unloaded from 1,000 Lbf is approximately 0.0014 in - much larger than that from its counterpart of glass-bead blasted surface. Note that the force-deformation curve does not follow the initial curve when the cylinder is re-loaded, however, the slopes of the initial curve and the reloaded curve do appear to be the same.

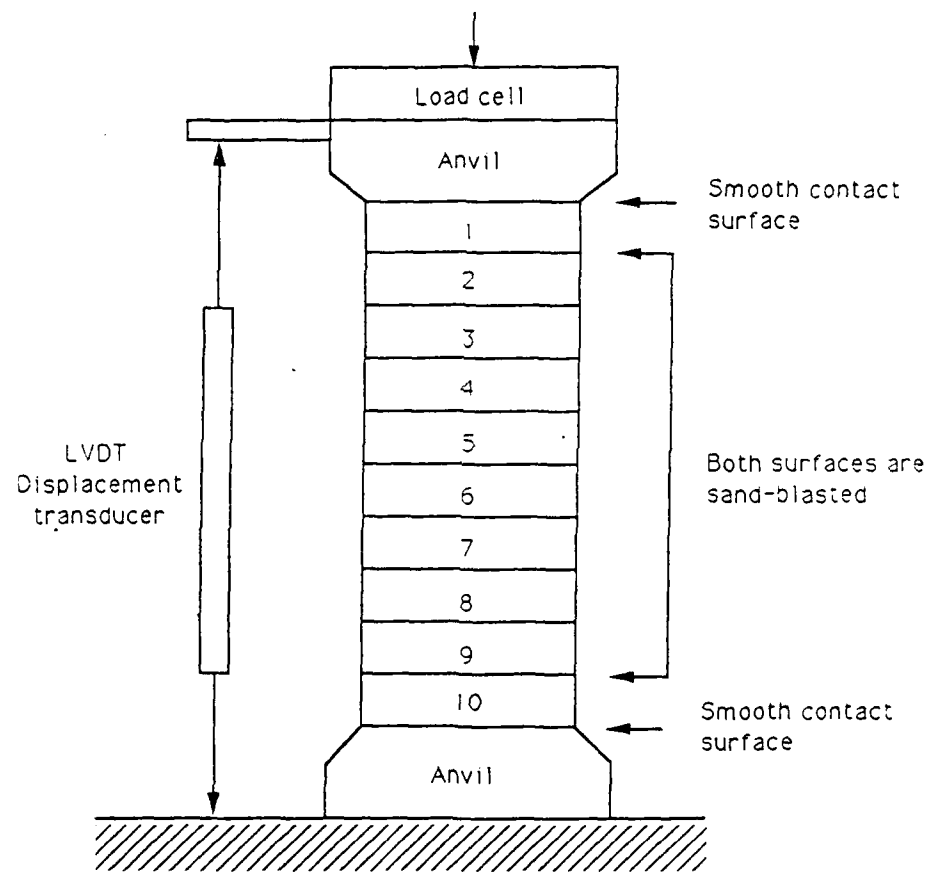


Figure 8.2: A sketch of experimental arrangement (Disk: dia= 1 inch, thickness = 1/8 inch)

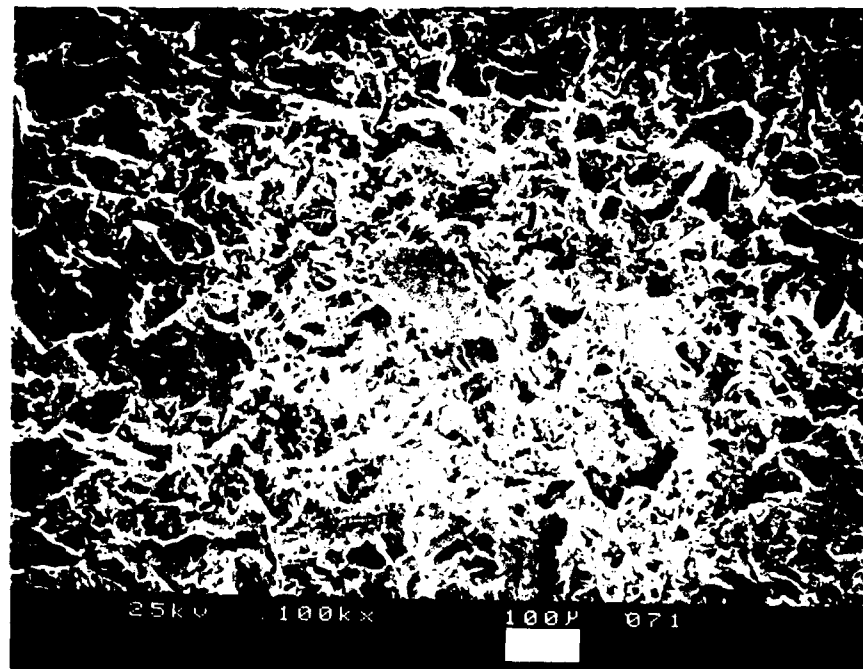


Figure 8.3: Top view of a surface sandblasted with glass beads (Amplification: $\times 100$, Scale: Shown as the white bar below the picture

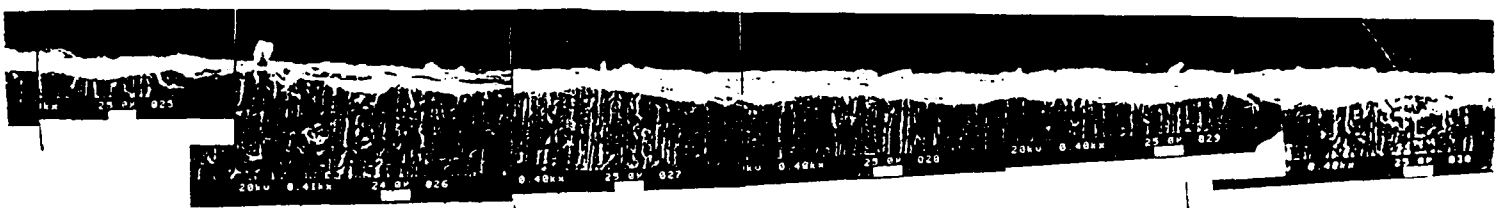


Figure 8.4: Profile of a surface sandblasted with glass beads - a side view (Amplification, and scale information are shown in the dark line below the pictures)



Figure 8.5: Variation of surface asperities traced from Figure 8.4.

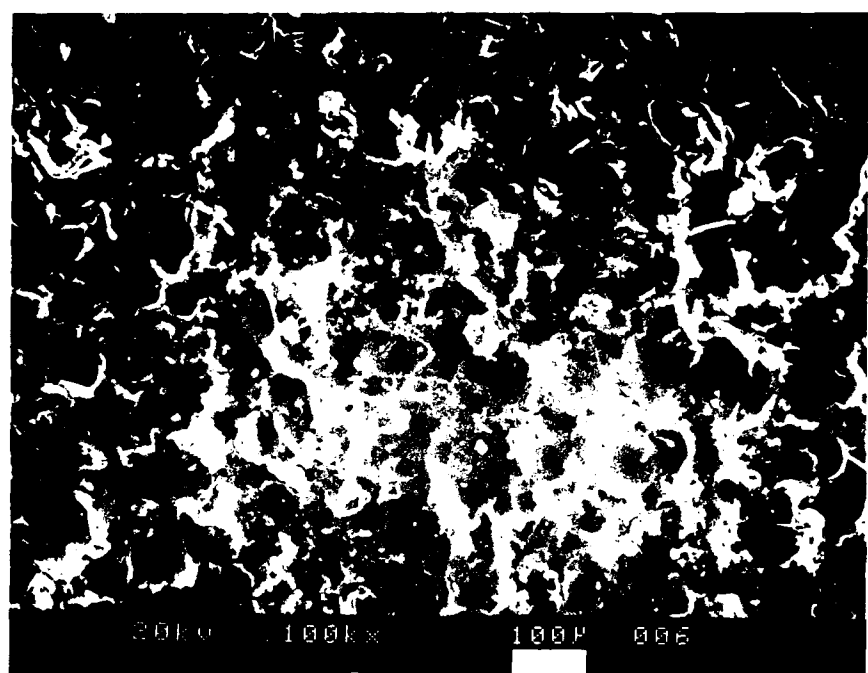


Figure 8.6: Top view of a surface sandblasted with steel beads (Amplification: $\times 100$, Scale: Shown as the white bar below the picture).

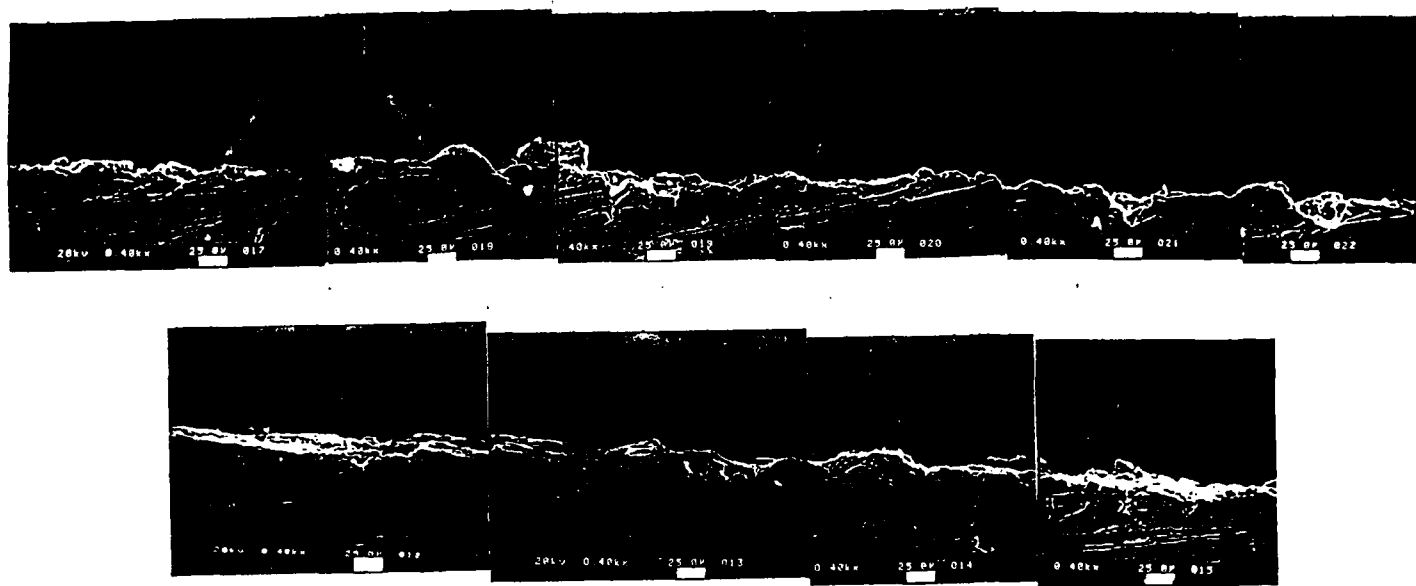


Figure 8.7: Profile (at two locations) of a surface sandblasted with steel beads - a side view (Amplification, and scale information are shown in the back line below the pictures)

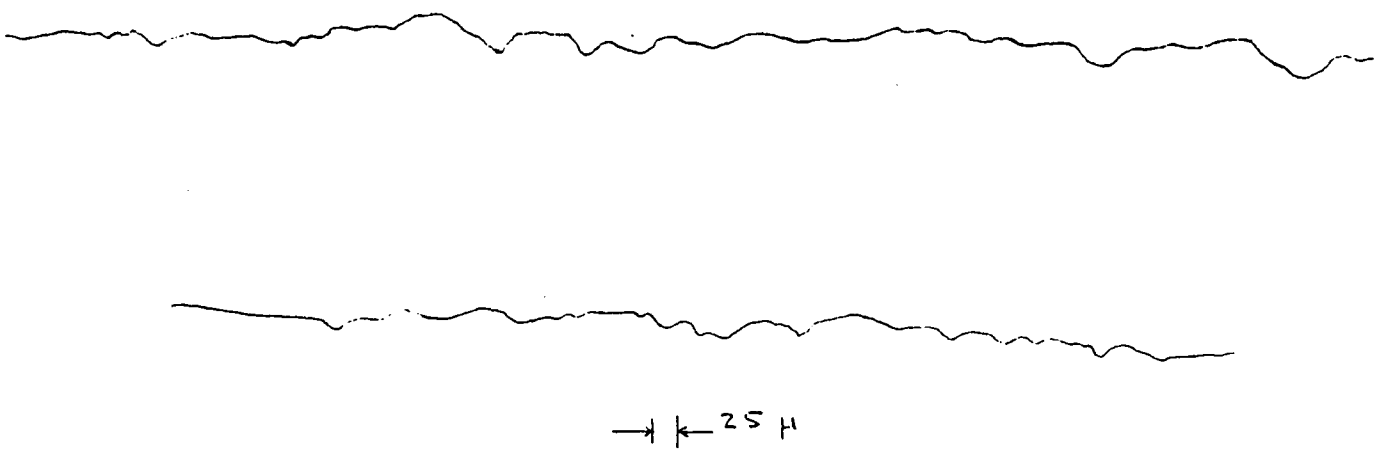


Figure 8.8: Variation of surface asperities traced from Figure 8.7.

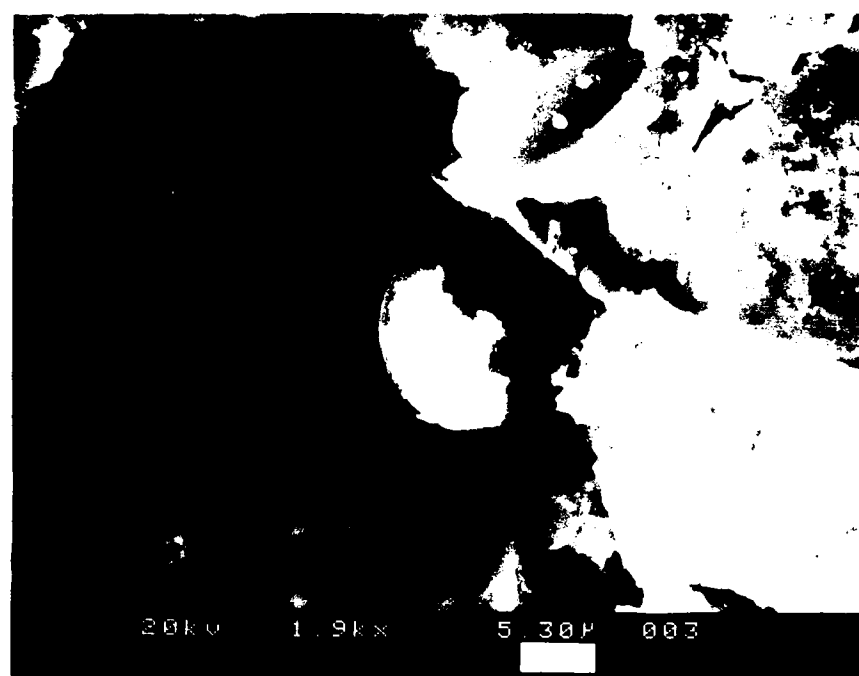


Figure 8.9: A steel bead wedged in the asperities

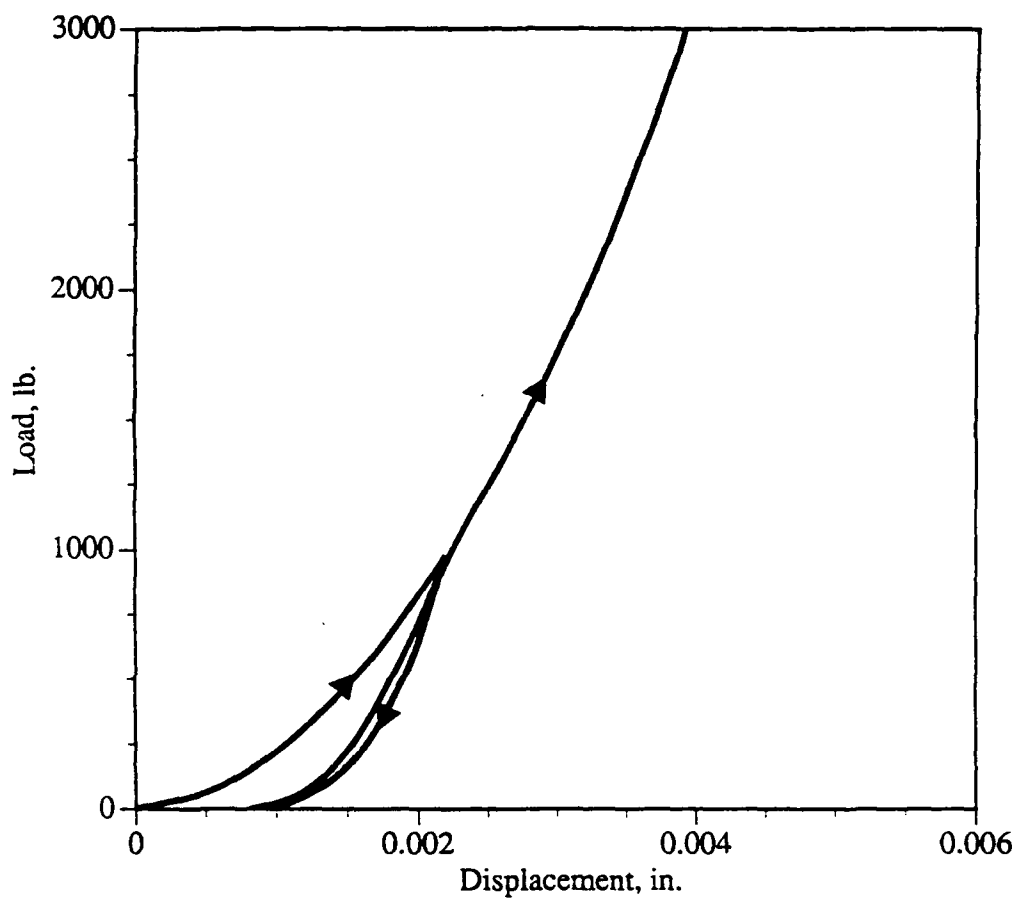


Figure 8.10: The force-displacement relationship of a cylinder made by stacking ten disks whose surfaces are sandblasted with glass beads.

8.1.4 Specimen Preparation and Experimental Arrangement for Determining the Coefficient of Friction

In order to measure the values of the coefficient of friction for the surfaces under consideration, a simple quasi-static experiment was performed. This experiment was oriented on basic measurement of the static coefficient of friction, as identified by visible inception of sliding. No attempt has been made to measure initial microslip, change of normal compliance or other more intricate phenomena associated with frictional sliding.

The disk specimens of 1/2 inch thick and 1 inch diameter were cut from a cold rolled 1020 steel rod. The rod is from the same stock of material used in the previous test. The material has an elastic modulus $E = 30 \times 10^6$ psi, a yield stress approximately 42×10^3 psi, and a hardness of $89 R_c$.

Both surfaces (top and bottom) of the disk specimen were prepared in a same manner as the previous test. The disk surfaces were first lapped with a milling machine, and then sand-blasted with steel beads or with glass beads to produce an artificial surface roughness. The average depth of surface asperities were estimated with a comparator which gave a value of 20μ for the glass-bead-blasted surface, and 40μ for the steel-bead-blasted surface - same as those reported in the previous tests.

The specimen was sandwiched between two steel anvil blocks which have a hardened (approximately $32 R_c$) and smooth surface. The entire assembly was then installed into the test apparatus. A normal compressive load of 250 Lbf was first applied slowly to the assembly. It should be mentioned that due to the smallness of the surface asperities, we were not able to record the deformation of the surface asperities during loading. After completing the normal loading, a horizontal load is slowly applied to the specimen disk until the disk begins to slip. The onset of slipping was observed visually. Two tests were carried out for each surface roughness and the results are summarized in the next section.

Test Results

(a) Glass-Beads-Blasted Surface:

$$\begin{aligned} \text{Normal load} &= 250 \text{Lbf} \\ \text{Horizontal load} &= 110 \text{Lbf} \text{ (first test)} \\ &= 105 \text{Lbf} \text{ (second test)} \\ &= 107.5 \text{Lbf} \text{ (average)} \end{aligned} \quad (8.37)$$

Since there are two contact surfaces between the test specimen (roughened on both surface) and the steel anvil blocks (with smooth surfaces), the coefficient of friction is

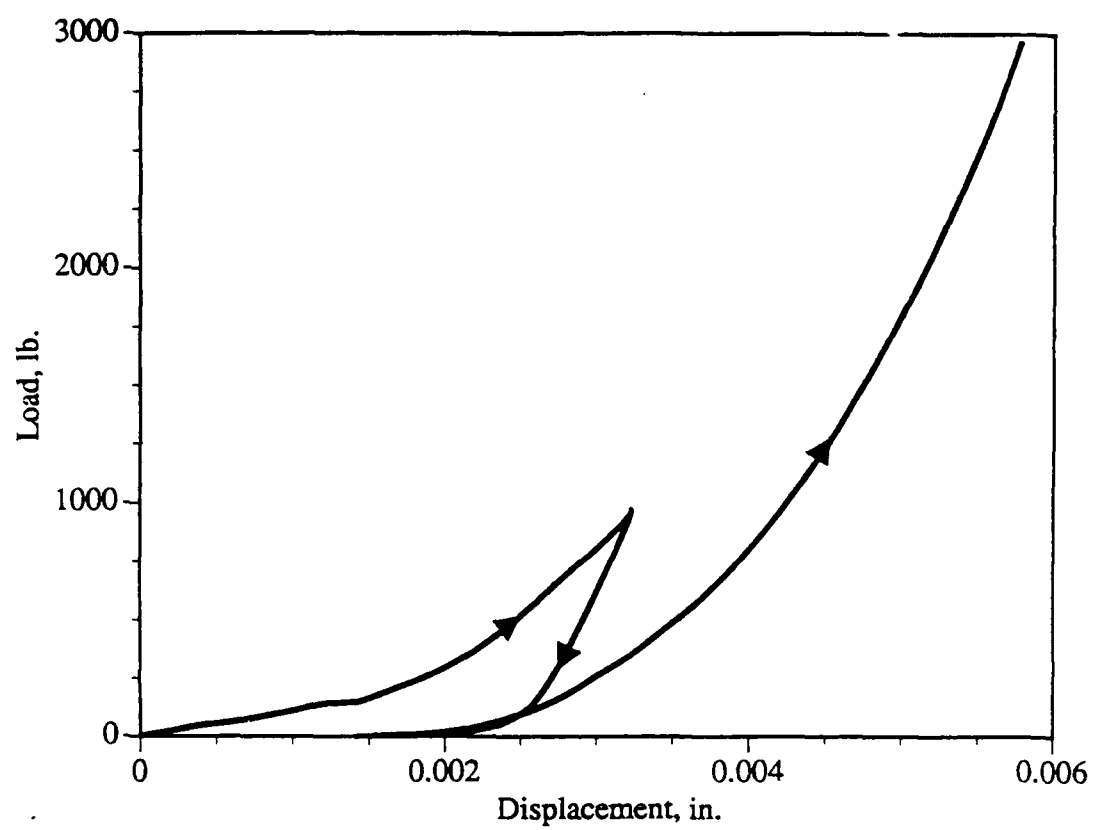


Figure 8.11: The force-displacement relationship of a cylinder made by stacking ten disks whose surfaces are sandblasted with steel beads.

$$n = \frac{107.5}{2 \times 250} = 0.215$$

(b) Steel-Bead-Blasted Surface

Normal load	= 250Lbf
Horizontal load	= 106Lbf (first test)
	= 100Lbf (second test)
	= 103Lbf (average)

(8.38)

The coefficient of friction is

$$\nu = \frac{103}{2 \times 250} = 0.206$$

It should be mentioned that the exact magnitude of horizontal load at the onset of slipping is difficult to ascertain visually. We estimate the error for the above listed horizontal loads has a range of ± 5 Lbf.

8.2 Numerical Prediction of Interface Contact

We used the new microasperity based model of frictional interfaces to predict numerically the force-deformation relation for the surfaces studied in the experiment. The computation was performed only for the surface sandblasted with glass beads. We did not analyze the surface blasted with steel beads, because it was very rough and did not meet at least two assumptions of our model. Those assumptions are: small deformations of asperities, and non-interference of neighboring asperities. Moreover, the experimental force-displacement curve for this surface indicates that the error of measurements on unloading-loading part was rather large (see Figure 8.11).

8.2.1 Data for Numerical Calculations

To calculate statistical characteristics of the surface we used scans obtained from an electronic microscope. We digitalized the side view of the sectioned disk specimen in aim to get the surface profile as a function. Graph of this function (height versus distance) for a segment of the profile is shown in Figure 8.12. The figure also shows the actual scan of the corresponding segment of the real profile.

Using the sampling method, we obtained the following statistical characteristics of the surface:

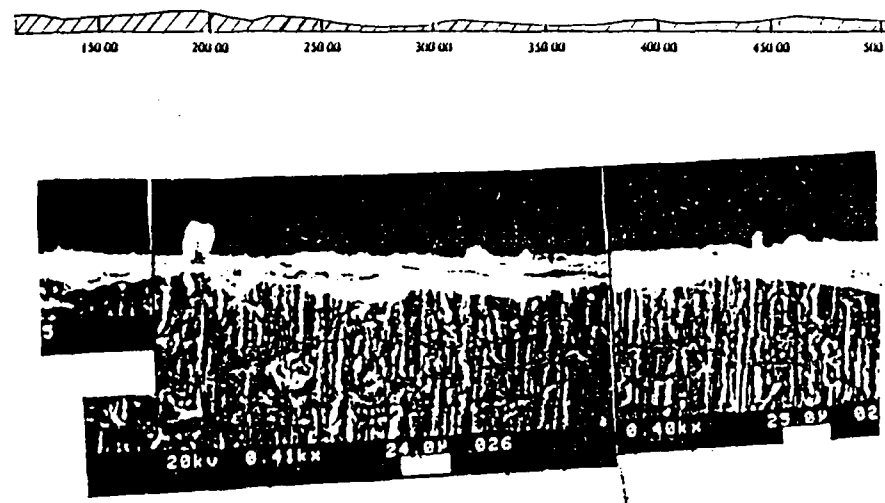


Figure 8.12: Digitized and original profile of the specimen used in the experiment.

Mean height: 112 μm ,
 Mean Slope: 0.000729 $= 2.4^0$
 Mean Curvature: $-0.000288 \mu m^{-1}$,

 Standard deviation of height: 4.91 μm ,
 Standard deviation of slope: 0.160
 Standard deviation of curvature: 0.0227 μm^{-1} ,
 Surface peak density: 0.000508 peaks/ μm^2 ,
 Wavelength spectrum parameter: 0.304.

Another microscopic scan of the specimen (Figure 8.3) indicates that the surface is isotropic so that the above coefficients fully characterize the shape of the surface.

To be able to perform mechanical analysis of asperities we also need to know material constants of the specimen material (cold rolled SAE 1020 steel). Bodner-Partom constitutive constants for steel are given in reference [10]. These generic constants were tuned for our particular sample, using the results of the tension test (Figure 8.13). The final values of the constants used for numerical calculations are listed below.

$$\begin{aligned}
 E &= 209 \text{ GPa} \\
 m_1 &= 0.05 \text{ MPa} \\
 n &= 2.28 \\
 \nu &= 0.3 \\
 Z_0 &= 600 \text{ MPa} \\
 D_0 &= 10000 \text{ s}^{-1} \\
 Z_1 &= 1050 \text{ MPa}
 \end{aligned}$$

These constants provide good correlation of numerical and experimental results for the tension test - see Figure 8.13.

8.2.2 Modeling of Surface Loading

As a first step of the homogenization procedure, the above surface statistics was used to determine effective support of joint probability density of asperity peaks, in particular the range of surface peak heights and curvatures. This range is defined by:

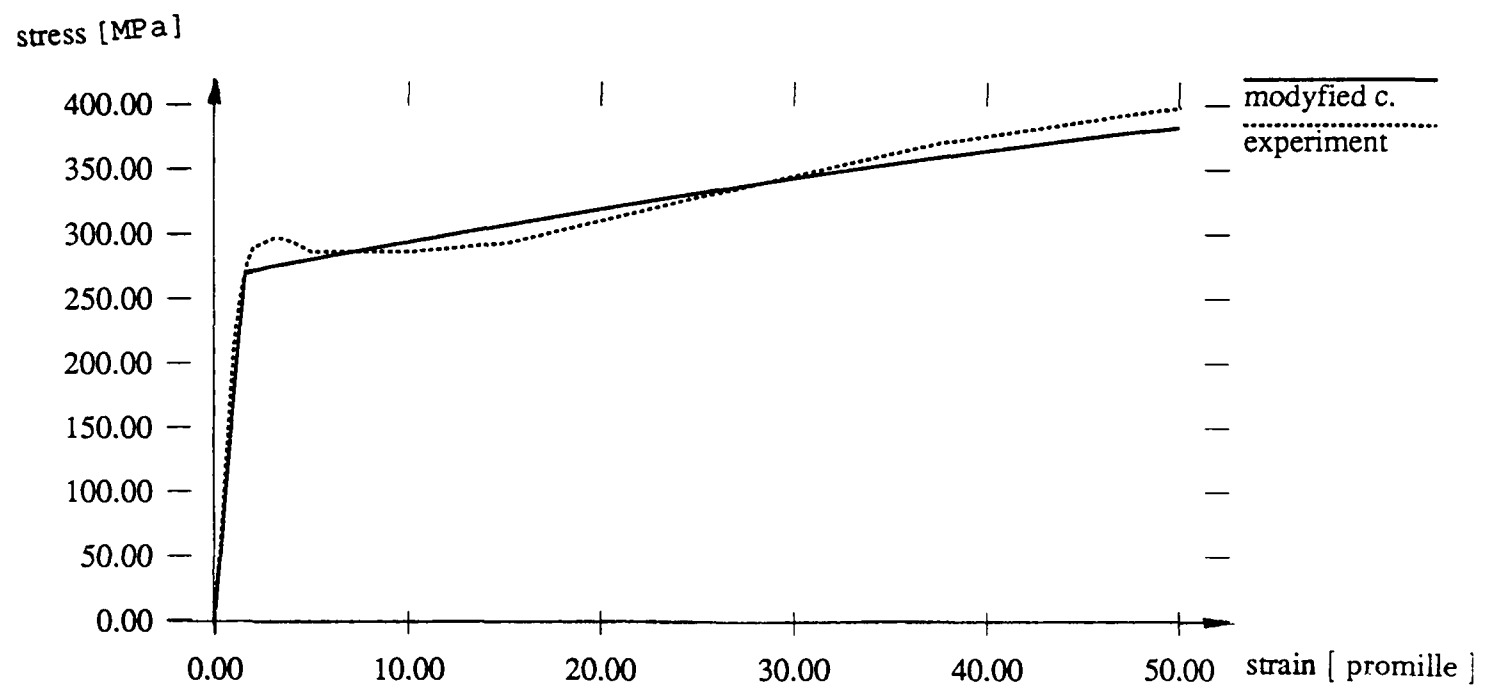


Figure 8.13: Comparison of tensile stress-strain relationships obtained experimentally and numerically.

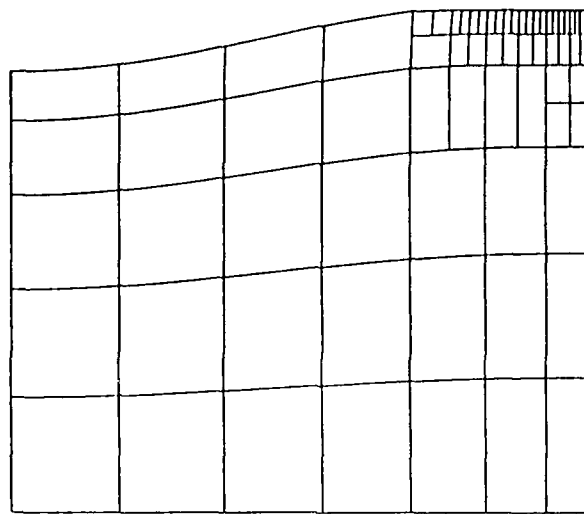


Figure 8.14: Adaptively refined mesh for an axisymmetric asperity (deformed shape is shown).

$$-12\mu m \leq z_p \leq 16\mu m \quad (8.39)$$

$$0.004\mu m^{-1} \leq k_p \leq 0.08\mu m^{-1} \quad (8.40)$$

Within this range, several sample asperities under normal load were modeled by the finite element method. Because the experimental surface was very rough and no effort has been made to make it extremely clean, adhesion effects were neglected. It was assumed that the deformation of the asperity was elasto-viscoplastic.

Figure 8.14 shows a deformed mesh which was used to discretize half of the asperity cross section (the problem is axisymmetric). The rate of load application, controlled by the normal velocity, was equal to $0.25 \mu m/s$, and corresponded roughly to the one used in the experimental setup.

About 10,000 time steps were necessary to complete the analysis. At each of those points the values of approach contact force and area of contact were printed out. From those 10,000 discrete values about 40 were chosen as data for statistical homogenization. This was because not all of those 10,000 values were computed with the same accuracy. It can be explained

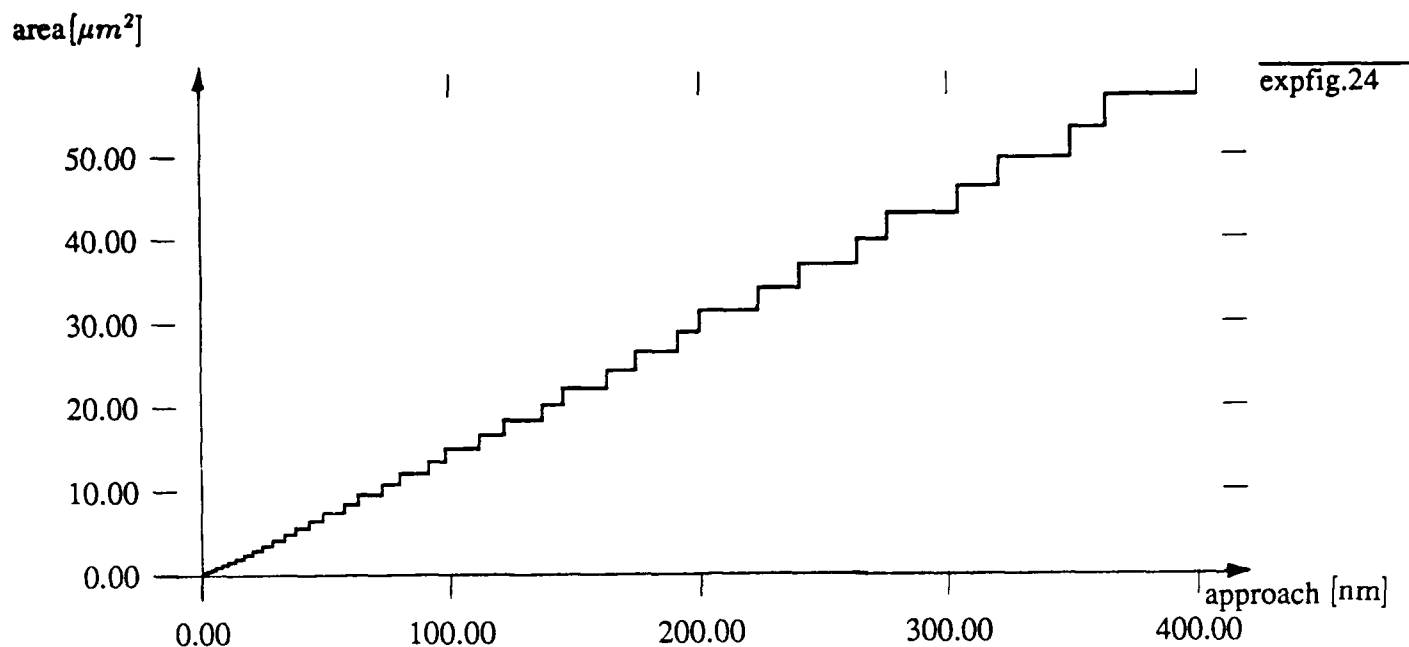


Figure 8.15: Area of contact as a function of approach obtained directly from the numerical analysis (about 10,000 data points).

on the example of area of contact. As a result of numerical analysis we obtain the area in terms of approach as a piecewise constant function (see Figure 8.15) while it is obvious that this relationship is at least continuous for a smooth asperity. The discontinuity of the numerical result is caused by the fact that the contact condition is examined at integration points. Therefore, the contact area increases incrementally, as new integration points join the contact zone. For further analysis the centroids of the horizontal segments on the graph of area versus approach were chosen as basic data points. Final graphs of contact force and area in terms of approach are shown in Figures 8.15 and 8.17, respectively.

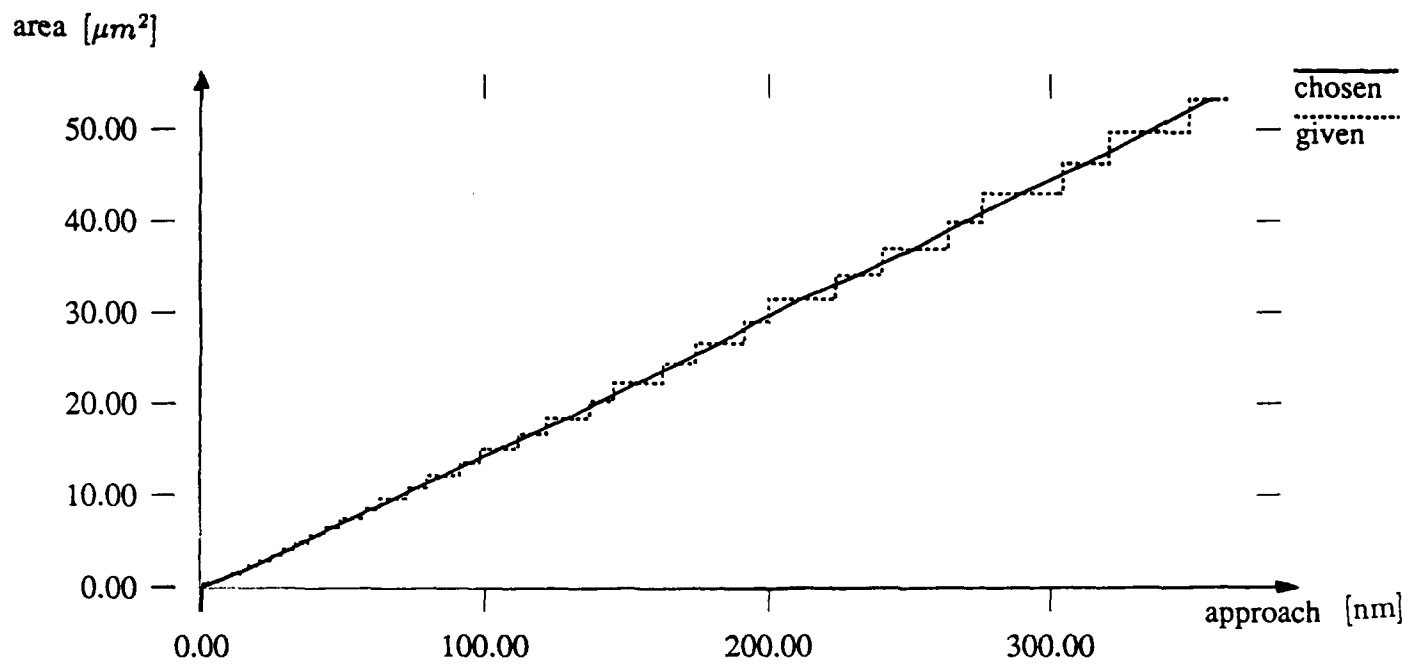


Figure 8.16: Final graph of contact area as a function of asperity deflection.

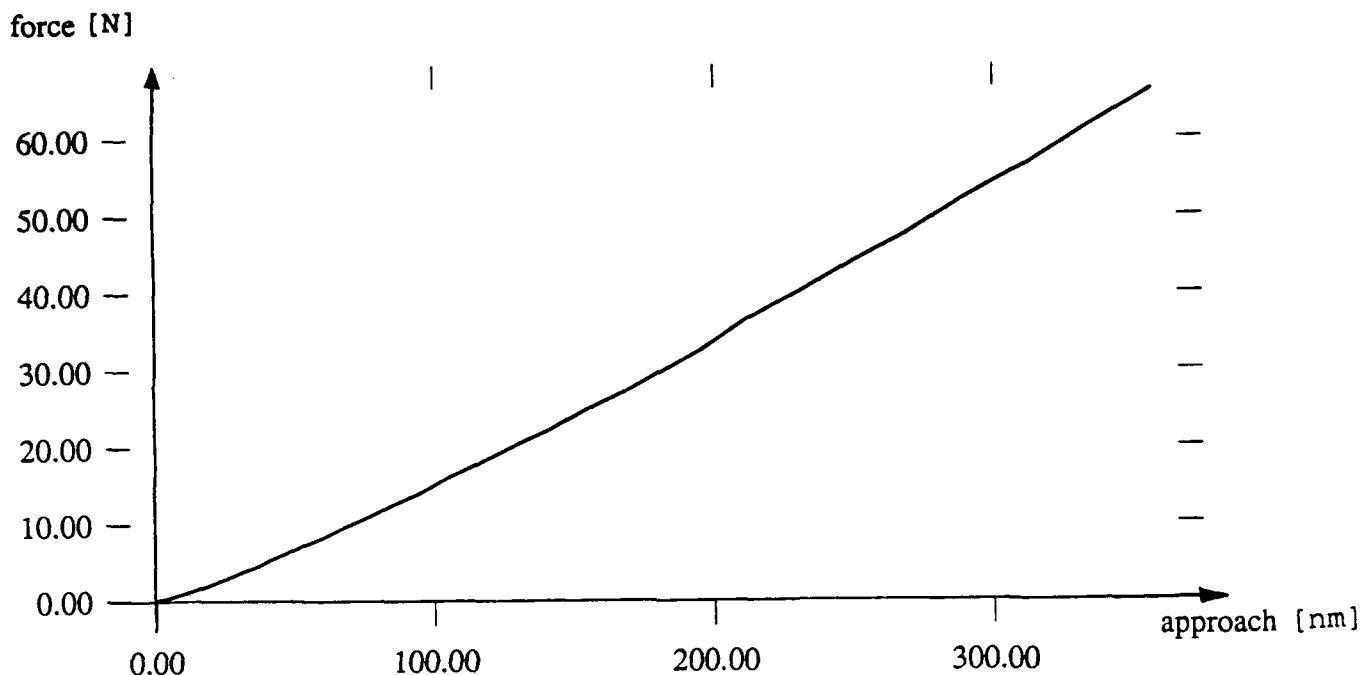


Figure 8.17: Final graph of contact force as a function of asperity deflection.

The results of mechanical analysis shown in Figures 8.15 through 8.17 were obtained for one representative asperity with width to height ratio $w/h = 13.4$. For exactly cosinusoidal profile this w/h ratio gives standard deviation equal to standard deviation of slope of the real surface. The wavelength spectrum parameter of the analyzed surface indicates that also asperities with other w/h could have an influence on the expected values of global force and area of contact. However, for the sake of simplicity and efficiency of the computation we limited our numerical analysis to the asperities with the most representative width to height ratio. Note that, due to absence of rate-dependent effects, the results obtained for the basic asperity (peak curvature equal to $0.042 \mu m^{-1}$) are also useful for asperities with different peak curvatures. The contact force and area for those asperities can be computed by simple rescaling of the existing values, because both force and area of contact are proportional to squared dimensions of an asperity.

The results of finite element asperity analysis, in particular contact force and real contact area, were used by statistical homogenization package, to produce force-approach and area-pressure curves shown in Figures 8.18 and 8.19. Note that, at this stage, we focus only on the loading part of the curve. The numerical predictions are compared with the experimental results. Note that the original experimental curve was rescaled to represent only one surface

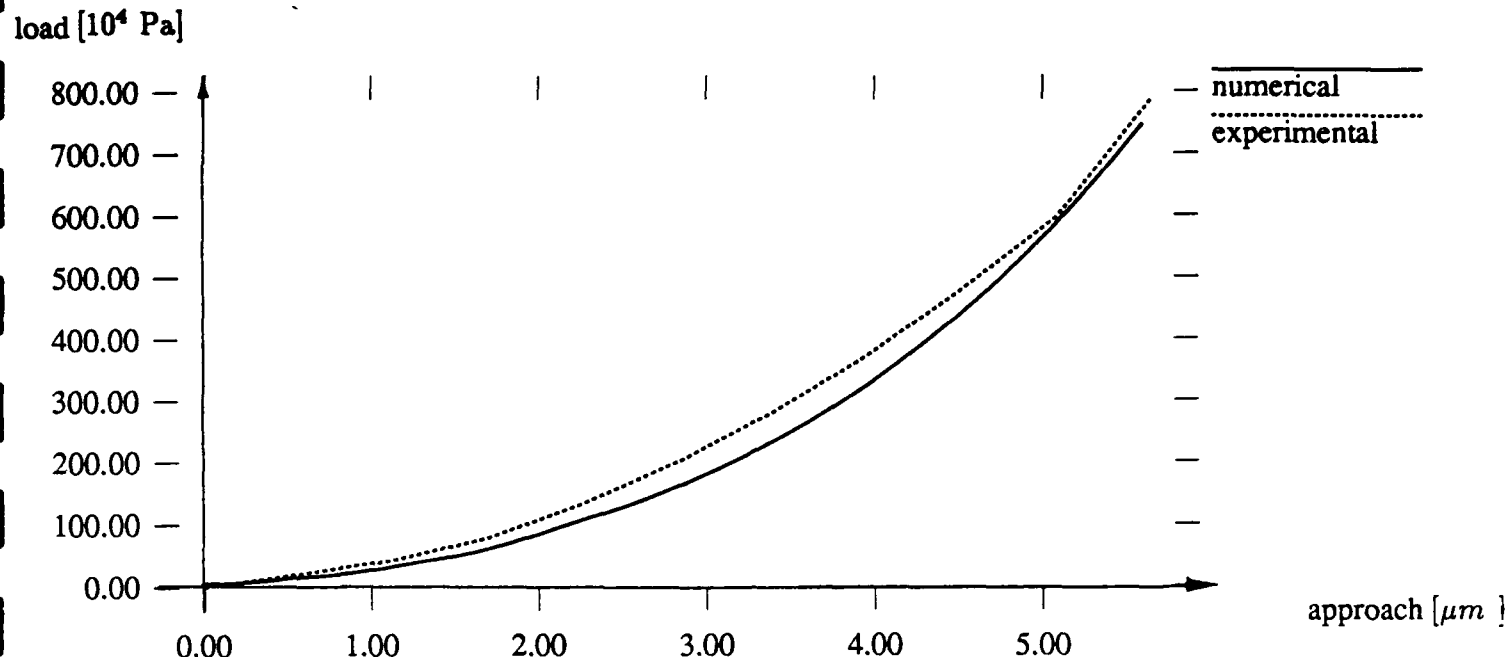


Figure 8.18: Numerical and experimental approach-pressure curves for the interface.

pair and normal pressure rather than total force. In the spirit on remark from Section 6.1, the zero point on the theoretical “approach” axis was chosen to match experimental load and surface stiffness at the initial contact of the surfaces.

contact area [$10^{-3} \text{ mm}^2 / \text{cm}^2$]
nominal area

expfig.28

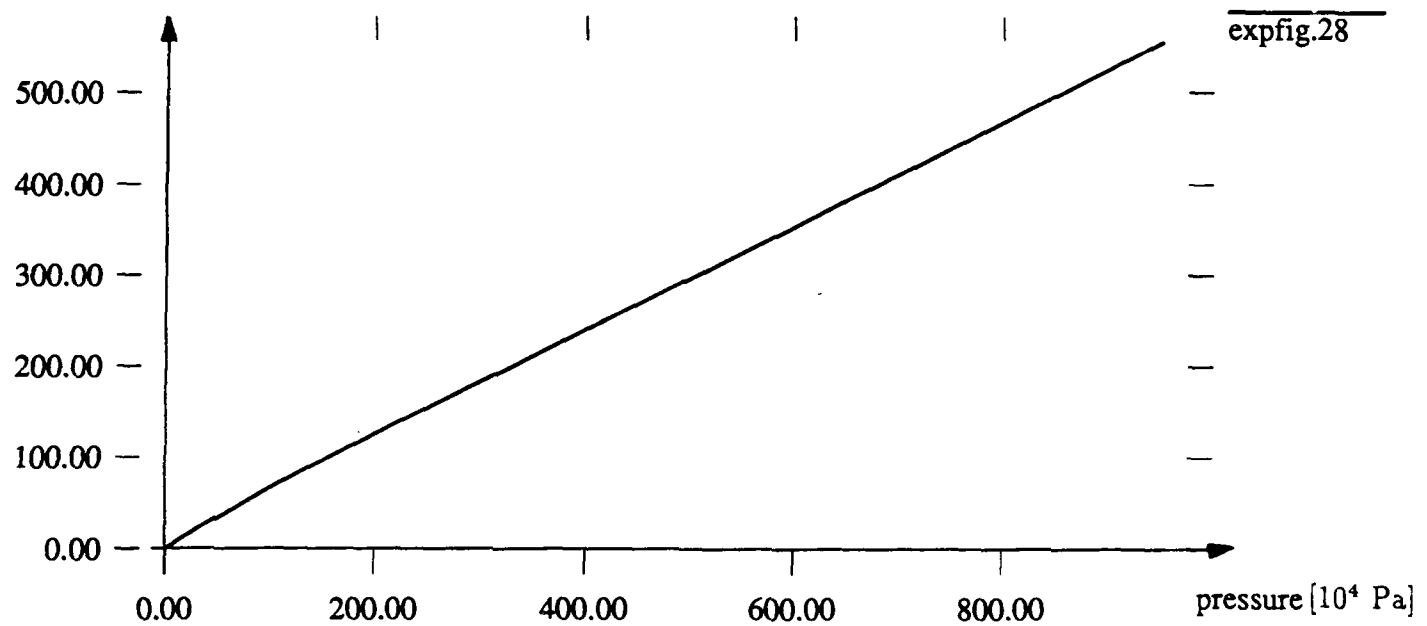


Figure 8.19: Numerical contact area vs. approach curves for the interface.

A comparison of experimental and numerical results shows a very good agreement up to a load of about $800 \text{ N}/\mu\text{m}^2$ (1000 psi). For higher loading an increasing discrepancy of the experimental and numerical curves can be observed (see Figure 8.20). There can be several reasons of that and some of them are discussed below.

1. To predict more precisely behavior of the specimen, the elastic deformation of the bulk material has to be considered. A graph of experimental normal stress reduced by bulk deformation is shown in Figure 8.21. Apparently, for higher loading bulk deformation is significant and has to be taken into account.
2. Another reason of discrepancy between numerical and experimental results can be additional deformation of the apparatus and stacked samples. Assuming proportionality of that deformation to the loading one can tentatively modify experimental data. Figure 8.22 shows original and modified experimental results. It was assumed that the experimental measurement has systematic error which depends linearly on loading and causes that the sensor indicates displacement exaggerated by $1.5 \mu\text{m}$ for the highest loading. In Figure 8.23, the modified experimental data are compared with numerical results. A good agreement of both curves can be observed for wide range of loading, which confirms strong possibility of systematic settling in the apparatus and in the samples.
3. Error of numerical results increases with increasing loading because at higher loads more asperities have large deformations, so that more asperities are beyond the assumptions of our theory (see Figure 8.24).
4. Another reason of the discrepancy for loads higher than $800 \text{ N}/\text{cm}^2$ can be loss of accuracy during experiment caused by unloading. Complete unloading might have been accompanied by a microdisplacement in a horizontal direction and then reloading would deform different asperities than the original loading.

pressure 10^7 Pa]

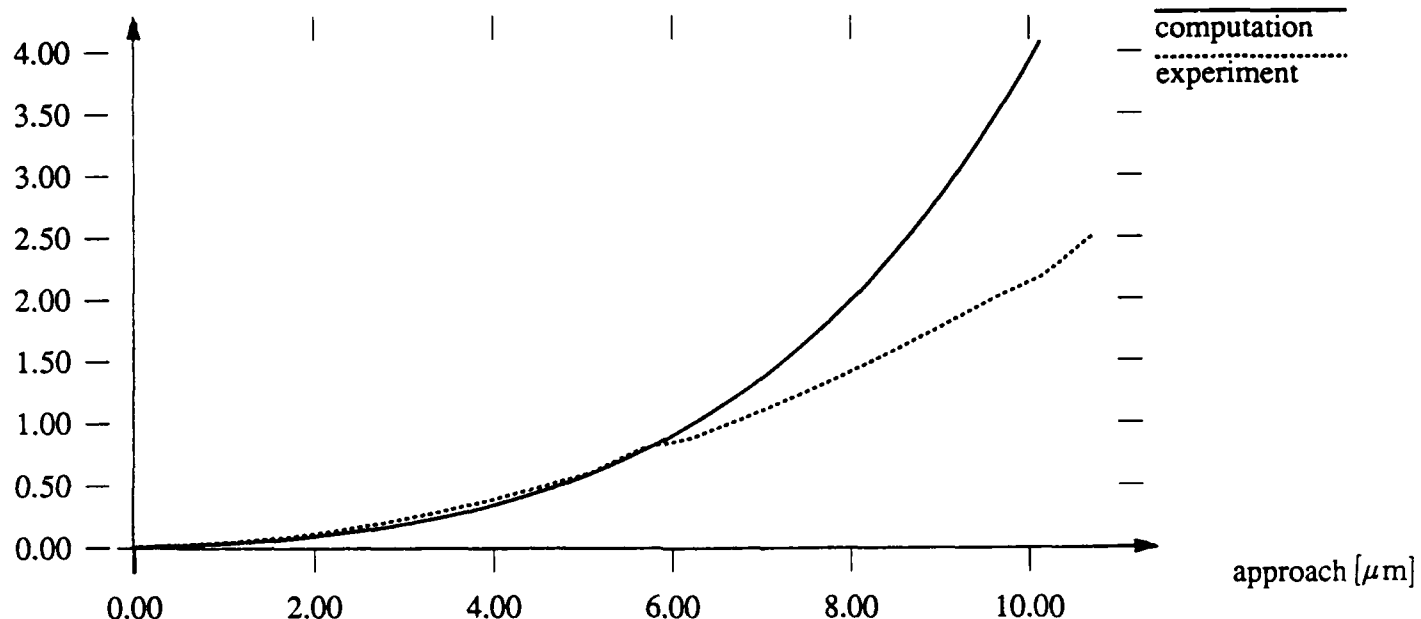


Figure 8.20: Numerical and experimental contact force in terms of approach for wider range of loadings.

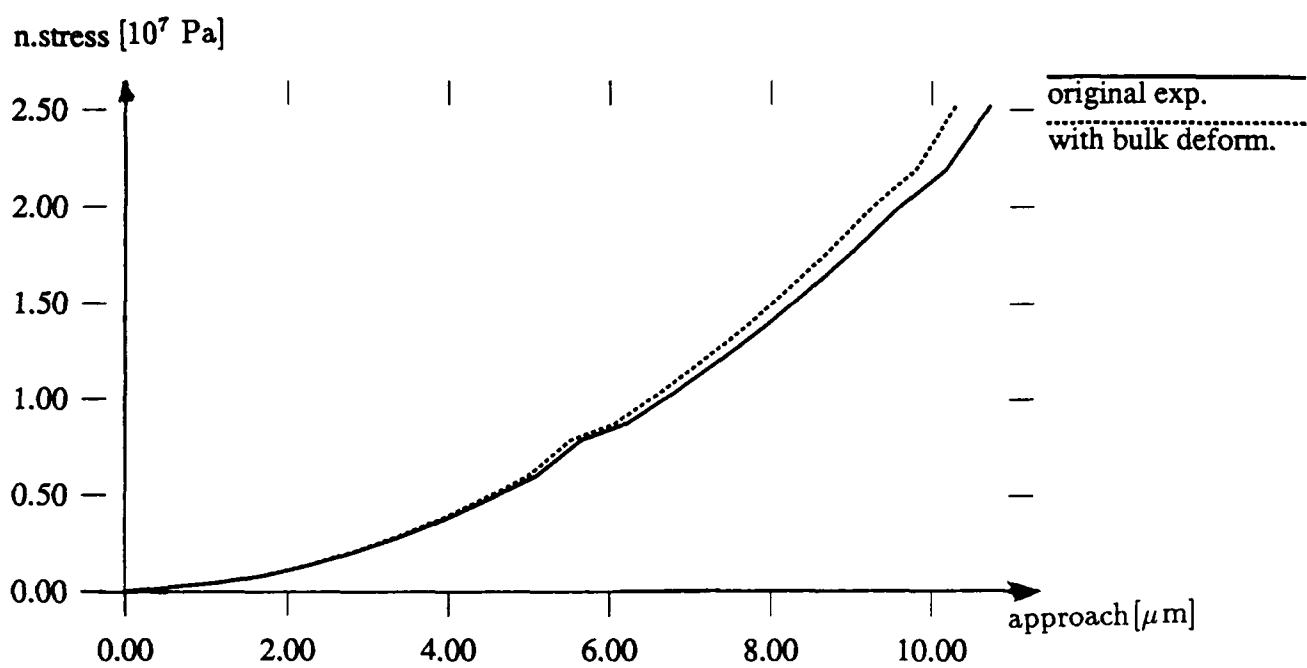


Figure 8.21: Experimental stress versus approach curves: (a) original and (b) corrected for bulk deformation of a sample.

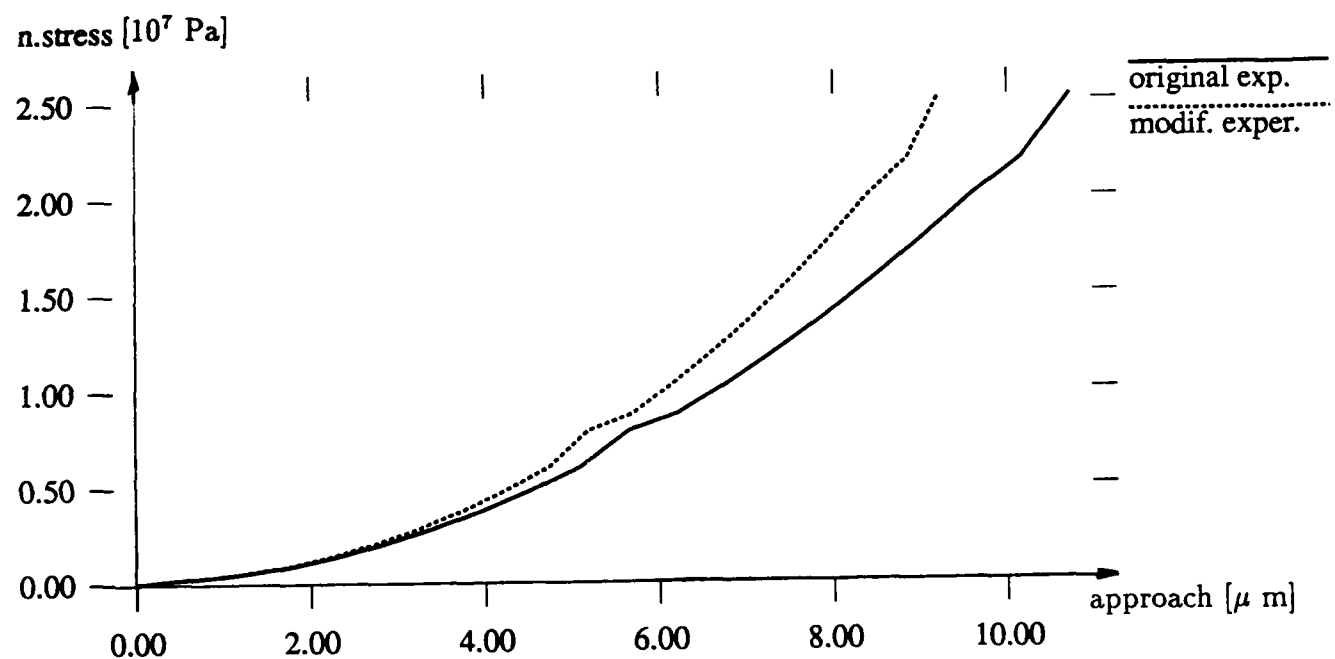


Figure 8.22: Experimental pressure-approach curves: (a) original and (b) corrected for additional settling of the setup.

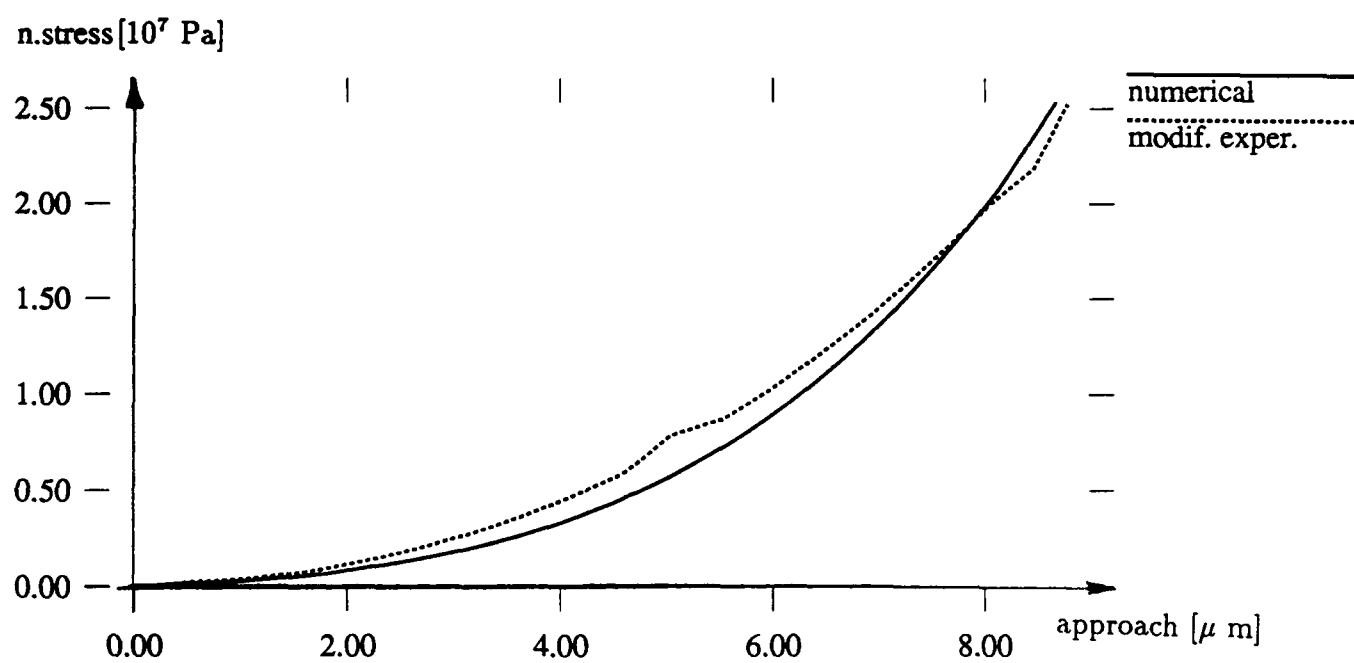


Figure 8.23: Comparison of numerical prediction of normal stresses with modified experimental results.

8.3 Studies of Unloading

An additional study that was performed for the experimental surface was focused on modeling of the static unloading path. By static unloading we understand the situation, wherein the normal load is reduced to zero or almost zero *without* relative sliding on the interface. This means that the asperity tips, which became "conformal" during loading due to plastic deformation, remain conformal and aligned. This situation is illustrated in figure 8.25.

Importantly, modeling of the unloading path required additional extension of the homogenization package to monitor the displacement and load corresponding to the beginning of surface unloading. Moreover, even for single unloading of the interface, the results at the asperity level must consider a whole family of unloading curves, starting at different normal deflection. This is a consequence of random asperity height; at the beginning of surface unloading each individual asperity is "caught" at a different stage of deformation.

For practical modeling, it would not be feasible to consider an infinite number of unloading paths at the asperity level. Instead, we adopted the following procedure:

- (a) analyze in detail a few (three to four) unloading paths for the asperity, starting at different deflection levels, and
- (b) use approximation techniques to represent unloading paths which start at the intermediate load level.

This approach is illustrated in figure 8.26. Importantly, the finite element analysis of the unloading path was performed using exactly the same methods as for the loading curve - the unified viscoplastic constitutive theories applied here do not require special treatment of elasto-plastic unloading. The approximation method used for the construction of intermediate unloading paths was based on the blending function formula [].

The formula is a mapping of a unit square into a domain which has four curvilinear sides. Coordinates of the square ($s, t \in [0,1]$) can be treated as parameters. They parametrize sides of the curvilinear domain. Let the parametric equations of these curves $\gamma_1 = AB$, $\gamma_2 = BC$, $\gamma_3 = DC$, $\gamma_4 = AD$ (Figure 8.26) be given generally in the form

$$\gamma_k = \{(x, y) \in \mathbb{R}^2 : x = x_k(p), y = y_k(p), p \in [0, 1]\}, \quad k = 1, 2, 3, 4$$

where in our case:

x are approaches,
 y are contact forces,

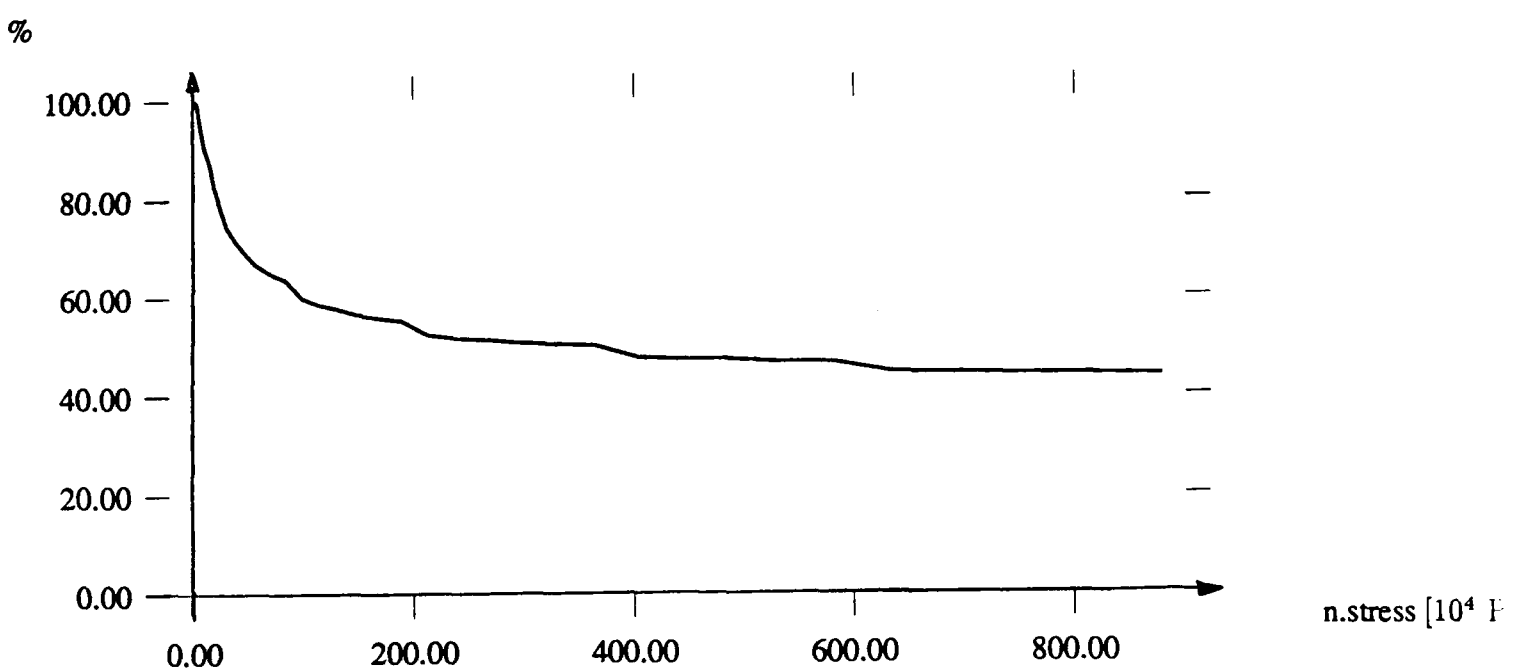


Figure 8.24: Percentage of asperities satisfying small deformation assumption.

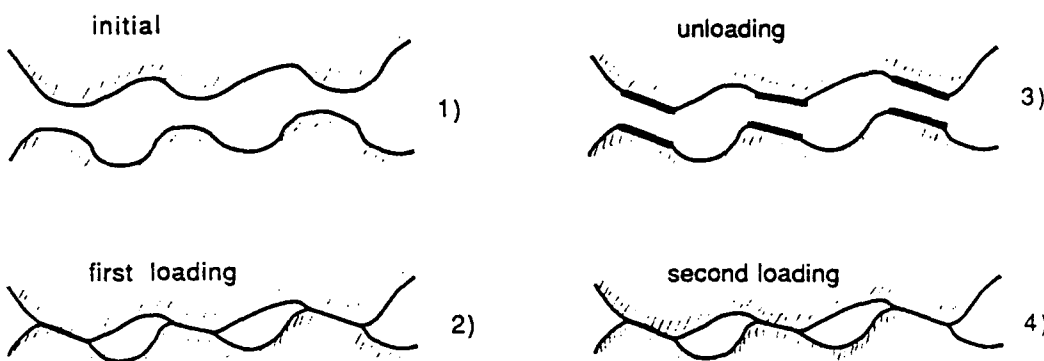


Figure 8.25: Static loading, unloading and reloading of the interface

$$p = \begin{cases} s & \text{for } k = 1, 3, \\ t & \text{for } k = 2, 4. \end{cases}$$

Using the above notations the blended functions provide mapping of parameters s, t into x and y coordinates in the following way

$$\begin{aligned} x(s, t) = & x_1(s)(1-t) + x_2(t) \cdot s + x_3(s) \cdot t + \\ & + x_4(t) \cdot (1-s) - x_A(1-t)(1-s) - x_B \cdot (1-t) \cdot s \\ & - x_C \cdot t \cdot s - x_D \cdot t \cdot (1-s) \end{aligned}$$

$$\begin{aligned} y(s, t) = & y_1(s)(1-t) + y_2(t) \cdot s + y_3(s) \cdot t + \\ & + y_4(t) \cdot (1-s) - y_A(1-t)(1-s) - y_B \cdot (1-t) \cdot s \\ & - y_C \cdot t \cdot s - y_D \cdot t \cdot (1-s) \end{aligned}$$

where $(x_A, y_A), (x_B, y_B), (x_C, y_C), (x_D, y_D)$ are coordinates of corners A, B, C, D correspondingly. Figure 8.27 shows a family of unloading curves generated by the blending functions. Note that the blended curves can be generated also outside domain ABCD. Curve γ_0 was not generated but computed by solution of the unloading problem for the asperity. Comparison

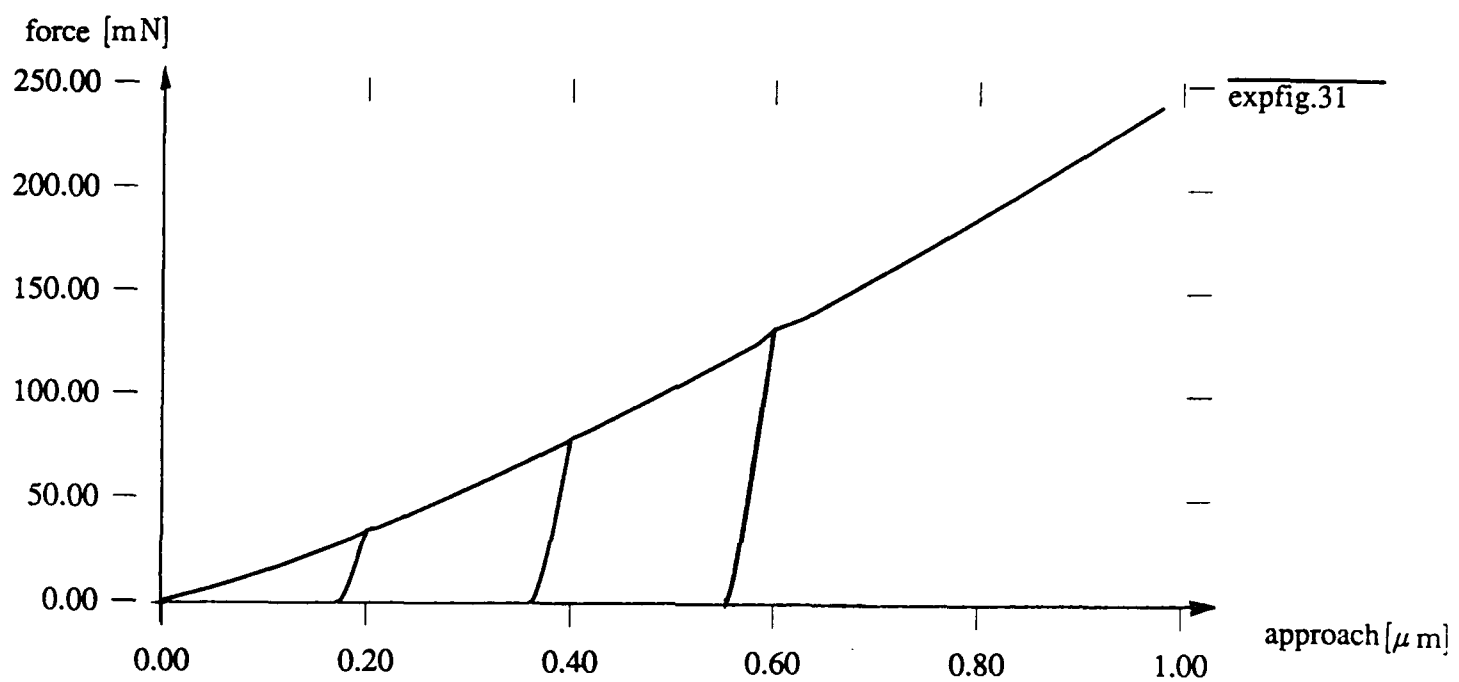


Figure 8.26: Contact force for an asperity in terms of deformation during loading and unloading at three different levels.

of this curve with blended functions indicates reasonably good correlation. This correlation improves with increasing number of calculated unloading curves.

After application of the statistical homogenization, the loading-unloading curves were obtained for the surface, and are shown in figure 8.28. Clearly, the theoretical unloading path is steeper than the one observed in the experiments. At present time we do not have a precise explanation of this fact. However, we believe, that the asperity-based theoretical curve better represents the actual behavior of the interface. This is supported by the following arguments:

1. For the loading section of the curve, random asperity height has a significant smoothing effect, because different asperities are contacted at different loading stages. However, the unloading path is only supported by elastic "rebound" of all the deformed asperities - see figure 7.26. Therefore, the unloading deflection cannot essentially be higher than the maximum elastic rebound of a single asperity. Since the unloading path for a single asperity is rather steep (see figure 8.26), the elastic rebound, even for the largest asperities, does not exceed 1.0μ .
2. The additional normal compliance, present in the experimental setup, can have a much more significant distorting effect on the (very steep) unloading path than on the loading path. Indeed, presence of additional deflection of about 1.5μ would modify the theoretical unloading curve to match the experimental one. It is conceivable that such deflection can be present due to departure of the surfaces from ideal flat, and the resulting "plate bending" effect.

It is also possible, that there may be some infinitesimal tangential sliding present on the surface during unloading - this would spoil the alignment of deformed asperities shown in figure 8.25 and cause additional separation of the surfaces.

The above arguments are supported by the experimental work of Connolly, Shoffield and Thornley [30], wherein experimental unloading curves were much steeper than these obtained in the experiment reported here.

In view of these remarks, the question of interface unloading will require some additional, extremely precise experimental studies. Furthermore, the phenomenon of unloading during tangential sliding will need a dedicated study. The unloading curve in this case will, due to mechanical interaction of the sliding asperities, differ significantly from the static case.

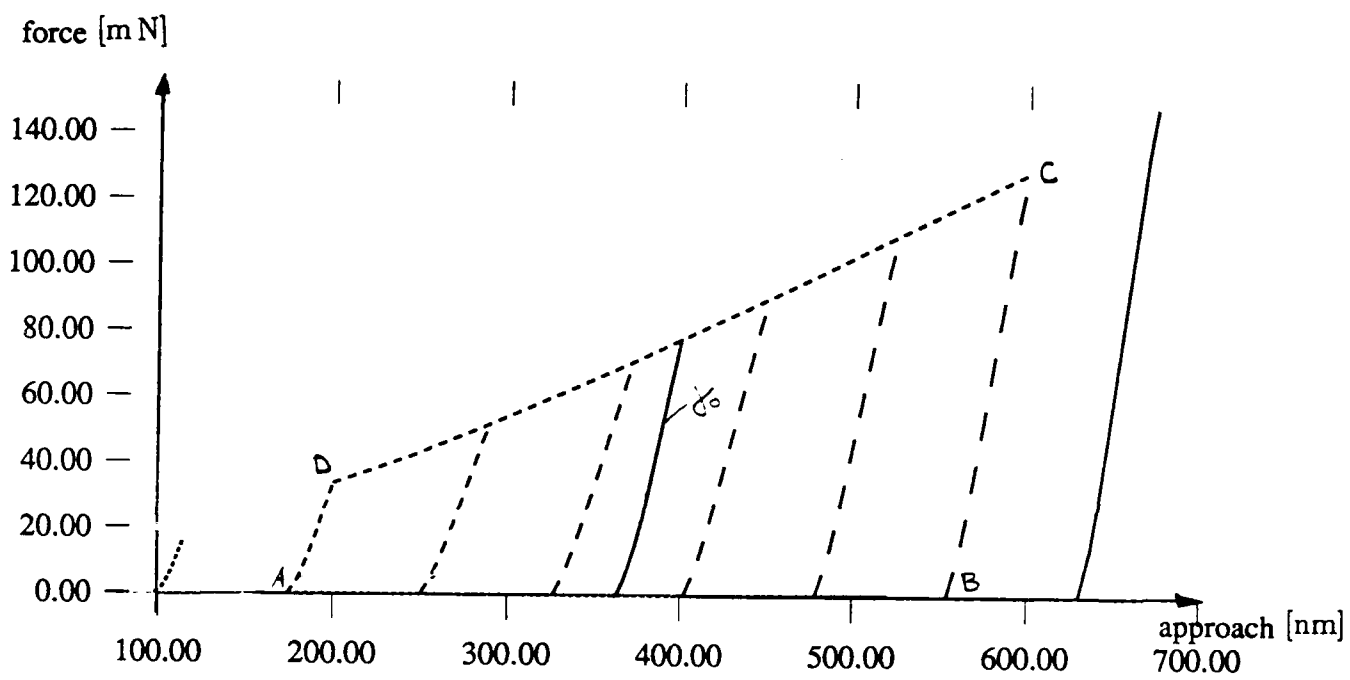


Figure 8.27: A family of unloading curves generated by blending functions.

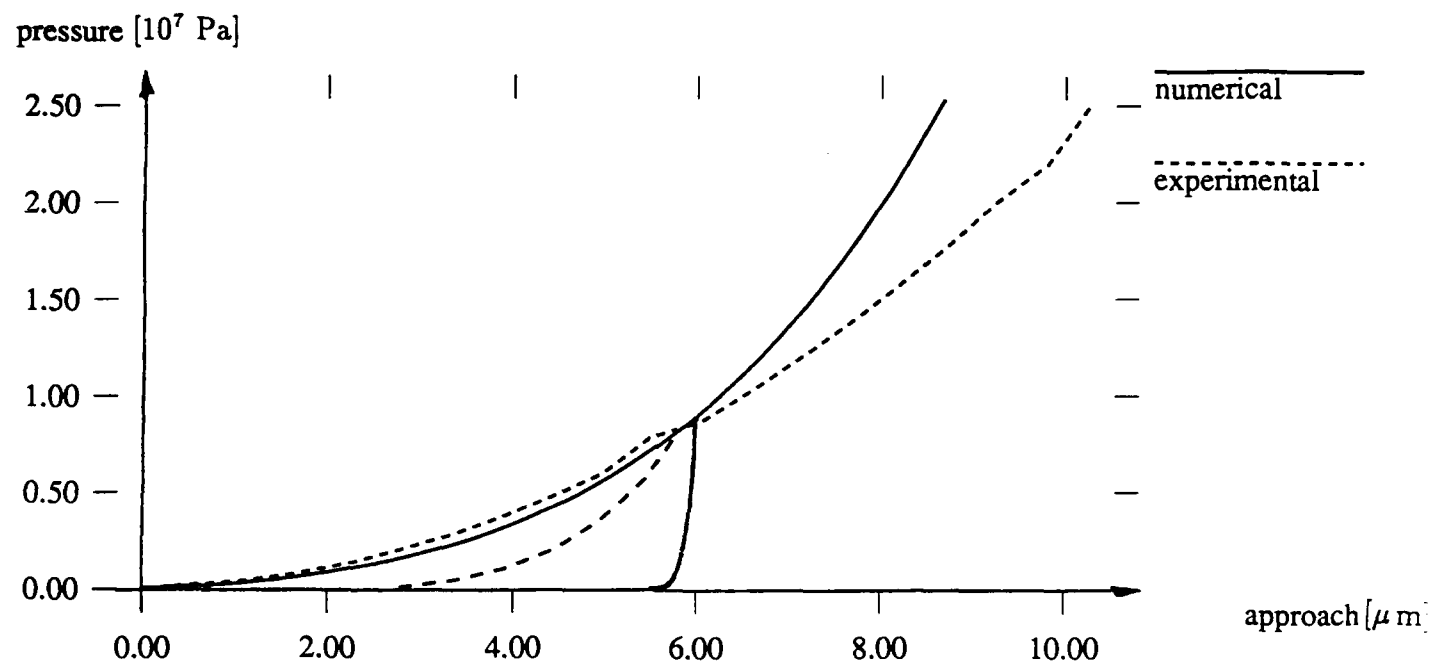


Figure 8.28: Loading and unloading curves obtained numerically and experimentally.

9 Studies of Friction

In this section, we present some introductory studies of frictional characteristics of the interface. In particular, we aim to:

- estimate the value of the static coefficient of friction, and
- study frictional deformation of microasperities.

9.1 Static Coefficient of Friction

For the sample surfaces studied in previous sections, introductory studies of the coefficient of friction were performed. These studies were based on the following two assumptions:

1. sliding resistance between similar metallic surfaces is caused primarily by formation and shearing of junctions between the contacting asperities,
2. the value of tangential force necessary to shear a junction is defined as:

$$T = \tau_s A_c \quad (9.41)$$

where τ_s is shear resistance of the material and A_c is the real contact area between the asperities.

In the first approximation the shear strength of a junction can be considered to be independent of normal pressure and equal to the shear strength of the bulk material.

The formula (9.41) can be easily used to calculate the coefficient of friction on the interface level:

$$\mu = \tau_s A_c / F$$

where A_c is a real contact area per unit nominal area and F is the normal force per unit nominal area.

Smooth Surface

The above formula, combined with pressure-area curves presented for the smooth aluminum surface in Figure 7.9, produces the values of the coefficient of friction shown for increasing normal load in Figure 9.1. For the case with adhesion (clean smooth surfaces in vacuum), the value of the coefficient of friction is very high at light loads – this is caused by

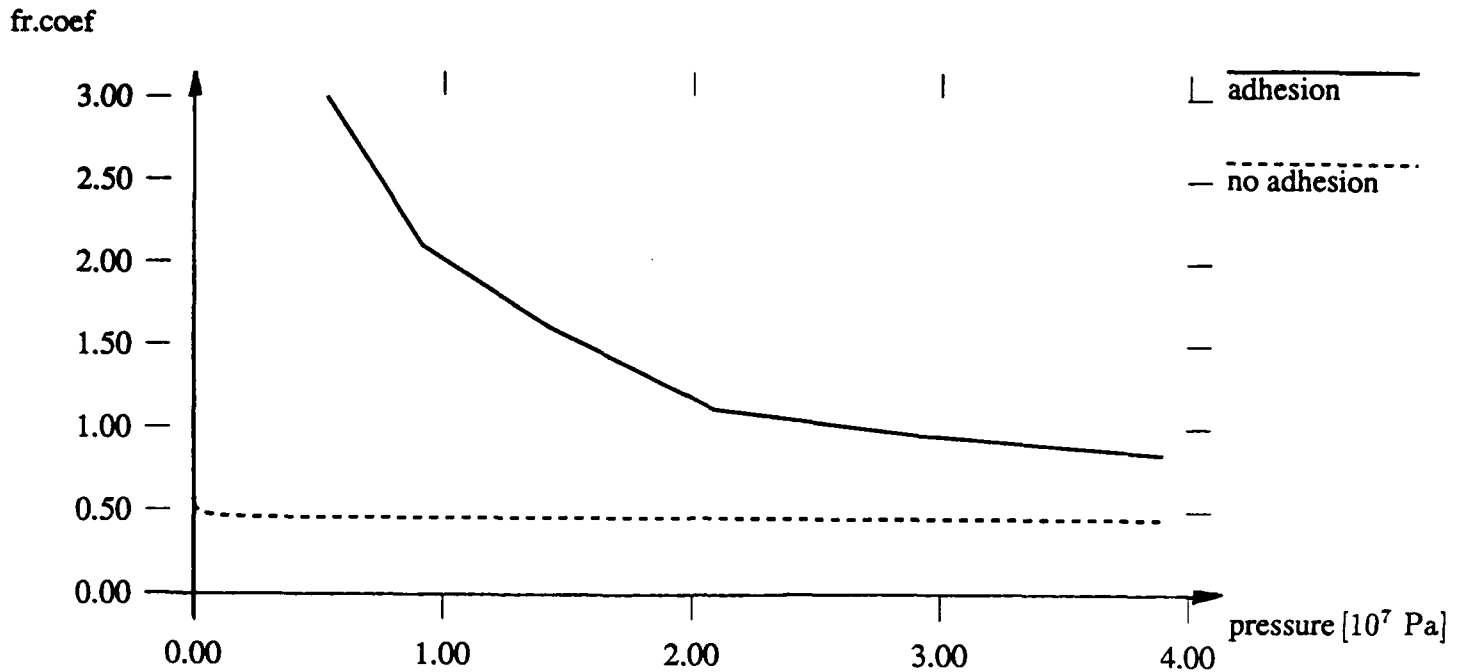


Figure 9.1: Smooth aluminum surface: coefficient of friction for increasing loads

additional normal attraction due to adhesion. In the absence of adhesion the coefficient of friction is almost constant over a wide range of loads, with a value slightly below 0.5. Note that this value is essentially overestimated – junction strength of oxygenated aluminum surfaces is lower than the shear resistance of the bulk material, assumed here. A more detailed studies of this phenomenon, including frictional microdisplacements, are currently underway.

Rough Surface

Some interesting observations can be made when the above analysis is applied to the rough surface, studied in Section 7.4. The values of the coefficient of friction calculated for this surface using elastic and elasto-plastic models are compared in Figure 9.2. Clearly, a purely elastic approach underestimates the value of the coefficient of friction. This is a result of an underestimated contact area predicted by the elastic solution on the asperity level. The elasto-plastic approach produces more realistic values of the coefficient of friction, of the order of 0.3.

Experimental Surface

The above simplified model was used to estimate the coefficient of friction for the rough steel surface studied experimentally and numerically in Section 8. Figure 9.3 shows the calculated value of the coefficient of friction for increasing normal load (approach). In the absence of relevant data, it was assumed, that the shear resistance of asperity junctions is equal to shear strength of the bulk material. For the actual normal pressure tested in the

fr.coef.

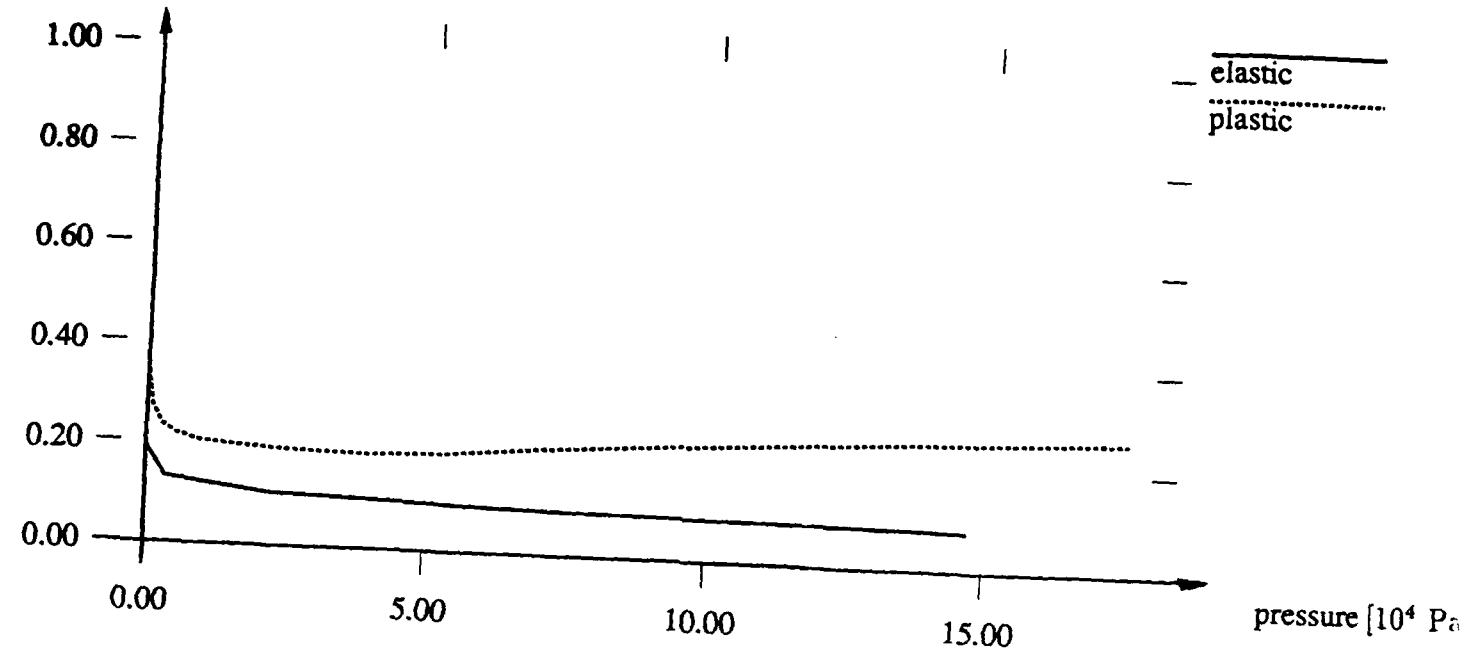


Figure 9.2: Rough aluminum surface: coefficient of friction (shearing component) for increasing loads

fr.coef.

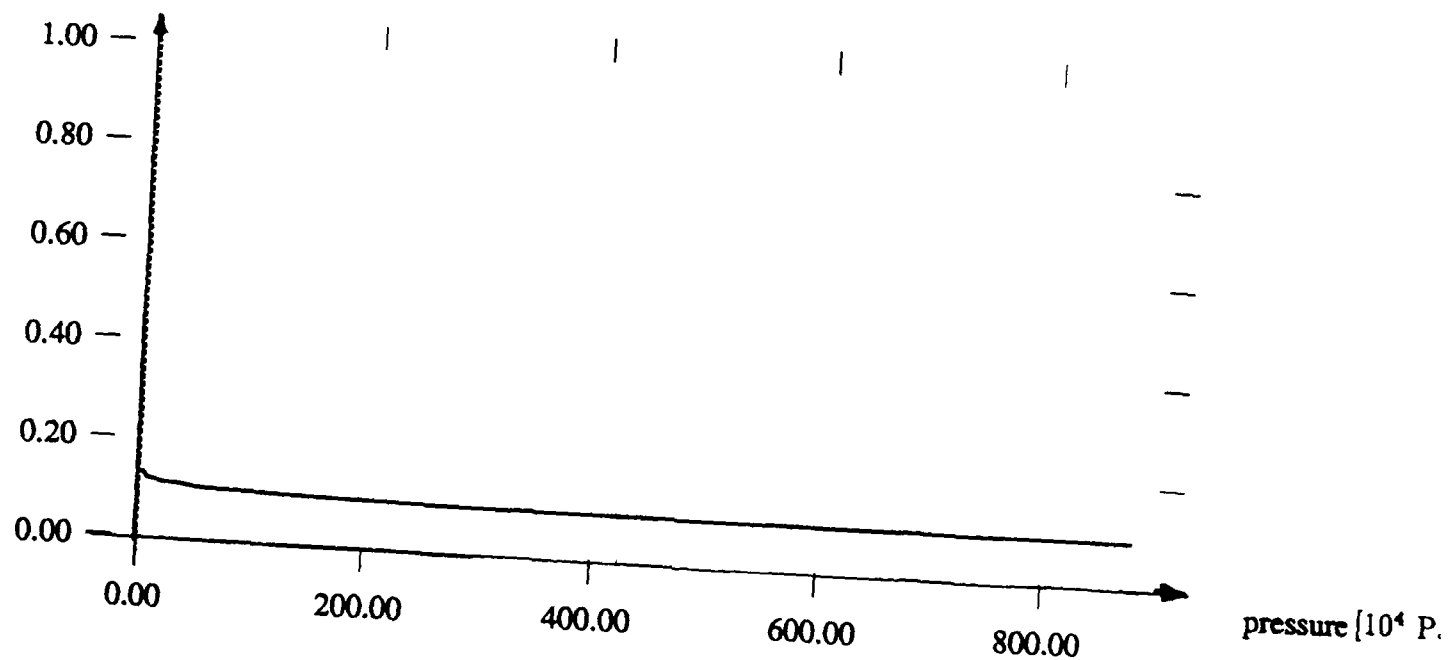


Figure 9.3: Rough steel surface: shearing component of the coefficient of friction for increasing normal approach (load)

experiment, the estimated value of the coefficient of friction due to junction shearing was equal to 0.093, while the measured value was 0.215.

However, for this rather rough surface there exists an additional contribution to friction due to *interlocking of asperities*. While for relatively smooth surfaces this component can usually be neglected, for this rough surface this is not the case. A very approximate estimate of the interlocking component of friction, based on relative motion of inclined surfaces [32,89], leads to a conclusion that the additional contribution to the coefficient of friction is equal to the average slope of the asperities. For the surface under consideration this is equal to 0.16, which leads to the final value of the coefficient of friction equal to 0.253, as compared with experimental value of 0.215.

This is a quite good correlation of numerical and experimental results, especially that, due to a lack of relevant data, the shear resistance of asperity junctions was assumed to be independent of the normal pressure (which is not exactly the case in practice).

9.2 Studies of Frictional Sliding

The simplified approach discussed in the previous subsection can only be used for general estimates of sliding resistance of the interface. It cannot represent such intricate phenomena as:

- tangential micro-displacements before inception of macro-scale sliding,
- damage of asperities by shearing *below* the contact junction, rather than at the junction,
- normal “settling” of the junction due to combined normal and tangential stress,
- ploughing component of friction, etc.

Studies and understanding of the above phenomena can only be accomplished by modeling of the actual sliding process, wherein two asperities in contact are subject to tangential motion. Numerical modeling of these phenomena is computationally rather expensive, because full three-dimensional asperity models need to be used, combined with extensive nonelastic deformation, complex stress states and sliding resistance of the metallic junction.

In this section, some introductory studies of tangential sliding are presented.

We analyzed a representative cosinusoidal asperity with height equal to 2 microns and diameter at the base equal to 10 microns. The asperity was made of the steel studied in the experiment, with full elasto-viscoplastic representation. The contacting flat was first subjected to normal motion (0.125 microns), followed by tangential sliding of 1.0 micron. The first step was performed in time 0-1800 s. The tangential loading step was applied in time

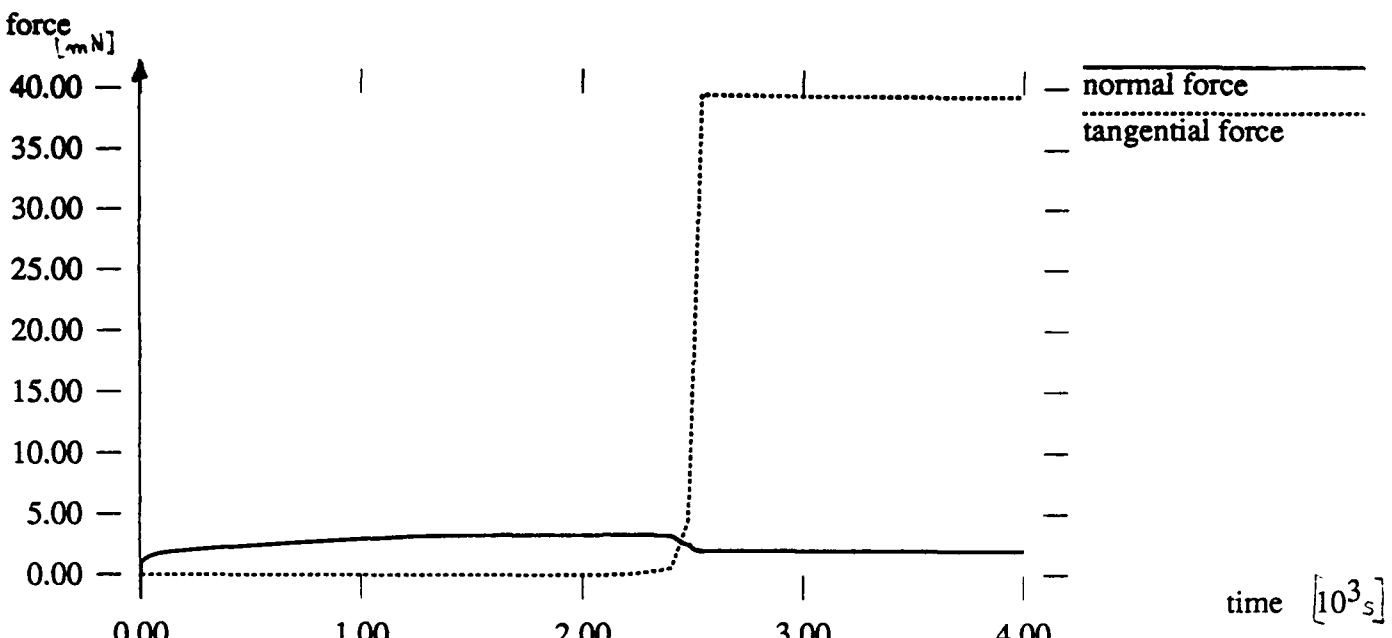


Figure 9.4: Evolution of normal and tangential forces for the asperity

1800-4000 s. In order to model shear resistance of the metallic junction, large coefficient of friction (20) was assumed. The main objective here was to identify, whether the maximum deformation would occur on the surface (shearing of the junction) or below the surface (shearing at the asperity tip).

The asperity was discretized by FEM mesh which, after h-adaptation, had 666 degrees of freedom. Introductory results of this study are shown in Figs. 9.4 and 9.5. In particular, figure 9.4 shows evolution of normal and tangential forces during the loading process. Figure 9.5 shows deformation of the asperity at the end of the analysis (at time 4000s).

During the analysis, no signs of destruction of the asperity were observed. In fact, the average tangential traction on the contact surface due to tangential motion of the flat was approximately 64 MPa, which is well below the shear strength of steel. This means, that representing shear strength of the junction by high coefficient of friction was not sufficient. Instead, exact modeling of shear resistance on the junction surface is necessary. This required additional modification of the finite element code and study of asperity sliding. These studies are currently underway and will be presented in the forthcoming publications..

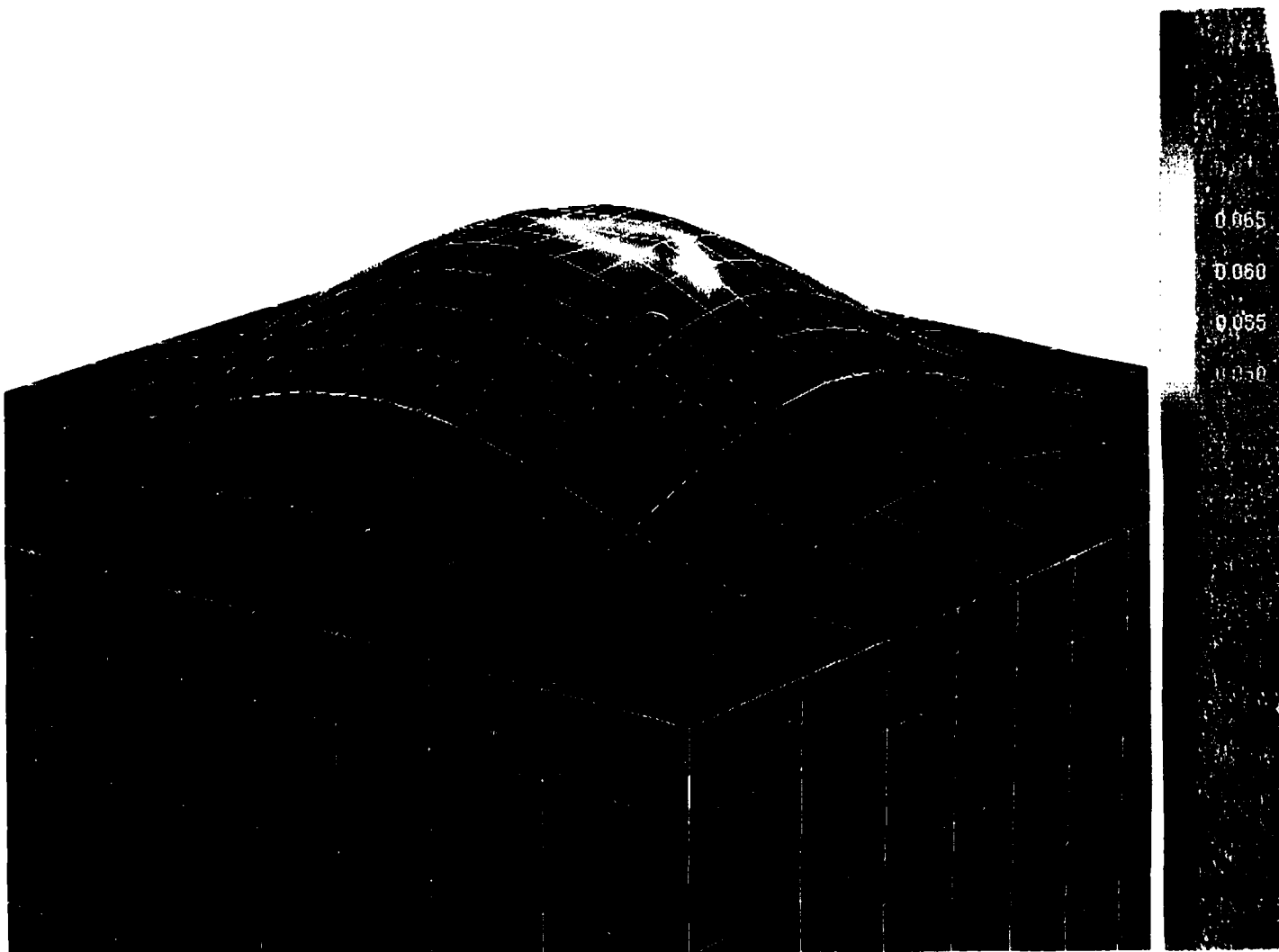


Figure 9.5: Deformed configuration and contours of horizontal displacement in the asperity sliding study.

10 Towards Application of Asperity-Based Models in Modeling of Dynamic Friction

The micro-asperity-based models developed in this work produce the values of normal pressure, real contact area, sliding resistance, etc., as a function of approach of the two surfaces. These functions are given in the form of series of discrete points or graphs.

However, application of these constitutive models in the analysis of dynamic friction requires an analytic (and differentiable) formulas. Towards this end, some effort was dedicated to development of automated tools that would produce analytical formulas representing the interface constitutive laws.

A basic approach used is as follows:

1. micro-asperity based model is given as a series of discrete points, for example a sequence of approach-pressure values $(A_k, p_k) k = 1, M$
2. the user chooses the formula to be used, say the Oden-Martins law or logarithmic compliance curve,
3. the coefficients of the constitutive formula are determined automatically through the minimization procedure described below.

The above procedure will be illustrated on the example of the fitting of the asperity-based approach-pressure relationship into the Oden-Martins interface model [71]. The Oden-Martins normal compliance law can be written in the following generalized form:

$$p = c \left(\frac{a - g}{a_0} \right)^m \quad (10.42)$$

where

- p – nominal pressure,
 a – approach,
 c, g, m – unknown material constants,
 a_0 = $1\mu\text{m}$ (dimensionality factor).

Note that a_0 was introduced to assure proper dimensionality, and g is a translation (initial gap) which appropriately locates the zero point for the approach axis. The constants in the above formula were determined in such a way which provides the best fitting of the function

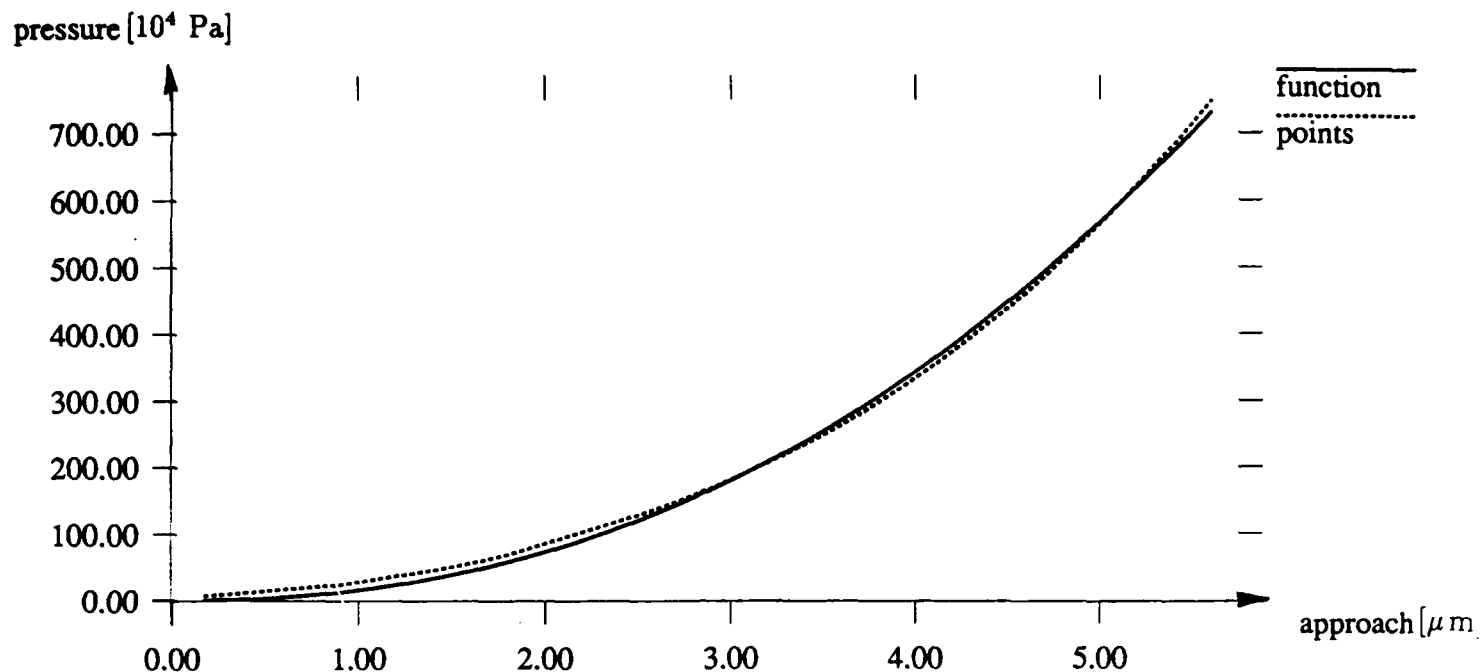


Figure 10.1: Fitting of the Oden - Martins formula to the sequence of asperity-based data points for the steel surface studied in Section 8

10.42 to the sequence of M given points (a_k, p_k) . The best fitting means here that a function B , which is square of a norm of difference between discrete and continuous laws, attains its infimum.

Function B has the following form:

$$B(c, g, m) = \sum_{k=1}^M [p(c, g, m, a_k) - p_k]^2 \quad (10.43)$$

where

$p(c, g, m, a)$ — nominal pressure given by formula 10.42

(a_k, p_k) — k -th discrete point.

For the load-approach curve representing our experimental surface (see Section 8), we obtained $g = 0 \mu\text{m}$, $c = 15.2 \text{ N/cm}^2$, and $m = 2.25$. Figure 10.1 shows pressure - approach relationships for both discrete and the best fitting continuous forms.

A similar procedure was applied to the hypothetical very smooth surface described in section 7. We obtained $g = 0.0025 \mu\text{m}$, $c = 3.17 \times 10^9 \text{ N/cm}^2$, and $m = 5.17$. The graphs of

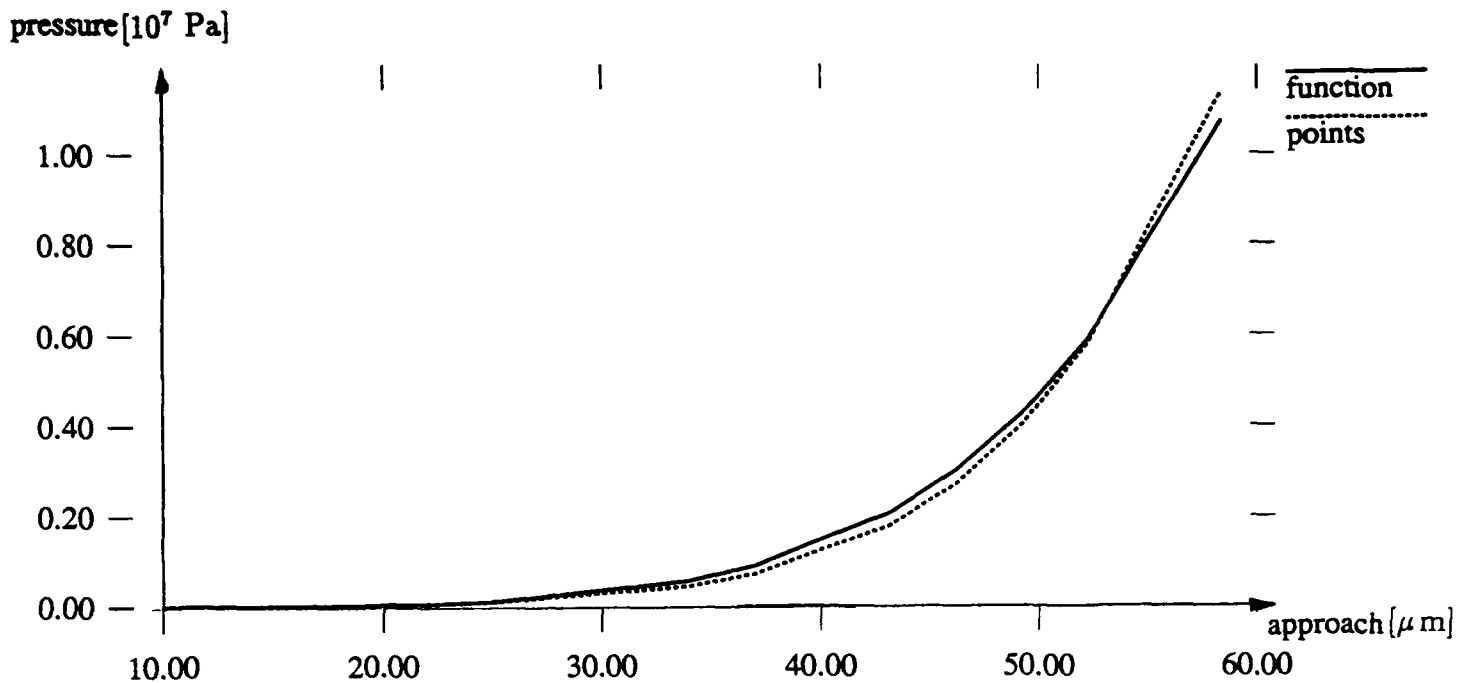


Figure 10.2: Fitting of the Oden - Martins formula to the sequence of discrete points for the very smooth surface

aseperity-based and analytical pressure-approach relationships are shown in figure 10.2.

These examples indicate, that Oden-Martins law provides a good representation of typical constitutive models of metallic interfaces. Note that the approach presented here is applicable to other formulations, such as exponential normal compliance law.

11 Conclusions

This report presented a detailed theoretical background, numerical algorithm, and practical results of the development of new asperity-based constitutive models of frictional interfaces. While the main idea stems from previous works on asperity-based approaches, the application of the adaptive finite element method to the modeling of nonlinear asperity deformation brought these models to a level of practical application to the modeling of real engineering surfaces. This is confirmed by successful comparisons of the asperity-based predictions with the results of carefully designed verification experiments.

The new models developed in this work will find application in many diverse aspects of the modeling of friction, such as:

- simulation and control of friction-induced squeaks, stick-slip motion, chatter, and other unstable phenomena,
- precise modeling of tribological surfaces, such as rollers, bearings, etc.
- modeling the conductivity of thermal and electrical connections, including microelectronic devices and semiconductors,
- understanding and modeling of surface damage and wear mechanisms,
- and many others.

Indeed, the results of this research project are already finding their way into practical applications in several of the above areas.

It is important to note, however, that there remain many open questions and challenges in this topic, including:

- extensions to hyperelastic and brittle materials,
- extensive studies of surface sliding and various components of frictional resistance (shearing, interlocking, and ploughing),
- studies of mechanisms of surface damage and wear,
- extensions to hydrodynamics lubrication,
- dynamic loading of the surface and high-velocity sliding, etc.

These issues need to be addressed in the future to provide a full understanding and control of the complex phenomena occurring in frictional interfaces.

12 References

1. Abbott, E. J., and Firestone, F. A., "Specifying Surface Quality," *Mechanical Engineering*, Vol. 55, p. 569, 1933.
2. Amontons, G., "De la Résistance Causeé dans les Machines," *Memoires de l'Academie Royale*, pp. 275-282, 1699.
3. Andrew, C., Cockburn, J. A., and Waring, A. E., "Metal Surfaces in Contact Under Normal Forces: Some Dynamic Stiffness and Damping Characteristics," *Proc. Instn. Mech. Engrs.*, 182(3K), pp. 92-100, 1968
4. Back, N. Burdekin, M., and Cowley, A., "Review of the Research on Fixed and Sliding Joints," *Proc. 13th Internat. Machine and Tool Design and Research Conference*, pp. 87-97, ed. by S. A. Tobias and F. Koenigsberger, MacMillan, London, 1973.
5. Bank, R. E., Sherman, A. H., and Weisr, A., "Refinement Algorithms and Data Structures for Regular Mesh Refinement," in *Scientific Computing*, R. Stepleman, *et al.* (Eds), IMACS, North Holland, 1983.
6. Bass, J. M., and Oden, J. T., "Adaptive Finite Element Methods for a Class of Evolution Problems in Viscoplasticity," *Int. J. Eng. Sci.*, Vol. 25, No. 6, pp. 623-653, 1987.
7. Bass, J. M., and Oden, J. T., "Numerical Solution of the Evolution Equations of Damage and Rate-Dependent Plasticity," *Int. J. Engng. Sci.*, Vol. 26, No. 7, pp. 713-740, 1988.
8. Bay, N., and Wanheim, T., "Real Area of Contact and Friction Stress at High Pressure Sliding Contact," *Wear*, 38, pp. 201-209, 1976.
9. Bobrik, P. I., **Effect of the Surface Finish of Metals on Loaded Joints**, Thesis, Moscow Inst. Aircraft Technol. (MATI), 1947.
10. Bodner, S. R., "Review of a Unified Elastic-Viscoplastic Theory," in *Unified Constitutive Equations for Plastic Deformation and Creep of Engineering Alloys* (Edited by A. K. Miller), Elsevier and Applied Science, London, 1985.
11. Bodner, S. R., and Chan, K. S., "Modeling of Continuum Damage for Application in Elastic-Viscoplastic Constitutive Equations," *Engineering Fracture Mechanics*, Vol. 25, Nos. 5-6, pp. 705-712, 1986.

12. Bodner, S. R., and Partom, Y., "A Large Deformation Elastic-Viscoplastic Analysis of a Thick Walled Spherical Shell," *Journal of Applied Mechanics*, **39**, p. 751, 1972.
13. Bowden, F. P., and Tabor, D., **The Friction and Lubrication of Solids**, Clarendon Press, Oxford, 1950.
14. Bowden, F. P., and Tabor, D., **The Friction and Lubrication of Solids, Part II**, Clarendon Press, Oxford, 1964.
15. Boyd, J., and Robertson, B. P., "The Friction Properties of Various Lubricants at High Pressures," *Trans. ASME*, **67**, pp. 51-59, 1945.
16. Brandt, S., "Statistical and Computational Methods in Data Analysis," North Holland, 1976.
17. Briscoe, B. J., Scruton, B., and Willis, F. R., "The Shear Strength of Thin Lubricant Films," *Proc. Roy. Soc. (London)*, A333, pp. 99-114, 1973.
18. Briscoe, B. J., and Tabor, D., "The Effect of Pressure on the Frictional Properties of Polymers," *Wear*, **34**, pp. 29-38, 1975.
19. Brockley, C. A., and Davis, H. R., "The Time Dependence of Static Friction," *Journ. Lubr. Technol.*, **90**, pp. 35-41, 1968.
20. Broniec, Z., and Lenkiewicz, W., "Static Friction Process Under Dynamic Loads and Vibration," *Wear*, **80**, pp. 261-271, 1980.
21. Buckley, D., "The Metal-to-Metal Interface and its Effect on Adhesion and Friction," *Journ. of Colloid and Interface Science*, **58**, pp. 36-53 1977.
22. Burwell, J. T., and Rabinowicz, E., "The Nature of the Coefficient of Friction," *Journ. Appl. Phys.*, **24**, 2, pp. 136-139, 1953.
23. Bush, A. W., Gibson, R. D., and Thomas, T. R., "The Elastic Contact of a Rough Surface," *Wear*, **35**, pp. 87-111, 1975. Cartwright, D. E., Lonquet-Higgins, M. S., "The Distribution of the Maxima of a Random Functions," *Proc. Roy. Soc.*, **237**, Ser. A, pp. 212-232, 1956.
24. Chan, K. S., Lindholm, U. S., Bodner, S. R., Hill, J. R., Weber, R. M., and Meyer, T. G., "Constitutive Modeling for Isotropic Materials (HOST)," *Third Annual Report*, Southwest Research Institute, San Antonio, Texas, NASA Cr-179522, August, 1986.

25. Chan, K. S., Lindholm, U. S., and Bodner, S. R., "Constitutive Modeling for Isotropic Materials (HOST)," *Final Report*, Southwest Research Institute, San Antonio, Texas, NASA CR-182132, June, 1988.
26. Chang, H. T., Etsion, I., and Bogy, D. B., "An Elastic-Plastic Model for the Contact of Rough Surfaces," *University of California Berkeley Report*, No. UCB-MICRO 85-126 #1, March 1986.
27. Chang, W. R., Etsion, I., and Bogy, D. B., "Adhesion Model for Metallic Rough Surfaces," *University of California Berkeley Report*, No. UCB-MICRO 85-126 #2, March 1986.
28. Chang, W. R., Etsion, I., and Bogy, D. B., "Static Friction Coefficient Model for Metallic Rough Surfaces," *University of California Berkeley Report*, No. UCB-MICRO 85-126 #3, March 1986.
29. Choiu, Y. C., Kato, L., and Abe, H., "The Effect of Normal Damping in the Loading System on the Wear of Low Carbon Steel," *Wear*, 114, pp. 73-84, 1987.
30. Connoly, R., Schofield, R. E., and Thornley, R. H., "The Approach of Machined Surfaces With Particular Reference to Their Hardness," **Advances in Machine Tool Design and Research**, Proc. 8th Intern. M.T.D.R. Conf., Univ. of Manchester, Part 2, ed. by S. A. Tobias and F. Koenigsberger, Pergamon Press, Oxford, pp. 759-775, 1967.
31. Connoly, R., and Thornley, R. H., "The Significance of Joints on the Overall Deflection of Machine Tool Structures," **Advances in Machine Tool Design and Research**, Proc. of the 6th Intern. M.T.D.R. Conf., ed. by S. A. Tobias and F. Koenigsberger, pp. 139-156, Pergamon Press, Oxford, September 1965.
32. Coulomb, C. A., "Theorie des machiens simples," *Memoire de Mathematique et de Physique de l'Academie Royale*, pp. 161-342, 1785.
33. Courtney-Pratt, J. S., and Eisner, E., "The Effect of Tangential Force on the Contact of Metallic Bodies," *Proc. Royal Soc. Lond.*, A238, pp. 529-550, 1957.
34. Demkowicz, L., Oden, J. T., Rachowicz, W., and Hardy, O., "Toward a Universal $h-p$ Adaptive Finite Element Strategy. Part 1: Constrained Approximation and Data Structure," *Comp. Meth. in Appl. Mech. and Engrg.*, 77, pp. 79-112, 1989.
35. Demkowicz, L., and Oden, J. T., "A Review of Local Mesh Refinement Techniques and Corresponding Data Structures in h -Type Adaptive Finite Element Methods,"

TICOM Report 88-02, The Texas Institute for Computational Mechanics, The University of Texas at Austin, Texas 78712.

36. Derjaguin, B. V., Muller, V. M., and Toporov, Y. P., "Effect of Contact Deformations on the Adhesion of Particles," *Journal of Colloid and Interface Science*, **53**, pp. 314-326, 1975.
37. Drucker, D. C., "Coulomb Friction, Plasticity and Limit Loads," *J. Appl. Mech., Trans. ASME*, **21**, pp. 71-74, 1954.
38. Felder, E., "Formulation thermodynamique des interactions superficielles entre deux corps," *Journal de Mecanique Theorique et Appliquee*, **4**, 2, pp. 283-303, 1985.
39. Ferrante, J., Smith, J., and Rose, J. H., "Metallic Adhesion and Bonding," *Tribology in the 80's*, NASA CP2300, pp. 143-163, 1983.
40. Ferrante, H. A., "Phenomenological Analysis of Plastic Spherical Indentation," *ASME Journal of Engineering Material Technology*, **98**, pp. 272-281, 1976.
41. Francis, H. A., "Application of Spherical Indentation Mechanics to Reversible and Irreversible Contact Between Rough Surfaces," *Wear*, **45**, pp. 261-269, 1977.
42. Fuller, K. N. G., and Tabor, D., "The Effect of Surface Roughness on the Adhesion of Elastic Solids," *Proc. Roy. Soc. (London)*, A345, pp. 327-342, 1975.
43. Gordon, W. J. , Hall, Ch. A., "Construction of CurvLinear Co-Ordinate Systems and Applications to Mesh Generation", *Int. J. Num. Meth. in Engng.*, **7**, pp. 461-477, 1973.
44. Greenwood, J. A., and Tripp, J. H., "The Elastic Contact of Rough Spheres," *Journal of Applied Mechanics*, **34**, pp. 134-159, 1967.
45. Greenwood, J. A., and Williamson, J. B. P., "Contact of Nominally Flat Surfaces," *Proc. Roy. Soc. (London)*, Series A295, pp. 300-319, 1966.
46. Gu, J. C., Rice, J. R., Ruina, A. L., and Tse, S. T., "Slip Motion and Stability of a Single Degree of Freedom Elastic System With Rate and State Dependent Friction," *J. Mech. Phys. Solids*, 1983.
47. Halling, J., and Nuri, K. A., in dePater, A. D. and Kalker, J. J. (Eds.) "The Mechanics of the Contact Between Deformable Bodies," **Delft University Press**, Delft, pp. 330-341, 1975.

48. Hertz, H., "Über die Beruhrun fester elast sche Korper und über die Harte," *Verhandlungen des Vereins zur Beforderung des Gewerbefleisses Leipzig*, Nov. 1882.
49. Hisakado, T., "Effect of Surface Roughness on Contact Between Solid Surfaces," *Wear*, **28**, pp. 217-234, 1974.
50. Hisakado, T., and Tsukizoe, T., "Effects of Distribution of Surface Slopes and Flow Pressures of Contact Asperities on Contact Between Solid Surfaces," *Wear*, **30**, pp. 213-227, 1974.
51. Johannes, V. I., Green, M. A., and Brockley, C. A., "The Role of the Rate of Application of the Tangential Force in Determining the Static Friction Coefficient," *Wear*, **24**, pp. 384-385, 1973.
52. Johnson, K. L., Kendall, K., and Roberts, A. D., "Surface Energy and the Contact of Elastic Solids," *Proc. Roy. Soc. (London)*, A234, pp. 301-313, 1971.
53. Kato, S., Sato, N., and Matsabayachi, T., "Some Considerations on Characteristics of Static Friction of Machine Tool Slideway," *Journ. Lubr. Technol.*, **94**, pp. 234-247, 1972.
54. Kikuchi, N., and Oden, J. T., *Contact Problems in Elasticity: A Study of Variational Inequalities and Finite Elements*, SIAM, Philadelphia, 1988.
55. Kumar, V., Morjaria, M., and Mukherjee, S., "Numerical Integration of Some Constitutive Models of Inelastic Deformation," *J. Engineering Materials and Technology*, Vol. 102, pp. 92-96, Jan. 1980.
56. Lindholm, U.S., Chan, K.S., Bodner, S.R., Weber, R.M., Walker, V.P., Bassenti, B.N., "Constitutive Modeling for Isotropic Materials", annual report NASA CR 174980, Contract No. NAS3-23925, 1985.
57. Lonquet-Higgins, M. S., "The Statistical Analysis of a Random Moving Surface," *Phil. Trans. of Roy. Soc.*, **249**, Ser. A, pp. 321-387, 1957.
58. Lonquet-Higgins, M. S., "Statistical Properties of an Isotropic Random Surface," *Phil. Trans. of Roy. Soc.*, **250**, Ser. A, pp. 157-174, 1957.
59. Lonquet-Higgins, M. S., "The Statistical Geometry of Random Surfaces," in *Hydrodynamic Stability*, Proc. 13th Symp. on Appl. Math., American Math. Society, 1962.

60. Martins, J. A. C., "Dynamic Frictional Contact Problems Involving Metallic Bodies," *Ph.D. Dissertation*, The University of Texas, Austin, Texas, 1985.
61. McCool, J. J., "Predicting Microfracture in Ceramics Via a Microcontact Model," *Trans. ASME, Journal of Tribology*, **108**, pp. 380-386, 1986.
62. McFarlane, J. S., and Tabor, D., "Adhesion of Solids and the Effect of Surface Films," *Proc. Roy. Soc. (London)*, A202, pp. 224-243, 1950.
63. Michalowski, R., and Mroz, Z., "Associated and Non-Associated Sliding Rules in Contact Friction Problems," *Archives of Mechanics*, **30**, pp. 259-276, 1978.
64. Mindlin, R. D., "Compliance of Elastic Bodies in Contact," *Journal of Applied Mechanics*, **16**, pp. 259-268, 1949.
65. Moore, D. F., **Principles and Applications of Tribology**, Pergamon Press, Oxford, 1975.
66. Muller, V. M., Derjaguin, B. V., and Toporov, Y. P., "On Two Methods of Calculation of the Force of Sticking of an Elastic Sphere to a Rigid Plane," *Colloids and Surfaces*, **7**, p. 251, 1983.
67. Muller, V. M., Yushchenko, V. S., and Derjaguin, B. V., "On the Influence of Molecular Forces on the Deformation of an Elastic Sphere and Its Sticking to a Rigid Plane," *Journal of Colloid and Interface Science*, **77**, pp. 91-101, 1980.
68. Nayak, P.R., "Random Process Model of Rough Surfaces," *ASME Journal of Lubrication Technology*, **93**, pp. 398-407, 1971.
69. Nolle, H., and Richardson, R. S., "Static Friction Coefficient for Mechanical and Structural Joints," *Wear*, **28**, pp. 1-13, 1974.
70. Oden, J. T., Demkowicz, L., Rachowicz, W., and Westermann, T. A., "Toward a Universal h - p Adaptive Finite Element Strategy. Part 2: *A Posteriori* Error Estimation," *Comp. Meth. in Appl. Mech. and Engrg.*, **77**, pp. 113-180, 1989.
71. Oden, J. T., and Martins, J. A. C., "Models and Computational Methods for Dynamic Friction Phenomena," *Computer Methods in Applied Mechanics and Engineering*, **52**, pp. 527-634, 1985.
72. Oden, J. T., Martins, J. A. C., and Tworzydlo, W. W., "Computational Methods for Nonlinear Dynamic Problems in Solid and Structural Mechanics: Progress in the

Theory and Modeling of Friction and in the Control of Dynamical Systems With Frictional Forces," COMCO Technical Report, Bolling Air Force Base, AFOSR Contract F49620-86-C-0051, 1989.

73. Pashley, M. D., "Further Consideration of the DMT Model for Elastic Contact," *Colloids and Surfaces*, **12**, pp. 59-77, 1984.
74. Pashley, M. D., and Pethica, J. B., "The Role of Surface Forces in Metal - Metal Contacts," *Journal Vac. Sci. Tech.*, A3, pp. 757-761, 1985.
75. Pashley, M. D., Pethica, J. B., and Tabor, D., "Adhesion and Micromechanical Properties of Metal Surfaces," *Wear*, **100**, pp. 7-31, 1984.
76. Rabier, P., Martins, J. A. C., Oden, J. T., and Campos, L., "Existence and Local Uniqueness of Solutions to Contact Problems in Elasticity with Nonlinear Friction Laws," *International Journal of Engineering Science*, Vol. 24, No. 11, pp. 1755-1768, 1986.
77. Rabinowicz, E., "The Nature of the Static and Kinetic Coefficients of Friction," *Journ. Appl. Physics*, **11**, **22**, pp. 1373-1379, 1951.
78. Rabinowicz, E., "The Intrinsic Variables Affecting the Stick-Slip Process," *Proc. Phys. Soc.*, **71**, pp. 668-675, 1958.
79. Rabinowicz, E., "The Determination Between Solids in Vacuum; II. Deformation and Interfacial Energy," *Journal of Physics*, Vol. 11, pp. 39-54, 1978.
80. Rice, J. R., and Ruina, A. L., "Stability of Steady Frictional Slipping," *ASME Applied Mechanics, Bioengineering, and Fluids Engineering Conference*, Paper No. 83-APM-16, Houston, Texas, June 1983.
81. Richardson, R. S. H., and Nolle, H., "Surface Friction Under Time-Dependent Loads," *Wear*, **37**, pp. 87-101, 1976.
82. Ruina, A. L., **Friction Laws and Instabilities: A Quasistatic Analysis of Some Dry Frictional Behavior**, Ph.D. Thesis, Brown University, Providence, R.I., 1980.
83. Ruina, A. L., "Slip Instability and State Variable Friction Laws," *J. Geophys. Res.*, 1983.
84. Ruina, A. L., "Constitutive Relations for Frictional Slip," *Mechanics of Geomaterials*, ed. by Z. Bazant, John Wiley and Sons, pp. 163-187, 1985.

85. Sampson, J. B., Morgan, F., Reed, D. W., and Muskat, M., "Friction Behaviour During the Slip Portion of the Stick-Slip Process," *Journ. Appl. Physics*, **14**, pp. 689-700, 1943.
86. Sanchez-Palencia, E., and Suquet, P., "Friction and Homogenization of a Boundary," 1983.
87. Soom, A., and Kim, C., "Interactions Between Dynamic Normal and Frictional Forces During Unlubricated Sliding," *Journ. Lubr. Technol.*, **105**, pp. 221-229.
88. Soom, A., and Kim, C., "Roughness-Induced Dynamic Loading at Dry and Boundary-Lubricated Sliding Contacts," *Journ. Lubr. Technol.*, **105**, pp. 514-517, 1983.
89. Tabor, D., "Friction—The Present State of Our Understanding," *Journ. Lubr. Technol.*, **103**, pp. 169-179, 1981.
90. Tallian, T. E., *Wear*, **21**, p. 49, 1972.
91. Timoshenko, S. and Goodier, J.N., **Theory of Elasticity**, McGraw-Hill, New York, 2nd edition.
92. Towle, L. C., "Shear Strength and Polymer Friction," *Am. Chem. Soc. Polymer Science and Technology*, Vol. 5A, pp. 179-189, 1974.
93. Tworzydlo, W., and Becker, E., "Influence of Forced Vibrations on the Static Coefficient of Friction—Numerical Analysis," *Wear*, **143**, pp. 175-186, 1991.
94. Tworzydlo, W., and Becker, E., "Numerical Study of Friction-Induced Vibrations and Dynamic Instabilities of Frictional Systems," in **Friction-Induced Vibration, Chatter, Squeal, and Chaos**, Ibrahim, R.A. and Soom, A., editors, ASME Publications, New York, 1992, pp. 13-32.
95. Tworzydlo, W., and Oden, J.T., "New Micro- and Macroscopic Models of Contact and Friction," annual report, AFOSR contract F49620-91-C-0011, 1991.
96. Tworzydlo, W.W. and Oden, J.T., "Towards an Automated Environment in Computational Mechanics", to appear in *Comp. Meths. Appl. Mech. Engng.* in 1993.
97. Villaggio, P., "An Elastic Theory of Coulomb Friction," *Archive for Rational Mechanics and Analysis*, Vol. 70, pp. 135-143, 1979.
98. Votinov, K. V., **The Rigidity of Machine Tools**, Leningrad Section, Machine Builders' Union (LONITOMASH), Leningrad, 1940.

99. Weic, W. L., "The Investigation of the Static Friction and the Direction of Sliding at Low-Frequency External Vibrations," *New in Friction Theory*, Lzd. Akad. Nauk SSSR, Moscow, pp. 60-82, 1962.
100. Whitehouse, D. J., and Archard, J. F., "The Properties of Random Surfaces of Significance in Their Contact," *Proc. Roy. Soc. (London)*, A316, pp. 97-121, 1970.
101. Wilson, Ph.D. Thesis, University of Cambridge, 1952.